Calculation Methodology for Turbine Rotor Fragment Containment

by

Mihai Ovidiu JIVAN

THESIS PRESENTED TO ÉCOLE DE TECHNOLOGIE SUPÉRIEURE
IN PARTIAL FULFILLEMENT FOR A MASTER'S DEGREE
WITH THESIS IN AEROSPACE ENGINEERING
M.A.Sc.

MONTREAL, JULY 10, 2022

ÉCOLE DE TECHNOLOGIE SUPÉRIEURE
UNIVERSITÉ DU QUÉBEC

BOARD OF EXAMINERS

THIS THESIS HAS BEEN EVALUATED

BY THE FOLLOWING BOARD OF EXAMINERS

Mr. Henri Champliaud, Thesis Supervisor
Department of Mechanical Engineering, École de technologie supérieure

Mr. Thien-My Dao, President of the Board of Examiners
Department of Mechanical Engineering, École de technologie supérieure

Mr. Ngan Van Lê, Member of the jury
Department of Mechanical Engineering, École de technologie supérieure

THIS THESIS WAS PRESENTED AND DEFENDED

IN THE PRESENCE OF A BOARD OF EXAMINERS AND PUBLIC

JULY 5, 2022

AT ÉCOLE DE TECHNOLOGIE SUPÉRIEURE

ACKNOWLEDGMENT

Without the support received from exceptional persons, a work of this complexity could not have been achieved. Their encouragements, technical challenges, critical thinking, and advice shaped this research into its final form.

Firstly, I would like to express my gratitude to Prof Henri Champliaud, my research director, for his patience, encouragement, guidance, technical support, and friendship during these years. I was very fortunate to have such a mentor guiding me through this complicated endeavour, with his down-to-earth approach making the many challenges easier than what they seemed.

Also, a big thank you to my friend and colleague Joshua Gladstone, for all his personal time spent on reviewing chapters of this work, and for sharing with me his feed-back, providing me with different perspectives.

My full gratitude as well for Mr. Paul Du Bois, for throwing a serious wrench into my work, with challenging me to adopt a Johnson-Cook material model. This experience opened a lot my perspective into all aspects of material definitions, making me a better engineering professional.

Many thanks to my workplace cheering group, Malak, Gabi, Allen, Josh and all my co-workers who supported me fully in this work, allowing me to disappear from time to time from work duties, when push came to shove.

Finally, my loving family. I cannot express enough my gratitude for the support received during these too many years. I cannot think of a better team, this work would not have been possible without all your support.

Méthode de calcul pour le confinement des fragments du rotor de turbines au gaz

Mihai Ovidiu JIVAN

RÉSUMÉ

Le processus de conception des turbines à gaz est complexe, soumis à de nombreuses réglementations imposées par les autorités nationales et internationales, et aussi gouverné par des impératifs économiques dans un marché concurrentiel. Partie intégrante de ce processus, les méthodologies analytiques actuelles utilisées pour déterminer l'épaisseur minimale de caissons de turbines à gaz mènent souvent à des résultats imprécis.

Cette étude propose une nouvelle procédure analytique pour déterminer l'épaisseur minimale du caisson de turbine requise pour le confinement d'un fragment de rotor. Cette méthode groupe les résultats d'investigation de trois domaines de recherche distincts: le confinement des fragments de rotor de turbine à gaz, la balistique terminale et l'analyse par éléments finis.

Les hypothèses généralement acceptées par l'industrie concernant le confinement des fragments sont que toute l'énergie cinétique de translation du fragment est échangée avec le caisson, que la zone d'impact est proportionnelle aux dimensions de la lame de l'aube, que le fragment est considéré comme non déformable et que l'impact des aubes suivantes est négligeable. Ce mémoire présente un modèle de confinement amélioré: l'énergie cinétique de translation du fragment est partiellement échangée avec le caisson, la déformation du fragment et son interaction avec les aubes suivantes ne sont pas négligeables. De plus, il s'avère que, contrairement à la modélisation traditionnelle, l'endommagement principal est créé par la section volumineuse (le pied, la plateforme ou le carénage) et non par la lame de l'aube. Enfin, cette étude met en évidence les principales différences entre la modélisation du confinement d'un fragment de l'aube carénée par rapport à un fragment de l'aube sans carénage, aspects non pris en compte dans la littérature actuelle.

Certains chercheurs, lors de la caractérisation du modèle balistique terminal, supposent que les dommages résultent du cisaillement du caisson, tandis que d'autres supposent que la tension et/ou la flexion sont les principaux modes de défaillance. Ce travail de maîtrise propose une nouvelle méthodologie qui considère les deux principaux modes de rupture, cisaillement et étirement, comme une fonction de la géométrie du fragment et des conditions cinématiques.

La méthode proposée a été validée avec des résultats obtenus lors d'essais de confinement sur deux moteurs Pratt&Whitney jugés représentatifs pour les grandes turbines à gaz: JT3D et JT8D. Le matériau du caisson (A-286) a été défini en utilisant le modèle de Johnson-Cook, qui est considéré comme le point de la technologie de définition du matériel en LS-DYNA. Les courbes de matériaux ont été calibrées avec les résultats obtenus à partir de essais effectués à différentes températures et vitesses de déformation. Le facteur de dommage des matériaux a été déterminé à partir d'une autre série d'essais en tant que fonction de surface de différentes triaxialités et de paramètres de Lode.

En résumé, ce mémoire propose une méthodologie analytique pour la conception préliminaire de caissons de turbines à gaz pour le confinement de fragments par suite d’une défaillance du rotor. Ce modèle amélioré du phénomène d'impact conduit à des résultats précis dans la phase de conception préliminaire et amène en conséquence des réductions de poids importantes.

Mots-clés: confinement, turbines au gaz, impact, fragment du rotor, défaillance du rotor, aube de turbine, LS-DYNA, Johnson-Cook

Calculation Methodology for Turbine Rotor Fragment Containment

Mihai Ovidiu JIVAN

ABSTRACT

The design process of gas turbine engines is complex, subjected to numerous regulations imposed by national and international authorities and driven by economical requirements in a competitive market. Within the design process, predictive analytical methods are used to determine the minimum case thickness necessary to contain the high-energy fragments that may be released by a compressor or turbine rotor failure. The current methodologies often lead to inaccurate results.

This study proposes a new analytical method to determine the minimum turbine case thickness required for the containment of a rotor fragment, based on investigation results from three distinct research areas: gas turbine rotor fragment containment, terminal ballistics, and finite element analysis.

The general agreement in the industry regarding fragment containment is that all the translational kinetic energy of the fragment is exchanged with the casing, the impact area is proportional with the blade dimensions, the fragment is considered not deformable, and the following blades contribution to the impact is negligible. The present research shows that a fraction of the translational kinetic energy of the fragment is exchanged with the casing and reveals that the deformation of the blade fragment and its interaction with the following blades are not negligible. In addition, it proves that contrary to the legacy modeling, the blade fragment airfoil does not significantly affect the casing, as the main damage is created by the bulky section (the shroud, the blade platform, or its root). Finally, this study highlights key differences between modeling the containment of a shrouded versus a shroudless blade fragment, aspects not considered in the current literature.

Some researchers, when characterizing the terminal ballistic model, assume the damage as resulting from shearing of the casing, while others assume tension and/or bending as primary failure modes. This thesis proposes a new methodology based on defining the threshold between the two main modes of failure, shearing and membrane stretching, as an established function of the fragment geometry and kinematic conditions.

The proposed methodology has been validated with results obtained during containment tests on two Pratt&Whitney engines deemed representative for large gas turbines: JT3D and JT8D. The casing material (A-286) has been characterized using the state-of-art material model definition (Johnson-Cook). The material curves have been calibrated with results obtained from tests performed at various strain rates and temperatures. The damage factor was determined from another series of tests as a surface function of different triaxialities and Lode parameters.

In summary, the present work proposes a new, refined analytical method to determine the minimum thickness required for a gas turbine case to successfully contain a single blade fragment released from the rotor. This improved model of the impact phenomenon leads to accurate results in the preliminary design phases, which translate subsequently in significant weight reduction.

Keywords: containment, gas turbine, impact, rotor failure, rotor fragment, turbine blade, LS-DYNA, Johnson-Cook

TABLE OF CONTENTS

Page

LIST OF TABLES

Page

LIST OF FIGURES

Page

LIST OF ABREVIATIONS

AC	Advisory Circular
AISI	American Iron and Steel Institute
APU	Auxiliary Power Unit
ASB	Adiabatic Shear Band
AWG	Aerospace Working Group (LS-DYNA)
CPU	Central Processing Unit
CT	Compressor Turbine
EASA	European Union Aviation Safety Agency
FAA	Federal Aviation Administration
FAR	Federal Acquisition Regulation
FE	Finite Element
FEA	Finite Element Analysis
FEM	Finite Element Model
GE	General Electric
GWU	George Washington University
HCF	High Cycle Fatigue
HPT	High Pressure Turbine
ID	Inner Diameter
IPT	Intermediate Pressure Turbine
JAA	Joint Aviation Authorities
J-C	Johnson-Cook
KE	Kinetic Energy

LCF	Low Cycle Fatigue
LPT	Low Pressure Turbine
MIT	Massachusetts Institute of Technology
MPP	Massively Parallel Processing
NAPC	Naval Air Propulsion Center
NAPTC	Naval Air Propulsion Test Center
NASA	National Aeronautics and Space Administration
NASA-GRC	NASA Glen Research Center
OEM	Original Equipment Manufacturer
OSU	Ohio State University
PT	Power Turbine
R-O	Ramberg-Osgood
SAE	International Engineering Society for Advancing Mobility Land Sea Air and Space (formerly Society of Automotive Engineers)
SCFE	Specific Containment Fragment Energy
SHB	Split Hopkinson Bar
SMP	Shared Memory Parallel
UTC	United Technologies Corporation
UTS	Ultimate Tensile Strength
YTS	Yield Tensile Strength

LIST OF SYMBOLS

a	impact area, area of contact
A	true stress at necking
b	circumferential length of the impact area
b_x	axial projection of the blade tip
B	true plastic strain at necking
B_h	blade height
C	slope at necking (hardening modulus)
c	correction factor for the effective circumferential length of the case
CF	containment factor
CV	containment volume
D	damage (failure criteria)
D_n	nominal diameter of casing
d	empirical dynamic factor
E	Young modulus
e	failure strain
E_c	plastic strain energy in compression
E_{fract}	kinetic energy fraction
E_s	shear strain energy
E_t	tensile strain energy
E_{TAN}	tangential kinetic energy
H	plate thickness
h	platform height
J_3	deviatoric stress invariant

K	experimental constant
K_1, K_2	constant determined empirically
$K_{exchange}$	kinetic energy exchange ratio
KE	kinetic energy
KE_B	kinetic energy of the rotor at burst
KE_{final}	kinetic energy threshold for determination of failure modes
KE_{fract}	fraction of kinetic energy
k	fitting parameter for Swift strain hardening equation
l	bending moment arm
L_A	axial length of the ring or casing
l_e	element size
MF	material factor
Mp	bending moment
n	hardening coefficient
n_b	number of blades in the rotor stage
P	perimeter
p	pressure
PE	plastic deformation energy
PE_{casing}	casing plastic deformation energy
$PE_{tensile}$	plastic tensile deformation energy
PE_{shear}	plastic shear deformation energy
PE_{th}	plastic energy threshold
Q	strained volume of the material
r_m	missile radius

r_i	inner radius of the containment ring
S_{ij}	deviatory stress tensor
t, T	casing or containment radial ring thickness
t_{shear}	containment thickness assuming shear
$t_{tensile}$	containment thickness assuming tensile
T*	normalized temperature
t_{cont}	containment thickness
t_{th}	threshold thickness
U	ultimate tensile strength
Uds	dynamic shear strength
$W_{bending}$	bending strain energy
w	axial width of the blade fragment
W_r	containment ring weight
W_R	weight of the ring
W_{shear}	shear energy
$W_{stretching}$	membrane stretching strain energy
α	area correction factor
β	perimeter correction factor
δ	deflection
ε	plastic strain
$\dot{\varepsilon}$	plastic strain rate
$\dot{\varepsilon}$*	strain rate
$\dot{\varepsilon_p}$	plastic strain rate
ε_{pf}	effective failure plastic strain

ε_f	effective plastic strain
ε_{fail}	elongation at tensile fracture
ε_e	hardening parameter for strain at necking (Swift's hardening equation)
ε_{eng}	engineering strain
ε_{pf}	effective plastic failure strain
ε_{pl}	effective plastic strain
ε_{true}	true strain
γ	strain correction factor
ω	angular rotation speed
$\theta_{bending}$	bending angular deformation (rotation around the hinge points)
θ_i , θ_L	Lode parameter characterizing the state of stress
ρ	material density
σ	stress
σ^*	stress triaxiality
σ_0	stress flow
σ_d	average dynamic plastic flow stress
σ_{eng}	engineering stress
σ_u	ultimate stress
σ_{true}	true stress
σ_{VM}	Von Mises stress
σ_{yield}, σ_y	yield stress
τ	stress triaxiality
τ_D	dynamic shear strength
τ_s	quasi-static shear stress

INTRODUCTION

One of the most remarkable inventions of the modern era is the gas turbine, which has revolutionized electric power generation and is the fundamental technology behind modern jet powered aviation. Formidable machine, the gas turbine is capable to generate tremendous power, while operating under extreme thermo-mechanical internal loading. Despite having addressed many of the technological challenges (through advances in materials and manufacturing technologies, computer aided methods and stringent quality standards), defects still can occur, leading to undesired local or even global effects, from localized permanent deformations, or initiation of fractures possibly followed by loss of material, which in turn increase the risk of fire or pressure or fragment non-containment. As gas turbine engines operate at high rotational velocities, potential fragments detached from the rotating assemblies are released with high kinetic energies. Fragments not contained by the surrounding structures constitute a threat to the safe operation of the engine.

For aeronautical application, international airworthiness authorities have imposed regulations on the development and design process of aircraft and engine manufacturers to ensure the safe operation of their products. Fragment containment represents one of the structural criteria verified during the development of the engines. Engine Original Equipment Manufacturers (OEM's) and airworthiness authorities collaborated with academia and suppliers to develop robust and efficient fragment containment design methods. However, currently there is no consensus on a consolidated method to be employed in the early phases of structural design when the geometries of components are still in the definition phase.

The existing analytical methods developed by the main engine manufacturers for preliminary design need further development, particularly in the appropriate selection of the failure mode, which is dependent of the fragment shape and energy exchange.

Most of the analytical methods consider shear-based failure as the governing principle, however as it was demonstrated by a plenitude of ballistic tests, the most efficient energy absorption by plastic deformation is through a combined tensile + bending failure mode. Designing the casings based on the shear failure mode is therefore not optimal.

Another aspect needing reconsideration is the assumption that the fragment deformation is negligible. This research demonstrates that only a small percentage of the initial kinetic energy of the fragment is transferred to the casing, as most of it is dissipated through own deformation and interaction with the following blades (neglected in the current methods).

The fragment geometry is another aspect on which gas turbines manufacturers do not commonly agree, considering different blade features such as blade height, chord, or empirically determined coefficients instead. The current analytical methods impact perimeter needs a more accurate definition. As it will be revealed in this work, the main damage to the casing is caused by the bulky feature of the fragment, when pushed into the casing by the following blades.

This research proposes a novel and consolidated approach to the preliminary design analytical method for determining the minimum necessary thickness of a gas turbine engine, to successfully contain (not allowing the casing penetration or perforation by) a blade released from the turbine rotor. As the physics of the containment problem resides on the same principles contributing to the development of the current methods (enumerated by Lane in (Lane, 1989)), particularly the dissipation of kinetic energy through plastic work, there is commonality with the existing methods developed by OEM's, the novelty being the definition of the blade fragment participating in the energy exchange, the quantification of the exchanged energy and the material properties effect on the containment capability of the casing, all contributing to its mode of failure.

The structure of this thesis consists in four sections, the first chapter detailing the background of the gas turbine rotor fragment containment research topic and provides a literature survey of the main aspects comprised in this topic: the rotor fragment containment (macro level, interactions between engine components, analytical methods), the ballistic (micro) perspective, and the last component being relevant findings from studies performed with finite element analyses (FEA).

The second chapter presents the objectives of this thesis and the methodology employed to reach these objectives.

The third chapter is dedicated to finite element analyses performed to determine the variables needed in the analytical method. The first part of this chapter details the actual testing on which the analytical method is validated, followed by the details of the model setup and results. In the last part of this third chapter are detailed the FEA results for different case studies.

The fourth chapter details some of the current analytical methods and proposes the formulation for the new analytical method to be used to determine the casing thickness for fragment containment, based on the results of FEA.

The last chapters collect the conclusions, observations, and future works recommendations.

CHAPTER 1

LITERATURE REVIEW

Since early days in their development, gas turbines preoccupied the engineering community involved in their development and operation, with searching to continuously improve their safe operation, and minimize the hazards of non-contained failure.

Hence, a vast technical literature domain is dedicated to the fragment containment topic. This chapter identifies several topics relevant to the object of this research, their sources and development. First subsection of this chapter is dedicated to introducing the gas turbines development, enumerating the risks of rotor failure, and presenting some of the rotor fragment characteristics. The second section describes the literature review covering the ballistic approach, the rotor fragment containment, and the progress in FEA dedicated to rotor fragment containment.

1.1 Gas turbine introduction

Although early development revealed a technology less efficient than the steam turbines and Diesel engines used to generate power at the beginning of the century, by 1970 gas turbines had become the main propulsion standard for aircrafts, opening the air travel to the masses (Saravanamuttoo, Rogers, Cohen, & Straznicky, 2009) (Trent 1000 turbofan (Rolls-Royce, 2022) shown in Figure 1.1).

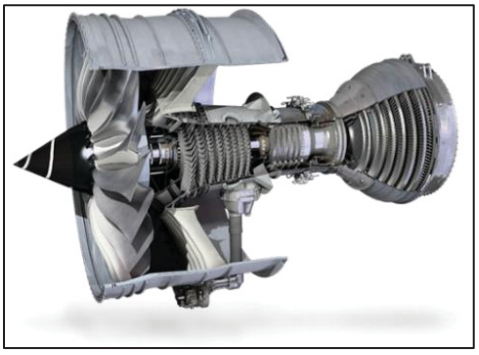

Figure 1.1 Trent 1000 optimized for Boeing 787 Dreamliner
Taken from the Rolls Royce presentation website (2022)

For non-aeronautical purposes, the development was relatively slower, but by the end of the 20th century, the thermal efficiencies and power outputs increased allowing them to be widely used in power generation (Saravanamuttoo, Rogers, Cohen, & Straznicky, 2009). Another application of gas turbine is in the Oil and Gas industry; where the power of gas turbines is harnessed to compress natural gas into a liquid and transport it via pipeline (Figure 1.2, (Stewart, 2018)).

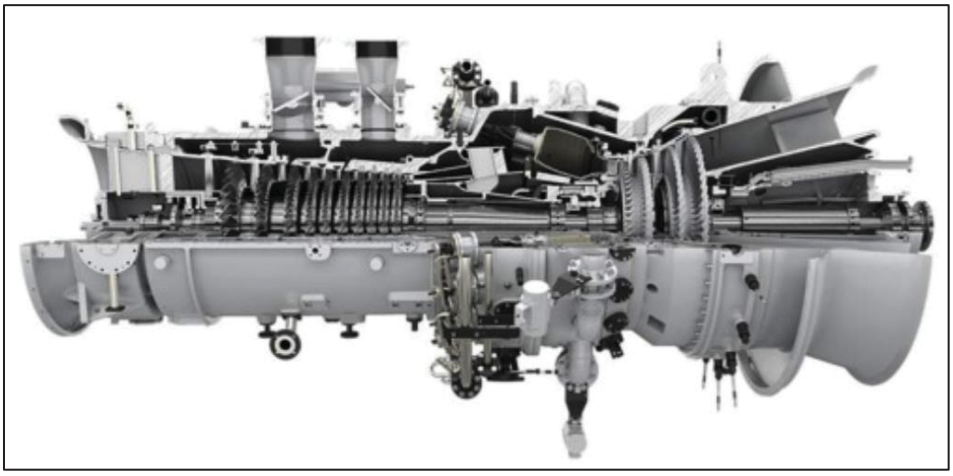

Figure 1.2 Industrial gas turbine
Taken from Stewart (2018)

In gas turbines, all rotating components are subjected to centrifugal forces, shear and torsional aerodynamic forces generating bending moments on the airfoils, dynamic, aeroelastic and thermal loading. Static structures (vanes, cases, bearing and baffles) are also subjected to thermo-mechanical loading and need to be allowed to expand without generating high stresses, nor generate interferences with the rotating components.

As gas turbine engines operate at high rotational velocities, potential fragments are released from the rotating assemblies (may be a single blade, multiple blades released as shown in Figure 1.3 (Japan Transport Safety Board, 2011), combinations of multiple blades and disk fragments or even fully bladed discs) with high kinetic energies. Fragments not contained by the surrounding structures constitute a threat to the safe operation of the engine (Figure 1.4, as reported in (Australian Transport Safety Bureau, 2010)).

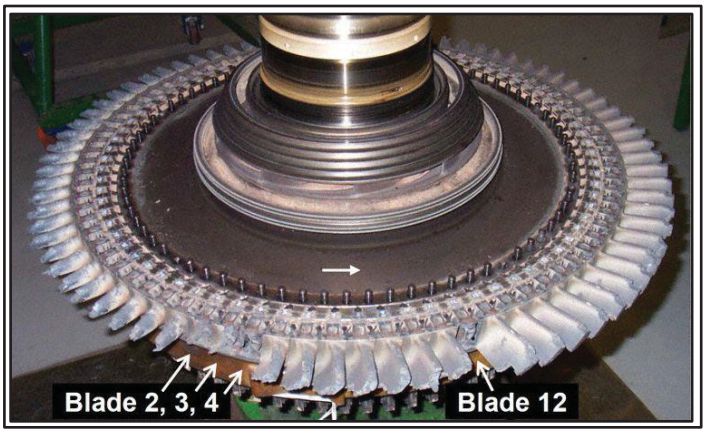

Figure 1.3 HPT Blade released from a General Electric CF6 engine
Taken from Japan Transport Safety Board" (2011, p. 21)

Figure 1.4 IPT Disc tri-hub uncontained failure on a Rolls-Royce Trent 972-84
Taken from Australian Transport Safety Bureau, (2013, p. 54, 258)

General guidance detailing design precautions minimizing the risks to aircraft was harmonized internationally between Aviation Authorities (Federal Aviation Administration, U.S. Department Of Transportation, 1997).The development of design methods for fragment containment (Rossman, Axel; Institute of Thermal Turbomachinery and Machine Dynamics; Graz University of Technology, 2021) was substantiated with component and assembly spin pit testing and even full engine tests.

Despite the precaution taken during the development, manufacturing and operation of gas turbines, un-expected events or defects can occur on components of a gas turbine, causing rotor failure. Multiple studies and reports identified the different causes, types of failure and fragment characteristics (as shown in Figure 1.5), from some of the early studies (McCarthy, Definition of engine debris and some proposals for reducing potential damage to aircraft structure, 1976), (McCarthy, Types of rotor failure and characteristics of fragments, 1977), leading to more recent statistics (SAE International Engineering Society for Advancing Mobility Land Sea Air and Space, 1996). The Society of Automotive Engineers (SAE) Aerospace Information Report AIR1537, reveals that the total number of non-contained failures for turbines is higher than the number of failures occurring in the compressor module, and much higher than the non-contained cases of fan discs or blades (Table 1.1).

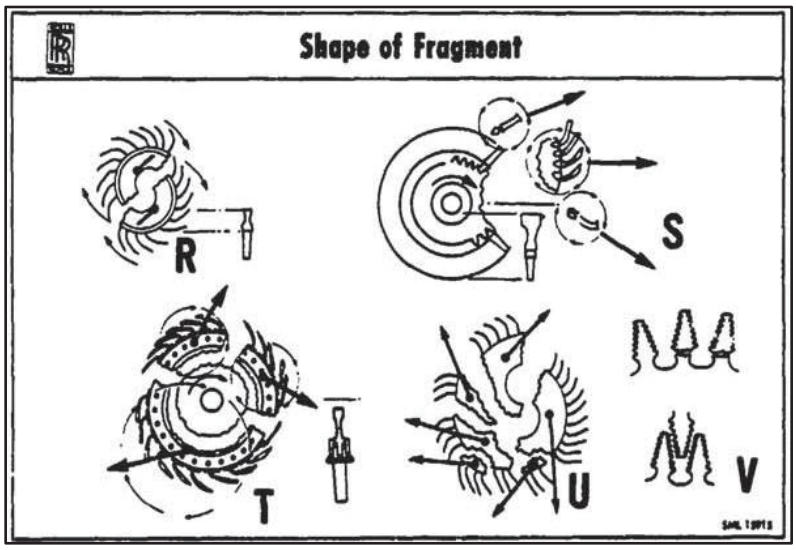

Figure 1.5 Different shapes of fragments
Taken from McCarthy (1977, p. 77)

As per the SAE AIR1537 (SAE International Engineering Society for Advancing Mobility Land Sea Air and Space, 1996), the first three main causes for non-contained failures were: high cycle fatigue (HCF), rubbing against static parts and material defects (Table 1.2).

Table 1.1 Non-contained failures classified by fragment origin
Taken from SAE International (1996, p. 12)

Fragment Type	Number of Failures: All Categories	Number of Failures: Category 3 and 4	Failure Rate Per Million Hours: All Categories	Failure Rate Per Million Hours: Category 3 and 4	Percent of Failures: All Categories	Percent of Failures: Category 3 and 4
Fan Disk, Spacer	23	12	0.055	0.029	8.4	4.4
Fan Blade	32	2	0.077	0.005	11.6	0.7
Compressor Disk, Spacer	77	17	0.185	0.041	28.0	6.2
Compressor Blade	22	2	0.053	0.005	8.0	0.7
Turbine Disk, Spacer	56	9	0.134	0.022	20.4	3.3
Turbine Blade	65	7	0.156	0.017	23.6	2.5
Total Non-Contained	275	49	0.66	0.119	100.0	17.8

January, 1962 - December, 1975: 417 Million Engine Hours

A thin line is drawn between the initiation of different failure modes, as in many cases there are superpositions of several conditions, such as a material defect or corrosion initiating the fracture which in turn propagates rapidly in high-cycle fatigue HCF or at a slower rate in low-cycle fatigue (LCF).

Table 1.2 Non-contained failures for disks, Spacers and Blades by cause of failure
Taken from SAE International (1996, p. 13)

Cause of Failure	Primary or Secondary Failure	Number of Failures	Failure Rate per Million Hours	Percent of Failures
Unknown	--	58	0.139	21.1
High Cycle Fatigue	Primary	52	0.125	18.9
Rubbing Against Static Parts	Secondary	28	0.067	10.2
Material Defects	Primary	25	0.060	9.1
Foreign Object Damage	Secondary	15	0.036	5.5
Overtemperature	Secondary	15	0.036	5.5
Low Cycle Fatigue	Primary	15	0.036	5.5
Other	--	14	0.034	5.0
Manufacturing Defects	Primary	14	0.034	5.0
Shaft and Shaft Retention Bolt Failure	Secondary	13	0.031	4.7
Overhaul Procedures	Primary	11	0.026	4.0
High Cycle Fatigue	Secondary	10	0.024	3.6
Mis-Assembly	Primary	3	0.007	1.1
Combination of HCF and LCF	Primary	1	0.002	0.4
Overspeed	Secondary	1	0.002	0.4
Total Non-Contained		275	0.659	100.0

January, 1962 - December, 1975: 417 Million Engine Hours

More details about failure mechanisms of gas turbine rotors are provided among others by McCarthy (McCarthy, Types of rotor failure and characteristics of fragments, 1977), the Institute of Thermal Turbomachinery and Machine Dynamics (Graz University of Technology) on their Aeroengine Safety site (Rossman, Axel; Institute of Thermal Turbomachinery and Machine Dynamics; Graz University of Technology, 2021), or by Hunter et al. (Hunter & al., 1999).

Some of the more usual shapes of rotor fragments are shown in Figure 1.6. The fragment shape depends on the rotor stage, and on the module. The compressor rotors tend to release big fragments (thus more detrimental, Table 1.1, (SAE International Engineering Society for Advancing Mobility Land Sea Air and Space, 1996)), but less frequently than the intermediate and small fragments released by turbines.

Due to the severe operating conditions to which they are subjected, the turbines develop multiple modes of failure (McCarthy, Types of rotor failure and characteristics of fragments, 1977), generating a slightly higher percentage of failures than the compressors, but with less severe consequences.

Hub originating disc fractures (Figure 1.6 (a) and (c), Figure 1.7) generate the largest fragments, thus developing the highest kinetic energies, with devastating effects on their surroundings. Designing the containment of these type of fragments severely penalizes the engine weight. Smaller engines using impellers might be designed against this type of rotor failure, although manufacturing processes ensuring the avoidance of such type of failure are more often considered. Manufacturers for Auxiliary Power Units (APUs) are also protecting their engines against tri-hub failure.

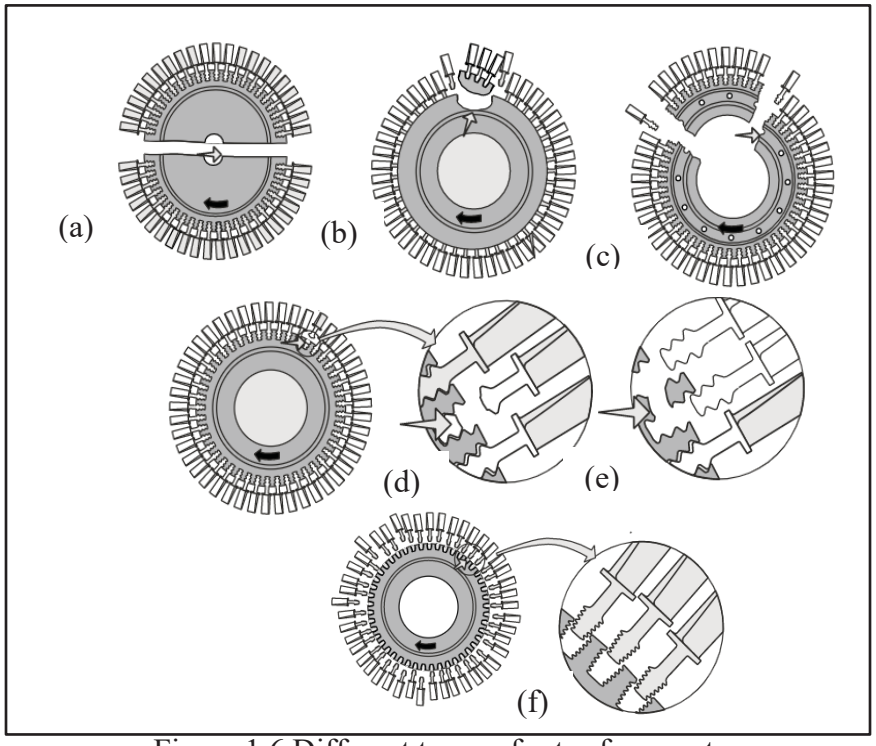

Figure 1.6 Different types of rotor fragments
Taken from Rossman (2021)

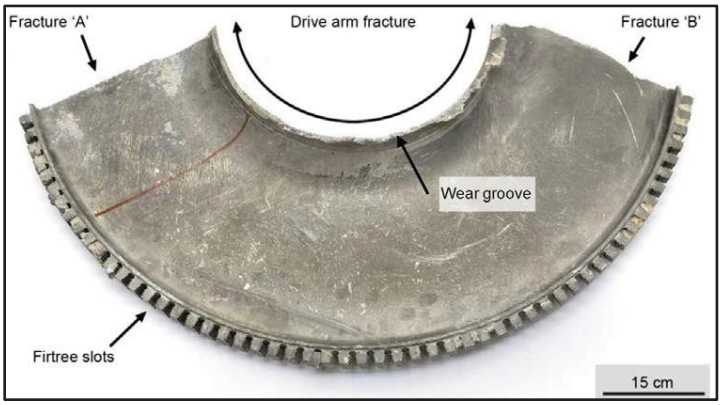

Figure 1.7 IPT Disc failure
Taken from ATSB (2013, p. 58)

Another type of failure occurs when a fracture initiated at the turbine disc bucket groove, converges circumferentially towards the adjacent or a more distant bucket groove, releasing a portion of the disc, including the attached blades, into what constitutes an intermediate fragment (Figure 1.6 (b) and Figure 1.8 (Transportation Safety Board of Canada, 2014)).

Figure 1.8 Segmented LPT Disc
Taken from TSB (2014, p. 33)

Small fragments vary in size, their definition being left at the latitude of the engine manufacturer. Blades can be released from their rotor as consequence of a defect leading to rotor failure, or intentional (blade shedding) to avoid overspeed. Designing for overspeed consists in developing a product that in case of a shaft failure, to avoid the acceleration of the rotor to disc burst speeds, releases the blades using different failure mechanisms: dimples on the airfoil section (weakening intentionally the blade such as past a centrifugal loading the blade tip will detach), or fixing release (past a designed speed, the fixings open up due to centrifugal loading, allowing the full blades to be released as shown in Figure 1.6 (f)). Blade shedding although generally considered benign, in some circumstances (a specific number of blades packing together) might cause an uncontained failure.

Non-intentional releases occur as failures of either blades or discs. Blades can fail at the airfoil (blade features shown in Figure 1.9 (Hardee, et al., 1999)) as consequence of a fracture propagating across the airfoil section (Japan Transport Safety Board, 2011), at shank (between the platform and the firtree, or at the outermost groove of the firtree (Figure 1.10) (Australian Transport Safety Report, 2008)

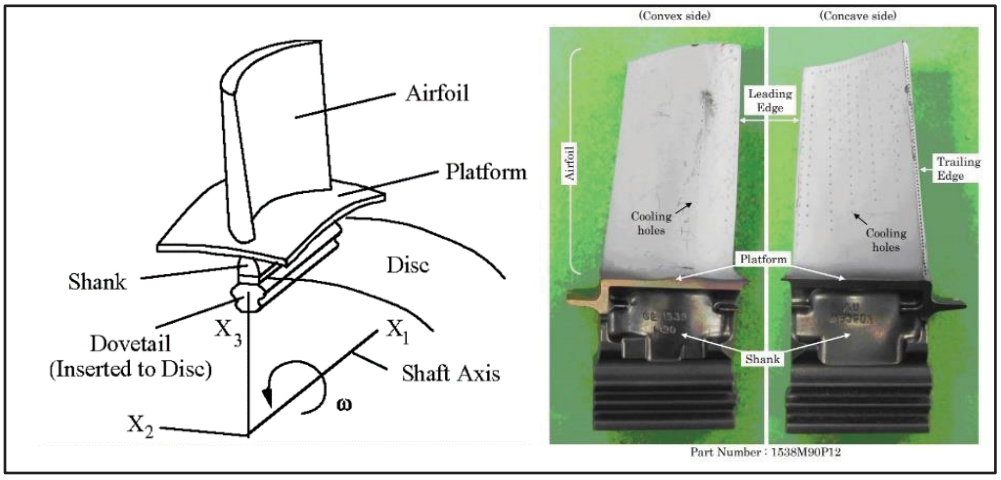

Figure 1.9 Blade features - Compressor blade (left), Turbine blade (right)
Taken from Hardee et al. (1999, p. 193), and JTSB (2011, p. 26)

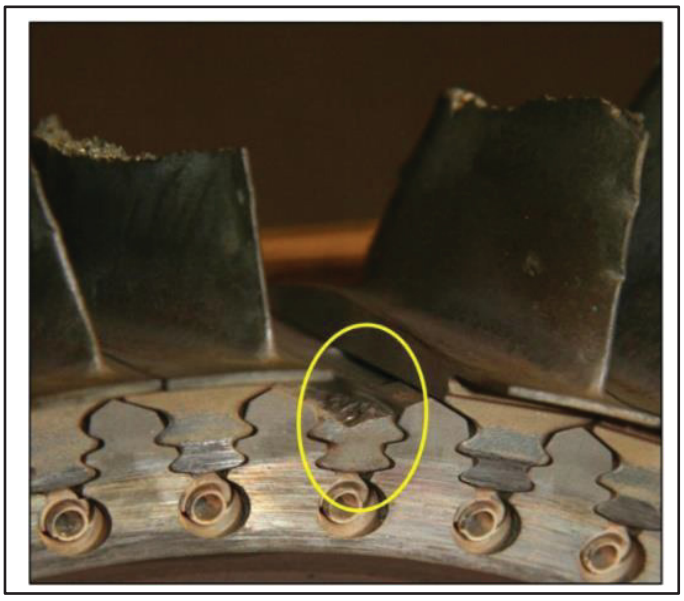

Figure 1.10 Power Turbine blades failures
Taken from ATSB (2008, p. 3)

Single released blades although usually not generating uncontained failures, can cause massive damage to the adjacent structures, generate heavy rotor imbalances, and cause the arrest of the engine. All engine manufacturers include the blade-off containment criterion as a mandatory structural requirement when designing a new or updated product. As mentioned previously, depending on the risk assessment, engine manufacturers include different scenarios to the release of their products, such as intermediate fragment release for the high-pressure turbine / compressor turbine (HPT/CT), trihub for impellers, blade shedding, one or a pair of blades released, etc. The most common of all possible structural criteria for containment is one compressor or turbine blade release, criterion verified individually for each and all rotor stages. This structural validation is performed using a design analytical method in early phases of design when the geometry of the casing is estimated but not yet fully determined.

In addition to the Advisory Circular (AC 20-128A (Federal Aviation Administration, U.S. Department Of Transportation, 1997)) from the U.S. Federal Aviation Administration and European Joint Aviation Authorities (JAA), which establishes guidelines for the design minimizing the hazard from uncontained rotor failures, FAA proposes definitions for the one-third, the intermediate or small fragment (shown in Figure 1.11) to be considered in design for containment, section 9.b of (Federal Aviation Administration, U.S. Department Of Transportation, 1997).

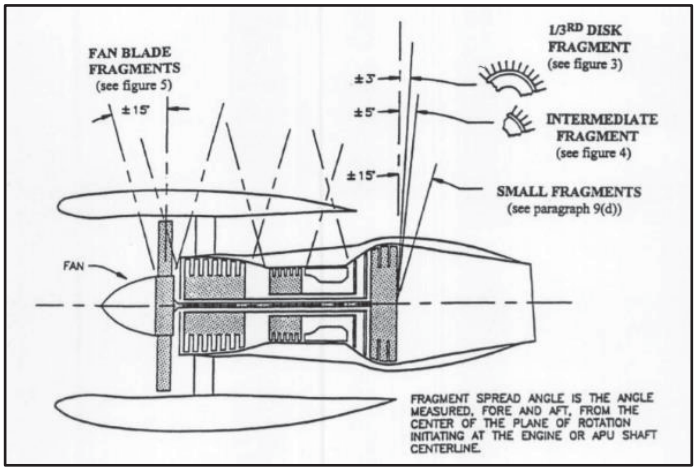

Figure 1.11 Estimated path of fragments and fragments sizes
Taken from FAA (1997, p. 6)

1.2 Literature Review

As mentioned earlier, the literature review covers the following topics relevant to this research: A first survey of relevant information from terminal ballistic perspective, a second review enumerating the major research done in the field of rotor fragment containment, a third review revealing the progress achieved in simulating the impact of a rotor fragment with the containment structure in Finite Element Analyses and a fourth review presents the works detailing the Johnson-Cook material characterization for LS-Dyna (a subset of the FEA category).

1.2.1 Ballistic Approach

A terminal ballistic (the study of the interactions between a projectile and a target (Backman, 1976)) perspective needs to be considered to understand and determine the failure mode of the casing when impacted by the released fragment. Experimental results of high-speed perforation for mild steel plates of different thicknesses (Zaid & Travis, 1974) revealed thermo-plastic instabilities occurring in thicker plates during impacts.

Another finding of the study was that bulging of the target increases with the increase of impact velocity, reaching a maximum when the projectile is just contained, and past that point, further increase in velocity will decrease the bulge height. Regarding the bulge height variation with the plate thickness, it was shown that the bulge height at containment increases initially, then drops due to the development of the thermo-plastic instabilities, and the dynamic containment energy variation follows a similar pattern (Figure 1.12).

It needs to be mentioned that in general, the ballistic experiments are performed on flat plates with different clamping options, which is not accurately representing the gas turbine fragment containment phenomenon.

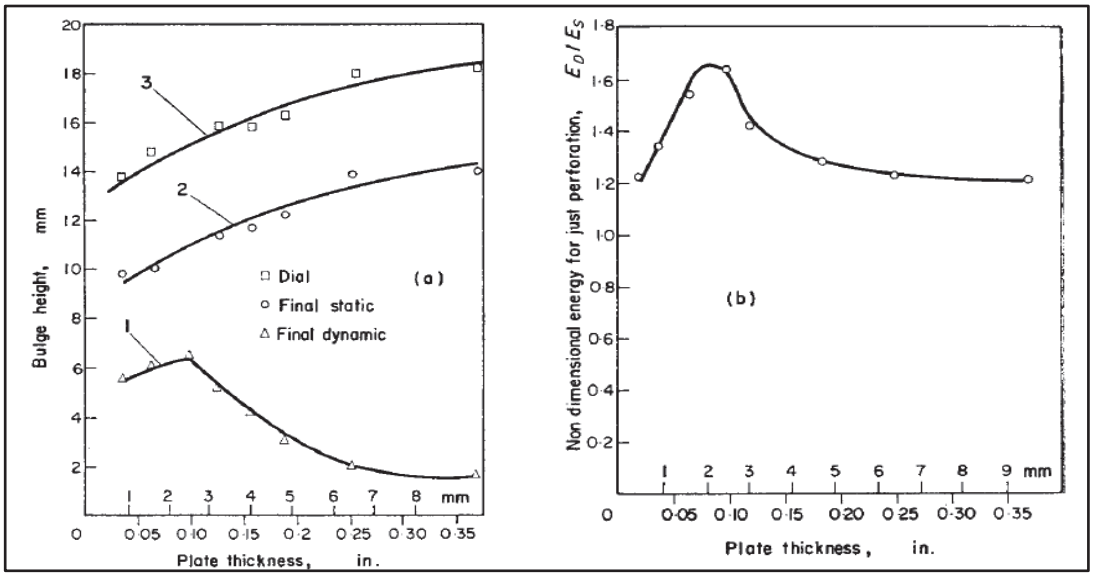

Figure 1.12 Bulge height (left image curve 1) and Energy (right image) variation function of the plate thickness
Taken from Zaid & Travis (1974, p. 380)

A study addressing the containment of fragments by cylindrical structures (Hagg & Sankey, 1974), concluded that the containment is a sequential two-stage process – stage 1 represented by the compression of the material over the impacted area, and eventually shearing of the material over the impacted perimeter; and stage 2 continuing if localized perforation did not occur in the first phase, with a dissipation of energy throughout an extended volume of the target material.

The dynamics, energy dissipation and the failure mode in stage 1 are the same for short and long cylindrical containment rings, and they are expected to be the same for a variety of steel targets, including plates impacted by blunt missiles.

In stage 2 however, the energy dissipation depends on the strain distribution, which in turn is dependent on the geometrical characteristics of the target. It was noted that the strain energy of the target is proportional with the volume of material involved in the impact.

It is also acknowledged the difference in response between short cylinders and long cylinders (Figure 1.13), observing a radius of gyration of the plastic hinge bounding the material adjacent to the impact zone of 3·t (target thickness, criterion determined for fragment velocities in the ranges of 700 – 900 feet per second). Also, the short cylinders develop rather uniaxial strains, versus biaxial for the longer cylinders.

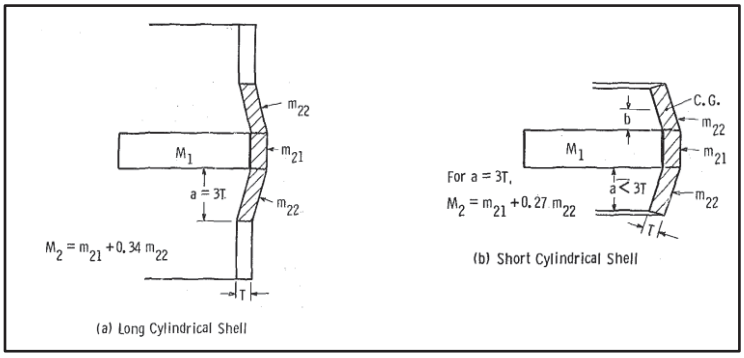

Figure 1.13 Effective target mass for long (left image) and short cylinders (right)
Taken from Hagg & Sankey (1974, p. 118)

Also, this study reveals that the possibility of perforation increases with the presence of flanges in the impact area. In the first phase of the impact, expressing the energies balance as a function of the two types of loading (compressive and shear), the criterion for non-perforation is:

$$E_c + E_s > \Delta E_1; \tag{1.1}$$

where E_c is the plastic strain energy in compression, E_s is the plastic strain energy in shear, and the energy dissipated during phase 1 impact is noted with ΔE_1. Further expressed, the plastic strain energy E_c is:

$$E_c = a \cdot T \cdot \varepsilon \cdot \sigma_d; \tag{1.2}$$

a being the area of contact, T being the target thickness, ε is the plastic strain and σ_d the average dynamic plastic flow stress of the material in compression.

The shear energy E_s is

$$E_s = K \cdot P \cdot T^2 \cdot \tau_s; \tag{1.3}$$

where K is an experimental constant, P is the perimeter of the sheared area and τ_s is the dynamic shear strength of the material.

For the second phase of impact, when the target plate was not perforated, the residual fraction of the kinetic energy (ΔE_2) is dissipated through uniaxial tension (for short cylinders) or biaxial tension (long cylinders), with the containment criterion being

$$E_t > \Delta E_2; \tag{1.4}$$

where $E_t$is the tension strain energy, expressed as:

$$E_t = Q \cdot \varepsilon \cdot \sigma_d; \tag{1.5}$$

With Q being the strained volume of material. The containment threshold is shown in Figure 1.14.

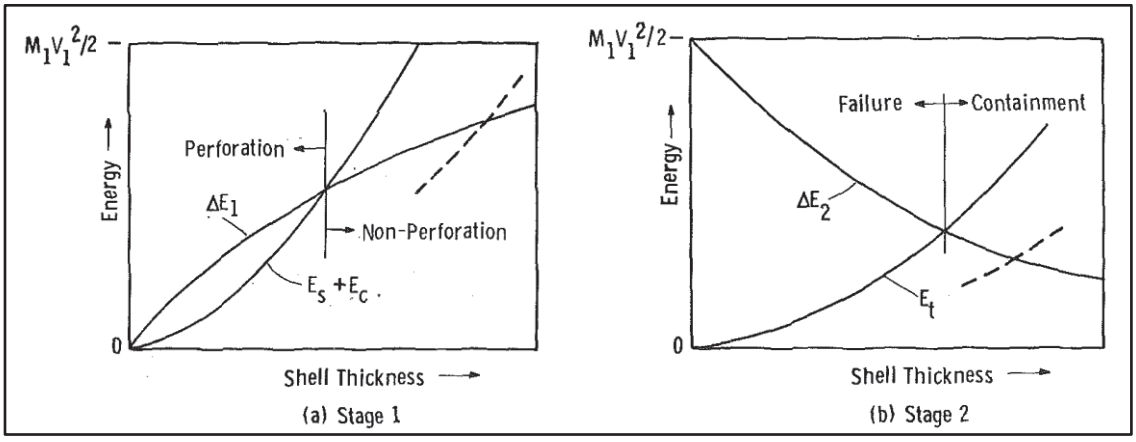

Figure 1.14 Containment thresholds for Phase 1 (left) and Phase 2 (right)
Taken from Hagg & Sankey (1974, p. 120)

For impact scenarios where the mass of the affected target area is large compared to the fragment mass, the containment is a phase 1 process; where the mass of the affected area is smaller than the fragment mass, the impact occurs as a phase 2. The fragments generated during the experiments were of regular shape (discs split in 4 fragments), therefore having a relatively known shape, not the case for gas turbine rotor fragments, for which determining the impact area is more challenging.

Another comprehensive study dedicated to terminal ballistics (Backman & Goldsmith, The mechanics of penetration of projectiles into targets, 1978) investigated the plate penetration and perforation from multiple perspectives and proposed analytical models for the impact analysis, while maintaining the primary emphasis on solid targets. “The Mechanics of Penetration of Projectiles into Targets” provided empirical relations and analytical models as well as multiple definitions and classifications for different aspects of impacts, such as classification of targets, projectiles, impacts, velocity ranges, deformation, and failure modes.

Prior to perforation, a thin target when impacted by a blunt projectile tends to deform as shown in Figure 1.15. With the target plate thickness and impact velocity increase, the plastic deformation and the fracture modes change. Most frequent types of failures are shown in Figure 1.16. The concept of ballistic limit is also discussed, as well as an enumeration of empirical formulations, analytical relations and experimental methods used in penetration mechanics.

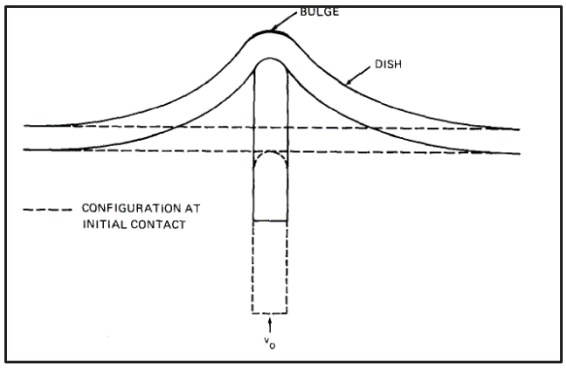

Figure 1.15 Permanent deformation of a thin target at impact
Taken from Backman & Goldsmith (1978, p. 4)

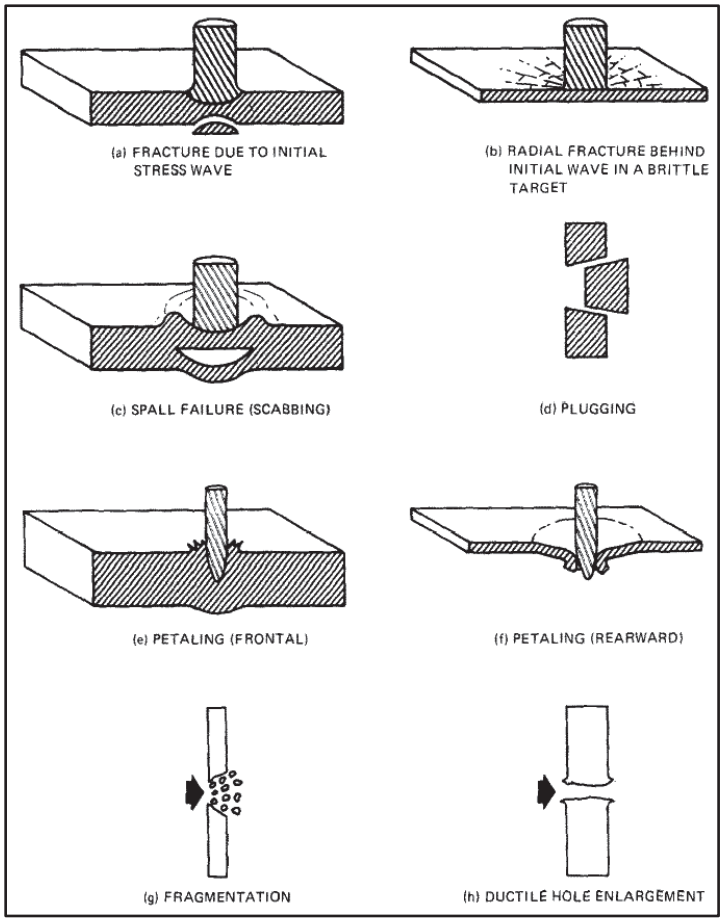

Figure 1.16 Most frequent types of perforation mechanisms of target plates
Taken from Backman & Goldsmith (1978, p. 5)

One of the recommendations of this research formulates the need to consider the effects of temperature and suggests further examination of coupled thermo-mechanical aspects of the impact. Another recommendation of this article is to investigate the dependence on strain rates and temperature, as well as the multi-axial state of stress.

The modes of impact energy absorption by plastic deformation were reviewed in “Impact Loading of Plates – An Experimental Investigation” (Corran, Shadbolt, & Ruiz, 1983), as well as the effect of the projectile mass, shape, and hardness on penetration.

One of the conclusions of the study is that increasing the projectile nose radius changes the failure mode of the plate from thinning due to tensile stretching and ductile hole enlargement (wedge missile) to shear failure (for a blunt cylindrical missile), as shown in Figure 1.17.

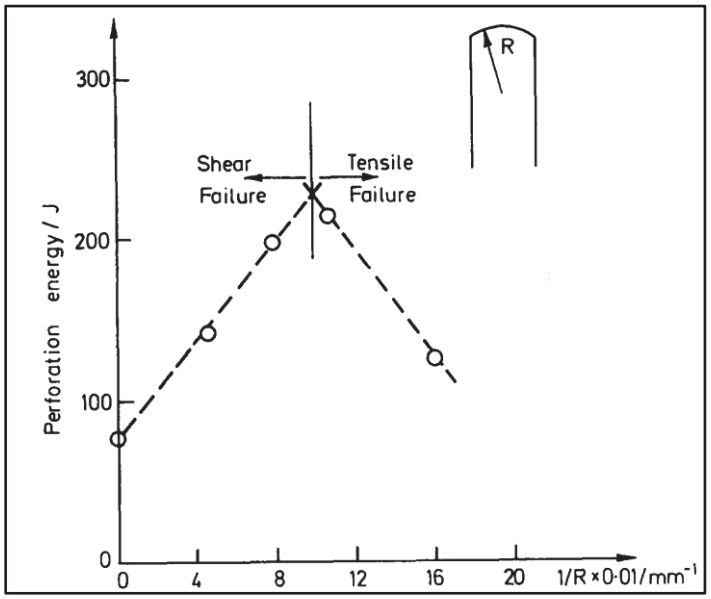

Figure 1.17 Variation of perforation energy function of the projectile nose radius
Taken from Corran, Shadbolt, & Ruiz (1983, p. 9)

The study reveals that the amount of membrane plastic work decreases with the increase of target plate thickness, while the opposite occurs for the bending plastic work and the plugging energy with the increase of thickness. The elastic energy decreases with the increase of plate thickness, until reaching a minimum value, from which it will start increasing (Figure 1.18). The membrane stretching offers the most efficient energy absorption.

Corran and Ruiz detailed the impact on multi-layered shields (Corran, Ruiz, & Shadbolt, On the design of containment shields, 1983), and concluded that a multi-layered structure might be beneficial for containment purposes, but only when used instead of a single containment layer having a thickness (and thus rigidity) promoting the plugging mode of failure.

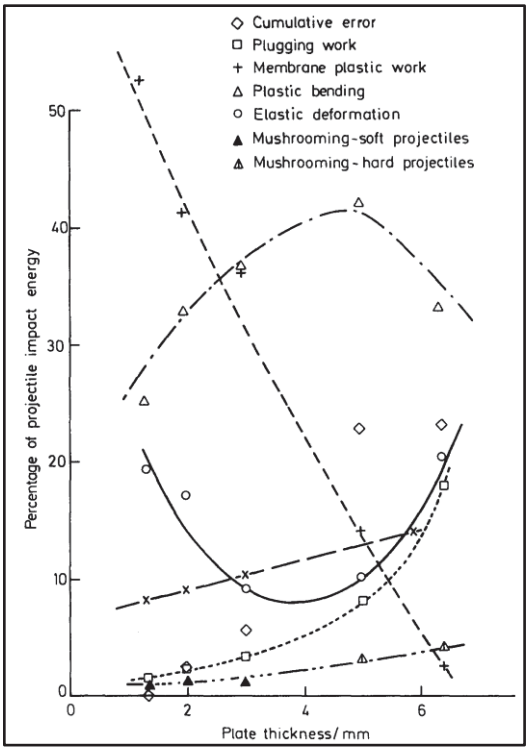

Figure 1.18 Energy absorption breakdown
Taken from Corran, Shadbolt, & Ruiz (1983, p. 15)

Design solutions placing thin shields before thicker ones optimize the overall energy absorption. The shear bands initiated and developing during plugging are shown in Figure 1.19.

Continuing in the multi-layered target investigation, Radin and Goldsmith (Radin, 1988) concluded differently that the resistance of adjacent layers of equal depth is less than the resistance of an equivalent monolithic target, and the spaced layers offer an even smaller containment capability that layered targets in contact. For different materials layers, the overall system ballistic limit was smaller than the lowest ballistic limit of a single plate having the same overall thickness. The merit of a thickness increase past a specific value from which the layered structures become more effective is recognized (thus eventually aligned with Corran and Ruiz).

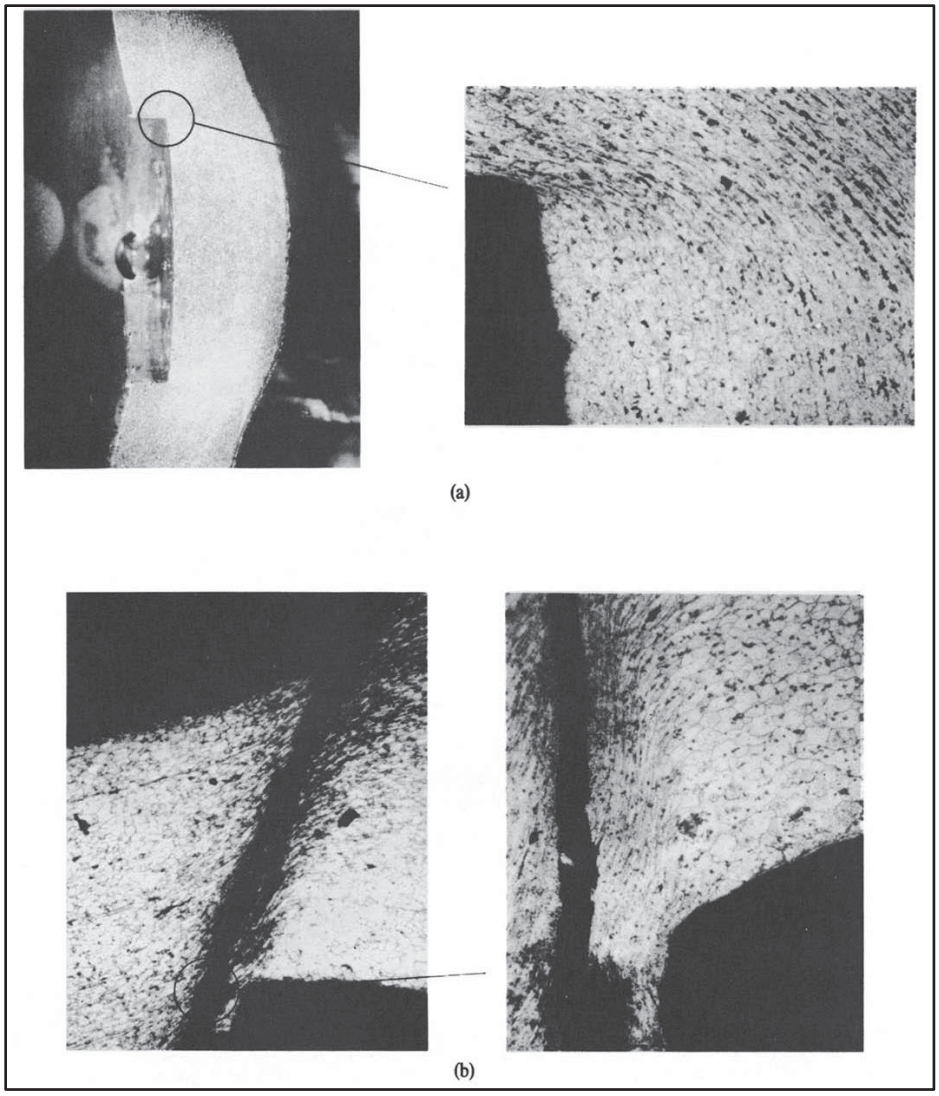

Figure 1.19 Plugging shear initiation (a) and completion (b)
Taken from Corran, Ruiz, & Shadbolt (1983, p. 570)

A comparison between quasi-static and dynamic loading of simply supported steel plates is reported by Corbett and Reid in (Corbett & Reid, 1993). The research work examines the differences produced by the two different types of loading, as well as the effects of hemispherical and flat cylindrical indenters. It also proposes two empirical formulations to determine the energy required for perforation (for the hemispherical tip indenter). One of the conclusions of this study revealed the proportionality of the required perforation energy (by plugging) to the plate thickness to the power of 2.

More insight into the adiabatic shear band formation is presented in “The Influence of Plate Hardness on the Ballistic Penetration of Thick Steel Plates” (Dikshit, Kutumbarao, & Sundararajan, 1995).

In “Impact Loading of Plates and Shells by Free-Flying Projectiles” (Corbett, Reid, & Johnson, Impact loading of plates and shells by free-flying projectiles: a review, 1996), Corbett, Reid and Johnson review the up-to-date progress made into the research of sub-ordnance velocity free-flying projectiles penetrating and perforating plates and cylinders. Many of the previously mentioned topics, such as ballistic limit, failure modes, energy absorption mechanisms, effects of different material properties, influences of the clamping loads, indenter/projectiles shapes, target hardness, empirical predictions and analytical relations are discussed in detail. The conclusions of this document reveal the progress in experimental studies as well as the needs for further research, especially in the prediction of the ballistic limit, impact loads and different scenarios of impact, such as pipe response, or concrete and steel -concrete response to impact.

Various parameters affecting the impact area, as well as further discussions about failure modes of the target plate are reported by Liu and Stronge in “Ballistic limit of metal plates struck by blunt deformable missiles: experiments” (Liu & Stronge, 2000). The novelty of this study is that it addresses the impact of mild steel plates with deformable missiles. In this work are discussed the ballistic limit, the threshold between the discing and plugging function of the ratio of the plate thickness and the missile radius. The global deformation surrounding the point of impact is called dishing (shown in Figure 1.15). Discing occurs when the plate develops large tensile strains by stretching and bending (thus discing is a predominantly tensile failure), while for plugging the fracture develops normal to the plate surface (shear failure mode). Also, another finding of this research is that at the same ratio of impact velocity over the ballistic limit, the plate in a material with a smaller fracture strain is prone to fail in discing. Energy dissipation for a thin plate was noted larger than for a moderately thick plate, same observation for the global deformation magnitude.

One of the conclusions of this study is that for mild steels and 1200 series aluminium plates, for plate thickness over the missile radius ratios H / r_m< 0.5, the failure mode of the plate is discing, whereas for ratios H / r_m> 0.5, the failure mode of the plate is plugging. Another conclusion was that the ratio of ballistic velocity over the plugging speed decreases with the ratio of plate thickness to the missile radius, approaching 1.0 when the plate thickness is equal to the missile radius (Figure 1.20).

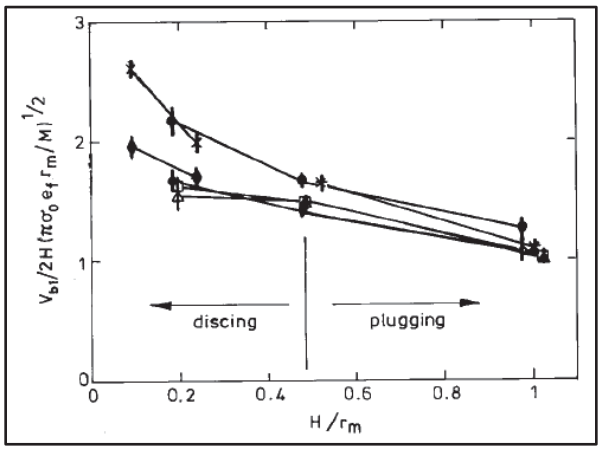

Figure 1.20 Ratio of ballistic velocity to plugging speed function of the ratio of plate thickness to missile radius
Taken from Liu & Stronge (2000, p. 1417)

One of the more recent publications correlated high-velocity tests with numerical results of finite element analyses (Di Sciuva, Frola, & Salvano, 2003). The impacted structure simulated response (deformed shape of the target plate) shown good correlation with the tests results (Figure 1.21).

Another achieved objective of the work was the determination of the ballistic limit curve for the plate material (Inconel 718). In this work, the authors used the MSC Dytran software, with a Cowper-Symonds material formulation for the impacted plate in Inconel 718.

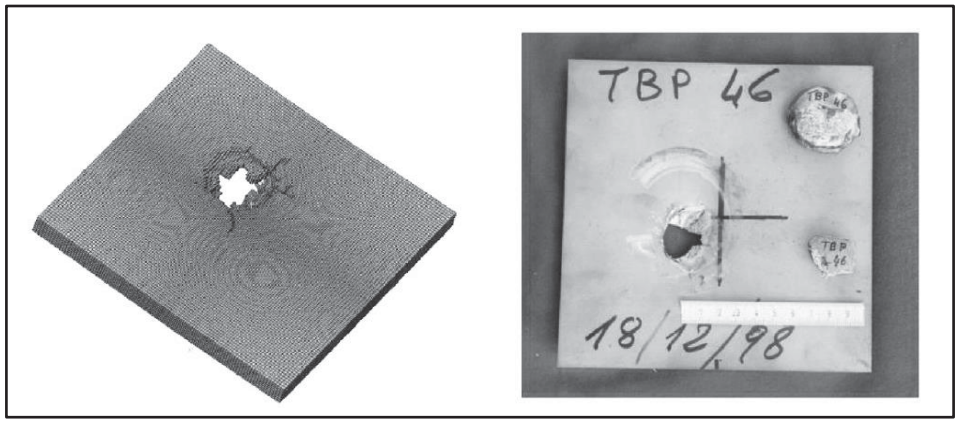

Figure 1.21 Numerical versus experimental results of plate impact
Taken from Di Sciuva, Frola, & Salvano (2003, p. 872)

Heat treatments effects on the failure mechanisms of Inconel 718 impacted plates are investigated by Pereira and Lerch (Pereira & Lerch, 2001). Ballistic tests were performed on two annealed (moderate strength, high strain to failure) and one aged (high strength, moderate strain to failure) conditions (Figure 1.22). Material properties were characterized using a Johnson-Cook material model.

The conclusion of the study was that the annealed Inconel 718 performed better (absorbing more energy) than the aged material, and the static toughness criteria acceptably predicts the ballistic resistance for failure modes corresponding to fan blade-off events.

An extensive study (100 impact tests and more than 150 finite element analyses) of the penetration and perforation of steel plates in Weldox 460E is presented by Borvik, Hopperstad, Langseth and Malo in (Børvik & al., 2003). This research addressed three main topics: impact tests for different plate thicknesses and impact velocities, the second topic being the estimation of ballistic limit velocities and residual versus impact velocity curves (Figure 1.23), and the third part detailing the conclusions from finite element analyses.

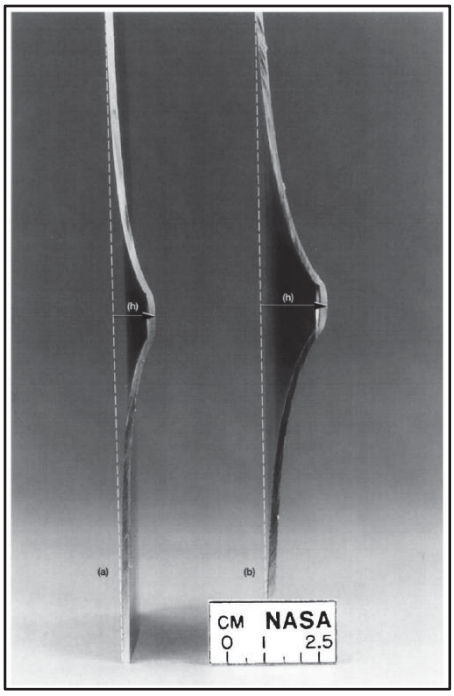

Figure 1.22 Inconel 718 impacted plate response, aged HT (left) and annealed (right)
Taken from Pereira & Lerch (2001, p. 728)

One of the conclusions of this research was that none of the analytical methods investigated succeeded in properly describing the response of the impacted structure for the whole range of thicknesses, due to considering a particular dominant physical mechanism. Another conclusion is that the LS-Dyna numerical simulations demonstrated an excellent agreement with the experimental data. A validated numerical model can provide a better understanding of the penetration problem.

Another good agreement between 3D numerical simulations and test results is reported by Tansel in (Tansel, 2010), in which is investigated the ballistic performance of hardened steel plates. The study enumerates different analytical models predicting the minimum target thickness, or projectile residual velocity. In the conclusions, it was confirmed that the AISI 4340 steel plates increase in hardness corresponds to an increase in the protection capabilities of the plates, and the numerical method used correctly replicated the plates impact response.

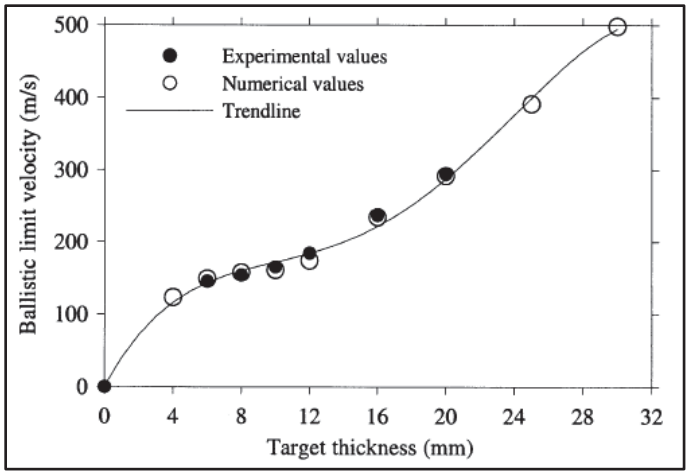

Figure 1.23 Ballistic limit velocity versus target thickness correlation numerical results with testing
Taken from Børvik & al. (2003, p. 451)

1.2.2 Analytical Methods

Due to the complexity of the phenomenon occurring at the impact of a rotor fragment with the surrounding structure, the ballistic aspect needs to be incorporated in a macro perspective, considering all interactions between the components involved in the impact.

A massive research program sponsored by NASA, executed by the Naval Air Propulsion Center (NAPC) in collaboration with the Massachusetts Institute of Technology (Martino & Mangano, 1969) conducted experiments on various containment rings impacted by different types of fragments. The program was developed in seven distinct phases and extended between 1965 until 1972, followed by numerous subsequent individual works.

The objective of this research was the development of design guidelines for optimum weight rings containing turbine engine rotor fragments.

This research program laid the foundations of fragment containment study, shedding light on many aspects of the fragment impact with the casing. Amongst the long list of conclusions, it was revealed that the energy absorbed by blade deformation is significant and should be considered in any analytical design method. Also, it was observed that containment rings in softer materials produce more fragmentations on the blades. Impacts from single blade releases can cause large ring displacements; any constraints preventing the casings excursions increase the stresses, thus increasing the damage on the containment rings, possibly leading to their failure. In addition to the eventual escape of fragments, the failed containment rings can also release hot gases increasing the risk of engine or aircraft structure fire. Some welded casings failed during impact before reaching significant deformations, raising concerns about any possible stress raisers induced by the manufacturing processes. For dimensioning the containment rings, the strain energy method was used (detailed at great extents in this thesis).

The weight of the ring (W_R) is expressed as a function of the kinetic energy of the rotor energy at burst (KE_B) over a function of engineering stress and strain ($f(\sigma, \varepsilon)$) (1.6), ρ being the casing material density, T being the ring radial thickness (1.7), r_i the inner radius, L_A.the axial length:

$$W_R = \frac{KE_B}{\frac{1}{\rho} \cdot \int_0^{\varepsilon_f} f(\sigma, \varepsilon)} = \frac{KE_B}{SCFE}; \tag{1.6}$$

$$T = \sqrt{r_i^2 + \frac{W_R}{\rho \cdot \pi \cdot L_A}} - r_i \tag{1.7}$$

This research program also observed the momentum imparted by the following blades to the released one and stated the necessity to consider this energy in the design analytical methodology.

An analytical relation for determining the necessary thickness of the containment ring, function of a Specific Containment Fragment Energy Factor (SCFE, shown in Figure 1.24) was detailed in the Phases VI and VII report (Mangano, 1972). The SCFE took into consideration the axial lengths of the rotor and the casing, the rotor diameter, and the number of fragments.

Another development in the collaboration of NASA, NAPTC and MIT on the Rotor Burst Protection Program consisted in the development of a FORTRAN based computer program called JET 1, a program computing the containment ring transient large plastic deformations (McCallum, Leech, & Witmer, 1969). A subsequent study of the same authors focused on the determination of containment variables (Leech, Witmer, & Yeghiayan, 1971). And further continuing the same line of research, Collins and Witmer developed in (Collins & Witmer, 1973) a method for estimating the interaction of a fragment impacting a containment structure.

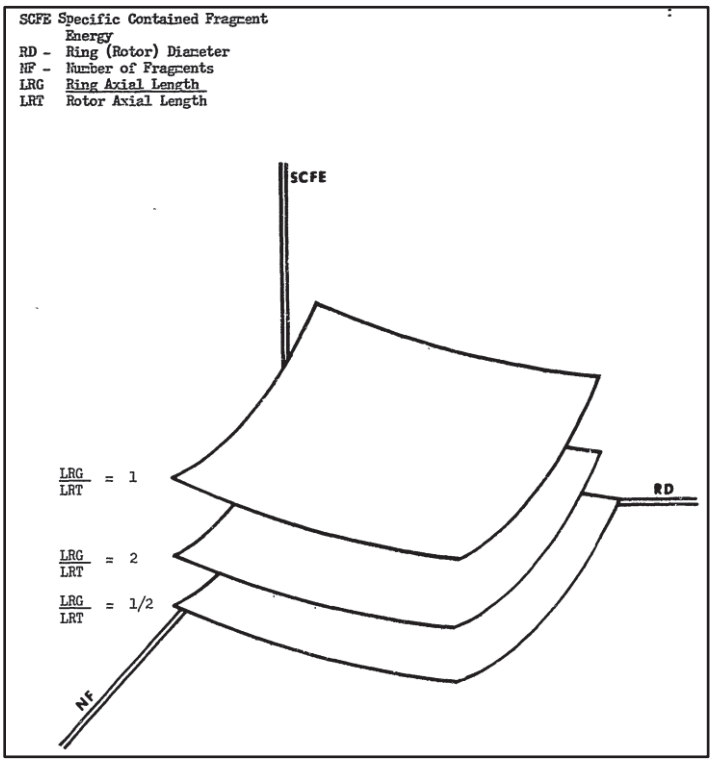

Figure 1.24 Specific Containment Fragment Energy plot
Taken from Mangano (1972, p. A1-4)

A detailed study dedicated to the improvement of the airframe for turbine engine rotor blade containment is reported by Gunderson in (Gunderson, 1977). As this research investigated the uncontained rotor failures from the aircraft manufacturer's perspective, the emphasis was on the airframe armour, assuming that no fragment energy is absorbed by the engine. The study considered a wide-body aircraft equipped with 3 or 4 engines (General Electric CF6-50 and Pratt & Whitney JT9D-59), with multiple fragment scenarios: 1 blade, 2 blades + disc serrations, 4 blades with disc serrations (Figure 1.25), possibly originating from either compressor or turbine stages, of both types of engines.

One of the conclusions of the study was that from weight saving perspective, the armour needs to be installed as close as possible to the engine, to properly prevent the scatter of fragments over a larger area. Some armour solutions appear to have advantages over others, preferred being the ones requiring less interventions during routine inspection and maintenance operations. A considerable effort has been devoted to the energy absorption capability for different materials (including fibre reinforced), in determining empirical and analytical equations, understanding the plates failure modes. This study considered that the containment capability of a material is proportional with the dynamic shear modulus.

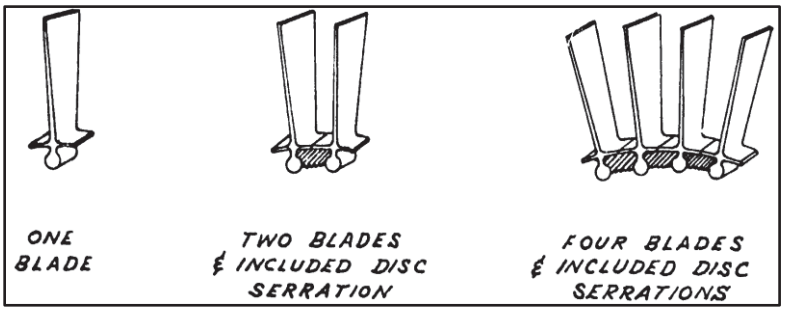

Figure 1.25 Fragment types considered
Taken from Gunderson (1977, p. 7)

An investigation of the types of rotor failure and the characteristics of fragments is detailed by McCarthy in (McCarthy, Types of rotor failure and characteristics of fragments, 1977). The study identified three different types of rotor failure, generating different shapes of fragments: Low Cycle Fatigue (LCF), Combined LCF with High Cycle Fatigue (HCF), and failure due to overheating and/or rotor overspeed.

One of the conclusions of the study was regarding the dispersion angle from the rotor plane of± 5° for large fragments and up to 33° for smaller fragments which can be deflected axially, as shown in Figure 1.26.

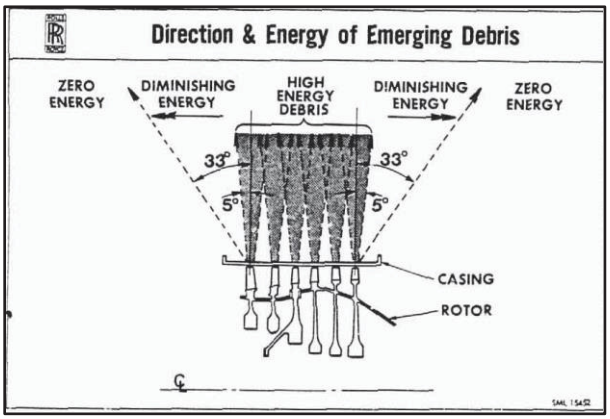

Figure 1.26 Fragment dispersion angles
Taken from McCarthy (1977, p. 86)

Additional research, conducted part of the Rotor Fragment Protection Program, is detailed in (Salvino, DeLucia, & Russo, 1988). First of the two tasks of this work was to investigate the containment capability of cloth containment rings. The second task focused on determining the thickness of metallic rings necessary to contain single blade and triple blades fragments. For the first task, several containment tests were performed on fabric discs in Kevlar 29 and ballistic nylon. For the cloth containment rings, the tri-hub failure (the rotor fails in three equal segments) was investigated. The rotors belonged to the Power Turbine stage of the General Electric T58 engine, and to Curtiss-Wright J65 Stage 2 Power Turbine. For the blade containment study were used blades from Pratt & Whitney engines JT3D and JT8D, deemed as representative for large turbine rotors. On the containment rings, the selected material was A-286 steel, with varying thicknesses, increasing until reaching satisfactory containment. A simplified empirical formula for determining the containment thickness for A-286 rings was proposed. The conclusions of the research were that neither Kevlar 29, nor ballistic nylon were appropriate for tri-hub containment, and from the two, the rings in Kevlar were slightly better than the ones in ballistic nylon.

For the second objective of the research, the A-286 casing minimum thickness required to contain a blade released from a JT8D PT rotor was 0.187”, and to contain a JT3D blade, the ring needs to be 0.250” thick. For the intermediate fragment consisting in 3 blades, the ring needs to have a minimum thickness of 0.375” to contain rotor fragments detached from both JT3D and JT8D engines (Figure 1.27).

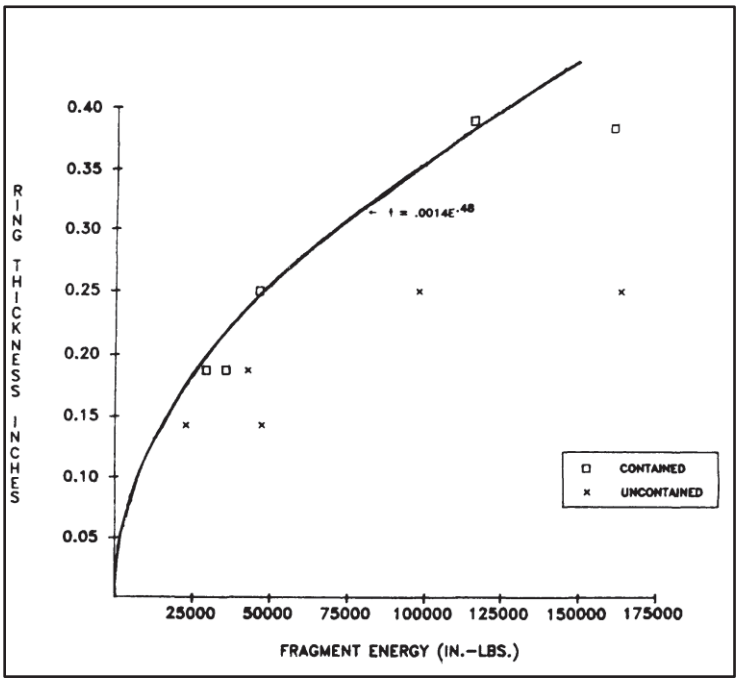

Figure 1.27 Fragment energies in containment tests
Taken from Salvino, DeLucia, & Russo (1988, p. 19)

Research into an advanced fan blade containment system is reported by Lane in (Lane, 1989). The objective of this work was to study the potential weight advantages of a ceramic-based containment system for fan blades. Although dedicated to fan blade containment, the research provided insight into the mechanics of containment, observing the two distinct modes of failure: large plastic elongation and its subsequent tensile failure, versus the penetration of the containment ring in a rather localized impact. Part of the literature review, several analytical design equations from gas turbine OEMs were presented.

From numerical computation perspective, a number of different impact scenarios (different types of fragments) were analysed using Dyna3D (a precursor of the current LS-Dyna software) and reported by Sarkar in (Sarkar & Atluri, Finite Element Analysis of Engine Rotor Failure and Containment, 1995). In the analyses, the effective plastic strain was used as failure criterion to model the deformation leading to casing failure. The results were compared with experimental results from spin pit tests performed on General Electric GE T58 rotors at NAPTC. In this study, it was observed the interaction of the following blades with the detached fragment, the increase in kinetic energy of the fragment due to this interaction, as well as the deformation of these following blades Figure 1.28. The results of these analyses agreed closely with the experimental results; therefore, it was concluded that the analytical method could be used for further investigations of rotor failures.

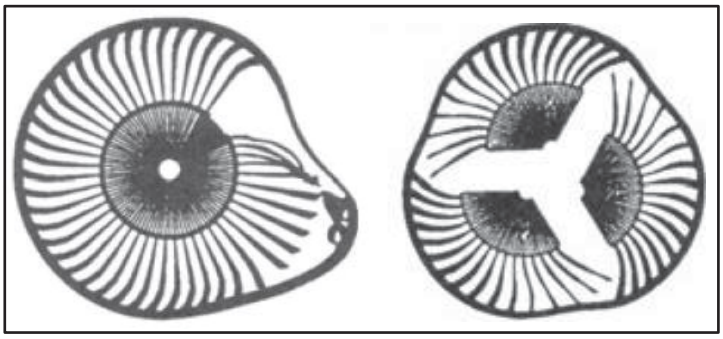

Figure 1.28 Numerical simulations of rotor fragments containment
Adapted from Sarkar & Atluri (1995, p. 487 & 488)

In subsequent research, the same authors detail the progress of their research into the computational modelling of rotor containment (Sarkar & Atluri, Failure analysis of aircraft engine containment structures, 1996). The constitutive material model was Johnson-Cook, allowing the consideration of strain rate hardening and thermal softening. More details are provided about the adiabatic shear localization in this work.

Federal Aviation Administration (FAA) delegated Wichita State University the task to do a literature survey of the existing design for fragment containment procedures. This study (Mathis, 1997) presented 23 years of research, between 1970 till 1993, with the 64 studies on the topic of engine rotor fragments containment, as well as presenting some of the perspectives of the industry representative manufacturers and suppliers.

A preliminary design method for compressor casings is reported by Bretschneider in (Bretschneider & al., 2008). The method addressed the structural integrity design methods considering the pressure, axial loading, and containment criteria (dominant). One of the conclusions of this study was that the method could be used for preliminary design, but requires further calibration due to the simplifications employed, especially towards the last compressor stages, where the thermal effect is non-negligible.

As the numerical analytical methods and the computational power evolved, the rotor fragment containment concept was predominantly studied through finite element analyses correlated with tests. Some of the main studies and their conclusions are presented in the next section.

1.2.3 Finite Element Analyses

The numerical evaluation of the fragment containment attracted interest from the research community since the initial phases of the Jet Engine Rotor Burst Protection Program (Martino & Mangano, 1969), (Mangano, 1972) funded by NASA with the main participation from NAPTC and MIT. An early attempt to address numerically the event of rotor fragment containment was researched by the Aeroelastic and Structures Research Laboratory (ASRL), Department of Aeronautics and Astronautics from Massachusetts Institute of Technology (MIT). The FORTRAN based, JET 1 program allowed the determination of the behaviour of a containment ring when impacted by a fragment; the program required as inputs the forces resulting from the interaction of the fragment with the casing, forces evaluated using another program called TEJ 1. The details of JET 1 and the associated TEJ 1 are documented by McCallum, Leech and Witmer in (McCallum, Leech, & Witmer, 1969).

Further developments of the JET program, such as transition from finite difference to finite element analysis procedure are described in (Collins & Witmer, 1973), (Witmer & Spilker, 1977).

An analytical technique validated by experiments was documented by General Electric Company for NASA (Stotler & Coppa, 1979). The resulting blade trajectory is shown in Figure 1.29.

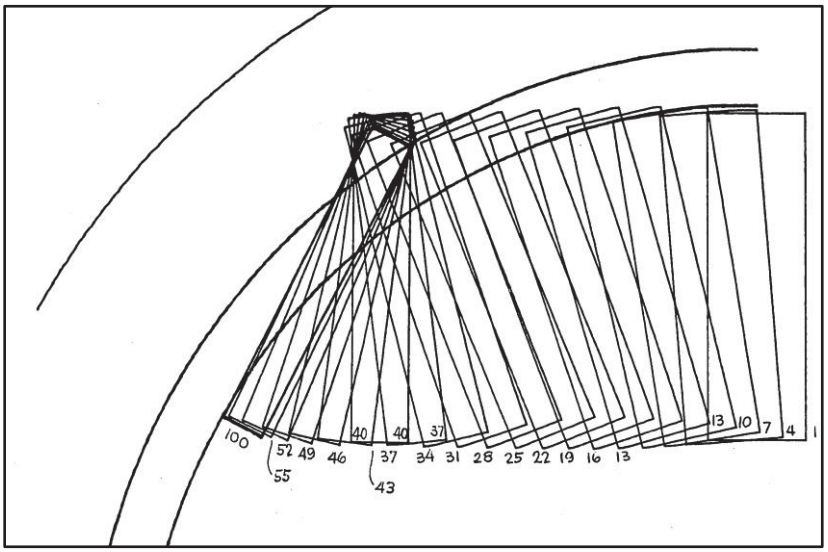

Figure 1.29 Fan blade computed trajectory
Taken from Stotler & Coppa (1979, p. 114)

Another numerical simulation correlating the experimental results from one of the NAPTC tests was performed using Dyna3D (Sarkar & Atluri, Impact Loads and Containment Aspects during a Rotor Failure in Aircraft Jet Engines, 1995). The technological advances in computational technology allowed more refinement in setting up the analyses, material modelling allowing elasto-plastic definition, thermal effects and a sophisticated contact interface allowing a more accurate response from the interacting components. The deformation of the case following a tri-hub failure is shown in Figure 1.30.

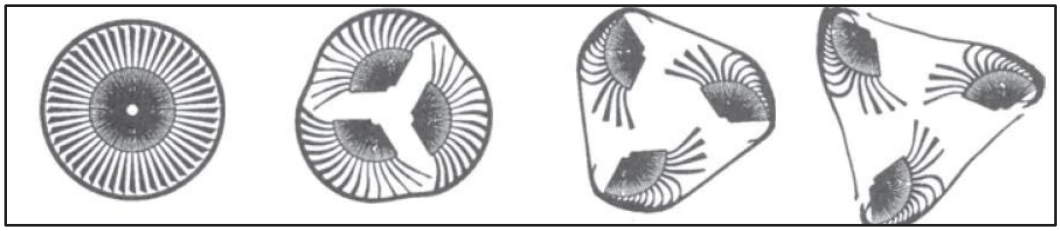

Figure 1.30 Tri-hub rotor burst simulation
Taken from Sarkar & Atluri (1995, p. 2170)

A comparison between the two major explicit codes allowing complex numerical simulations of the impact event is presented by Teng and Wierzbicki in (Teng & Wierzbicki, 2008). In addition to the numerical codes, the authors compared two predominant failure models, Bao-Wierzbicki versus Johnson-Cook fracture criterion. The mesh size influence and the impact pitch angle were observed and discussed. A comparison of the energies obtained with the two codes, and with using different failure models is shown in Figure 1.31. It was observed a better accounting of the dissipation energy in Abaqus due to contact compared to LS-Dyna. Also, to be noted is the results complexity level, element erosion shown in Figure 1.32.

Further developments in the analytical procedures using finite element methods are demonstrated by He, Xuan, Liu, Hong and Wu in (He & al., Perforation of aero-engine fan casing by a single rotating blade, 2013). A fan blade released impacting the casing is simulated with ANSYS/LS-Dyna, and the results were correlated with the experimental results.

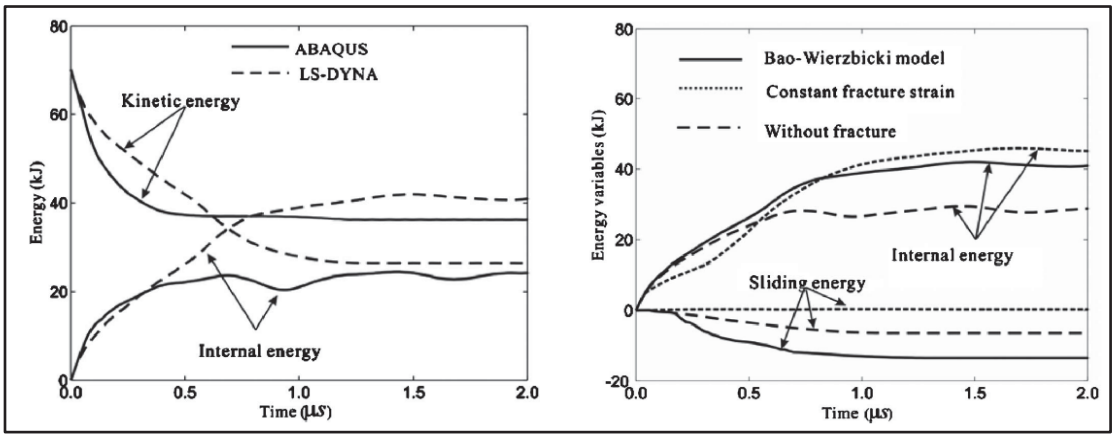

Figure 1.31 Energies comparison
Taken from Teng & Wierzbicki (2008, p.184)

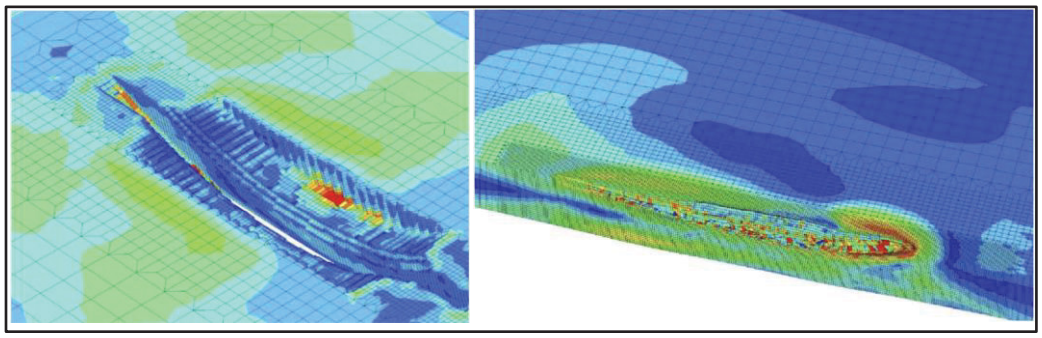

Figure 1.32 Failure pattern on the impacted plate
Taken from Teng & Wierzbicki (2008, p.181 & 183)

The perforation process was accurately represented, and the simulation allowed further details in understanding the impact event (impact timeline is shown in Figure 1.33).

Further studies in blade containment provided more details about the factors affecting the results of the numerical simulations (He & al., Simulation methodology development for rotating blade containment analysis, 2012). Mesh size and a minimum number of elements per thickness, contact penalty factor, friction coefficients, all play an important role in the accuracy of the finite element analyses (FEA) results. A very good correlation of the simulations with the physical test results is shown in Figure 1.34.

A study of multi-blade interaction is presented in (He & al., Multi-blade effects on aero-engine blade containment, 2016) by the same authors, evidencing differences between the containment of fan blades versus turbine blades. Also, this study reveals very good correlation of finite element results with test results (Figure 1.35)

Another extensive study dedicated to FEA evaluation of fan blade-off event is reported by Ridley in (Ridley, 2018). The research dedicated to the design of a new containment ring included ballistic simulations and tests, as well as rig testing dedicated to validating the FEA results of single fan blade-off containment.

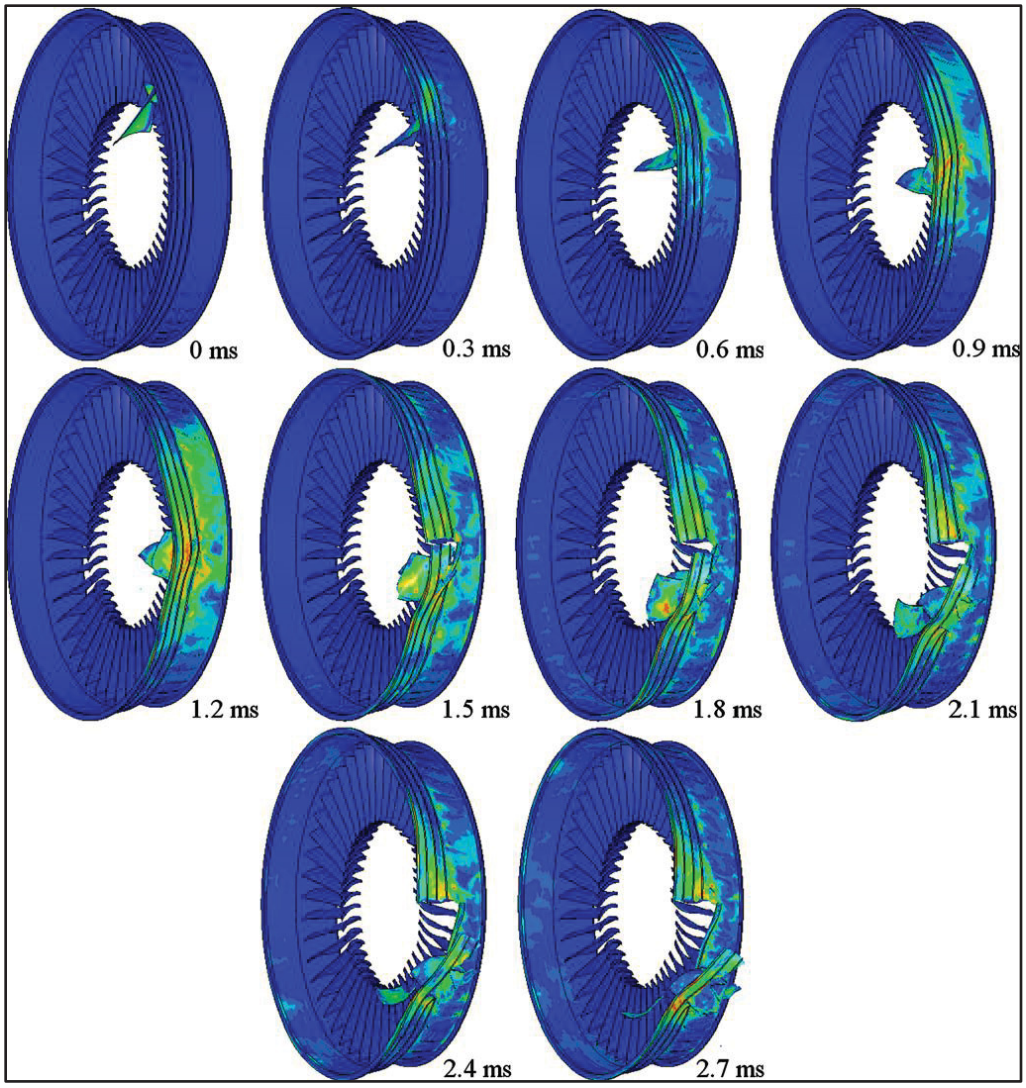

Figure 1.33 Turbine blade-off / Casing impact timeline
Taken from He & al. (2013, p.240)

Further refinement of factors affecting the containment capabilities of gas turbine casings is revealed by Eryilmaz, Guenchi and Pachidis in (Eryilmaz, Guenchi, & Pachidis, 2019), where the effects of blade tip geometries and casings geometrical shapes were investigated. The material model used in the analyses is Johnson-Cook, considering the material plasticity function of strain rate, temperature, and stress triaxiality; requiring more effort in the characterization of the material card to be used in the simulation, including material validation with tests.

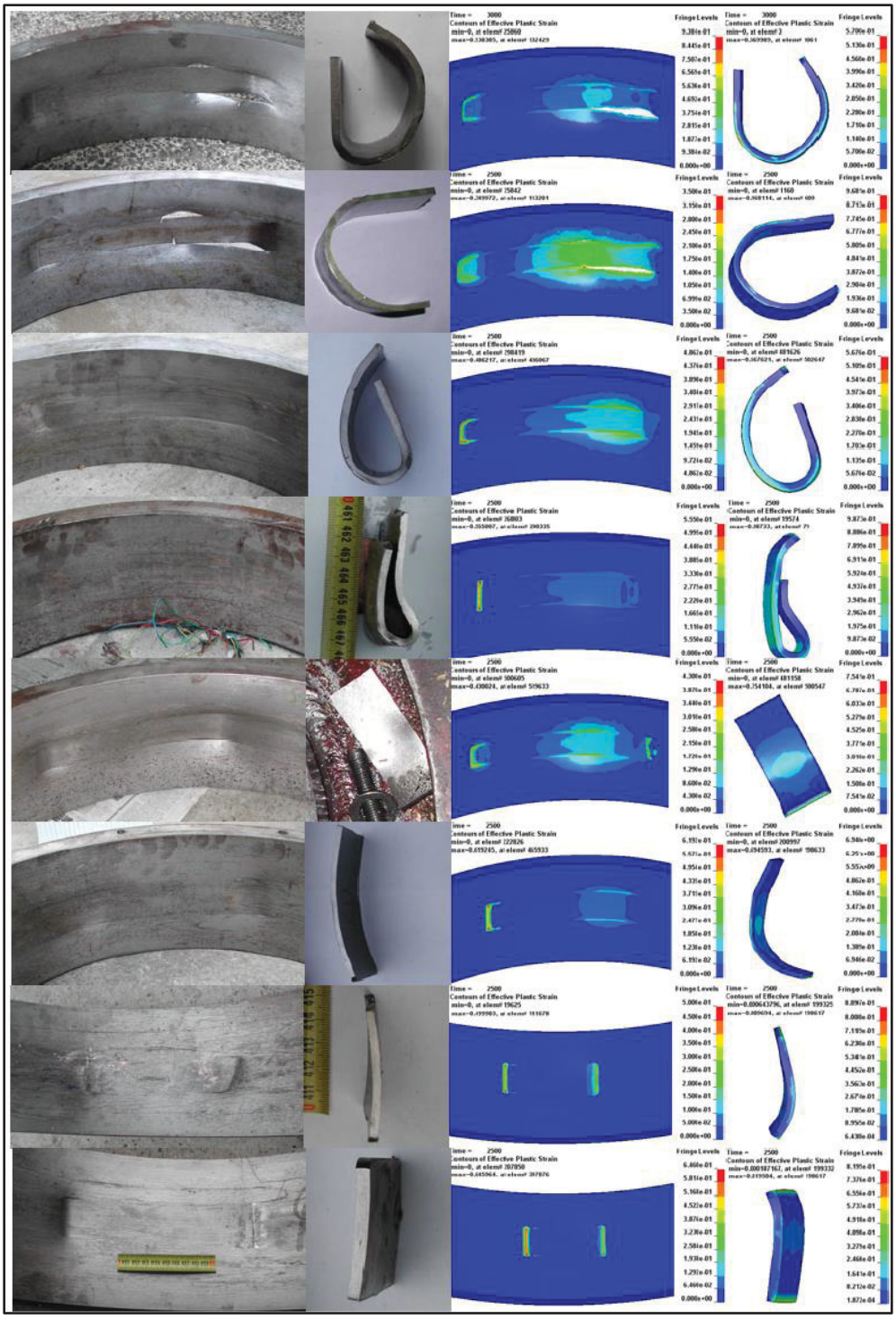

Figure 1.34 Correlation of FEA results with physical testing
Taken from He & al. (2012, p. 257)

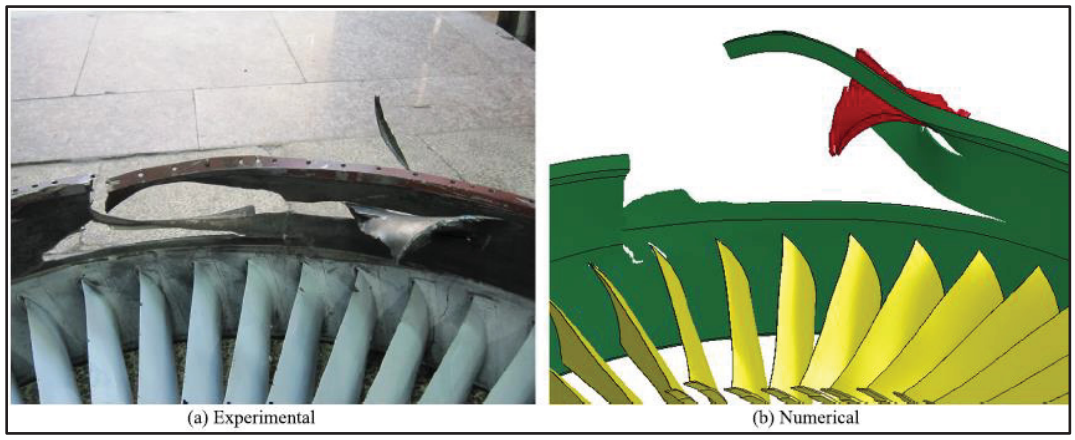

Figure 1.35 Fan blade-off simulation versus tests results
Taken from He & al. (2012, p. 103)

As studies in containment became more frequent, a set of guidelines were recommended by the LS-Dyna Aerospace Working Group for modelling different types of dynamic events in LS-Dyna (LS-DYNA Aerospace Working Group, 2011).

One of the material models suggested in this guideline is Johnson-Cook, an elasto-viscoplastic material, with the option to define the plastic failure strain function of stress triaxiality and Lode angle, in addition to function of strain rate, temperature and element size. The aerospace Working Group developed a procedure assisting LS-Dyna users with the definition of the required material card inputs.

1.2.4 Johnson-Cook Material Model Research

Due to the complexity of its development, a separate literature review is dedicated to the Johnson-Cook constitutive material model. The work detailing the cumulative damage fracture model for copper, iron and steel is referenced by Johnson and Cook in (Johnson & Cook, 1985).

Comprehensive research on the Al2024-T351 fracture is reported by Bao in (Bao, 2003). In addition to the extensive testing to understand the physical mechanisms of ductile crack formation, another outcome of the research is a procedure to determine the fracture locus of Al2024-T351 (Figure 1.36) based on the equivalent strain and stress triaxiality. A series of tests were complemented by their equivalent finite element analyses, performed in Abaqus. An almost perfect correlation of the numerical results with the test results was observed.

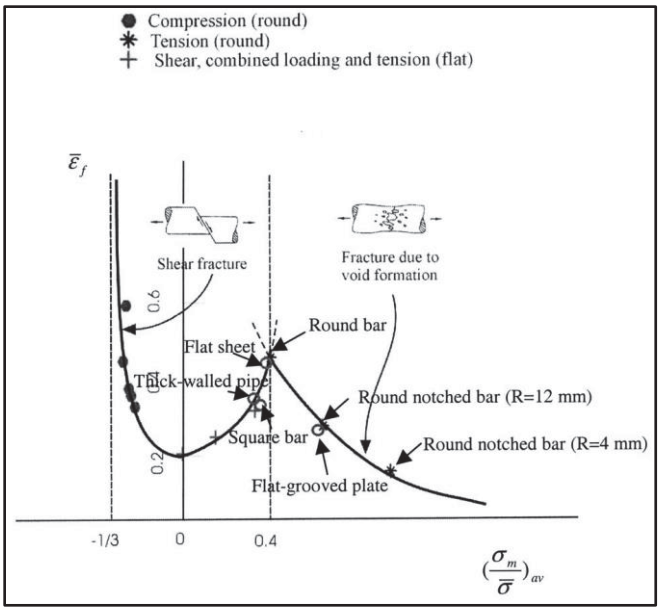

Figure 1.36 Fracture locus of Al2024-T351
Taken from Bao (2003, p. 128)

Under a collaboration program between NASA Glen Research Center (NASA-GRC), Federal Aviation Administration (FAA), Ohio State University (OSU) and George Washington University (GWU), a new material model for Al2024 was developed for usage in LS-Dyna simulations (Buyuk, 2014). In addition to the strain rate, temperature effects, mesh size, the adiabatic heating and softening of the material due to the plastic work was also considered. Various tests at different temperatures (Figure 1.37) and loading conditions supported the investigation of the ductile deformation and failure modes. The resulting material card was subsequently validated with ballistic tests.

Similar research issued by the same collaborating organizations determined the plastic deformation and the ductile failure characteristics for Ti-6Al-4V (Hammer, 2014). This research was also based on extensive testing at different temperatures and loading conditions, determining the ductile behaviour and failure locus for Ti-6A-4V (Figure 1.38).

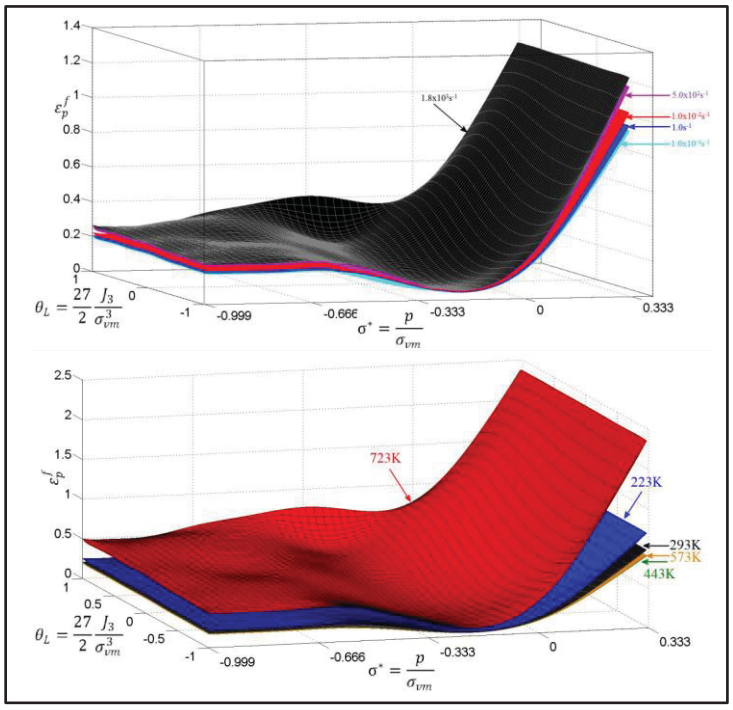

Figure 1.37 Al2024 Failure surfaces function of strain rates (upper image) and temperature (lower image)
Taken from Buyuk (2014, p. 430 & 433)

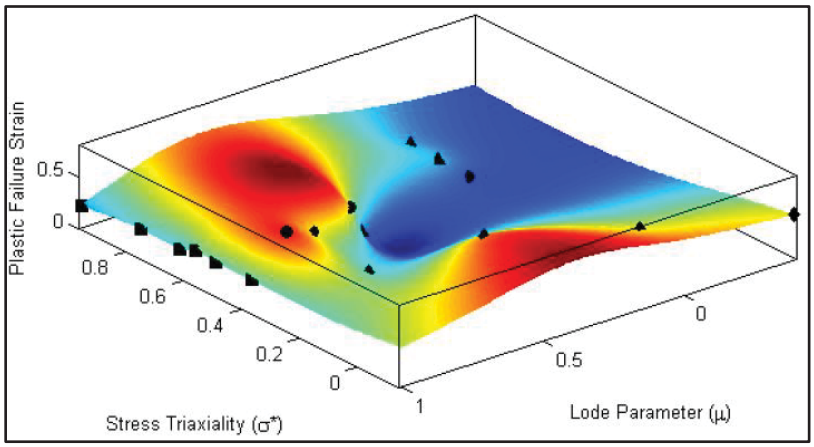

Figure 1.38 Ti-6Al-4V fracture locus
Taken from Hammer (2014, p. 111)

A subsequent work under the same research program completed the research with implementation of the material characteristics into an LS-Dyna material card (Haight & al., 2016). The output of this research work is the complete set of parameters assembled in a text file to be used in LS-Dyna simulations when components in Ti-6A-4V are involved in the impact.

The guideline for developing the material input parameters is developed in accordance with the works previously mentioned and presented the LS-Dyna Aerospace Working Group in (LS-DYNA Aerospace Working Group, 2019).

1.3 Summary

This chapter presented a literature review of the main published works relevant to the development of this study. Extensively researched, the terminal ballistic provides the understanding of the deformation modes and mechanisms of failure of gas turbine components involved in an impact following a rotor failure. The sub-ordnance impact of target plates revealed as dishing (membrane stretching, bending and shear plastic deformation) or plugging (local plastic deformation along the impact perimeter) being the two possible failure modes. Although responding to the question of failure mode, the equations determined for these scenarios are not directly applicable to the problem of fragment containment in gas turbines. Many of these studies considered the normal or oblique impact of plates with cylindrical, spherical or ogival projectiles (thus axisymmetric missile geometry), whereas the gas turbines containment case consists in cylindrical or conical structures impacted by an asymmetric fragment. From terminal ballistic perspective, this research proposes a method for selecting the proper mode of failure based on the shape of the turbine blade and on its kinematic conditions.

Another extensively researched topic presented in the literature review is the containment of a rotor fragment, studied as an engine macrostructural event. As the safe operation of the engine is at risk following a rotor failure, engine and aircraft manufacturers dedicated intense research efforts into developing analytical methods minimizing this risk.

Empirical, based on simplifying assumptions, these methods are rather coarse and need to be re-evaluated. One common lack of all the reviewed methods is the assumption of a unique failure mode (most methods considering shear), whereas ballistic studies revealed the existence of a threshold between shear and tensile + bending modes, depending on the shape and size of the impacting fragment. From terminal ballistic, it was repeatedly confirmed that the highest energy dissipation occurs during membrane stretching - Figure 1.18, (Corran, Shadbolt, & Ruiz, Impact loading of plates—an experimental investigation, 1983), therefore designing a casing based on a shear failure criterion (as for most of the current design methods) does not determine the optimum structure. Also, there is no consensus regarding the impact perimeter or the affected area. Another aspect needing consideration in the existing containment analytical methods is the blades interaction, which further contribute to the energy balance. As a final remark, no recent development (more recent than 1990) was recorded in the literature on the topic of fragment containment analytical (other than FEA) methods.

In the recent period, relevant progress was achieved in numerical methods, as presented in the FEA dedicated section of the literature review. Finite element analyses are nowadays commonly accepted in the gas turbines industry, airworthiness authorities accepting such results for certification, complementing the test experience of engine manufacturers. The progress in information technology allowed more computational intense analyses, therefore more components included in the analytical models, more mesh refinement, better contact interfaces and especially a more detailed material definition.

This research proposes a new and consolidated design method to be used in the preliminary design process of gas turbines casings, determining the minimum thickness of a casing required to contain one blade released from the turbine rotor. The proposed method defines the impact area, considers the threshold between the two possible failure modes and accounts for the energy exchanged between the released blade and the adjacent structures.

CHAPTER 2

RESEARCH METHODOLOGY

In the previous chapter was provided a general overview of the gas turbine rotor fragment containment topic, and the major aspects of this type of events were outlined. This section is dedicated to detailing the approach methodology of this research.

2.1 Research objectives

The objective of this research is the development of an analytical method to be used for designing the gas turbine casings to resist impact from rotor fragments, during early phases of design when the detailed geometry is not yet determined. As seen during the literature review, this is a multidisciplinary topic therefore the work is divided into three main areas of research:

1. Research the gas turbine rotor failure fragment containment phenomena (provides a macro perspective of this type of events), identify the relevant variables to be considered in the analytical method;
2. Investigate the fragment impact with the casing from terminal ballistic perspective (analyzes from a micro perspective of the impact event), and confirm the casing failure mode with the performed FEA;
3. Establish a FEA methodology supporting the analytical method development, and validate it with testing;

2.2 Approach

As all equation variables in this research are determined via FEA, the first step is the validation of the FEA analytical method with tests. A series of blade containment tests are simulated using state-of-art FEA methods, aligned with industry best practices and methods.

As the focus of these analyses is the casing behaviour during impact, a Johnson-Cook material model formulation is employed for the casing material, defining its mechanical properties function of strain rate, temperature, as well its damage function of stress triaxiality, Lode parameter, again strain rate, temperature, and element size. A simplified diagram of the research methodology is presented in Figure 2.1.

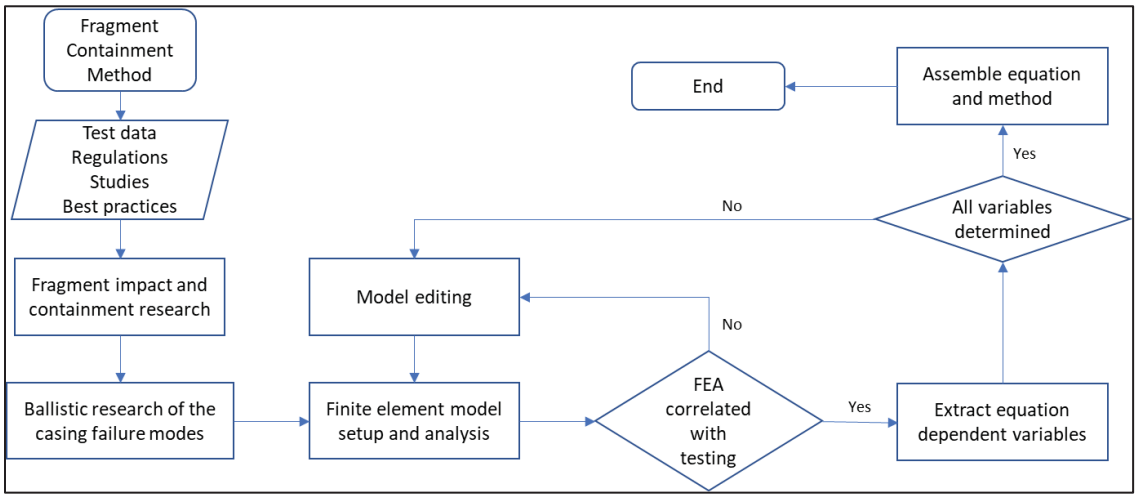

Figure 2.1 Fragment containment analytical method determination workflow

A detailed review and assessment of the fragment impact is performed from a terminal ballistic micro perspective to establish the variables to be extracted from the FE analyses, variables further implemented in the analytical equation. The failure modes of the casing are confirmed and monitored during the FEA. The validation of the FEA analytical method is considered successful and completed, when the simulated tests results match the results presented in the test report.

Following the FEA method validation, further post-processing reveals additional variables, accounting for the effect of blades interaction, blade erosion, and additional factors contributing to the impact.

In a final phase, the determined variables are assembled in the general equation, formulating the overall mathematical expression of proportionality between the plastic work and kinetic energy.

2.3 Methodology

For the development of the design analytical method, the following tasks are proposed:

1. Research into the existing design analytical methods, materials, geometric and kinematic parameters considered in these methods; retain the relevant variables and propose their validation with FEA
2. Investigate the containment process through terminal ballistics perspective, identify the gas turbine rotor fragment containment modes of failure; based on the previously determined fragment shape, formulate the threshold between the shear and tensile modes of failure and define the respective variable to be validated by FEA
3. Characterize the casing material properties used in the Johnson-Cook formulation. Assemble the material cards for the casing and blades to be used in FEA
4. Develop the FEA models corresponding to the JT3D and JT8D PT Blades containment tests and perform the tests simulations
5. From the FEA analyses correlated with tests in step 4, determine the equation variables
6. Assemble the variables in the design analytical equation

Resuming the previously mentioned, the objective of this current research is the development of an analytical method to be used for designing the gas turbine casings to resist impact from rotor fragments, during early phases of design when the detailed geometry is not yet determined. This analytical method determines the casing minimum thickness for resisting to an impact with a small fragment (single blade) released following a failure occurring in a turbine rotor. The novelty of the method consists in the consideration of the main impact as an effect of blades interaction, including the energy exchanged with the following blades, the energy dissipated through fragment deformation, as well as multiple modes of failure. All these contributions are evaluated through finite element analyses correlated with testing.

CHAPTER 3

FINITE ELEMENT ANALYSES

As revealed in the previous chapter, the FEA proved to be a reliable analytical method, with increasing accuracy greatly facilitated by the evolution of information technology. When coupled with experimental data, FEA increases the flexibility required by the engineering groups involved in the development of gas turbines. In the following sections of this chapter is detailed the correlation of a series of containment tests with numerical simulations. Hence, the finite element method, validated with these sets of tests, will be further used to determine the variables to be used in the design analytical equation.

3.1 Introduction

U.S. Federal Aviation Administration, Transport Canada, European Aviation Safety Agency and different other international airworthiness authorities require from engine manufacturers to demonstrate that their engines are able to contain one blade released from either fan, compressor or turbine rotor stages (Federal Aviation Administration, U.S. Department Of Transportation, 1984). As per Section 94 of the FAR 33 – Blade containment and rotor unbalance tests (Regulation, Federal Aviation, 1992), analysis can substitute testing based on service experience if it is shown to be equivalent to the test.

In later phases of design, when the geometries of components are determined, engine manufacturers dedicate an important effort to evaluate the engine containment capability analytically, experimentally, or both. Prior to testing for containment capability, Finite Element Analyses (FEA) are performed on the gas turbine components to determine their behaviour during the blade-off containment test.

The finite element models (FEM's) setup recreates the testing conditions, and both testing, and simulation replicate the worst ultimate loading that could occur during the engine operation.

For gas turbine manufacturers, correlating analytical with experimental results ensures the validity of the analytical methods used, and their further development.

In addition to the evolution of analytical methodologies, the information technology development allowed exponential increase on computational power, increasing the analyses accuracy, and hence promoting the acceptance of such analytical methods in lieu of testing, by the regulatory agencies.

Collaborations between gas turbine manufacturers, academia and governmental agencies focus on resolving aspects facilitating the acceptance of these analyses results by the regulatory agencies. Such a partnership, initiated by the FAA's Aircraft Catastrophic Failure Prevention Program in collaboration with NASA's Aviation Safety Program resulted in the creation of the LS-DYNA Aerospace Working Group (AWG). The goal of the AWG is to improve the reliability of high energy impact numerical simulations and ensure consistent FEA results, when using the well-established non-linear analysis program LS-DYNA. The modelling guidelines elaborated by the Group were developed following recommendations of industry representatives, and cover multiple aspects of aerospace impact simulations, such as blades impacting the engine containment, blade impacting aircraft structure, as well as other dynamic events affecting the safety of cabin interiors.

The analyses presented in this chapter are performed with LS-DYNA and follow two guidelines developed by the LS-DYNA AWG: 1. AWG Modeling Guidelines Document – MGD, and 2. AWG LS-DYNA Material Model User Guides.

3.2 Experimental Cases Test Description

A set of tests (Salvino, DeLucia, & Russo, 1988), part of the experimental Rotor Fragment Protection Program conducted by the Naval Air Propulsion Center (NAPC) under National Aeronautics and Space Administration (NASA) sponsorship, was used to validate the analytical method with numerical simulations. The scope of the study was to establish design guidelines for gas turbine casings considering turbine rotor fragment containment criteria.

The research consisted in two tasks, the first task studying the containment capability of cloth rings, and the second task being the determination of engine casing thickness necessary to contain single blade and triple blade fragments. The results of Task 2 pertaining only to the single blade release are used in this current research, the tests being simulated with FEA using LS-DYNA.

All tests were performed in a spin pit chamber (Figure 3.1). In a spin pit, a rotor is suspended under vacuum in a reinforced chamber and driven by an electrical motor to the critical rotational velocity. The test containment rings were placed at the bottom of the containment chamber, positioned concentrically around the rotor. An accelerometer was used to detect the time of failure.

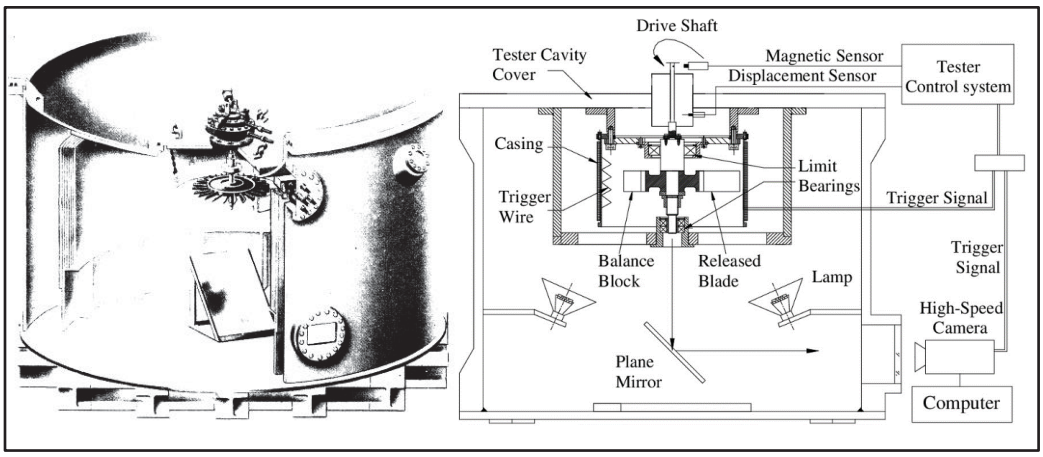

Figure 3.1 Test installation (left), typical spin pit test setup (right)
Taken from Salvino, DeLucia, & Russo (1988, p. 5), and from Xuan & al. (2018, p. 5)

In the Task 2 testing were used fully bladed rotors from JT3D and JT8D Pratt & Whitney engines. The choice of these two engines low pressure turbine stages was based on the consideration of them as being representative of large turbine rotors in use. Blades from these rotors were modified (fixing notched as shown in Figure 3.2) to fail at a specific rotational speed and impact the containment rings having different thicknesses.

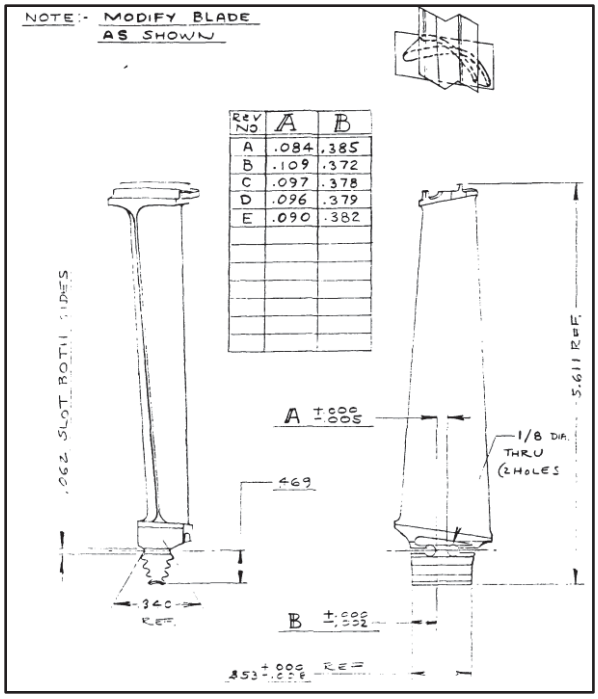

Figure 3.2 Single blade modification
Taken from Salvino, DeLucia, & Russo (1988, p. 16)

All containment rings were in A-286 steel, axial length of 9.0 in, ID of 28.00 in for JT8D, 35.05 in for JT3D and thicknesses varying from 0.140 in to 0.387 in (Figure 3.3).

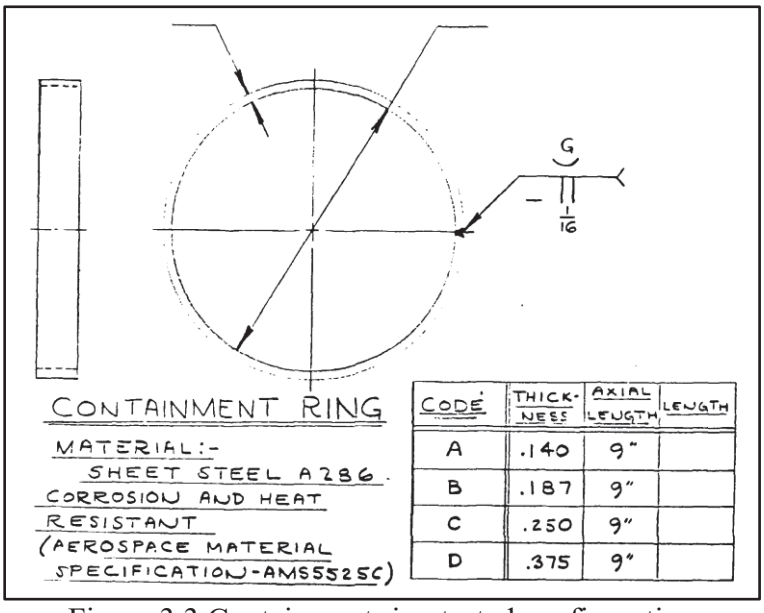

Figure 3.3 Containment ring tested configuration
Taken from Salvino, DeLucia, & Russo (1988, p. 15)

The succession of tests was performed using the following procedure: starting test on a ring of arbitrary thickness. If the ring contained the blade, another containment test was performed on the next smaller ring thickness and so on, until the ring no longer reached the fragment containment. A reversed logic (increasing ring thicknesses) was employed when the tests starting value of the ring thickness failed to ensure fragment containment (Figure 3.4).

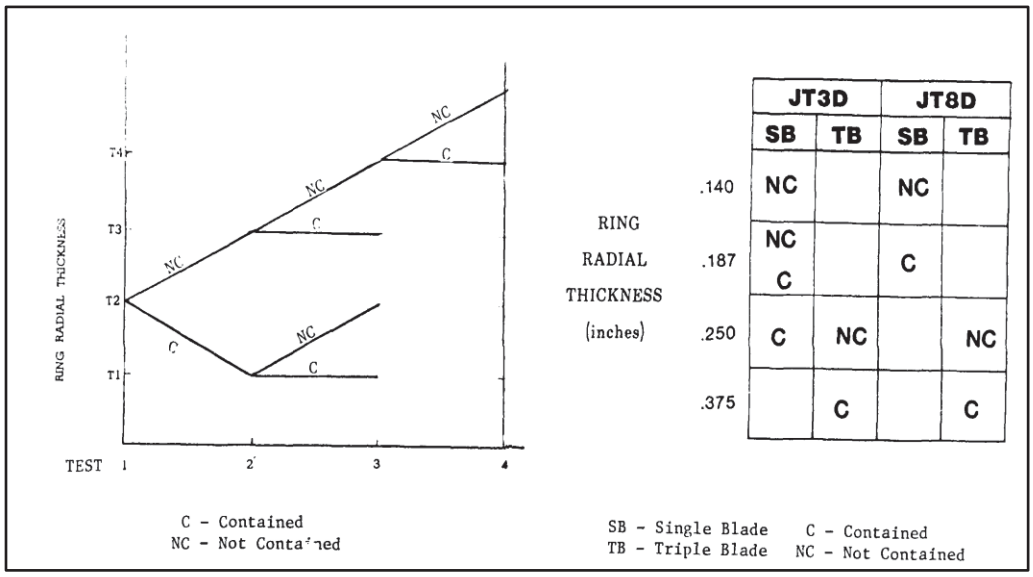

Figure 3.4 Single and triple blade containment tests
Taken from Salvino, DeLucia, & Russo (1988, p. 18)

The criteria for failure considered the state of damage suffered by the casings: no significant rupture, or hazardous distortion deemed the casing as containing the fragment.

An empirical formulation was developed for containment rings in A-286, considering the range of kinetic energies shown in Figure 3.5. A summary of the containment tests is shown in Table 3.1 (FE simulated tests shown in the red boxes). For the JT3D single blade failure, the minimum required thickness to contain the blade is reported as being 0.250 in, however in Figure 3.4, Figure 3.5 and Table 3.1 the 0.187 in thick ring also seems to have contained the blade. As in the test report there are no explanations about this, it can be speculated that the damage was borderline and the safest thickness value to be considered for containment was 0.250 in. In the case of JT8D LPT1 rotor, the minimum casing thickness required for containing a single blade was determined as 0.187 in.

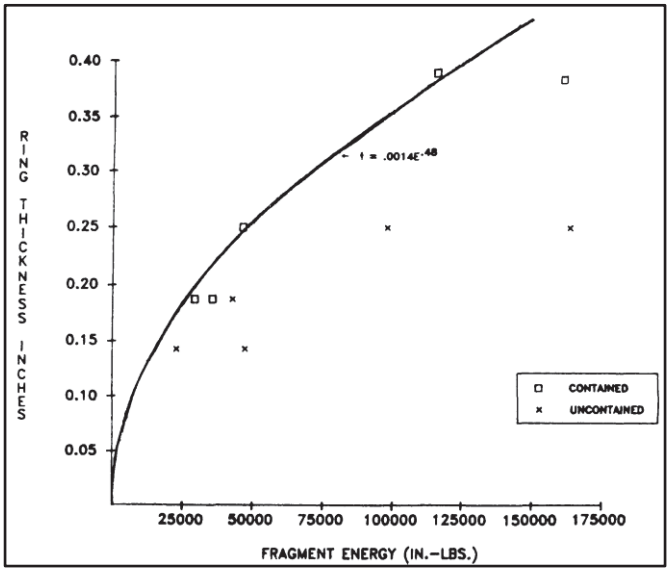

Figure 3.5 Containment ring thickness function of fragment kinetic energy
Taken from Salvino, DeLucia, & Russo (1988, p. 19)

Table 3.1 Blade containment experiments
Taken from Salvino, DeLucia, & Russo (1988, p. 21)

TABLE 2. BLADE CONTAINMENT EXPERIMENTS

TEST NO.	DATE	TYPE TEST	ROTOR/DISK TYPE	ROTOR/DISK MATERIAL	ROTOR/DISK DIAMETER INCHES	ROTOR/DISK NO. OF FRAGMENTS	ROTOR/DISK SPEED (RPM)	ROTOR/DISK ENERGY (IN-LBS)	CONTAINMENT/CONTROL CONFIGURATION	CONTAINMENT/CONTROL MATERIAL	CONTAINMENT/CONTROL ID INCHES	CONTAINMENT/CONTROL THICKNESS INCHES	CONTAINMENT/CONTROL AXIAL LENGTH INCHES	CONTAINMENT/CONTROL WEIGHT LBS	RESULTS
• 236	6/15/88	BB	JT3D LPT2	PWA 1003	34.9375	1	7152	50883	FLANGED RING	ALUMINUM	36	1/32	7	3	NOT APPLICABLE
• 237	6/2/88	BB	JT3D LPT2	PWA 1003	34.9375	1	6450	41319	FLANGED RING	ALUMINUM	36	1/32	7	3	NOT APPLICABLE
• 238	7/2/88	BB	JT3D LPT2	PWA 1003	34.9375	1	6000	35755	—	—	—	—	—	—	NOT APPLICABLE
• 239	6/15/88	BB	JT3D LPT2	PWA 1003	34.9375	1	6300	39419	—	—	—	—	—	—	NOT APPLICABLE
• 240	6/1/88	BB	JT3D LPT2	PWA 1003	34.9375	1	6492	41860	—	—	—	—	—	—	NOT APPLICABLE
• 242	6/12/91	BB	JT3D LPT2	PWA 1003	34.9375	1	7169	49373	RING	304 STAINLESS STEEL	35.05	.390	9	112	NOT APPLICABLE
246	7/14/91	BB	JT3D LPT2	PWA 1003	34.94	1	6145	36275	RING	A-286	35.05	.187	9	55	CONTAINED
248	8/5/91	BB	JT3D LPT2	PWA 1003	34.94	1	7020	47337	RING	A-286	35.05	.140	9	39	NOT CONTAINED
249	10/31/91	BB	JT3D LPT2	PWA 1003	34.9375	1	6736	43588	RING	A-286	35.05	.187	9	54	NOT CONTAINED
250	6/21/91	BB	JT3D LPT2	PWA 1003	34.9375	1	6942	46295	RING	A-286	35.05	.250	9	70	CONTAINED
• 251	12/11/91	BB	JT3D LPT-2	PWA 1003	34.9375	3	7245	174980	RING	304 STAINLESS STEEL	35.05	.390	99	112	NOT APPLICABLE
• 252	7/27/92	BB	JT8D LPT-1 (SD)	A-286	27.35	1	7600	19739	RING	304 STAINLESS STEEL	28	393	9	56.54	NOT APPLICABLE
• 253	8/25/92	BB	JT8D LPT-1	A-286	27.35	1	9900	33494	RING	304 STAINLESS STEEL	28	393	9	56.54	NOT APPLICABLE
• 254	9/13/92	BB	JT8D LPT-1	A-286	27.35	1	9024	27830	RING	304 STAINLESS STEEL	28	393	9	56.54	NOT APPLICABLE
256	11/18/92	BB	JT8D LPT-1	A-286	27.35	1	9360	29916	RING	A-286	28	187	9	40	CONTAINED
257	2/10/93	BB	JT8D LPT-1	A-286	27.35	1	8290	23486	RING	A-286	28	140	9	32.5	NOT CONTAINED
258	4/7/93	BB	JT8D LPT-1	A-286	27.35	3	8200	98945	RING	A-286	28	.250	9	55	NOT CONTAINED
259	7/1/93	BB	JT8D LPT-1	A-286	27.35	3	8888	116219	RING	A-286	28	.390	9	89.5	CONTAINED
260	12/14/93	BB	JT3D LPT-2	PWA 1003	34.9375	3	6907	163479	RING	A-286	35.05	244	9	69.5	NOT CONTAINED
261	5/28/94	BB	JT3D LPT-2	PWA 1003	34.9375	3	6805	161250	RING	A-286	35.05	304	9	110.5	CONTAINED

• Indicates preliminary test

These test results were deemed to be applicable to any turbine engine stages having release energies in the same orders of magnitude as reported, and casings in A-286 steel.

3.3 Finite Element Model Setup

The finite element models (FEM) for the two sets of tests (JT3D and JT8D) were prepared with information available in the public domain and following the guidelines from the LS-DYNA Aerospace Working Group (AWG). For both sets of tests, the FEM consisted in several meshed blades, and the containment rings of different thicknesses, models detailed in the following sections.

3.3.1 Geometry

For the JT3D series of tests, the blade (Figure 3.6) was digitized from the information provided in the test report (Salvino, DeLucia, & Russo, 1988).

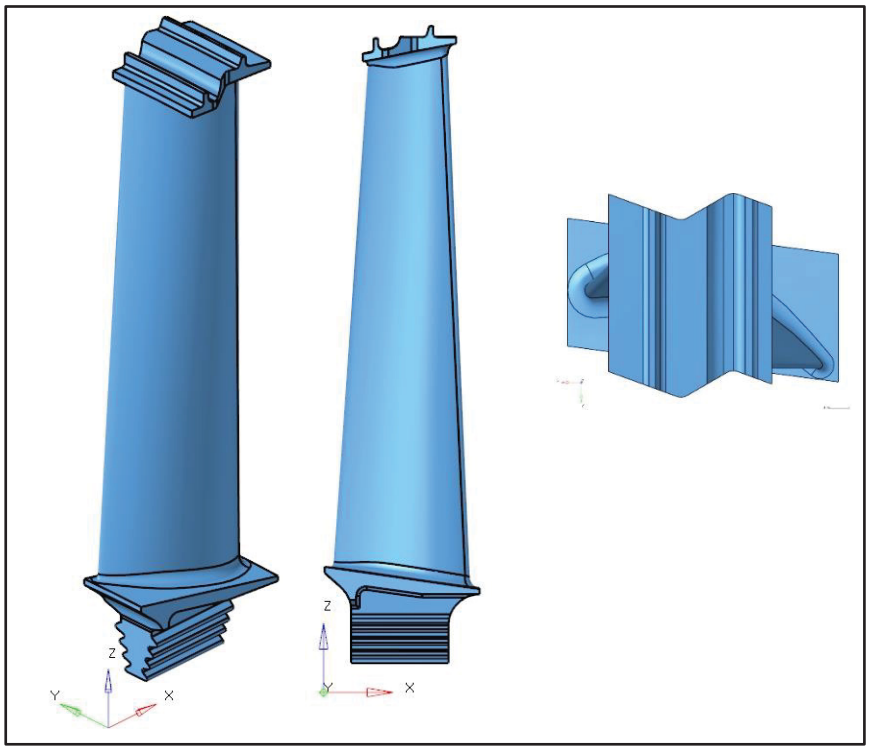

Figure 3.6 JT3D LPT2 Blade geometry

In the tests, the blades were notched under the platform (Figure 3.7), such as to initiate failure at the respective intended rotational speed. Similarly, only the blade fragment upward to the notch was considered in the test validation simulations.

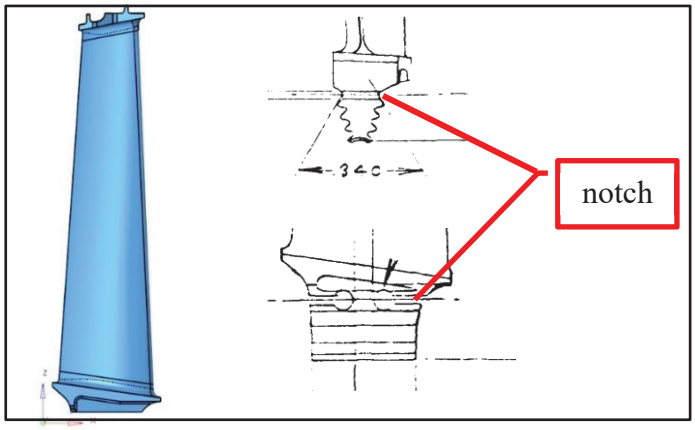

Figure 3.7 JT3D LPT2 Blade fragment

For the JT8D LPT1 blade, it was used an approximated geometry (Figure 3.8), obtained from GrabCAD Community and presented as "Shrouded Turbine Blade – Pratt & Whitney Standard", courtesy of Hamidreza Hoshyarmanesh. The blade geometry is deemed acceptable for the purposed usage. Similarly, as in the case of the JT3D LPT2 blade, the radial outermost groove (the closest to the blade platform) was assumed as being notched, hence disregarding the blade firtree in the analysis.

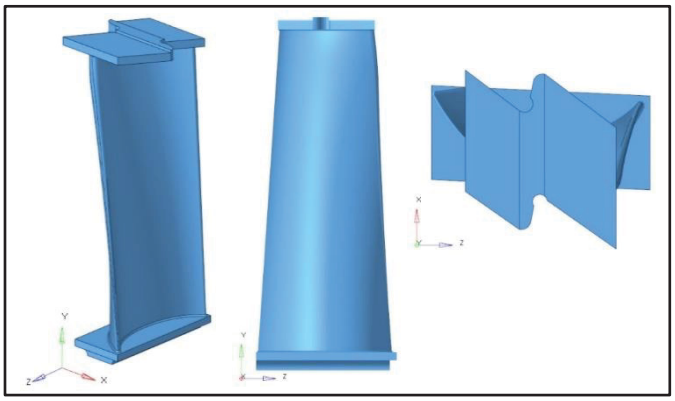

Figure 3.8 JT8D LPT1 Blade fragment

A comparison between the two blades is shown in Figure 3.9. The blades fragments were aligned approximatively for visual perspective.

Figure 3.9 Different views for JT3D LPT2 blade (blue) compared with JT8D LPT1 blade (magenta); isometric (left), front (centre) and lateral (right)

The containment rings are cylinders of the same axial length 9.0 in, however with an internal diameter (ID) of 35.05 in in the case of JT3D LPT2, and 28.00 in for the JT8D LPT1. For the simulations were considered the following thicknesses: 0.140 in, 0.187 in for JT8D, and 0.187 in and 0.250 in for the JT3D (also mentioned previously in Table 3.1). The assembled geometries are shown in Figure 3.10. For each series of tests, several configurations were considered (varying the number of blades). Details are provided in the following meshing section.

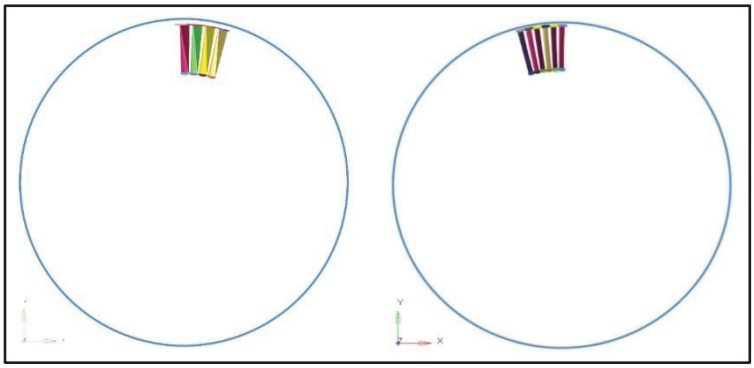

Figure 3.10 JT8D engine LPT1 (left) and JT3D engine LPT2 (right)

3.3.2 Mesh

All FE models developed for this research are based on solid, hexahedral elemental mesh. Each individual blade consists in 3 components: shroud, airfoil and platform. To replicate the fragmentation of the blade, the airfoil has an erosion criterion activated in its material card definition (detailed in the materials section of this chapter). Both platform and shroud are deformable, however erosion is not allowed. Also, all blade fragments were presumed to be released from a full blade fracturing above the firtree in the shank area under the platform.

The thinner sections of the model (platform, airfoil) have a minimum of 3 elements per thickness. The mesh is continuous, the shroud, airfoil and platform share the interface nodes. Due to the complicated transition between the airfoil and shroud (respectively platform), some elements belonging to the shroud and some more of the platform have a poor aspect ratio. However, as erosion is not allowed for these components, there will be no significant effect on the overall accuracy of the analysis.

The JT8D LPT1 blade model consists in 35,991 nodes and 27,688 elements, and the JT3D LPT2 blade fragment is made of 10,468 nodes and 7,670 elements, as shown in Figure 3.11.

All ring models included 3 elements per ring thickness, with mesh refinements to 9 elements per thickness in the impact areas (Figure 3.12). The mesh details are collected in Table 3.2.

To account for the poor elemental aspect ratios of the blade mesh, for all solids the formulation in LS-DYNA (element section property *SECTION_SOLID, ELFORM) is -2. As most casing elements have an aspect ratio of 1 (excepting mesh refinement transition areas), the element property type (ELFORM) was selected as 2, corresponding to a fully integrated solid element.

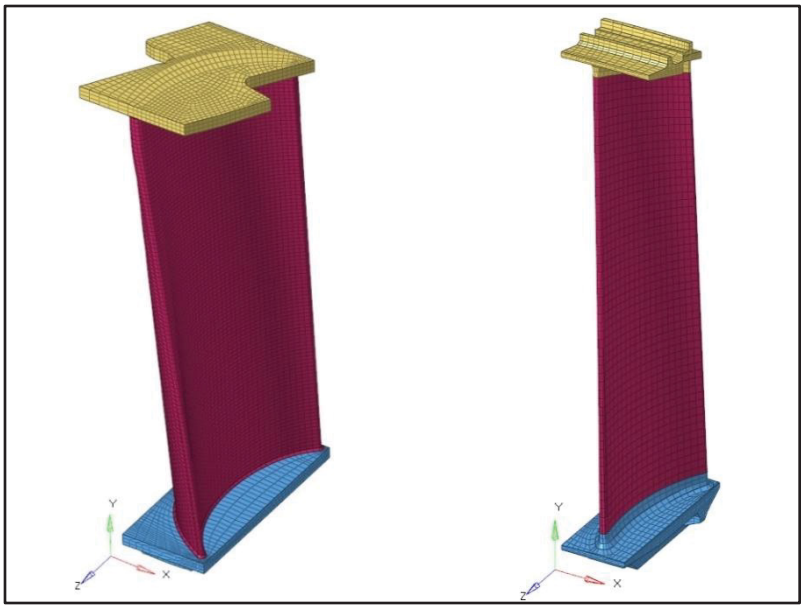

Figure 3.11 JT8D LPT1 blade mesh model (left); JT3D LPT2 blade mesh model (right)

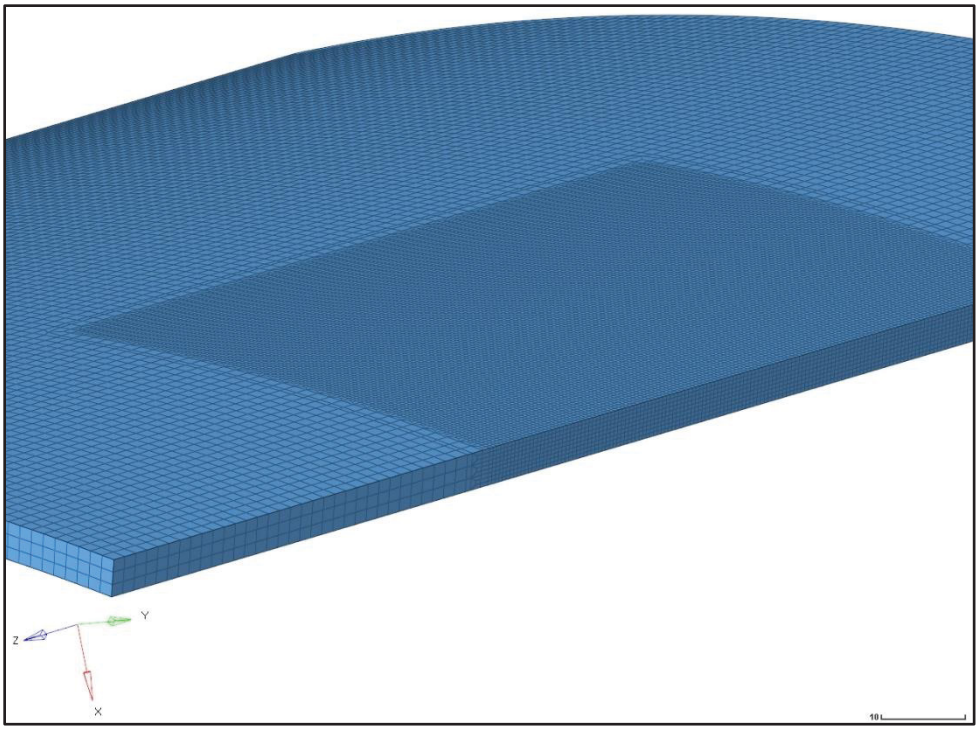

Figure 3.12 Containment ring refined mesh in the impact zone (cross section)

Table 3.2 Components mesh details

Component	Nodes	Elements
JT8D LPT1 Blade fragment (one single fragment)	35,991	27,688
JT8D LPT1 Casing (0.140” thick)	2,512,616	2,054,580
JT8D LPT1 Casing (0.187” thick)	1,707,120	1,416,108
JT3D LPT2 Blade fragment (one single fragment)	10,468	7,670
JT3D LPT2 Casing (0.187” thick)	1,954,708	1,548,390
JT3D LPT2 Casing (0.250” thick)	1,182,248	935,785

3.3.3 Finite element model components

All models included several blades and one cylindrical containment ring (Figure 3.13). Different model configurations were simulated iteratively, until an agreement was reached regarding the number of blade fragments to be included in each simulation. In the case of JT8D LPT1 blade fragment containment test, it was observed that 4 blades were sufficient to capture the overall energy exchange. For the JT3D LPT2 blade fragment containment, the model needed to include 6 blades to capture the whole energy exchange process. This is explained by the stiffness of each stage individual blades, in general the LPT1 blades being sturdier than the slender LPT2 blades.

3.3.4 Boundary and kinematic conditions

The setup of all models followed the guidelines elaborated by the LS-DYNA AWG (LS-DYNA Aerospace Working Group, 2011).

In all finite element models (for both JT3D and JT8D series of tests), as failure criteria were activated for some of the components, eroding contacts were defined to ensure the interaction between the components, while allowing the element erosion.

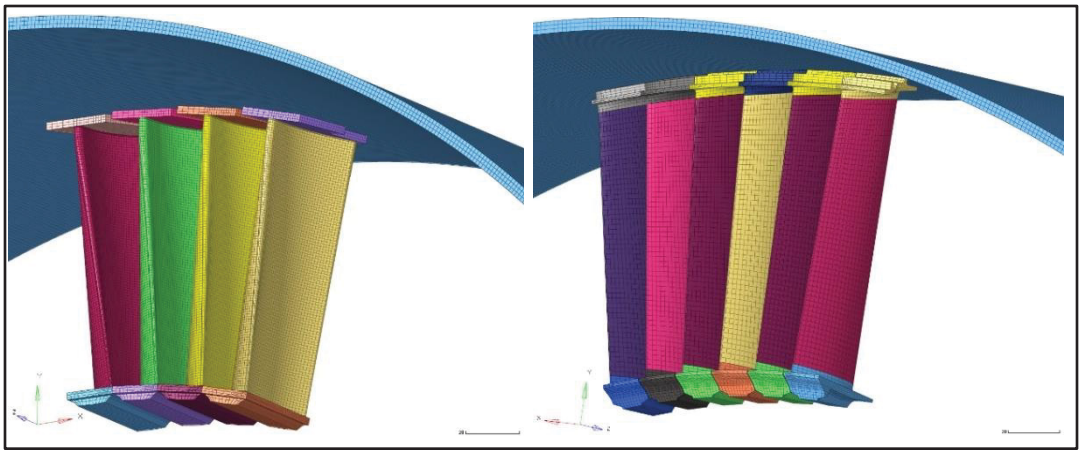

Figure 3.13 JT8D LPT1 (left) and JT3D LPT2 (right) finite element models

During all containment tests, the rings were simply supported on the platform at the bottom of the spin pit test chamber. Therefore, as the simulations did not consider the gravitational acceleration, the containment rings were not constrained in any direction.

As recommended in the AWG MGD (LS-DYNA Aerospace Working Group, 2011), the simulations were set up in two phases: initializing the blade centrifugal stresses in an implicit static solution, then subsequently performing the explicit transient analysis.

For the first phase, the centrifugal load is applied to each of the blades, which are fixed at their lowest nodes (Figure 3.14) to prevent any rigid body motion (*BOUNDARY_SPC_SET). The resulting *dynain* file containing the deformed geometry and the stress state (stresses and strain resulted from the centrifugal loading) is further input in the subsequent transient explicit analysis. As a validation of the stress initialization, a cross section (Figure 3.15) is defined on each blade and the force magnitude is verified with the calculated value corresponding to the centrifugal force.

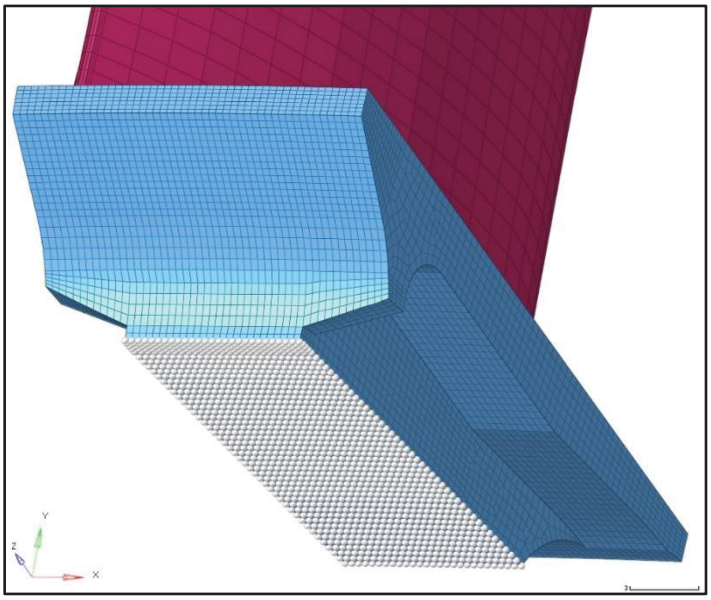

Figure 3.14 Set of nodes supporting static or kinematic constraints

During the preloading implicit analysis, the velocities of components are null, however in the second phase analysis, the velocities are initialized to the respective values for each case. In addition to the initial velocities (*INITIAL_VELOCITY_GENERATION), the blades are rotated by a prescribed motion (*BOUNDARY_PRESCRIBED_MOTION_SET). While the prescribed motion of the following blades is maintained for the full time of the analysis, the prescribed motion of the released blade is terminated after 5.0E-5 seconds, allowing it to move freely and interact with the adjacent structures.

The blades, in addition to their motion, are constrained in the axial direction (Z axis).

3.3.5 Material properties

As per the test report (Salvino, DeLucia, & Russo, 1988), the JT8D LPT1 blade material is AMS 5391 (INCONEL 713C), the JT3D LPT2 blade is a Cobalt alloy as per AMS 5382 (one commercial designation being Stellite 31) and all the containment rings are in AMS 5525C (A-286 steel), as shown in Table 3.3.

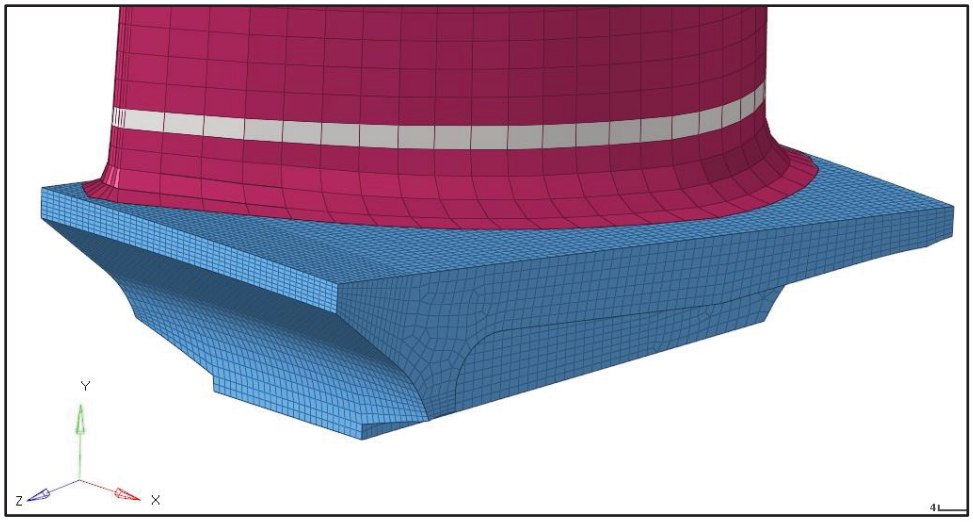

Figure 3.15 Airfoil cross-section element set

All material data used were obtained from the public domain (The Nickel Institute), (Haynes Stellite Company, 1960), (Kattus, Preston, & Lessley, 1958), (Nicholas, 1980), (Rice & al., 2003), and when details were missing, engineering judgment was employed to evaluate the missing information. The research object of this work is the determination of an analytical method for blade containment, and not presenting the most accurate characterisation of material properties for the analysed components.

Table 3.3 Component materials mechanical properties

Component	Material standard	Commercial name	Young modulus [MPa]	Tensile strength [MPa]	0.2%Yield strength [MPa]	Elongation [%]
LPT1 Blade	AMS 5391	INCONEL 713C	206429	848	735	7.9
LPT2 Blade	AMS 5382	Stellite 31, X-40	248211	779	548	8
Casing	AMS 5525	A-286	200637	965	655	15

In all test simulations presented in this research, the focus is on the material failure of the containment rings, for which a detailed response is facilitated when using a Johnson-Cook material model (LS-DYNA MAT_224). The blade failure mode is considered secondary. Therefore, for the blade fragments it was used a piecewise linear elasto-plastic material model (*MAT_024 in LS-DYNA). Although this material card allows strain rate dependency, due to

the unavailability of data in the public domain for these blades materials, this option was not used. The failure criteria used the effective plastic true strain corresponding to each material tensile elongation.

As definition curve for this material card, LS-DYNA uses the effective stress function of effective plastic strain, which for the uniaxial stress are equivalent with the true stress versus true strain. Further details about the material cards and their parameters can be found in (Livermore Software Technology, 2020).

Although non-negligible, as seen previously, the material definition for the blades is somewhat simplistic. The purpose of the blades modelling (more or less accurate) is to capture their energy exchange with the interacting structures, while fragmenting and deforming in a similar mode as observed in previously published testing. A more careful consideration was dedicated to the casing material, where a very complex (state-of-art) material model was employed. Also, for the casing, public domain test data was mostly available, allowing the material card calibration with tests.

For the casing material card was used *MAT_TABULATED_JOHNSON_COOK, or in short *MAT_224. This is an isotropic, elastic, thermo-viscoplastic material model allowing plastic failure strain definition function of any combination of triaxiality and Lode parameter (functions of the 3D stress state) (LS-DYNA Aerospace Working Group, 2011), (Johnson, A constitutive model and data for materials subjected to large strains, high strain rates, and high temperatures, 1983). The formulation for the von Mises flow stress is:

$$\sigma = \left[A_{JC} + B_{JC} \cdot \varepsilon^{n_{JC}}\right] \cdot [1 + C_{JC} \cdot \ln \dot{\varepsilon}^*] \cdot [1 - T^{*m_{JC}}]; \tag{3.1}$$

where ε is the equivalent plastic strain, $\dot{\varepsilon}^* = \frac{\dot{\varepsilon}}{\dot{\varepsilon}_0}$ is the dimensionless plastic strain rate for $\varepsilon_0 = 1.0 \cdot s^{-1}$, and T^* is the homologous temperature; A_{JC}, B_{JC}, C_{JC}, m_{JC}, n_{JC} are material constants.

The first term of the equation describes the stress variation function of strain hardening, the second bracket details the strain rate hardening and the third bracket captures the thermal effect (thermal softening).

The LS-DYNA implementation of this material definition includes consideration of the amount of plastic work converted into heat, as well as a complete definition of the effective plastic failure strain (ε_{pf}) as a surface, defined (LS-DYNA Aerospace Working Group, 2019), (LS-DYNA Aerospace Working Group, 2011) as:

$$\varepsilon_{pf} = f(\tau_{tria}, \theta_L) \cdot g(\dot{\varepsilon}_p) \cdot h(T) \cdot i(l_e); \tag{3.2}$$

where τ_{tria} is the stress triaxiality, θ_L is the Lode parameter, $\dot{\varepsilon}_p$ is the plastic strain rate, and l_e being the element size factor; more explanations on the element size factor in (Haight & al., 2016).

For this material, the failure criterion based on the accumulation of damage (LS-DYNA Aerospace Working Group, 2019), (LS-DYNA Aerospace Working Group, 2011) is expressed as:

$$D = \int \frac{\dot{\varepsilon}_p}{\varepsilon_{pf}} dt; \tag{3.3}$$

When $D \geq 1$, the element is considered as failed and is deleted from the analysis.

For the determination of $f(\tau_{tria}, \theta_L)$, a series of different types of tests are simulated to generate each failure curve, corresponding to a specific triaxiality (τ_{tria}) and state of stress (θ_L). The diagram for generating the *MAT_224 card is shown in Appendix III, Figure-A III-1.

The complete *MAT_224 card is shown in Figure 3.16.

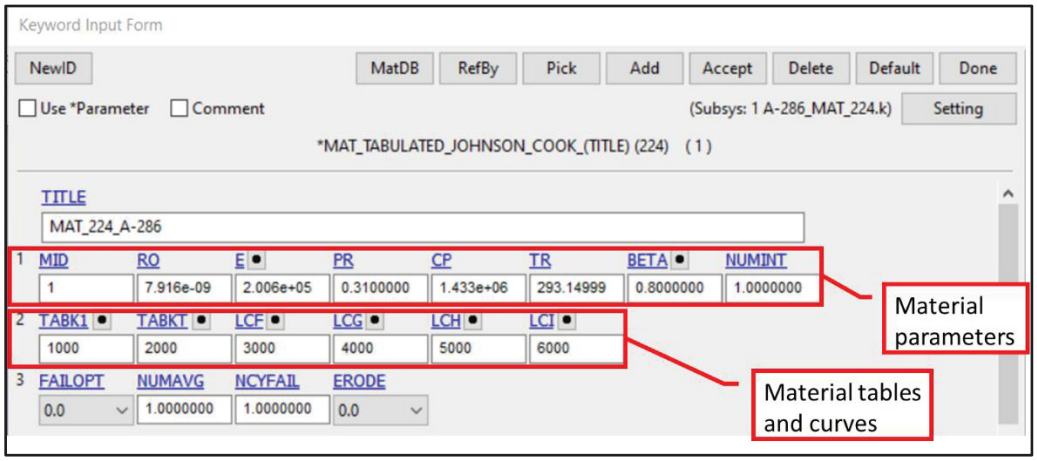

Figure 3.16 *MAT_224 card in LS-DYNA

In addition to the usual material input parameters (density, Young's modulus, Poisson's ratio), the following parameters were added: specific heat (C_p), room temperature (TR) and beta (β). Beta defines the percentage of plastic work converted into thermal energy (Taylor-Quinney coefficient). Although its definition can be very complex, for this work it was assumed a constant value of 80%, as considered in the previous similar works for Ti-6Al-4V in (Haight & al., 2016). A more accurate definition requires dedicated testing and is beyond the scope of this work.

At this moment, the Johnson-Cook material card is validated with one series of tests (SHB), hence it is ready to be used for the containment tests simulations, which can constitute a second, independent validation. The details of the material card definition are provided in Appendix III.

3.4 Finite Element Results

All containment tests explicit simulations, as well as the preloading implicit runs were performed using the double precision Shared Memory Parallel (SMP) LS-DYNA solver, with 16 CPU's.

3.4.1 JT8D contained test

The highest rotational velocity recorded during the tests (Salvino, DeLucia, & Russo, 1988), corresponds to the contained test for one blade released from the PT1 rotor of the JT8D engine. In the test report, a 0.187 in thick ring in A-286 steel, successfully contained the blade fragment released at a speed of 9,360 rpm and generating an energy of 29,916 in · lbf (3,380,054 N · mm). The results of the simulation of this test are presented in this sub-section.

As mentioned previously, the blades are preloaded during an implicit FE analysis, and the resulting stress generated by the centrifugal loading is shown in Figure 3.17. A maximum stress of 132 MPa occurs at the airfoil root.

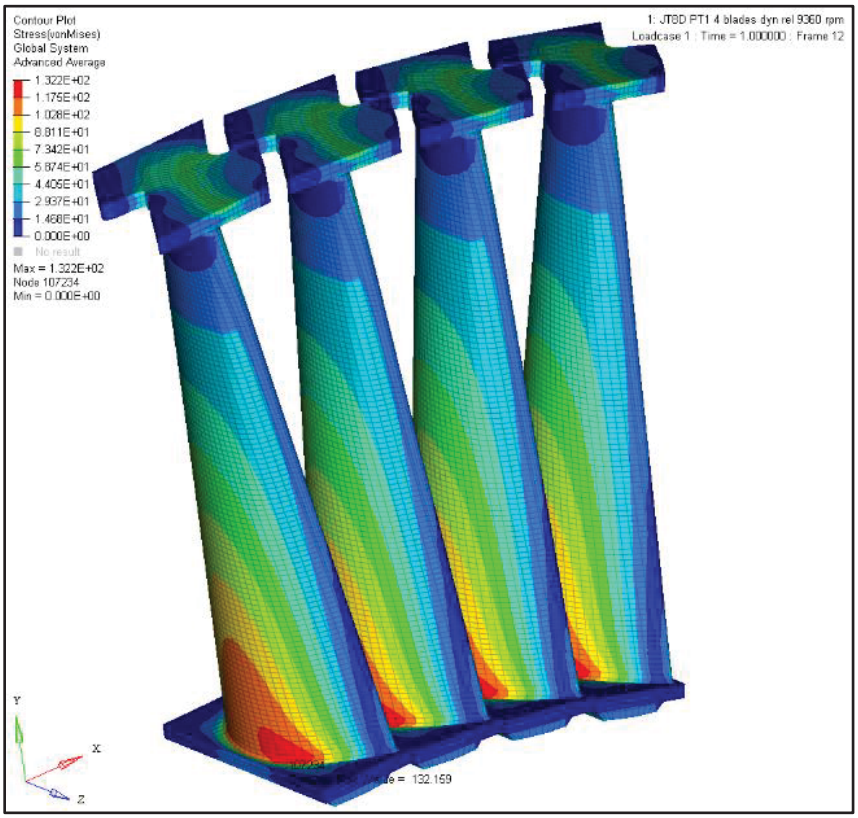

Figure 3.17 JT8D PT1 blades stress due to centrifugal preload at 9,360rpm

The deformed shapes (new nodal coordinates), as well as the elemental stresses and strains are input as an external file in the master file of the subsequent explicit analysis.

As observed in the explicit analysis, following the blade release, and after the first impact with the casing, the released blade centrifugal preload is lost due to the blade fragmentation, and the airfoil is subjected to highly oscillatory loading due to interactions with the casing and the following blades. The blades preload cross-sectional forces are shown in Figure 3.18.

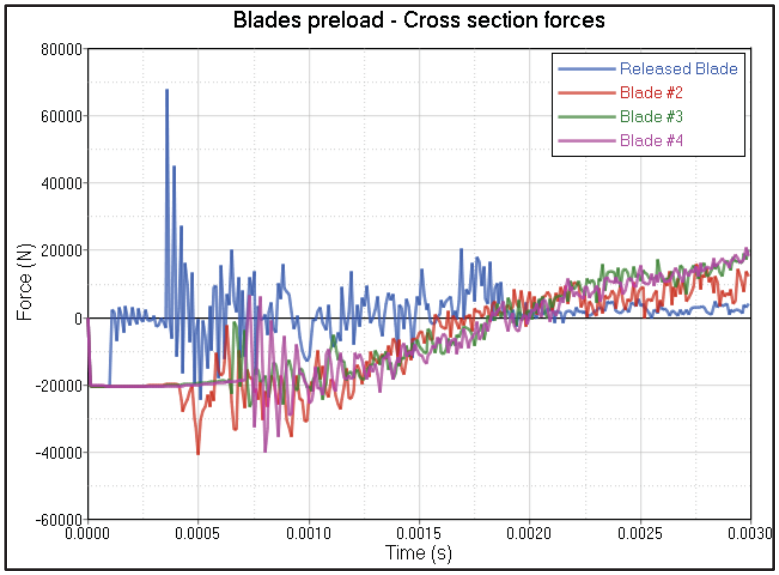

Figure 3.18 JT8D PT1 Blades preload cross section forces at 9360 rpm

Other than the blade preload, the released blade kinetic energy is to be verified early in the analysis. As the fragment geometry is not accurate (obtained from the public domain), the blade material density was adjusted to obtain the reported kinetic energy (KE) for the reported rotational velocity. After this adjustment, the FEA resulting released blade KE is 3,379,990 mJ (1 mJ = 1 N · mm), representing a 0.002% difference from the reported KE of 29,916 lbf · in generated at 9,360 rpm, for the JT8D PT1 contained test.

For the structural explicit models, multiple configurations were analysed, with different meshing options (coarse blade mesh, fine blade mesh, coarse mesh casing, refined mesh casing – one patch corresponding to the main impact, or two patches corresponding to both major impacts). All these variants revealed an overall very similar energetic exchange (same energetic jumps during the main impacts), the differences being only in the amount of eroded energy (higher slope of the internal energy curves). For the JT8D, only one FE model

configuration generated an un-contained event (more details are provided in the next section, and in the discussion chapter), therefore for the contained test it was consistently considered the same configuration (coarse continuous mesh for the blades, and two refined mesh patches on the casing).

The FE analysis revealed three distinct phases of the fragment containment process:

1. Initial contact of the released blade with the casing, contact during which the blade loses rapidly part of its kinetic energy;
2. Continuous contact of the blade fragment with the casing; important damage of the released blade airfoil due to the interaction with the following blade, and with the casing;
3. Second impact of the released blade, when the platform is pushed into the casing by the following blades.

The first impact of the released blade with the casing occurs when the shroud of the released blade contacts the casing. During this impact, the only exchange of energy is between the released blade and the casing. The velocity variation due to aerodynamic loading is neglected, hence the full kinetic energy of the fragment is available for the transfer. During this first impact, the weakest section of the components involved in the impact (airfoil tip, at the fillet radius under the shroud) fractures (Figure 3.19). The casing suffers permanent damage (an effective plastic strain of 0.036), however resists well to the impact. The first impact phase concludes when the effective plastic strain on the outer face of the casing stabilizes at its maximum value.

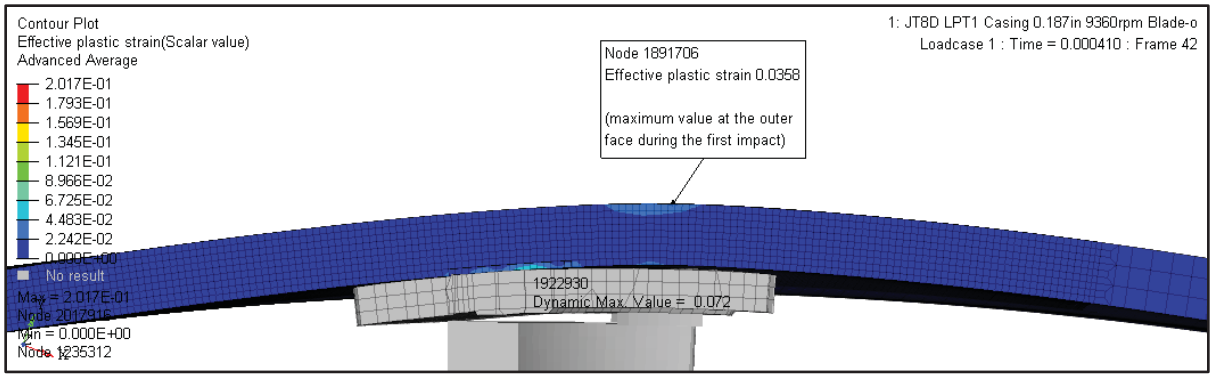

Figure 3.19 Effective plastic strain at the end of the first impact of the released blade with the casing

The second phase of the containment process is represented by a continuous erosion / damage of the remaining airfoil due to the interaction with the casing and the following blades. During this phase (Figure 3.20), the casing exchanges continuously energy with the blade fragments. As during this phase, the fragment impacts zones with different mesh densities, and due to the erosion of elements in the fine mesh areas, the slope of the casing internal energy curve varies (steeper during the fragment passage through the fine mesh areas), however the energy exchange is relatively constant.

The next energy jump occurs during the third phase (Figure 3.20), when the remaining fragment is pushed into the casing by the following blades (Figure 3.21). Also, during this phase, the casing resists to the impact, accumulating a local effective plastic strain equal to 0.03. Past this second impact, the kinetic energy of the fragment is greatly reduced (Figure 3.22), the fragment being driven by the following blades circumferentially along the inner face of the casing (Figure 3.23).

After the second main impact (thus after the end of Phase 3), there is no important energy exchange between the remaining fragments and the casing (Figure 3.20), the variations in the remaining KE (Figure 3.22) being due to the energy exchange between the fragments and the remaining following blades. As no additional structures (such as stators) were included in the model, there is no damage on blades #3 and #4, however in reality all rotor blades are damaged during a blade release event.

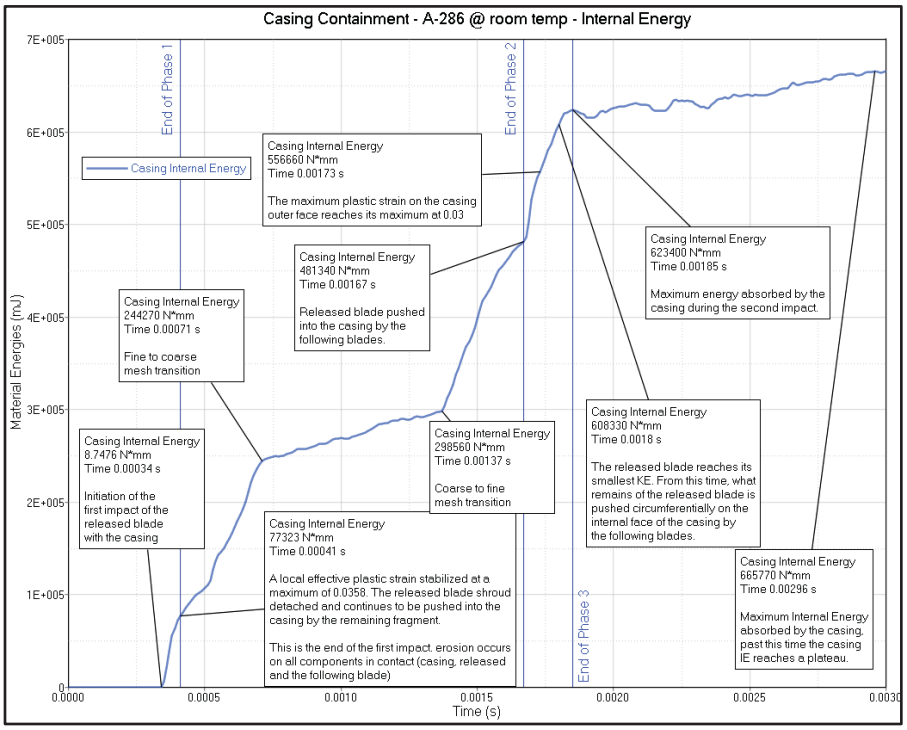

Figure 3.20 JT8D 9360rpm Casing energy absorption during the impacts with the released fragment

The impact zone on the casing is strained in a narrow band, with its size proportional with the blade platform thickness and width (Figure 3.24).

On the outer face of the casing, the extent of the impact area subjected to plastic deformation is shown in Figure 3.25.

The extent of the secondary impact zone, as radial displacement, is shown in Figure 3.26. The second main impact peak radial displacement on the outer face, reaches 1.158 mm and occurs at time 0.00174 s, hence almost at the same time with the maximum effective plastic strain. The delay is due to the high impact velocity and to the impact area material volume inertia. Due to the elastic component of the deformation, after the fragment exits the impact zone, the radial deformation decreases.

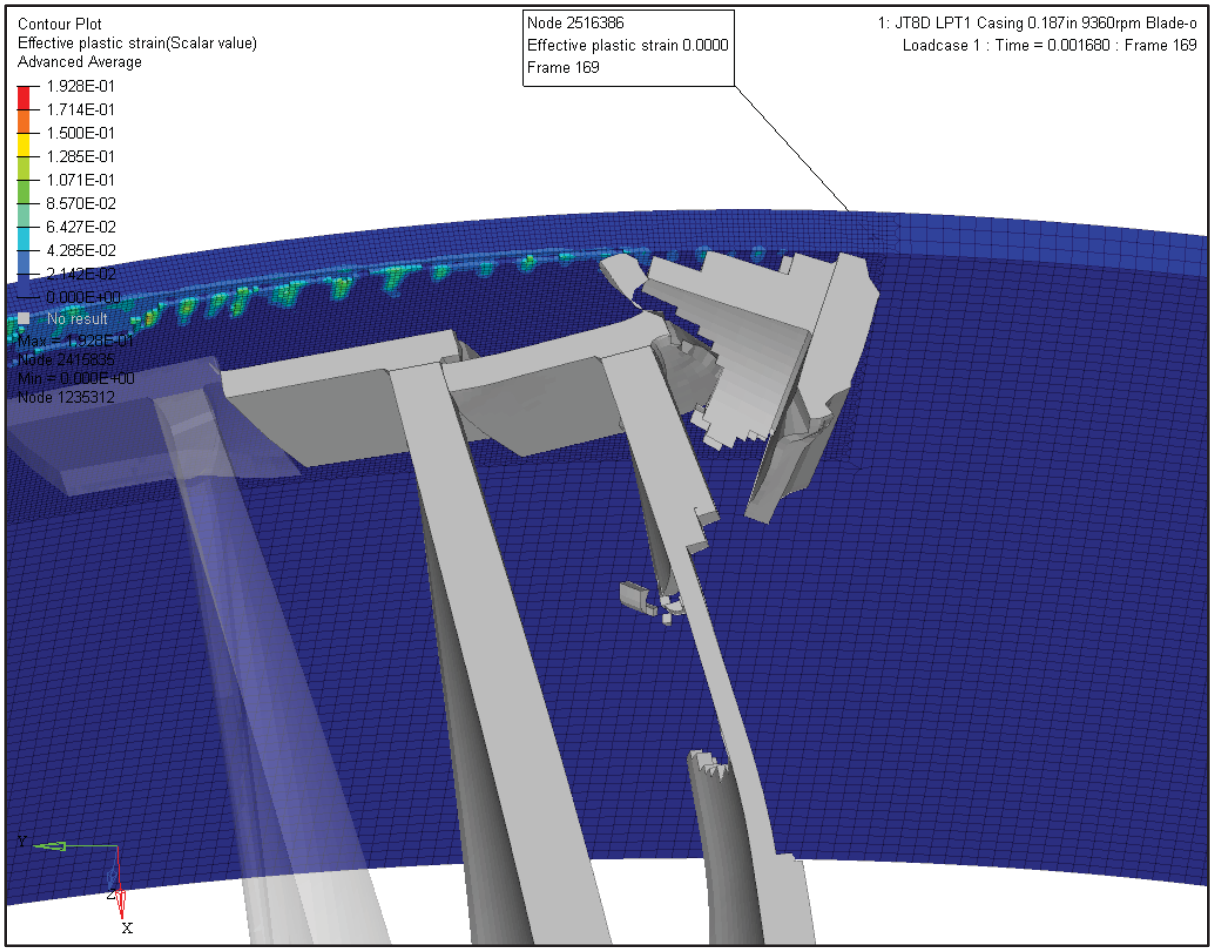

Figure 3.21 Start time of the second impact of the blade fragment with the casing

At the end of the first impact, the casing internal energy is 77.323 J, which represents 2.288% of the released blade KE (3379.67 J). During the second impact (at times between 0.00167 s and 0.00185 s), the casing absorbs through plastic deformation 137.58J, representing 4.071% of the released blade KE.

As observed in the plot of internal energies shown in Figure 3.27, after detaching from the airfoil, the released blade shroud is no longer active in the energy exchange. The airfoils of the first two blades and the casing are damaged, as shown in the eroded internal energy plot shown in Figure 3.28.

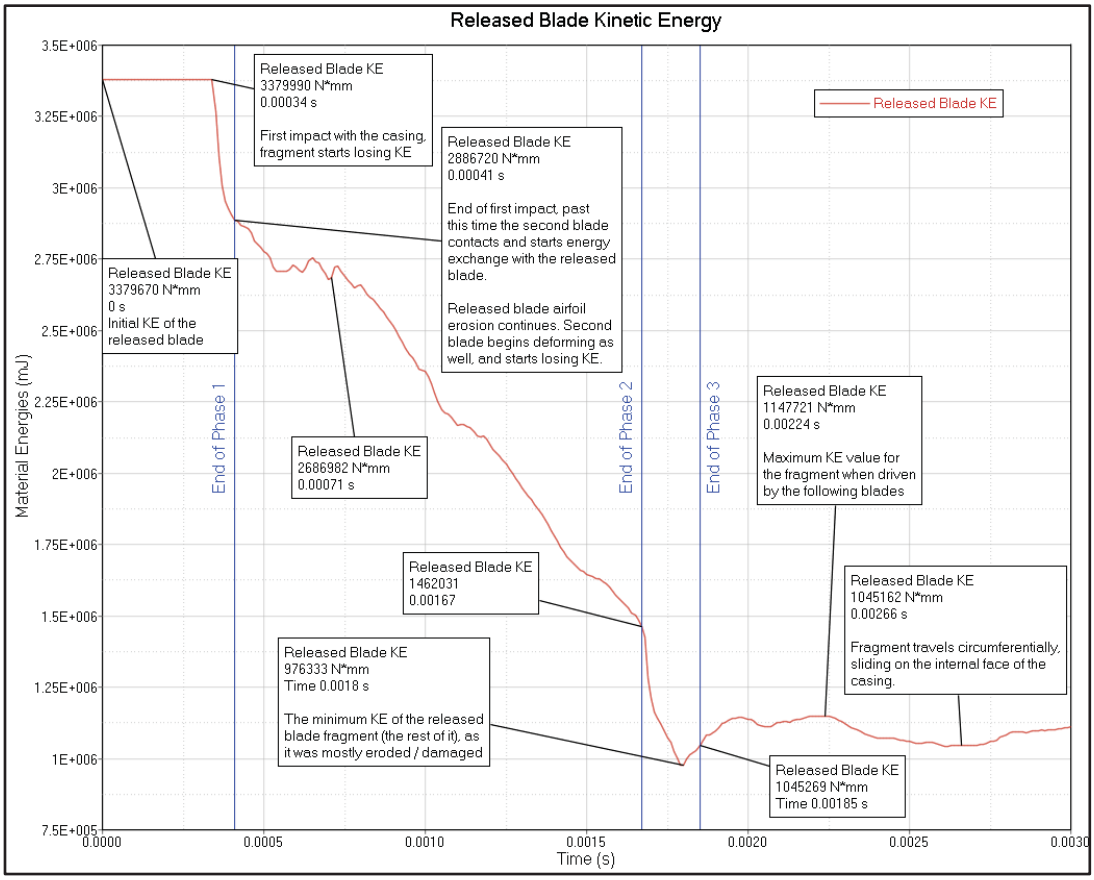

Figure 3.22 Released blade kinetic energy

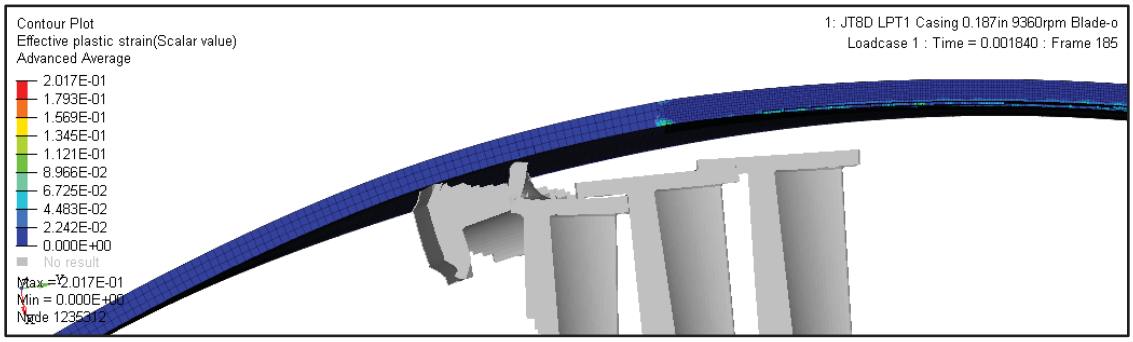

Figure 3.23 Released blade fragment pushed circumferentially along the inner face of the casing by the following blades at time t = 0.001840 s

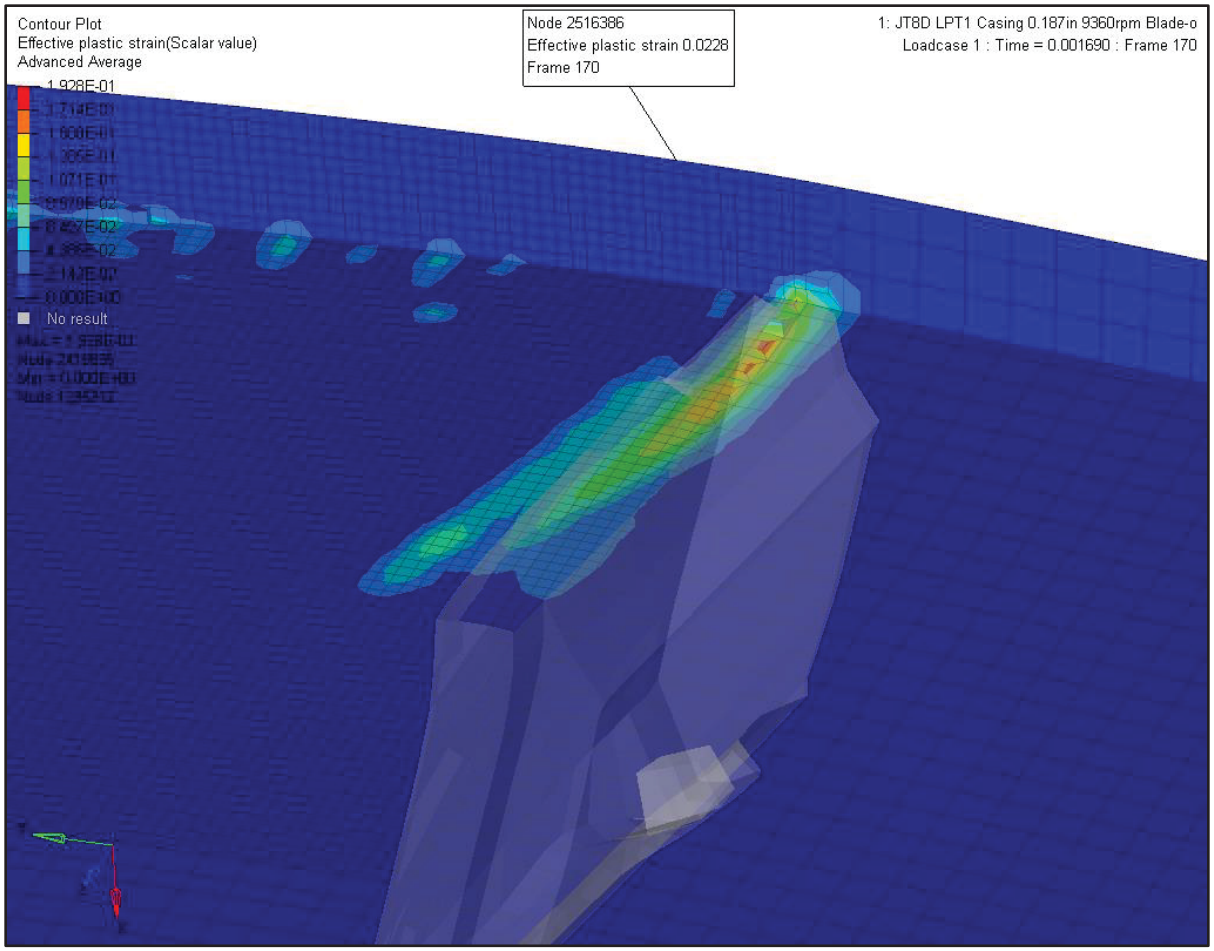

Figure 3.24 Second impact of the fragment with the casing (released blade transparent)

The increase in the casing internal energy after Phase 3 is due to the additional energy transferred by the remaining blades to the casing.

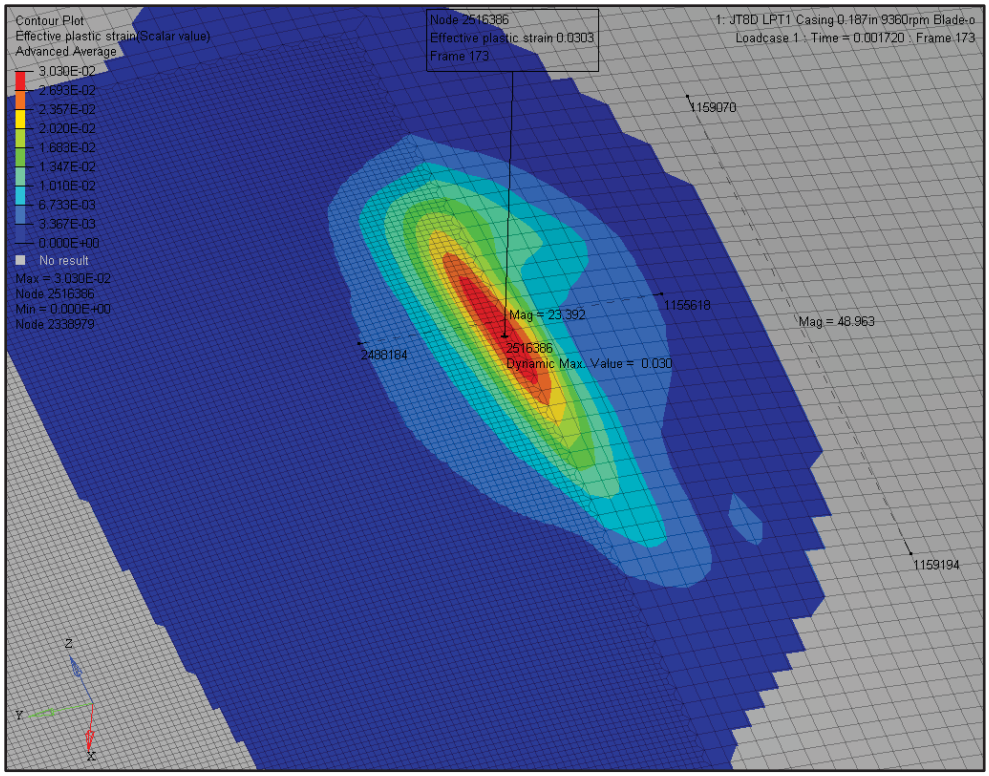

Figure 3.25 JT8D 9360rpm casing outer face impact area during the second impact

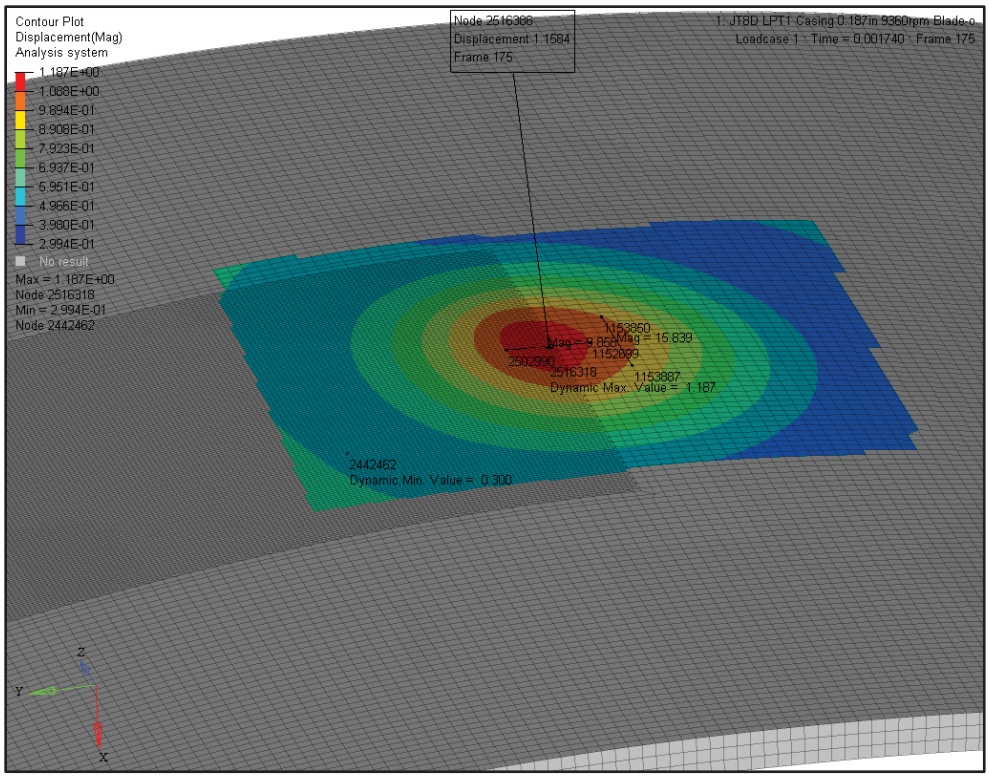

Figure 3.26 Second impact, casing outer face radial displacement in the impact area

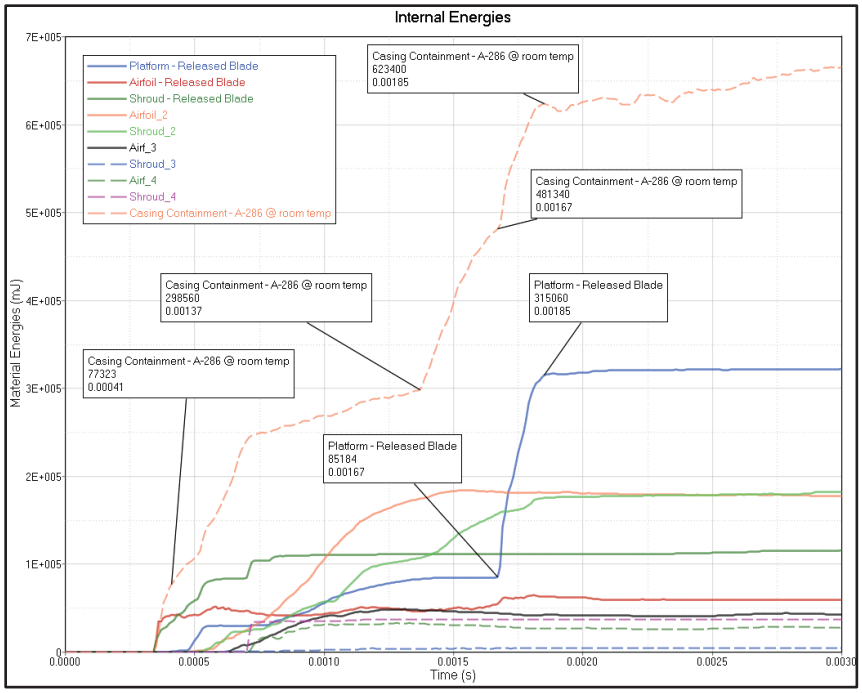

Figure 3.27 JT8D 9360rpm Internal Energies

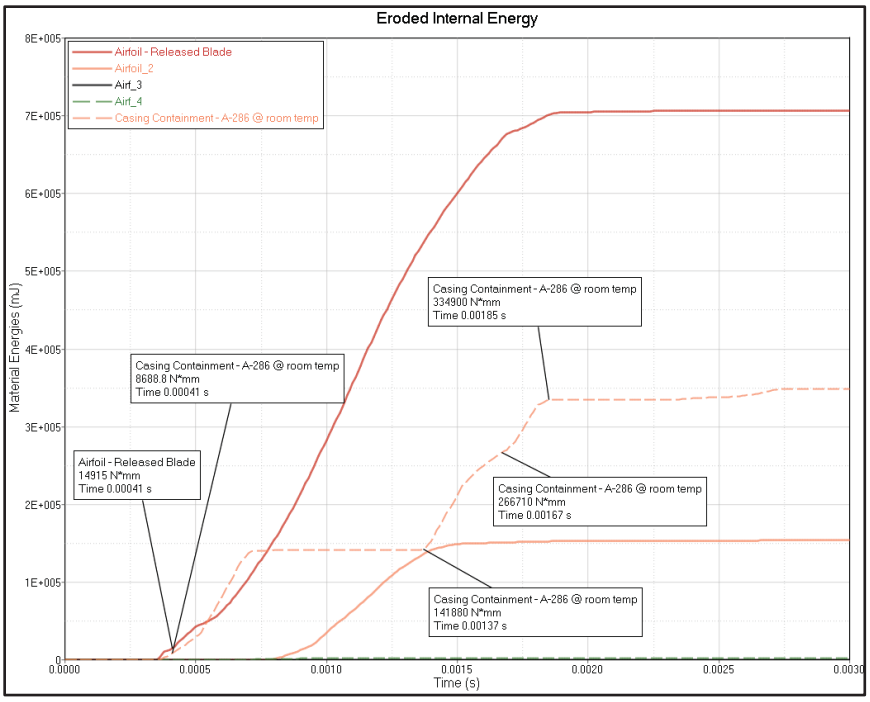

Figure 3.28 JT8D 9360rpm Eroded Internal Energies

3.4.2 JT8D un-contained test

For the non-contained test simulation of the JT8D LPT1 blade fragment, the rotor turns at 8,290 rpm, and the A-286 ring thickness was reduced to 0.140 in (3.556 mm). The reported KE is 23,486 lbf · in (2,653,562 N · mm).

As for the contained model, the blades were preloaded with the centrifugal loading during an implicit dynamic relaxation analysis, revealing a maximum stress of 105 MPa at the root of the airfoil (Figure 3.29), close to the fillet rad with the platform, similarly as for the contained case.

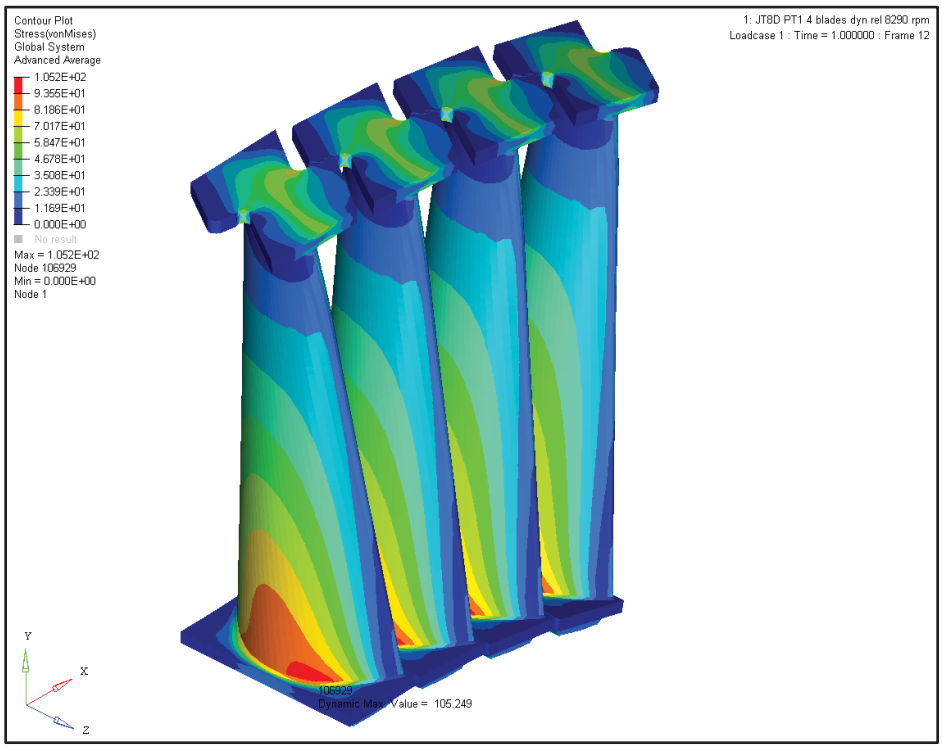

Figure 3.29 JT8D PT1 blades preload stress at 8290 rpm

The blades preload is shown in Figure 3.30. Similarly as for the contained case, the following blades are subjected to a highly oscillatory axial loading, as effect of the interaction with the released blade and its contact with the casing.

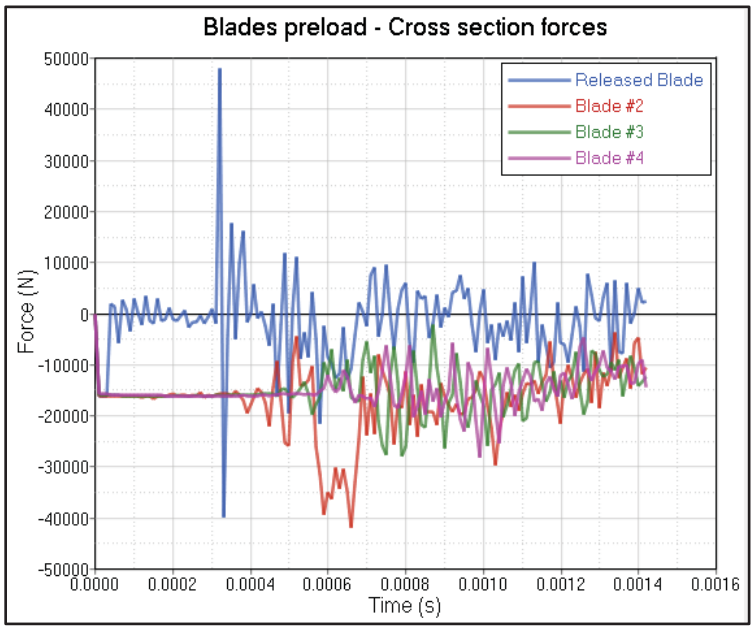

Figure 3.30 JT8D LPT1 Blade preload - cross section forces at 8290 rpm

With the adjusted density mentioned in the previous section, the FEA resulting KE for one single blade is 2,653,820 N · mm, which represents a -0.251% difference compared with the reported value (2,653,562 N · mm, or 23,486 lbf · in) at 8,290 rpm.

As for the JT8D contained test simulation described in the previous section, the first phase consists in the impact of the released blade with the casing. The outer face of the casing develops an effective plastic strain of 0.05 during the first impact with the released blade, as shown in Figure 3.31 and detailed in Figure 3.32. Following this first impact, the weakest section of the blade fractures underneath the shroud fillet, and as its kinetic energy drops, is impacted by the following blade. Phase 1 is considered complete when the outer face plastic strain reaches 0.05 (the maximum at the impact location) and stabilizes at that value.

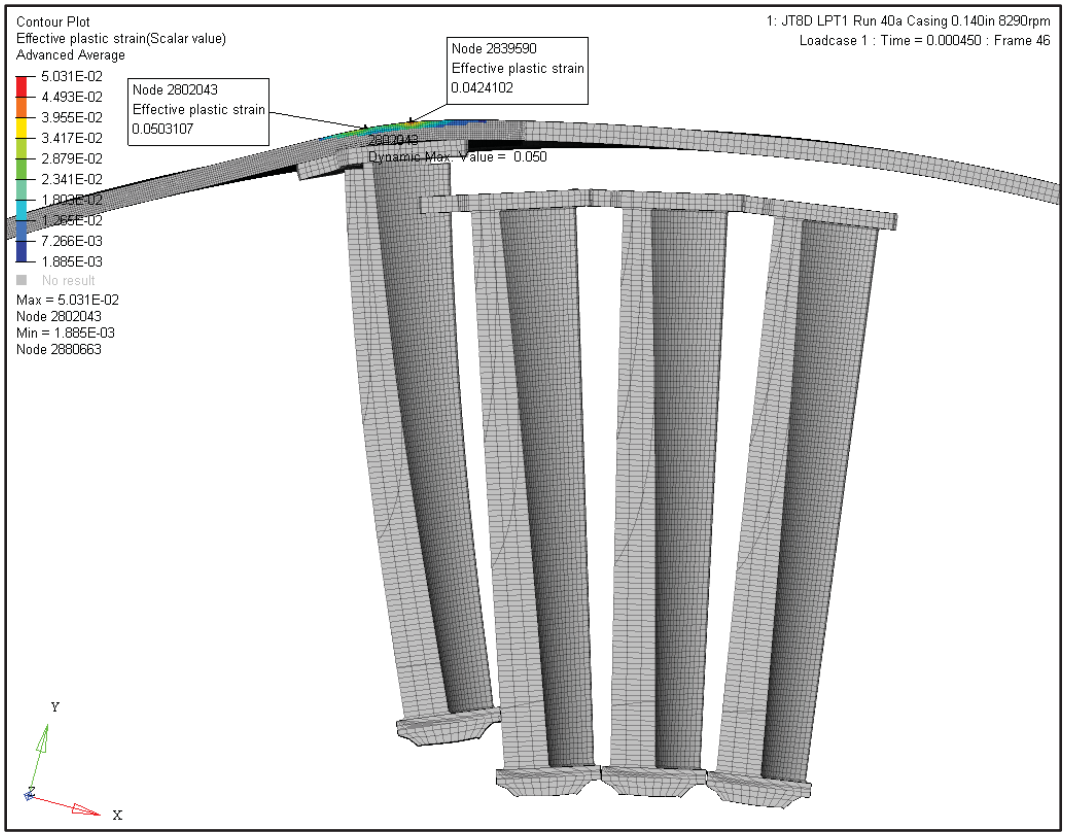

Figure 3.31 JT8D 8290rpm - First impact of the released blade with the casing, mid cross section

Subsequently, Phase 2 of the process consists in a relatively continuous contact of the fragment with the casing, during which damage (simulated by erosion) occurs on the casing, released blade fragment, but also on the blade #2, following the impact with the fragment. In a similar pattern as for the contained model, as the casing FE model contains patches with refined mesh, due to a faster erosion of the refined elements in contact with bigger and thus stiffer elements (as can be observed in Figure 3.32), the casing internal energy changes its slope – steeper for more important erosion of the fine mesh, and less steep for the coarse mesh (Figure 3.33). During this phase, the kinetic energy of the released blade fragment varies, however decreases overall (Figure 3.34). Phase 2 ends when the released blade fragment impacts the casing with its platform.

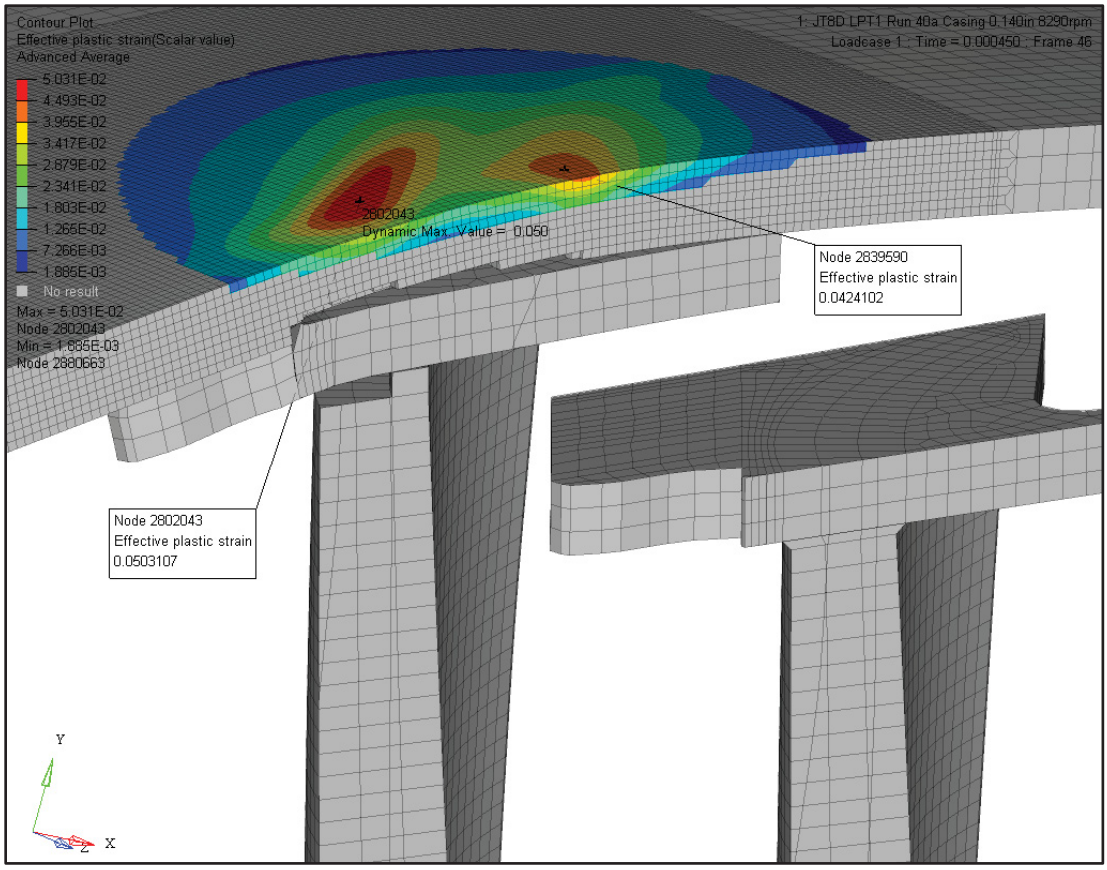

Figure 3.32 JT8D 8290rpm detail of the first impact, mid cross section

At the initiation of the second main impact (and thus start of the Phase 3), a narrow band of plastic strain propagates throughout the full thickness of the casing (Figure 3.35). This was not observed during the contained simulation of JT8D PT1, where the plastic zone is superficial at the inner and outer faces of the casing (Figure 3.24 and Figure 3.25). As similarity, the impact zone has the same shape as for the contained simulation, as the platform of the released blade is pushed into the casing at a very similar orientation (Figure 3.36 compared with Figure 3.24).

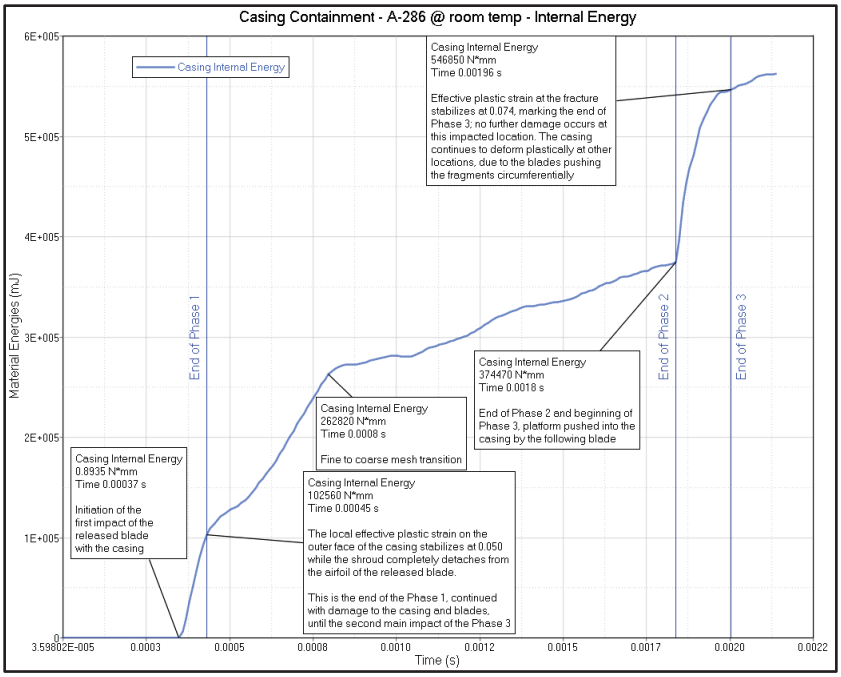

Figure 3.33 JT8D 8290rpm Casing energy absorption during the impacts with the released fragment

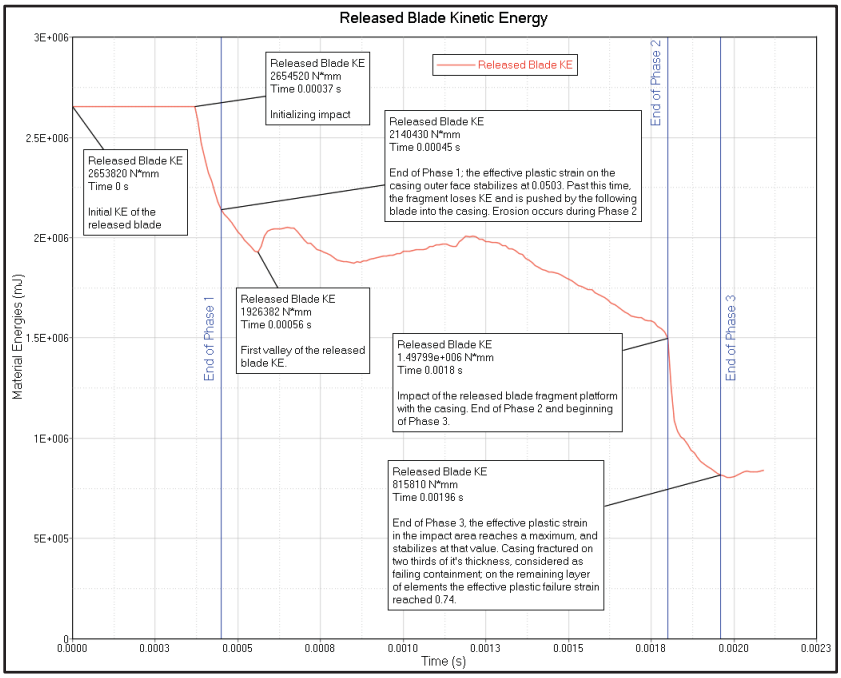

Figure 3.34 JT8D 8290rpm - Released blade KE

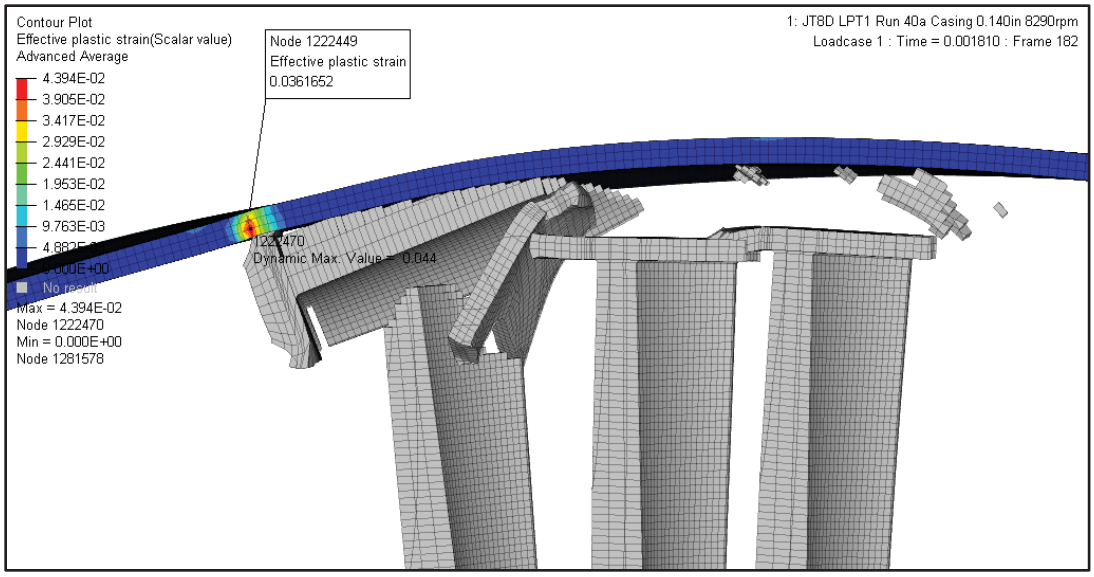

Figure 3.35 JT8D 8290rpm initiation of the second impact of the released blade fragment with the casing

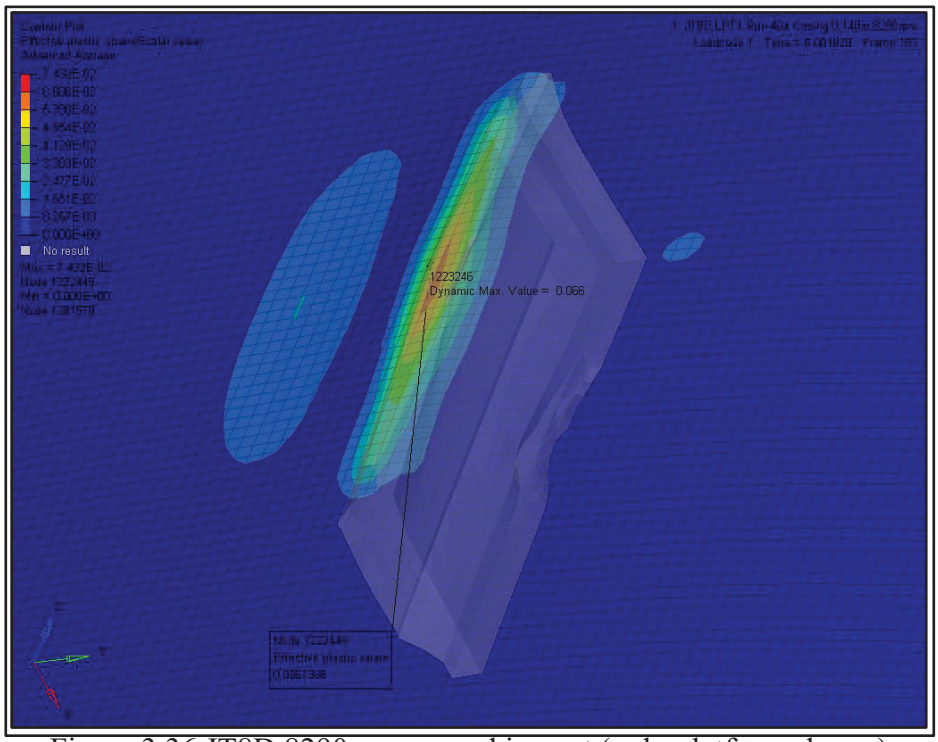

Figure 3.36 JT8D 8290rpm second impact (only platform shown)

As mentioned previously, several FEM configurations were analysed, all revealing overall similar results, but no full penetration. Even without full penetration, fractures occurring over two thirds of the thickness are considered as being significant ruptures for the purpose of this research. In the JT8D simulation at 8290rpm, the casing impact zone was fractured over two thirds of its thickness, as shown in Figure 3.37 below.

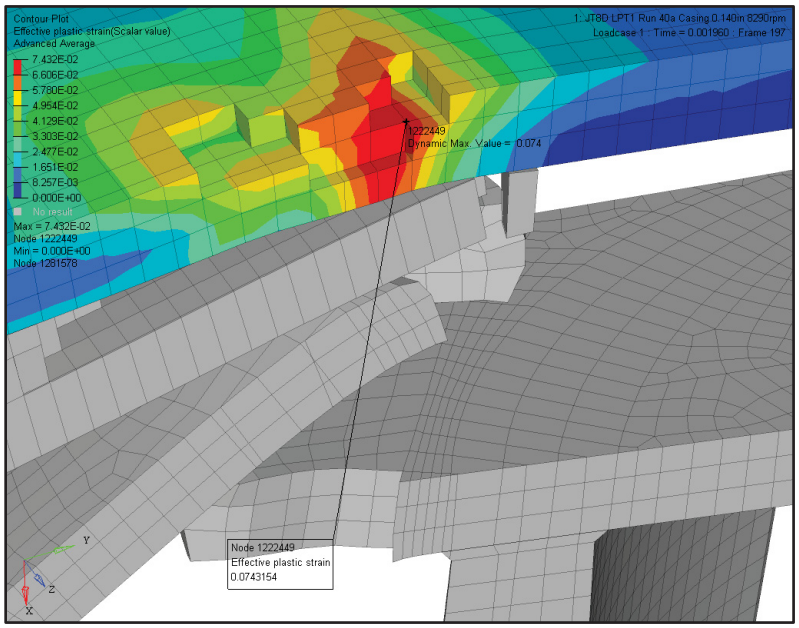

Figure 3.37 JT8D 8290rpm casing fracture at the end of Phase 3

Internal energies for the components participating to the energy exchange are shown in Figure 3.38 and the eroded internal energies in Figure 3.39. The sequence of events starts with the initial impact, where the shroud, airfoil of the released blade exchange energy, and the airfoil and the casing lose elements through erosion. After the release blade losing part of its KE, it is impacted by the following blade, thus receiving KE to reach the second peak in Figure 3.34. At this time, the energy transfer is done via two load paths, the shroud of the blade #2 pushing the top of the airfoil of the released blade into the casing (Figure 3.40), and the lower part of the airfoil of the following blade (blade #2) pushing the platform of the released blade (Figure 3.41). As there is a gap between the shrouds (deficiency of the public domain geometry), the remaining blade airfoils and shrouds are starting to see the loading after the closing of the gap (and thus after developing internal energies), but this has no effect overall.

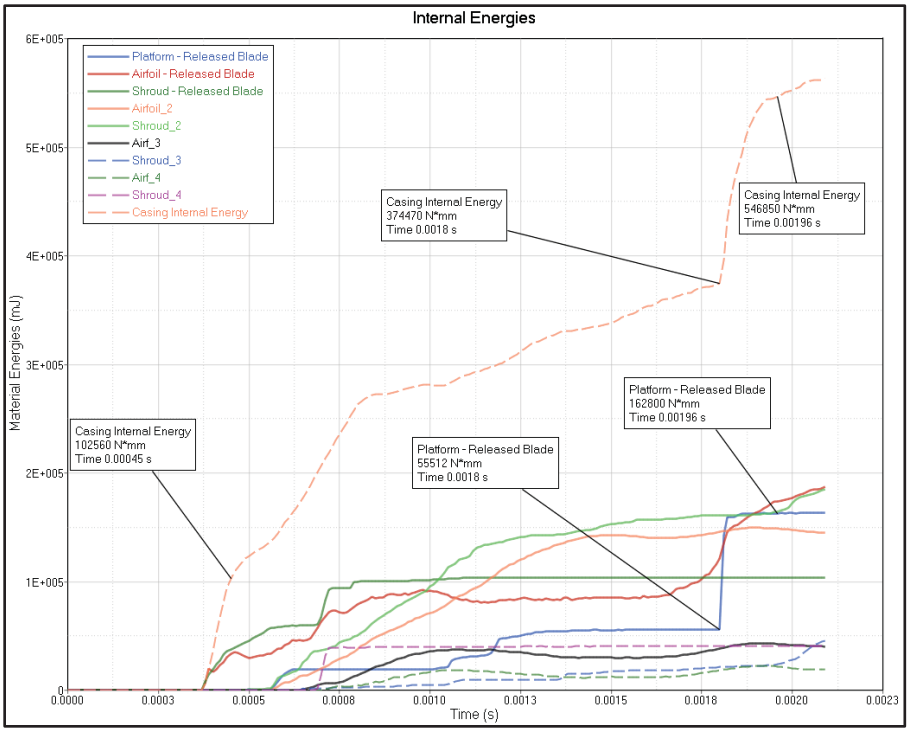

Figure 3.38 JT8D 8290rpm Internal Energies

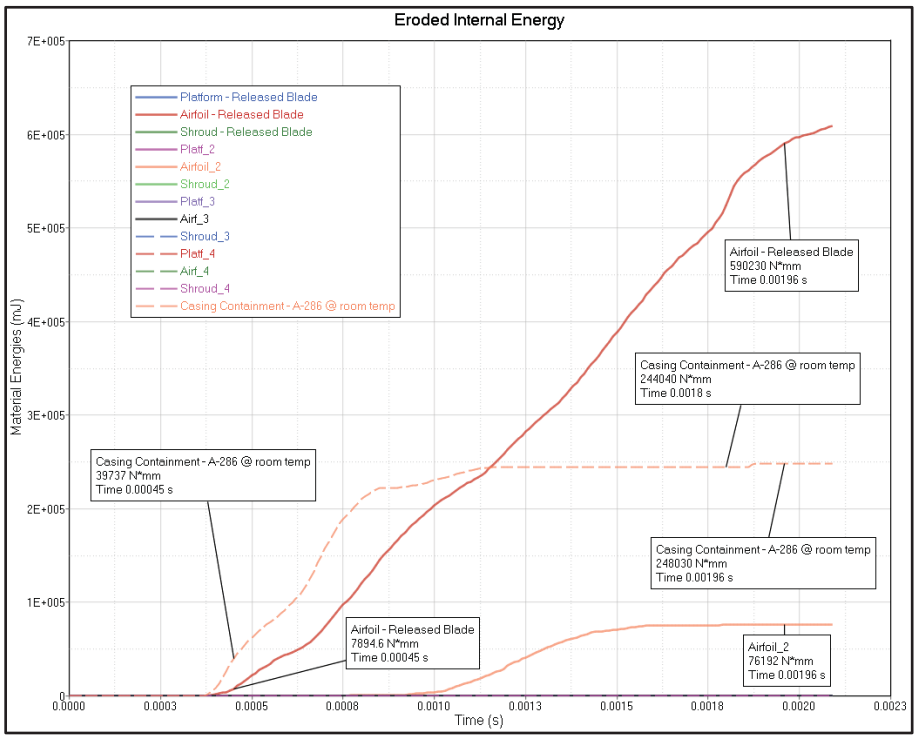

Figure 3.39 JT8D 8290rpm Eroded Internal Energies

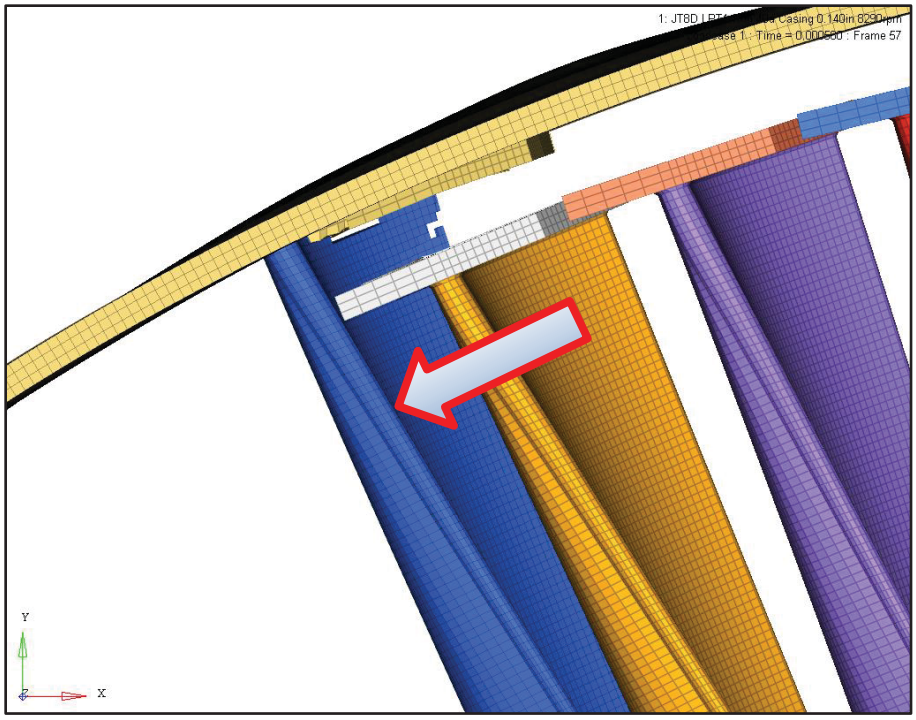

Figure 3.40 JT8D 8290rpm upper load path during Phase 2

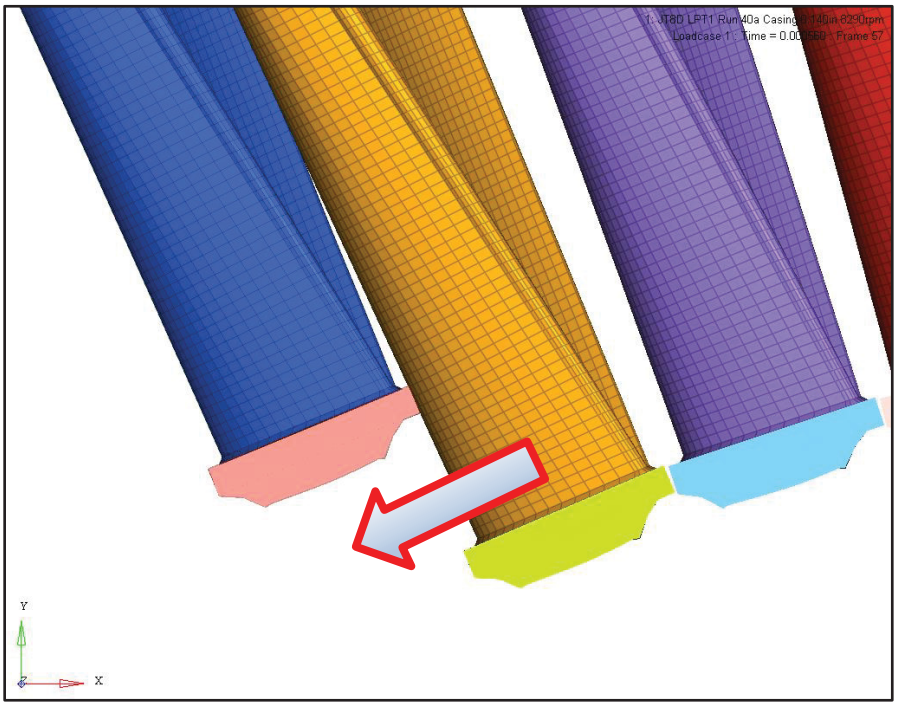

Figure 3.41 JT8D 8290rpm lower load path during Phase 2

As observed in Figure 3.38, at the first impact, the casing absorbs through internal energy 102.560 J, which represent 3.865% of the initial KE of the released blade. During the Phase 3 of the impact (between times 0.00180 s and 0.00196 s), it develops an internal energy of 172.380 J, which is 6.496% of the initial KE of the released blade. If comparing with the contained analysis, the uncontained failure occurs at a casing internal energy 25.294% bigger than in the contained case, and at a thickness 25.134% smaller.

3.4.3 JT3D contained test

For the JT3D LPT2 contained test simulation, the blade fragment was released at 6145rpm, at an equivalent KE reported of 36,275 lbf · in and impacted a containment ring of 0.187 in made of A-286 steel.

As for the previous models (JT8D), the blades density was slightly adjusted to generate the reported KE; the resulting KE is (4,083,570 N · mm, or 36,142.64 lbf · in, which represents a -0.366% deviation from the reported value of 4,098,525 N · mm). Also, the blades were preload with centrifugal forces during an implicit dynamic relaxation analysis. The dynamic relaxation analysis revealed a maximum equivalent stress of 233.48 MPa towards the root of the blade, close to the fillet rad on the pressure side (Figure 3.42). As for the JT8D analyses, a highly oscillatory response resulted due to the blade interactions (Figure 3.43, only the first 4 blades shown), with the released blade losing its preload following the shroud separation.

As for the JT8D LPT1 blade release, the first impact of the JT3D LPT2 blade fragment with the casing is more detrimental to the blade than to the casing, which records a maximum effective plastic strain of 0.026 on the outer face of the casing (cross section shown in Figure 3.44), while the blade fractures completely towards the tip (at time 0.00047s), under the shroud fillet. Casing erosion occurs due to the difference in elements size, however analyses with similar meshes on both casing and blade shroud revealed very similar effective plastic strain values and plastic deformation pattern on the outer face of the casing.

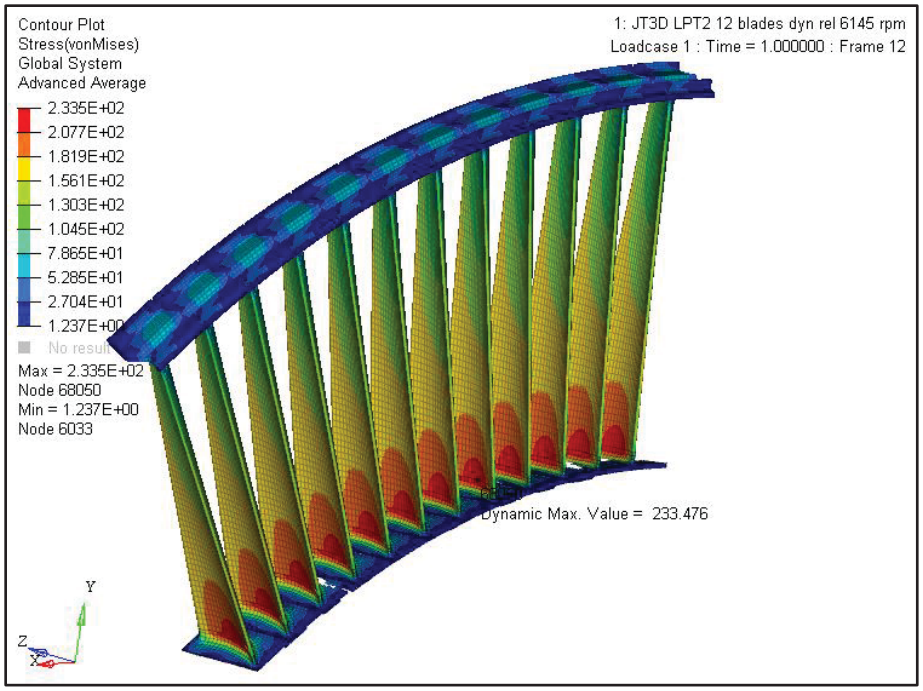

Figure 3.42 JT3D PT2 6145 rpm blades preload

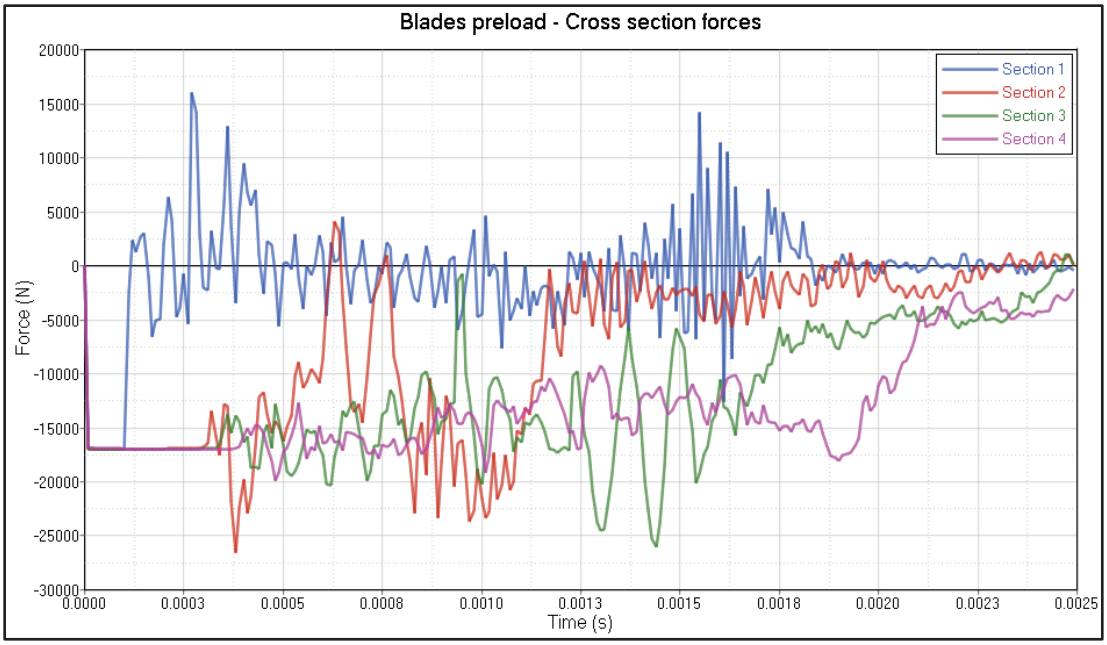

Figure 3.43 JT3D LPT2 Blades preload – cross section forces at 6145 rpm

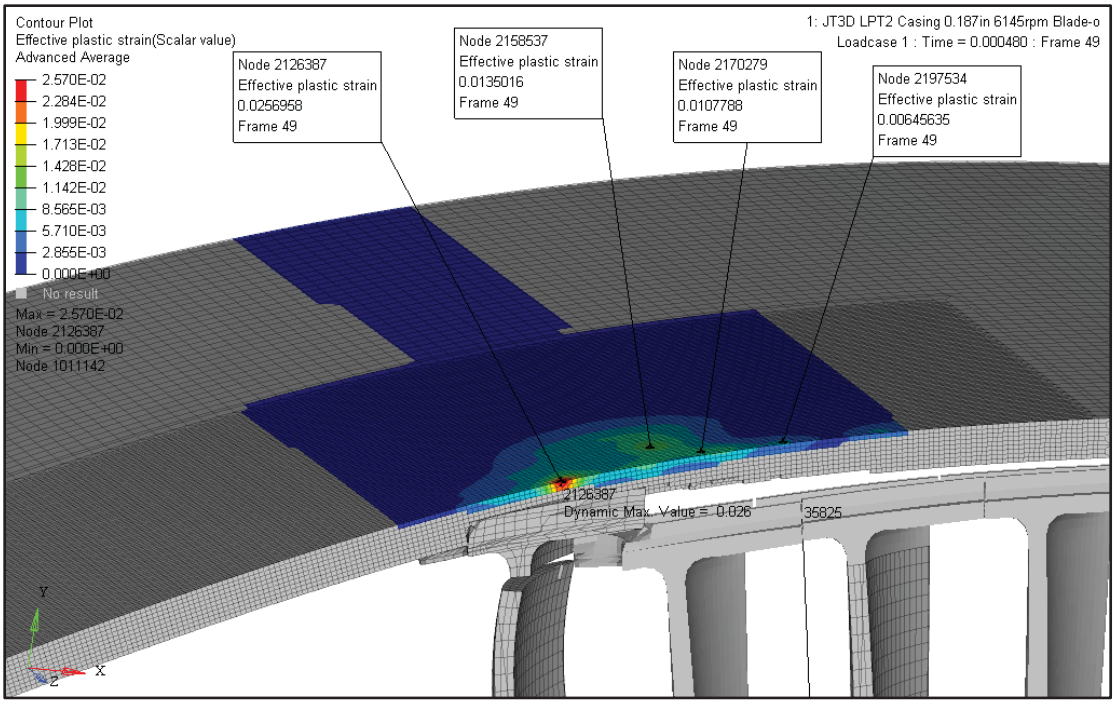

Figure 3.44 JT3D 6145 rpm first impact of the blade with the casing (maximum strain on the outer face reached at time 0.00042 s)

The shroud complete separation from the blade, with the maximum effective plastic strain value stabilized at 0.0256, marks the end of Phase 1 of the containment process (Figure 3.45). The released blade reaches a minimum KE after the shroud separation, followed by a temporary increase when pushed circumferentially by the following blades (Figure 3.46). The minimum value of the KE is reached at the beginning of the Phase 3, when the platform is pushed into the casing.

Phase 2 is represented by further damage of the released blade airfoil, which is impacted by the following blade (Blade #2) and pushed into the casing. As the JT3D PT2 blades are taller, slenderer than JT8D PT1, the released blade platform causes more damage on the following blades compared with the JT8D: the released blade platform damages two of the following blades, subsequently impacting the pack of debris. Phase 2 of the impact ends when the platform of the release blade pushes the pack of accumulated debris into the casing, at time 0.00186s; this represents the beginning of the Phase 3 of the containment process.

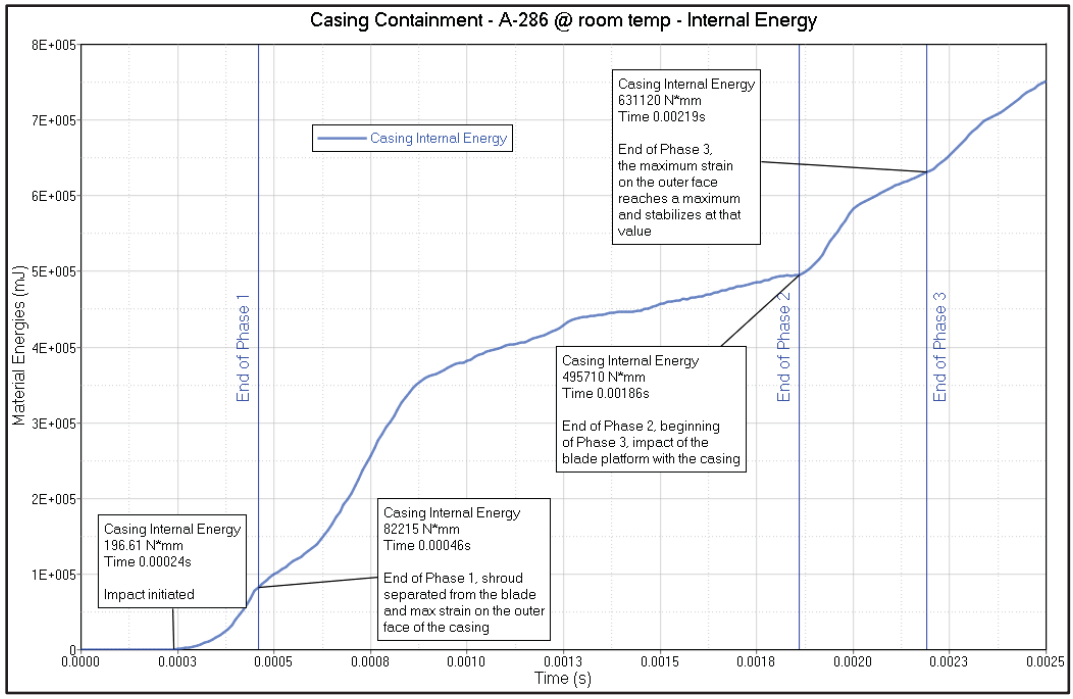

Figure 3.45 JT3D 6145rpm Casing internal energy

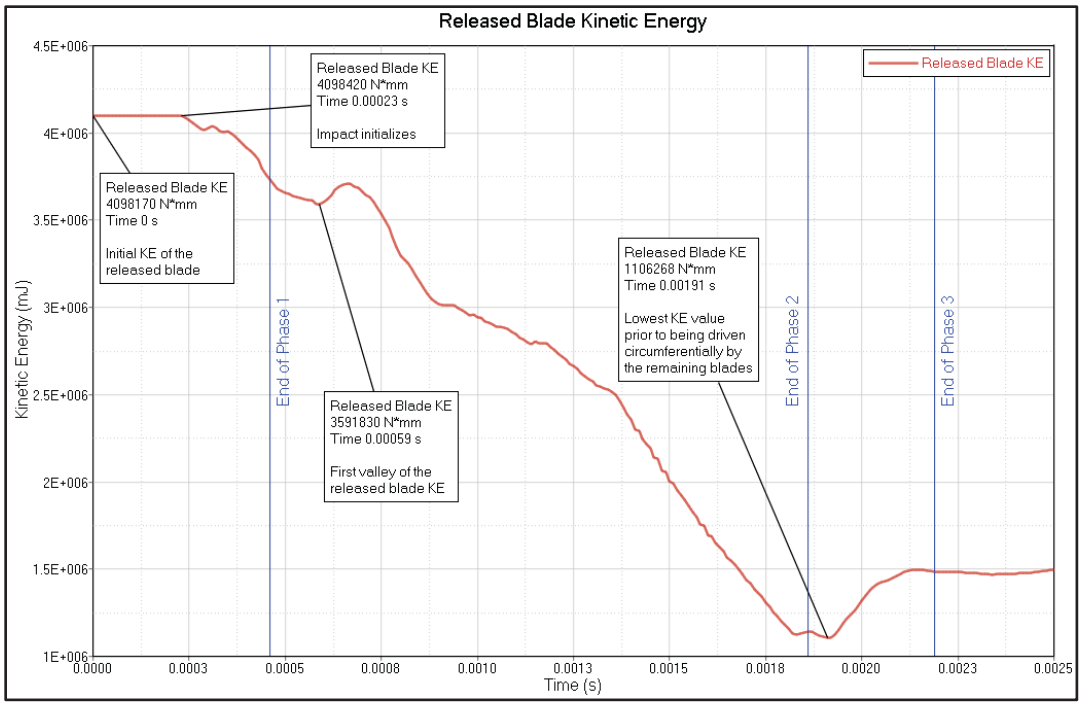

Figure 3.46 JT3D 6145rpm Released Blade KE

Phase 3 completes when the outer face of the casing develops a maximum plastic strain and stabilizes at that value (Figure 3.47).

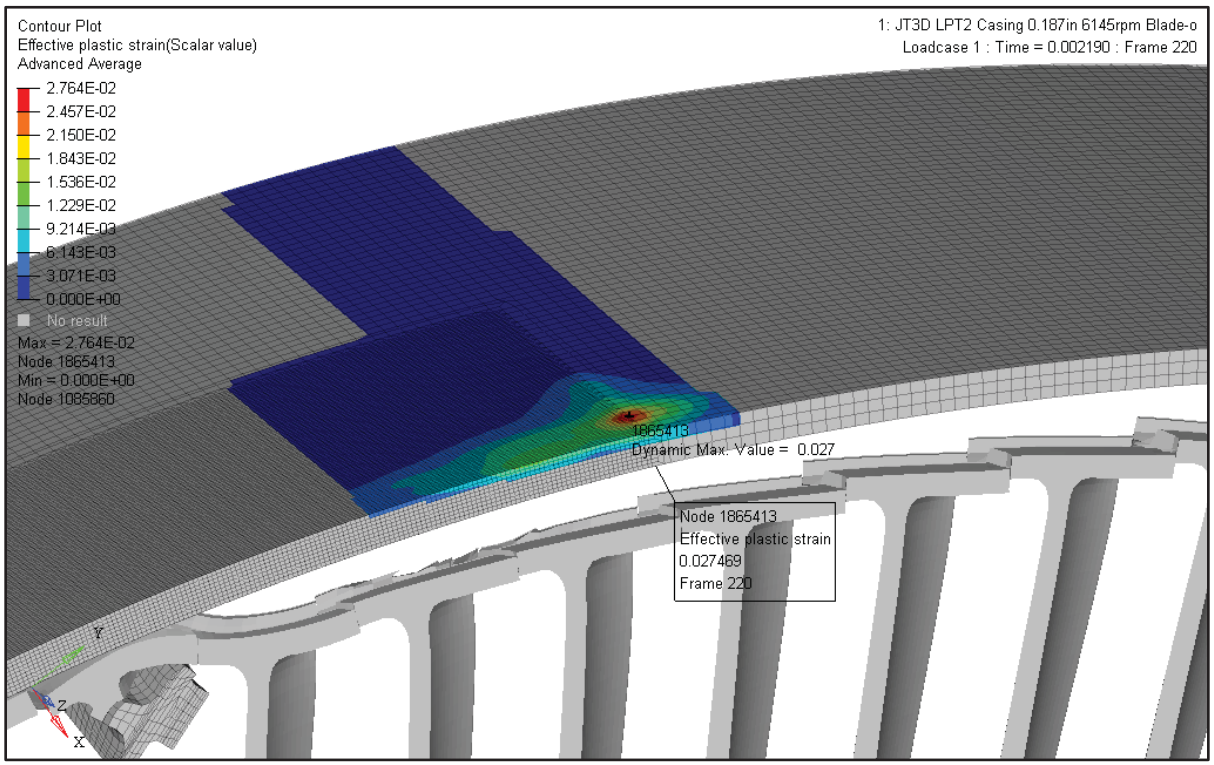

Figure 3.47 JT3D 6145rpm Plastic strain on the casing outer face at the end of Phase 3

The sequence of events is very similar with the sequences presented for the JT8D tests. The released blade impacts the casing, buckles and fractures, and a maximum plastic strain on the outer face of the casing stabilizes at a value between 0.01 and 0.03 (different mesh models were analysed for JT3D, as for JT8D). Following this time, the released blade fragment continues to be damaged by the following blade, which pushes it into the casing. The released blade fragment KE reaches a first valley after the shroud completely detaches from the fragment (Figure 3.46), then the subsequent second peak due to the addition of energy by the following blades, until the remaining blade fragment airfoil reaches again the casing; following that moment the released blade fragment consumes at an almost constant rate its kinetic energy.

Due to the damage inflicted by the blade fragment on the following blades (second blade completely fractures at approximatively one third of its airfoil height at time 0.001170 s as seen in Figure 3.48 and the third blade completely fractures close to its tip, under the shroud at time 0.001810 s, as show in Figure 3.49), the platform of the released blade does not impact the casing, but the detached fragments of the following two blades (Blade #2 and Blade #3). A new maximum value for the plastic strain on the outer face of the casing is 0.027 and stabilizes beginning with time 0.002190s (Figure 3.47). This strain is generated by the detached shroud of the released blade while being pushed into the blade fragments (in contact with the casing) by the following blades (Blade #4). As all the detached blade fragments (from the released blade, blade #2 and #3) are driven circumferentially by the following blades, this second impact value remains the maximum strain occurring on the outer face of the casing until the end of the analysis. In the contained analysis of the JT3D PT2, the released blade fragment does not have enough energy to reach and be embedded into the casing by the following blades shrouds. Excepting the released blade, the shrouds maintained their contact throughout the full time of all analyses.

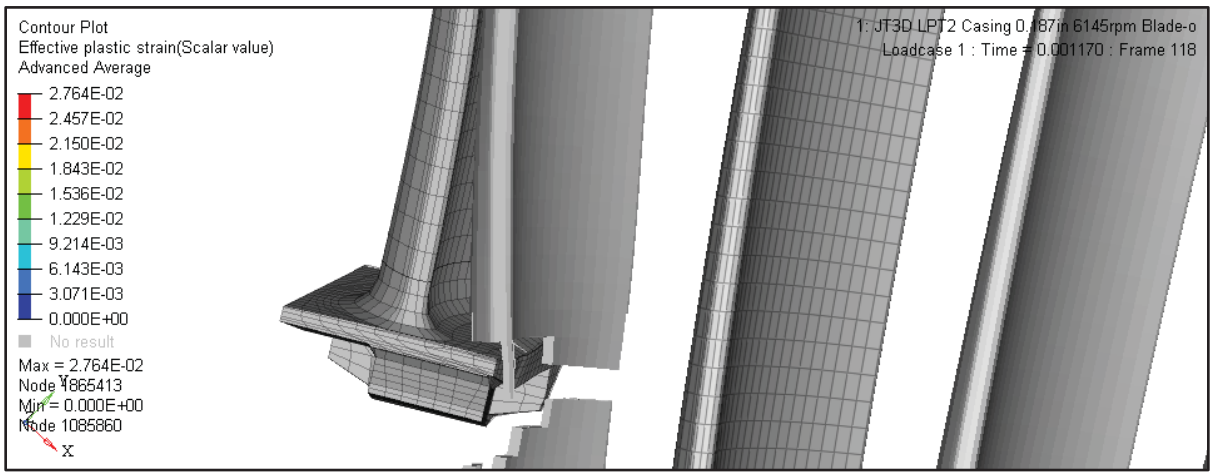

Figure 3.48 JT3D LPT2 at 6145 rpm following blade (Blade #2) fracture

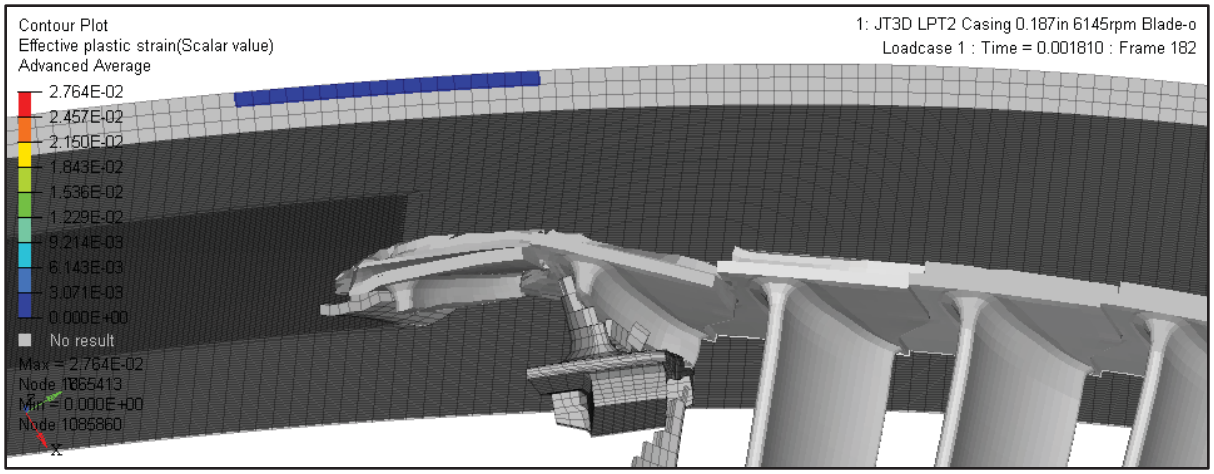

Figure 3.49 JT3D LPT2 at 6145 rpm, third blade (Blade #3) failure
(airfoil 2 removed to provide unobstructed view to airfoil 3)

The energy plot in Figure 3.50 reveals a slight difference from the JT8D impact shown in Figure 3.38. Whereas in the JT8D case, due to the "tip clearance" the following blades pass the detached shroud, which does not contribute much to the energy exchange after its separation. The JT3D model does not have such a tip clearance, hence the released blade shroud remains in the front of the moving blades, constituting a pack of debris with the fragments of airfoils and eventually (after blades #2 and #3 fragmentation) with shrouds #2 and #3. The main contributors to the energy exchange are the released blade shroud, shroud #2 and shroud #3, released blade platform, airfoil and airfoil #2, in addition to the casing. The remaining components have energies close to 0 and are not shown in the graph.

Also, in addition to the casing, the most erosion occurs on the released blade airfoil, airfoil #2 and #3 (Figure 3.51). All other components are not eroded, hence not shown.

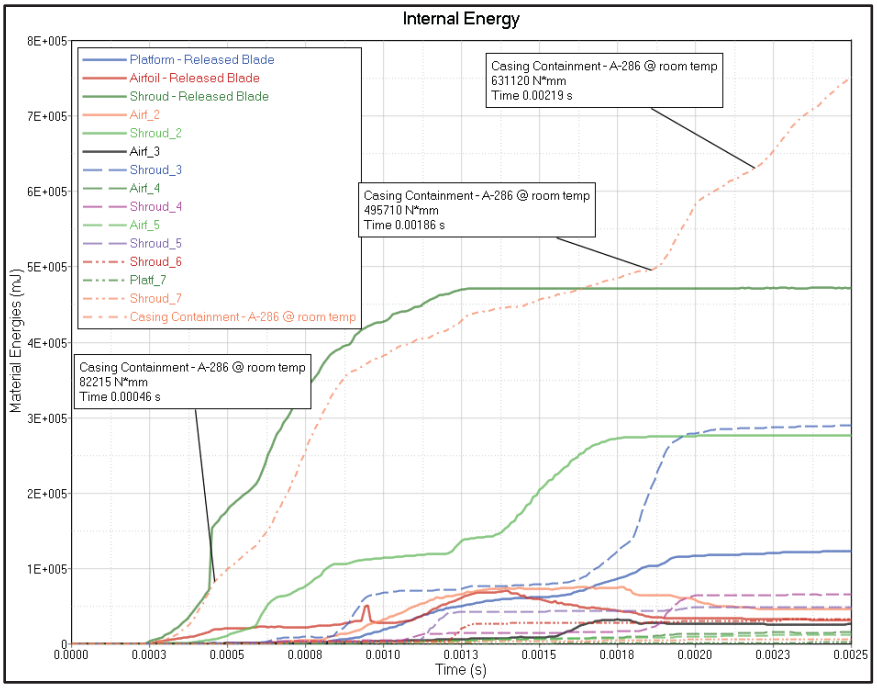

Figure 3.50 JT3D 6145rpm Internal Energies

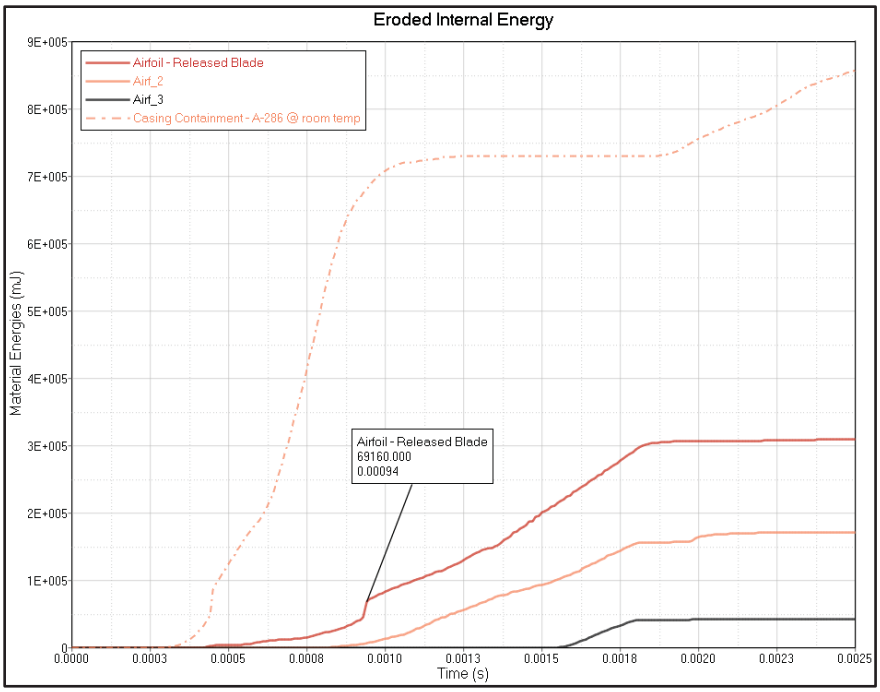

Figure 3.51 JT3D 6145rpm Eroded Internal Energies

As for the JT8D PT1 tests, at the first impact the casing absorbs a relatively low percentage of the fragment initial KE (82.215 J, representing 2% of 4098.17 J, smaller than the JT8D 3.87%). This is due primarily to the material properties (JT3D blades in Stellite 31, whereas JT8D are in IN713C), and to the blade geometry. The second impact (between time 0.00186 s and 0.00219 s) develops 135.41 J, representing 3.304% of the total KE of the released fragment. No penetration occurred in this test simulation.

3.4.4 JT3D un-contained test

The JT3D PT2 uncontained test simulation consists in the blade fragment being released at 6736 rpm, at an equivalent KE reported of 43,588 lbf · in (4924.783 J) and impacted a containment ring of 0.187 in made of A-286 steel.

As for the previous models, an implicit dynamic relaxation analysis was performed to generate the centrifugal stresses on the blades. A maximum equivalent stress of 280.80 MPa is observed in the lower airfoil, close to the fillet rad on the pressure side (Figure 3.52). Similarly as for the other simulations for the JT8D and JT3D PT containment tests, the released blade preload is lost after the initial impact with the casing, followed by a highly oscillatory preload in the remaining blades. Also, the previous blades density adjustment (JT3D contained test) was maintained for this simulation, yielding to a resulting KE of (or 43,586.03 lbf · in, which represents a -0.005% deviation from the reported value of 4,924,783 N · mm)

As observed in all previous simulations, the first impact of the JT3D PT2 blade fragment with the casing is more detrimental to the blade than to the casing, with a maximum effective plastic strain of 0.006 (reached at time 0.00032 s) on the outer face of the casing (cross section shown in Figure 3.53), while the blade fractures completely towards the tip (at time 0.00034 s), under the shroud fillet. End of Phase 1 is considered when there is no further energetic exchange at the impact area (thus the plastic strain remaining constant on the outer face of the casing), and the shroud separates from the released blade (usually these occur at the same time, or immediately following one another).

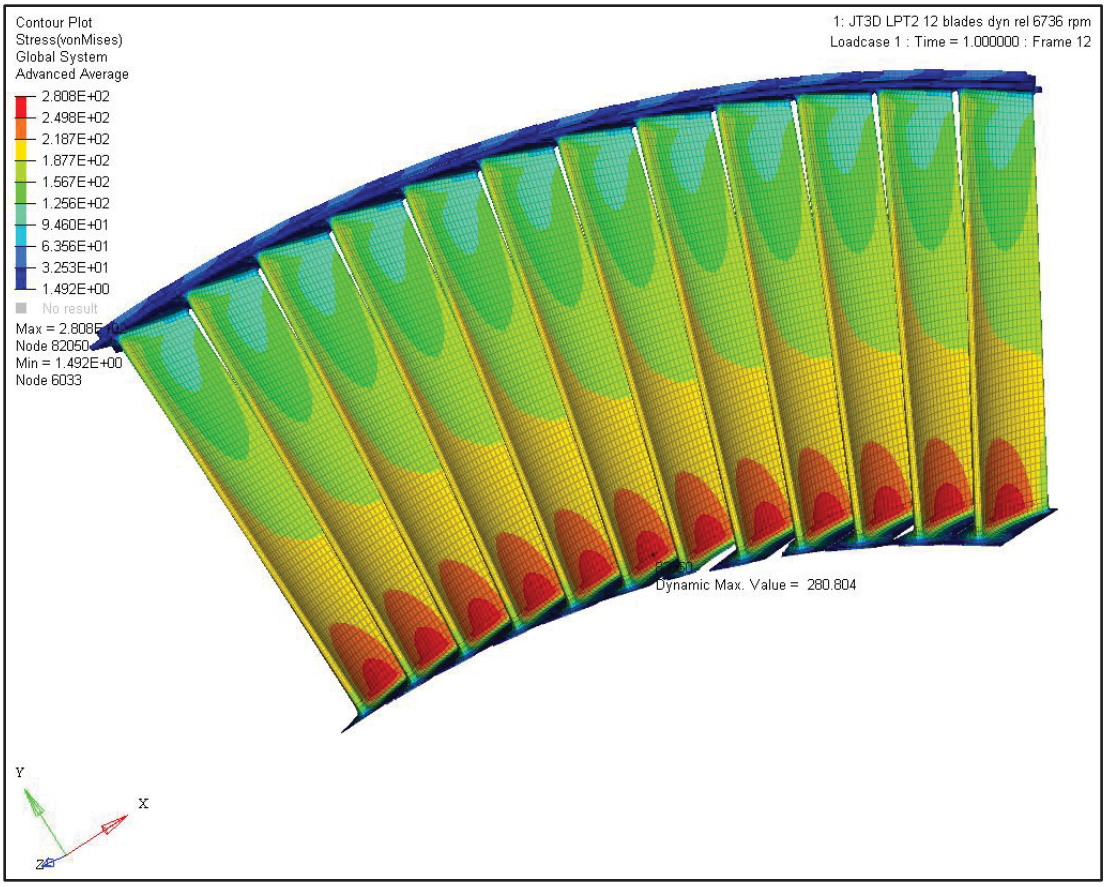

Figure 3.52 JT3D 6736rpm centrifugal stress preload

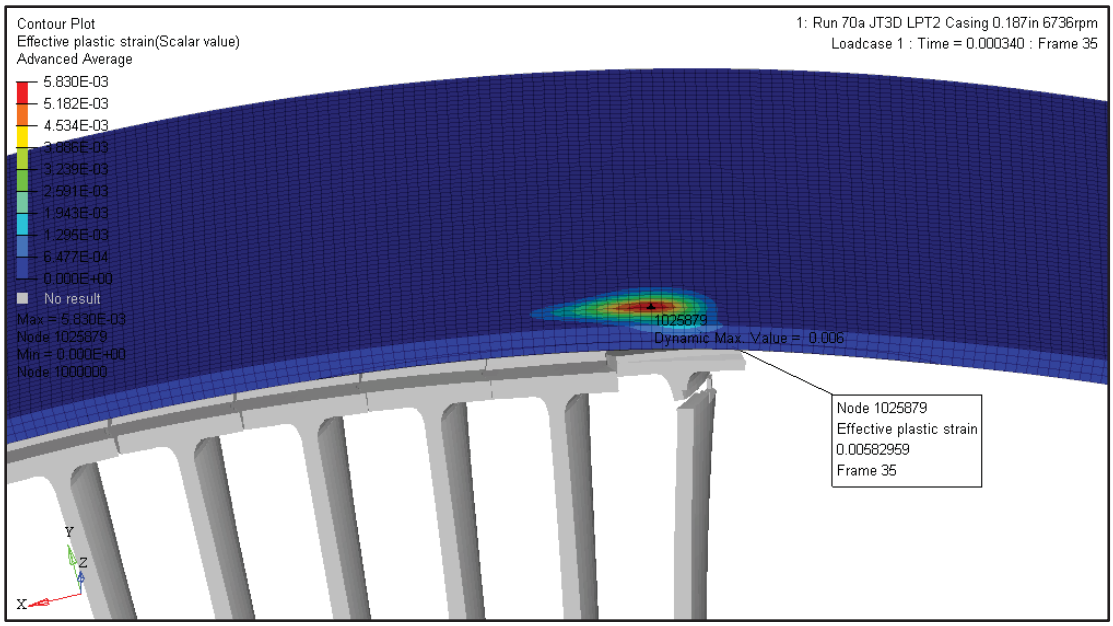

Figure 3.53 JT3D 6736rpm first impact

The first impact completion marks the initiation of Phase 2, which consists in a quasi-constant energy absorption by the case of the kinetic energy of the moving parts. The transition to the refined mesh is marked by the beginning of the steeper slope, due to elements erosion (Figure 3.54).

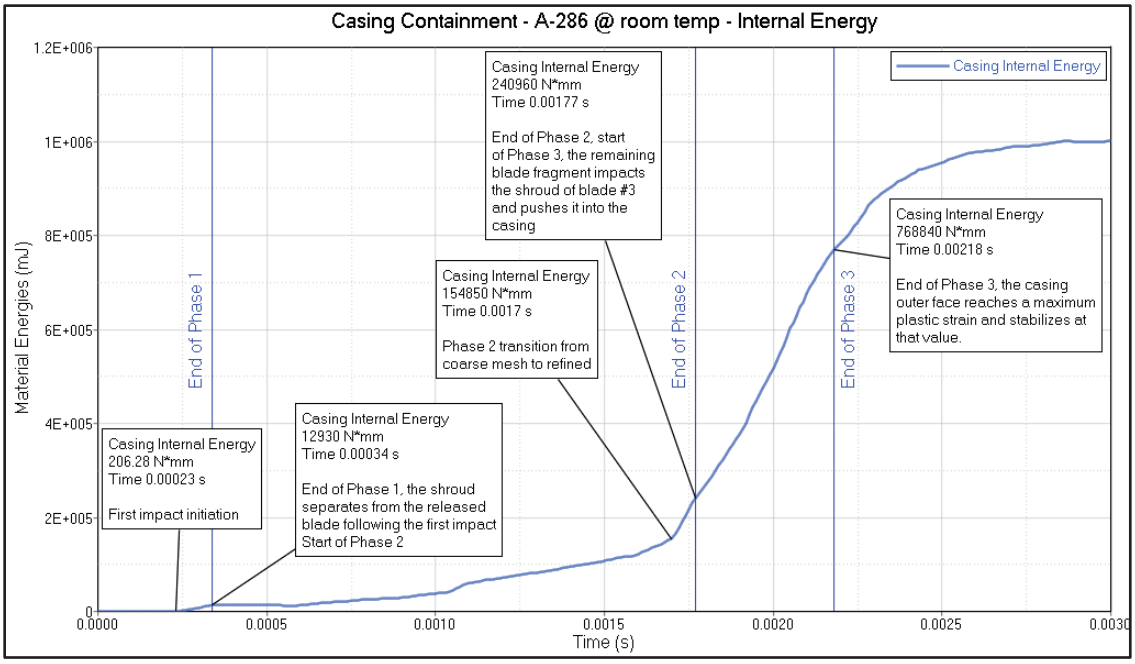

Figure 3.54 JT3D 6736rpm Casing internal energy

During this Phase 2, the released blade fragment maintains its contact with the casing and loses its kinetic energy (Figure 3.55), while also damaging the following blades. Airfoil #2 fractured at time 0.00088 s (Figure 3.56), and airfoil #3 at 0.00127 s (Figure 3.57). Most energy is exchanged by the shrouds, as they remain in contact with the ones from the following blades (Figure 3.58). Airfoil damage is completed during this phase (Figure 3.59). Phase 2 ends when the released blade fragment impacts the shroud #3 and the casing, initiating the second impact (at time 0.00177 s).

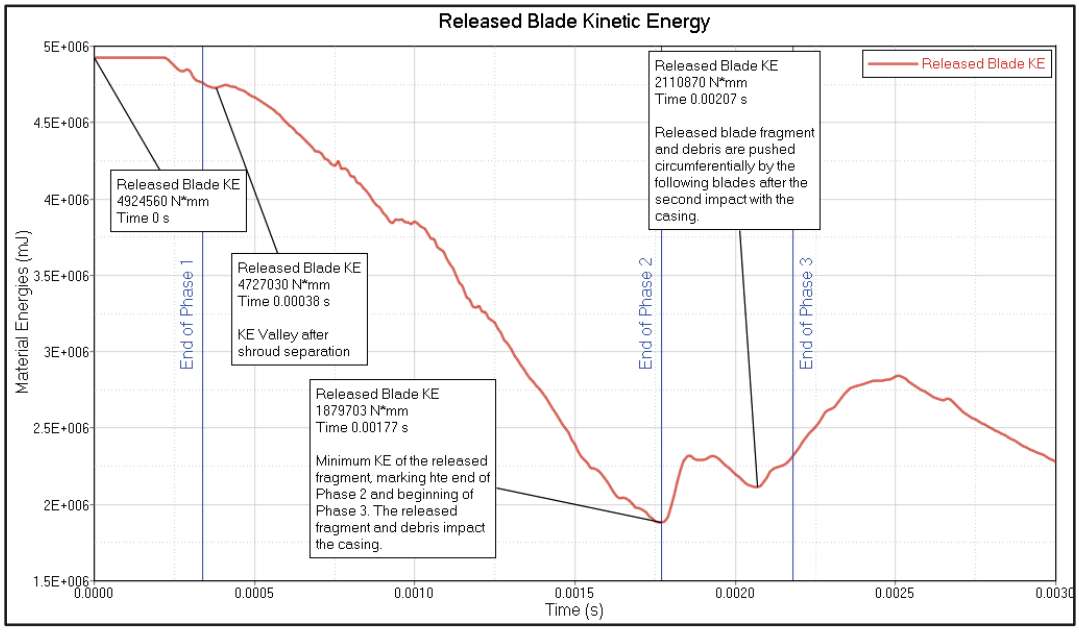

Figure 3.55 JT3D 6736rpm Released blade kinetic energy

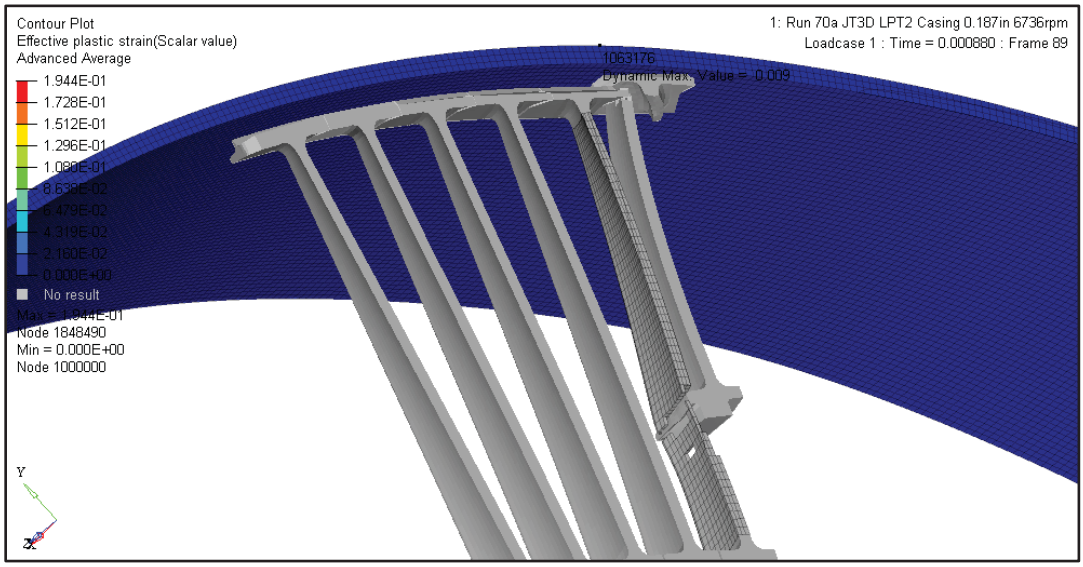

Figure 3.56 JT3D 6736rpm Airfoil #2 fracture

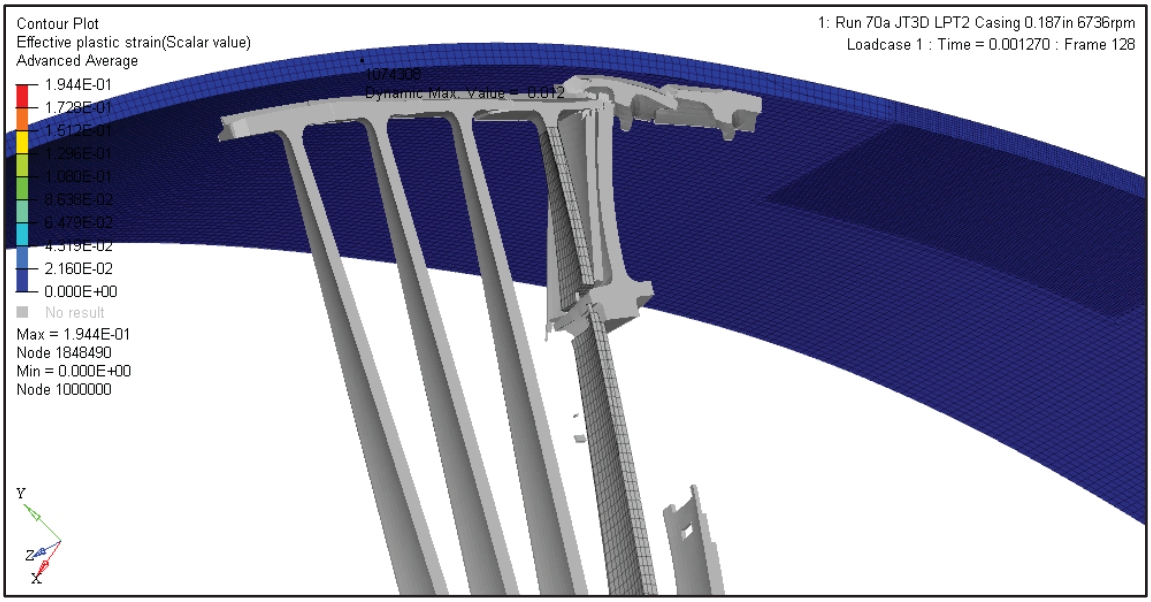

Figure 3.57 JT3D 6736rpm Airfoil #3 fracture

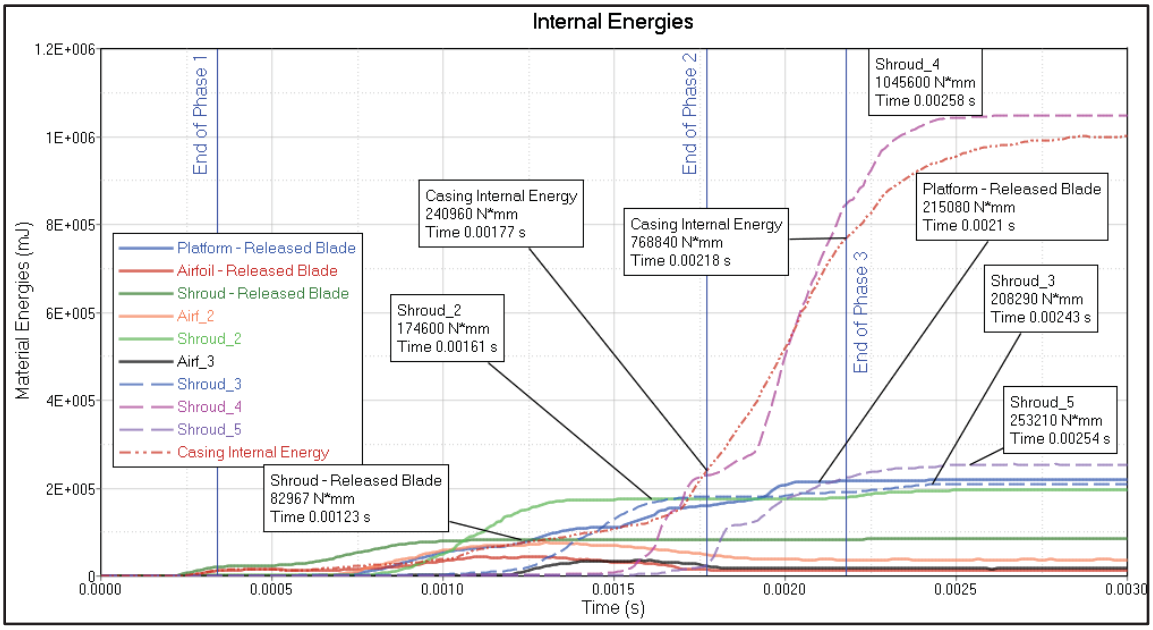

Figure 3.58 JT3D 6736rpm System components internal energies

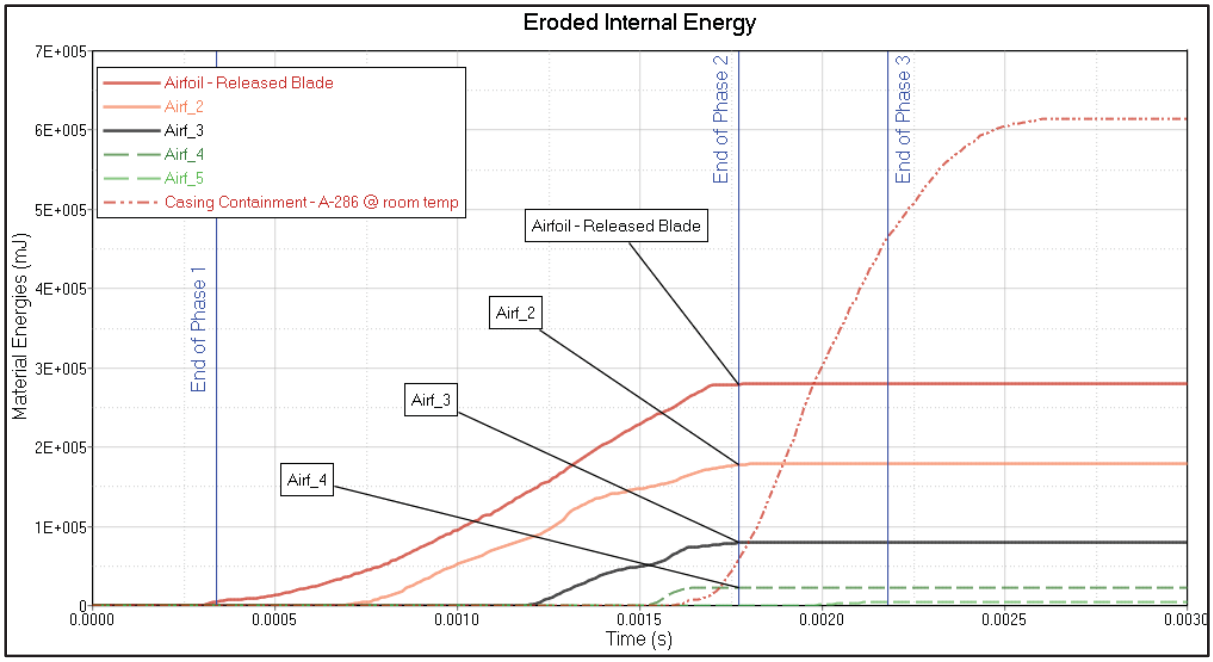

Figure 3.59 JT3D 6736rpm System components eroded internal energies

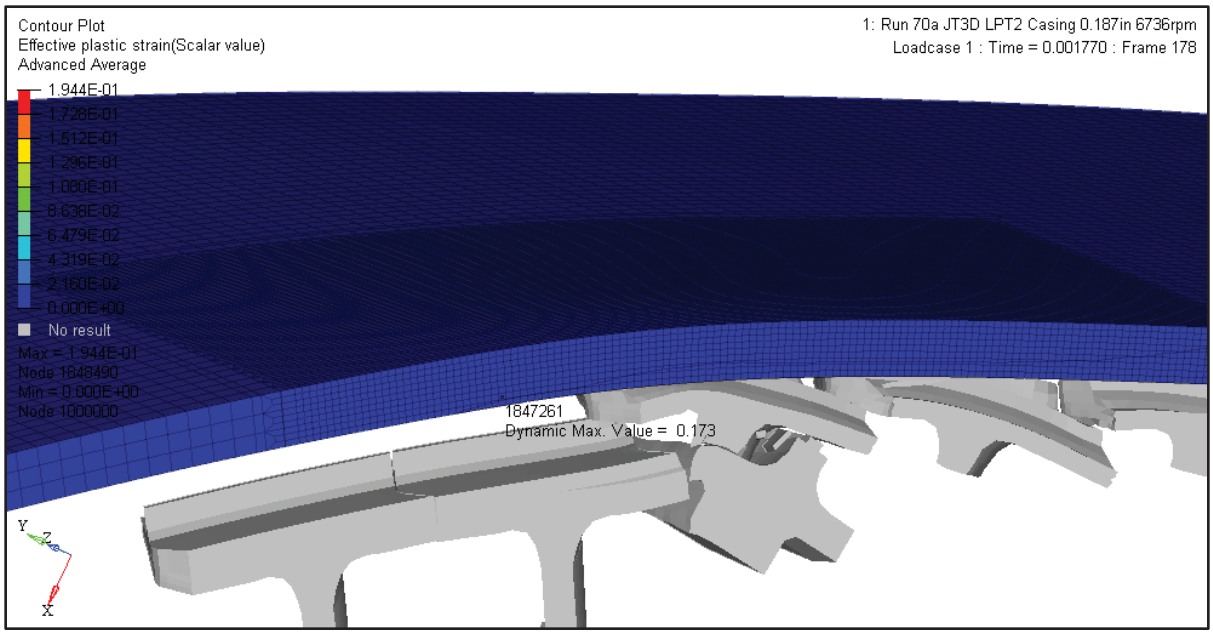

Figure 3.60 JT3D 6736rpm Beginning of Phase 3

The Phase 3 of the JT3D uncontained test simulation is composed of two sequences: 1. the shroud #3 is pushed further into the casing and loses the frontal contact with shroud #4 (Figure 3.60), and 2. released blade platform continues to push radially outwards the shroud #3, while shroud #4 pushes both debris (released blade platform and shroud #3) circumferentially, creating the second impact area (Figure 3.61). The plastic strain on the casing outer face increases gradually until the end of Phase 3 (time 0.00218 s, shown in Figure 3.62).

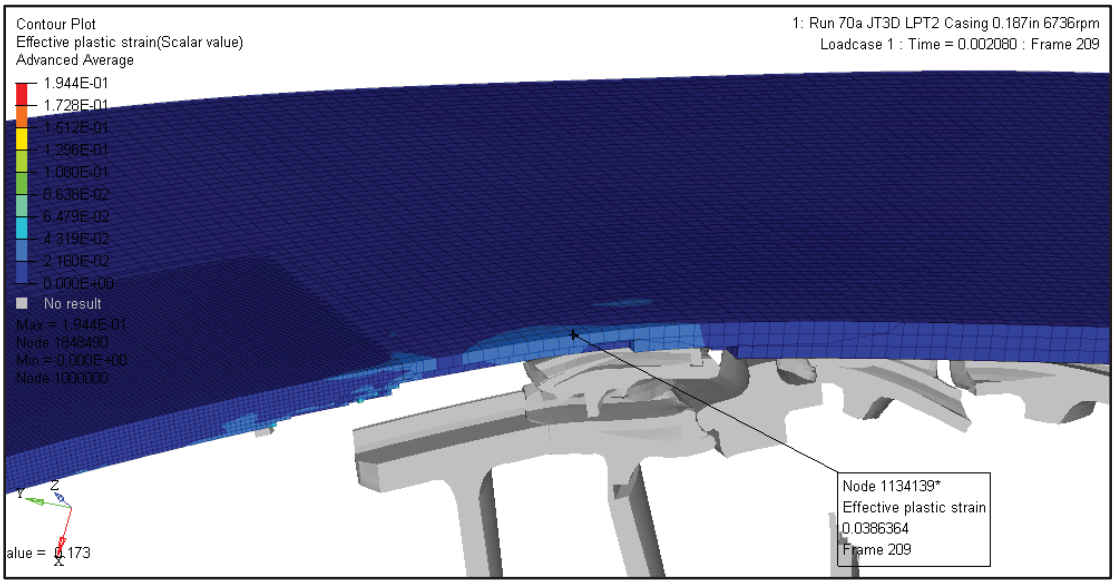

Figure 3.61 JT3D 6736rpm Initiation of the second impact bulge

Although for JT3D uncontained test simulation was not obtained a full penetration, as the damage in the coarse mesh region occurred over two thirds of the thickness, the casing is considered as compromised for the containment purpose.

After Phase 3, the casing continues to absorb energy, but as observed during Phase 2, the damage is not localized as during Phases 1 and 3, hence deemed not relevant.

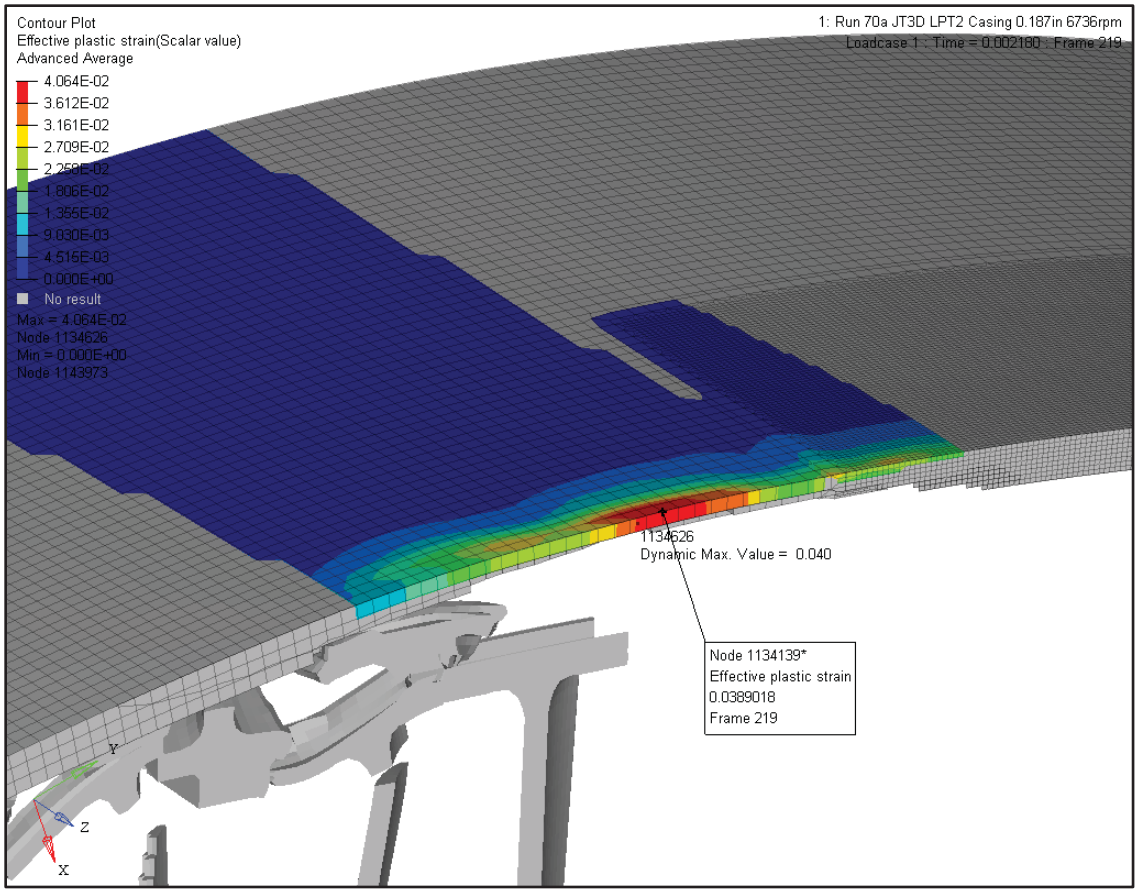

Figure 3.62 JT3D 6736rpm end of Phase 3

As for all the other simulations for JT8D and JT3D fragment containment, the initial impact with the casing is detrimental only to the blade, the effect being a plastic strain of maximum 0.03 on the outer face of the casing, and the released blade damage in the form of shroud separation. The casing internal energy at the end of Phase 1 is only 12.93 J, or 0.263% of the released blade initial KE.

At the end of the Phase 3, the energy exchanged with the casing is 527.88 J (difference between the casing IE at time 0.00218 s and at 0.00177), representing 10.7% of the released blade initial KE.

3.5 Summary

In this chapter were presented the details of the containment tests used to validate the analytical method, subject of this research. In the first section of this chapter, it was described the test installation, explained the test methodology, tested components, test sequence and shown the results. From the sets of tests referenced (Salvino, DeLucia, & Russo, 1988), there were selected only the single blade release test cases for JT3D and JT8D engines, deemed representative for large aerospace engines. Two sets of single blade fragment containment tests for each engine were considered in this research (one being contained, and the other not contained), to determine the containment threshold thickness for each engine.

These tests are used to generate the data necessary to assemble the design analytical method for blade containment. This data is obtained from the above-mentioned tests simulated in FEA. Therefore, in addition to the physical test description, the FEA model setup is also presented in this chapter. Details regarding the geometries used, meshing, boundary conditions and loading are provided.

Part of the FEA models setup, the material definition also constitutes a major section in this chapter. The state-of-art material definition for the casing, based on the Johnson-Cook model including the material definition function of the plastic strain, strain rate and temperature, as well the failure criteria defined as a 3D surface are explained at great extents.

In the final section of this chapter are presented the results of the FEA for the four selected test cases. All analyses revealed the pattern of the containment phenomenon, evidencing the sequence of individual events leading to the containment or un-containment of the released fragment, as well the factors influencing the outcome. The first three distinct phases of fragment containment were identified, and the energetic exchange was determined for all considered test cases. These results (internal energies, impact area dimensions) are used in the next chapter, dedicated to assembling the design analytical method.

CHAPTER 4

ANALYTICAL METHOD FOR ROTOR FRAGMENT CONTAINMENT

Based on the FE analytical data generated in the previous chapter, a series of parameters can be assembled in a calculation method for estimating the gas turbine casing capability to contain one blade fragment detached from a turbine rotor. As seen previously in the literature review section of this research, such methods were already developed by gas turbines manufacturers, however the assumptions on which they are based on, and their accuracy, need further detailing and discussions. This chapter details the commonalities and improvement opportunities for these methods and proposes a novel approach (the objective of this research) for such a design analytical method, based on the validated FEA results presented previously.

4.1 Released rotor fragment impact with casing - process timeline

This work studies the containment of a shrouded single blade fragment (compressor or turbine, shown in Figure 4.1), this being the most common type of rotor fragment released (SAE International Engineering Society for Advancing Mobility Land Sea Air and Space, 1996). Less frequent rotor failures releasing intermediate fragments or tri-hub failures should be the objectives of further studies.

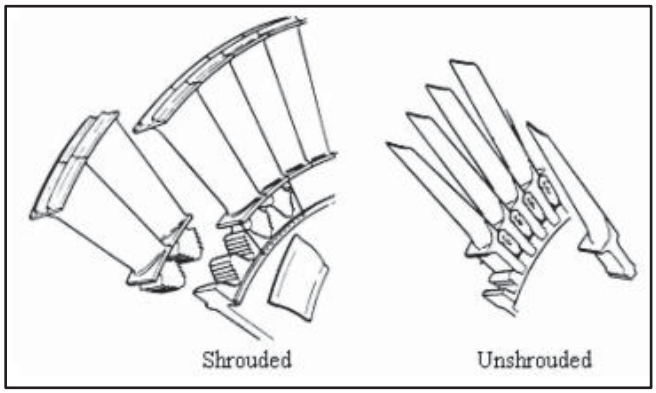

Figure 4.1 Shrouded and shroudless turbine blades
Taken from O'Dowd (2010, p. 4)

A full blade released from a rotor disk develops a higher kinetic energy, and thus can cause more damage to the casing than a fragment of a blade, especially if the latter is detached above the blade platform (Figure 4.2).

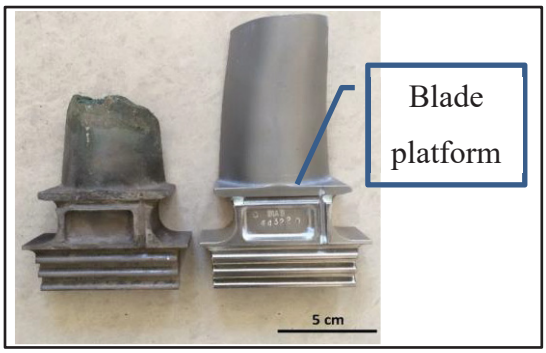

Figure 4.2 Failed versus new turbine blade
Taken from Kazempour-Liasi, Shafiei, & Lalegani (2019, p. 1674)

Although the AC 20-128 (Federal Aviation Administration, U.S. Department Of Transportation, 1997) recommends the tip half of the blade airfoil in the containment calculations for small fragments, this work proposes a more conservative case of including the blade platform when designing the respective gas turbine casing, as being the bulkier feature, causing the most damage to the casing.

Shortly after the blade fragment release, the tip of the blade impacts the casing. As seen in the previous chapter, this first impact usually is not causing a major damage on the casing (bulging shown in Figure 4.3, right image). Slender blades (such as the IPT or LPT blades) buckle under the axial compressive loading (Figure 4.3, left image). As the released blade loses velocity (due to the impact and the subsequent friction with the adjacent surrounding structure), it is impacted by the following blade. Significant damage starts to occur on the released blade, which eventually loses its shroud due to the impact with the casing, and as well due to the impact with the following blade shroud. A somewhat lesser damage occurs on the first following blade, which pushes forward the fragment already in contact with the casing. A load path between the remaining attached blades and the casing is created via the released blade (Figure 4.3, right image).

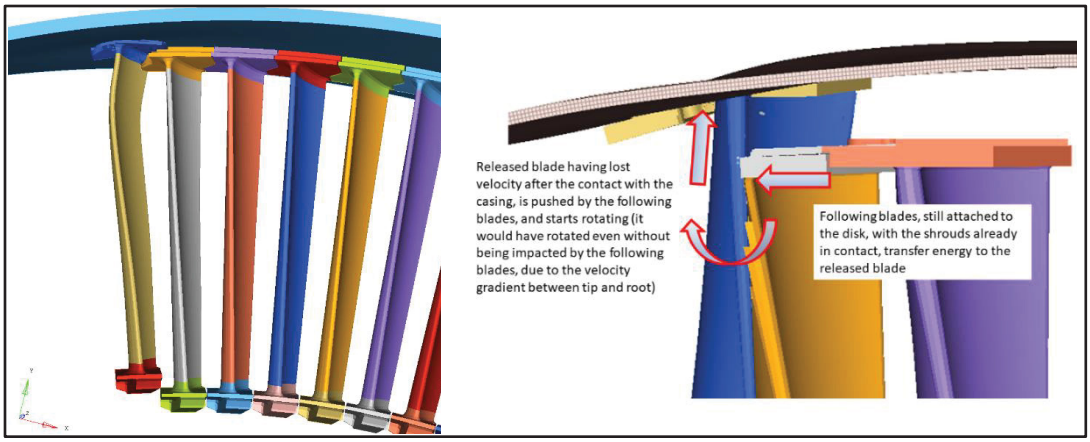

Figure 4.3 Blades interaction during the early impact; overall view (left), detail with blades-casing interaction (right)

For a shroudless rotor, the impact between the released blade fragment and the following blade is usually more detrimental to the following blade, which can fracture close to its midspan. Based on different blades geometries and material properties, small variations to the presented succession of events can occur: a blade in a more ductile material will bend rather than fracture (Figure 4.4), a bulkier geometry (for example HPT blades) will release rather the upper portion of their airfoil, etc.

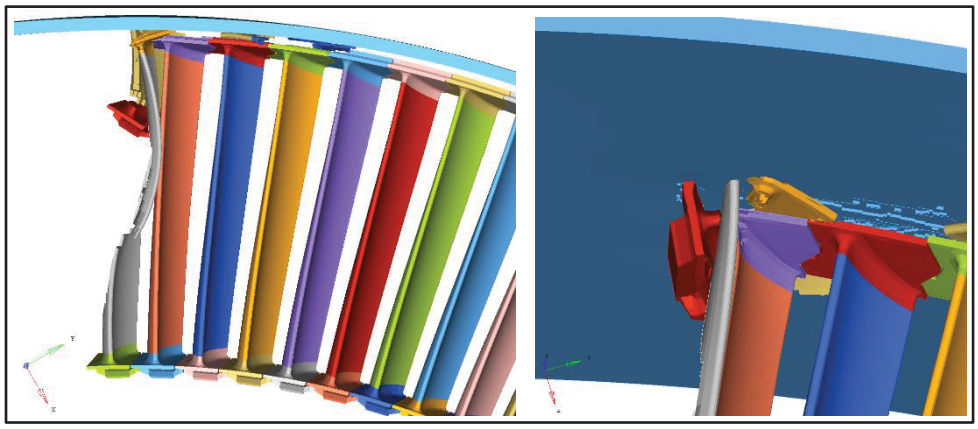

Figure 4.4 Following blade fragmentation (left) and platform impacting casing (right)

Regardless of the blade geometries, materials or stage, the commonality of the impact of the blade released from the firtree or beneath the platform is that the damage to the casing is caused by the bulky features of the blade (shroud or platform, but not the airfoil), when pushed in the impacted zone by the following blades.

After the main impact between the released blade platform with the casing, the fragment suffers severe deformation and material loss, damaging the adjacent static or rotating structures, however lacking the energy sufficient to cause significant damage to the casing. Subsequently, all remaining following blades are fractured by the impact with the increasing number of blade fragments (Figure 4.5).

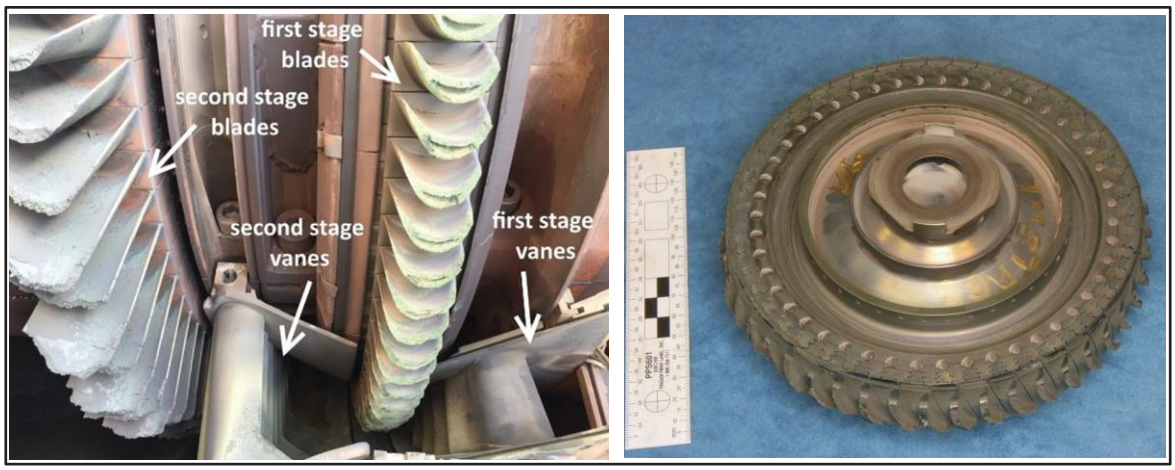

Figure 4.5 Fractured turbine blades (left), PT Disc with fractured blades (right)
Taken from Kazempour-Liasi, Shafiei, & Lalegani (2019, p. 1674), and from ATSB AO-2008-008 (2008, p. 19) (right)

The shrouded blades impact scenario is slightly different than the shroudless blades impact, however overall, still respects the succession of events mentioned above. Small variations of this scenario include the platform impacting indirectly the casing, via another debris (fragment of the airfoil, another shroud separated from a following blade, etc) however, the mass of the released blade causes the damage on the casing.

4.2 Ballistic perspective into the fragment containment

The identification of the failure mechanisms during the impact of the released fragment with the casing is essential to determine the energy absorption capability of the casing. In previous works (Zaid & Travis, 1974), (Hagg & Sankey, 1974), (Backman & Goldsmith, The mechanics of penetration of projectiles into targets, 1978), (Corran, Shadbolt, & Ruiz, Impact loading of plates—an experimental investigation, 1983), (Liu & Stronge, 2000), it was observed the existence of a threshold between the predominant modes of failure during the impact, threshold function of the projectile shape and target thickness.

Considering the impact velocity, the rotor fragment containment problem is in the sub-ordnance range of 25 – 500 m/s (Corran, Ruiz, & Shadbolt, On the design of containment shields, 1983), corresponding to strain rates in the order of $x10^2$ /s (Zukas, 1980) (Figure 4.6).

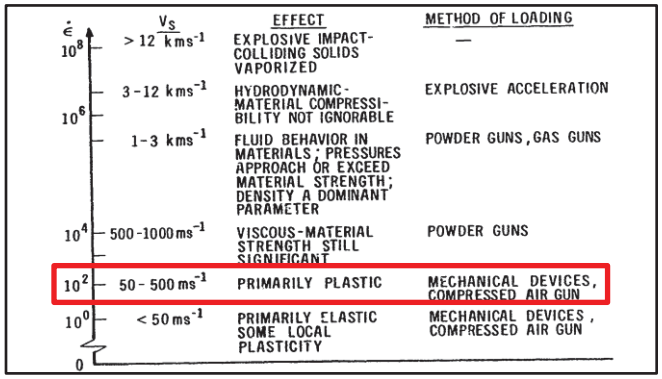

Figure 4.6 Classification of impacts function of impact velocity
Taken from Zukas (1980, p. 8)

Corran, Shadbolt and Ruiz (Corran, Shadbolt, & Ruiz, Impact loading of plates—an experimental investigation, 1983) identified four energy dissipation types: stored elastic energy, plastic energy (tensile, bending and shear plastic deformation), plugging energy (localized plastic deformation at the impact area) and plastic deformation energy of the fragment (corresponding to ballistics blunt missiles mushrooming).

Based on ballistic tests on mild steel plates using blunt projectiles (Corran, Shadbolt, & Ruiz, Impact loading of plates—an experimental investigation, 1983), the following conclusions were stated:

1. The membrane plastic work decreases rapidly with the plate thickness increase (Figure 4.7)
2. The bending plastic work increases with the plate thickness until reaching a maximum, then decreases
3. The plugging energy increases as well with the plate thickness
4. The elastic energy decreases until reaching a minimum, then increases back with the increase of plate thickness

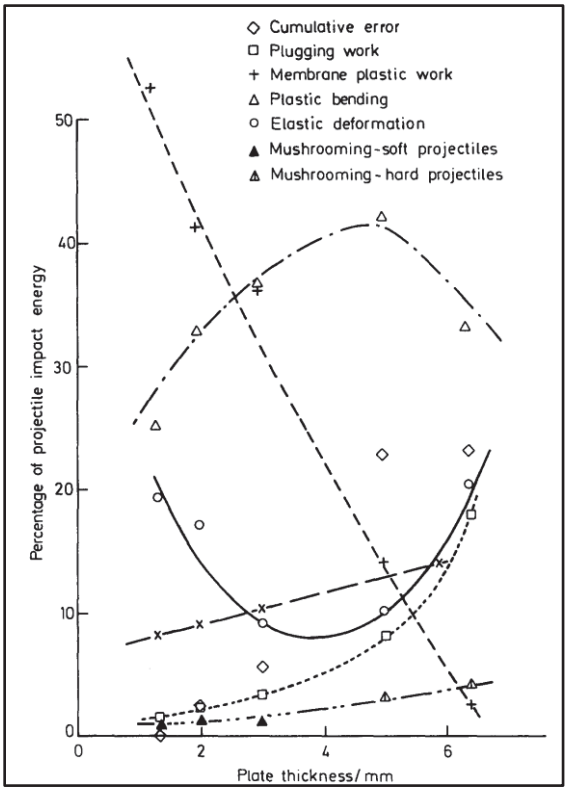

Figure 4.7 Plates impacted by projectiles, energy balance function of plate thickness
Taken from Corran, Shadbolt, & Ruiz (1983, p. 15)

Also, it was evidenced that the membrane stretching is the most effective mechanism of energy absorption, due to more material participating in the energy exchange (plugging is more localized compared to dishing). In addition to these, it can be observed that either soft or hard projectiles plastic deformation energies are small compared to the target energies. From containment events it was observed that severe deformation occurs on the airfoil section (usually completely fragmented), whereas the blade sturdier features (shroud or platform) suffer significantly less deformation (Figure 4.8, Figure 4.9).

Hardness and projectile shape influence the balance of energies (Corran, Shadbolt, & Ruiz, Impact loading of plates—an experimental investigation, 1983); the shape of the projectile changes the mechanism of penetration from ductile hole enlargement (wedge projectiles), or tensile stretching (hemispherical, conical or ogival heads) to shear plugging (blunt cylindrical projectiles).

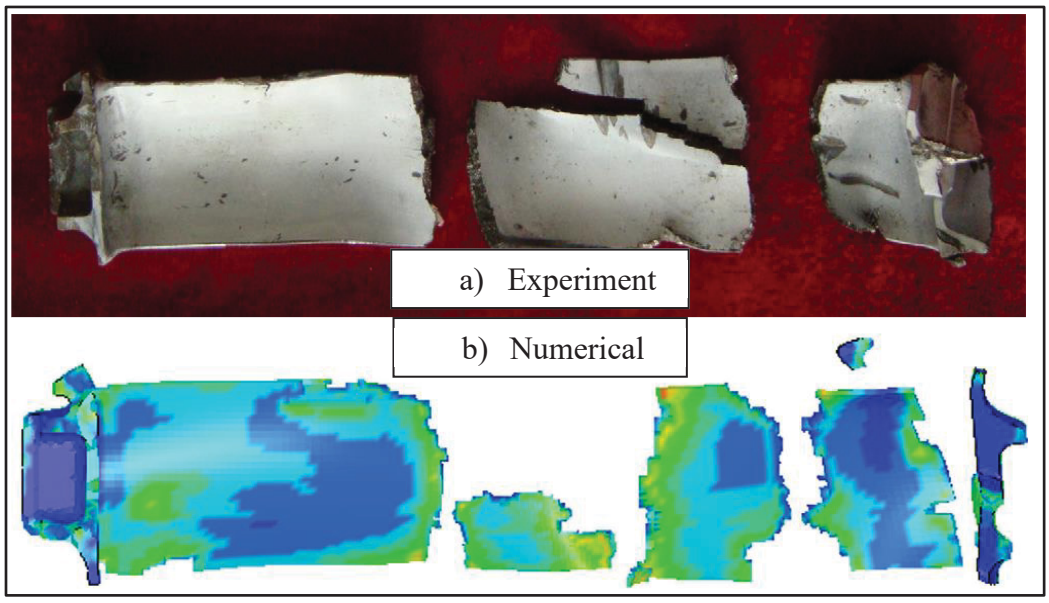

Figure 4.8 Turbine released blade fragmentation
Taken from He & al. (2016, p. 104)

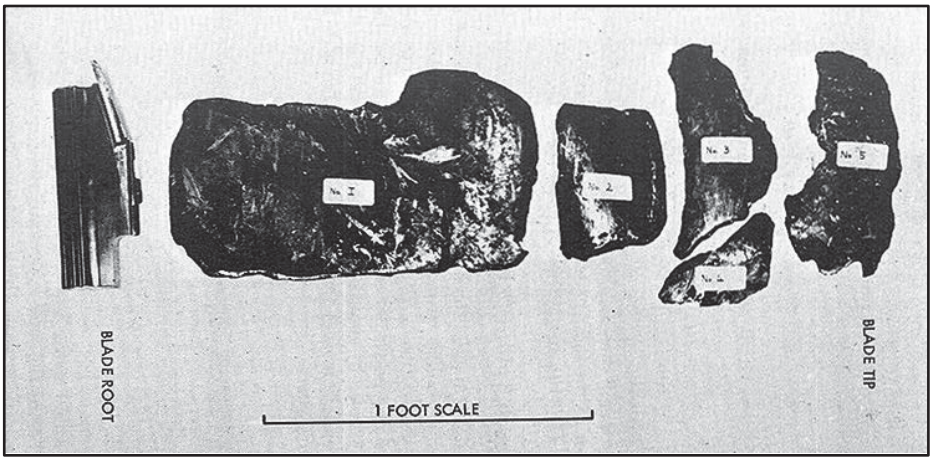

Figure 4.9 Released blade after a rotating test
Taken from Goatham & Stewart, (1976, p. 161)

Due to the irregular shape of the released blade, it can be assumed that in general the main impact (causing maximum damage) occurs with one corner of the platform contacting the casing (Figure 4.10), thus corresponding to the impact of a sharp projectile, favouring the initiation of tensile stretching in the casing bulged area in thin plates (relative to the fragment dimension).

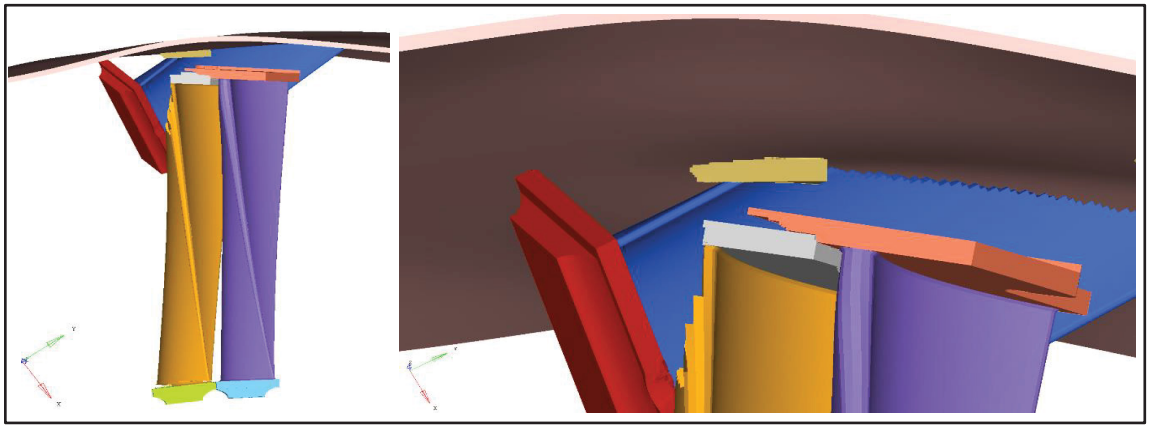

Figure 4.10 FEA Blade fragment impact (left), detail view (right)

A thin plate impacted by a non-blunt projectile deforms in a tensile + bending mode (dishing), where thinning is observed in the immediate vicinity of the impact area (Figure 4.11).

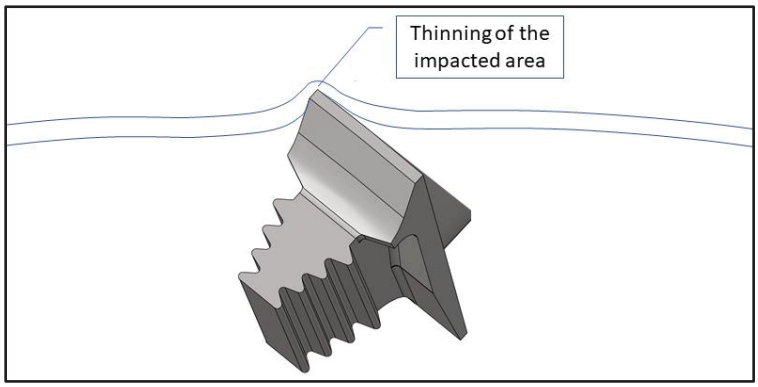

Figure 4.11 Dishing of a thin plate impacted by a non-blunt projectile

As mentioned previously, the hardness of the components involved in the impact influences the failure mode of the casing. When the fragment hardness is bigger than the casing hardness, it indents the casing, displacing the casing material around the edge in contact. If the casing material has a higher hardness, the fragment deforms (deformation referred to as projectile mushrooming) and increases the impact area, however the deformation mode of the casing does not change fundamentally, the target continues to deform until reaching failure tensile stresses at its distal face (Figure 4.12). If the projectile did not consume its kinetic energy, the casing fracture on the distal face propagates radially inwards until reaching the internal face, thus causing the casing perforation.

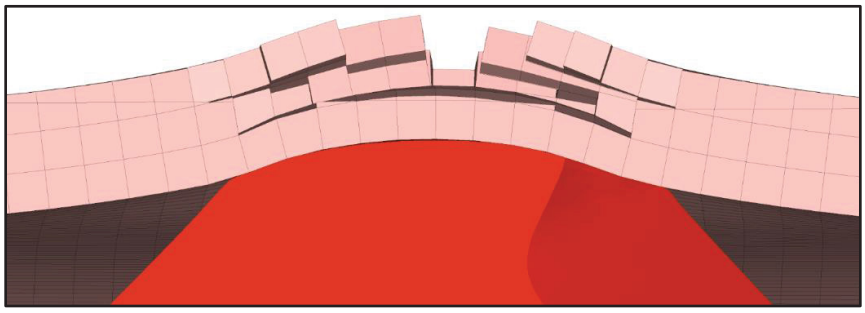

Figure 4.12 Soft projectile impacting a thin casing

While increasing the thickness of the casing, as more material opposes to the advancement of the fragment, localized shearing appears at the impact perimeter. In an intermediate mode of transition from tensile to shear (thickness close to the threshold value), some local shearing occurs at the impact face at the same time with tensile failure at the outer face; the distal face fracture coalesces with the adiabatic shear band failure of the inner face (Figure 4.13, Figure 4.14).

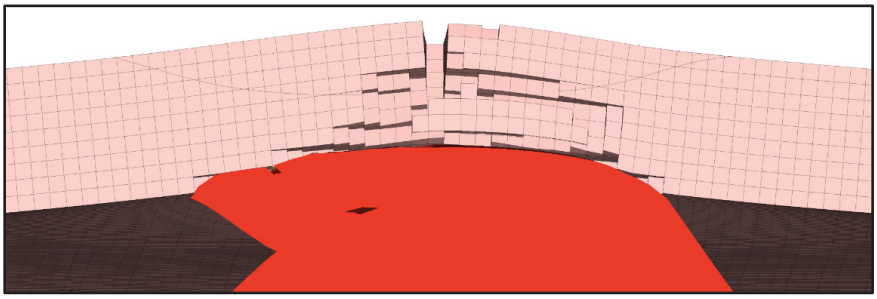

Figure 4.13 Dual failure modes, plugging initiation with tensile stretching

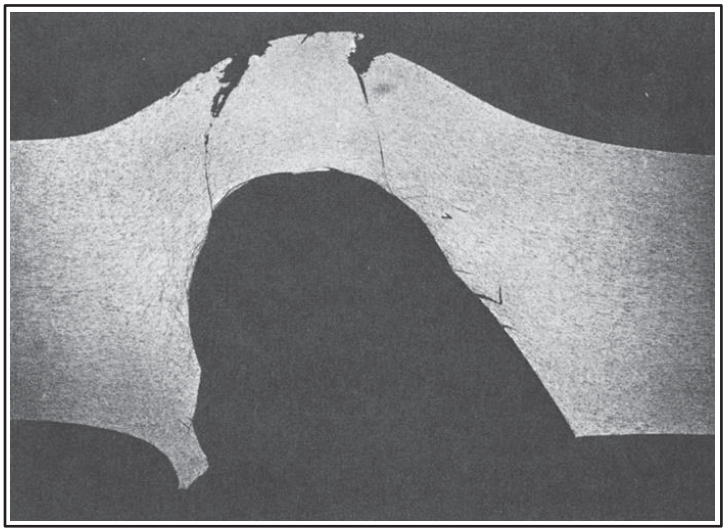

Figure 4.14 Plugging failure with distal face stretching at angled impact with a plate
Taken from Backman & Goldsmith (1978, p. 8)

For a plate impacted by a projectile, further increasing the casing thickness diminishes the bulging / dishing deformation, establishing instead the plugging as the dominant mode of failure (Figure 4.15) (Zaid & Travis, 1974), (Backman & Goldsmith, The mechanics of penetration of projectiles into targets, 1978), (Tansel, 2010), (Crouch & Baxter, 1990).

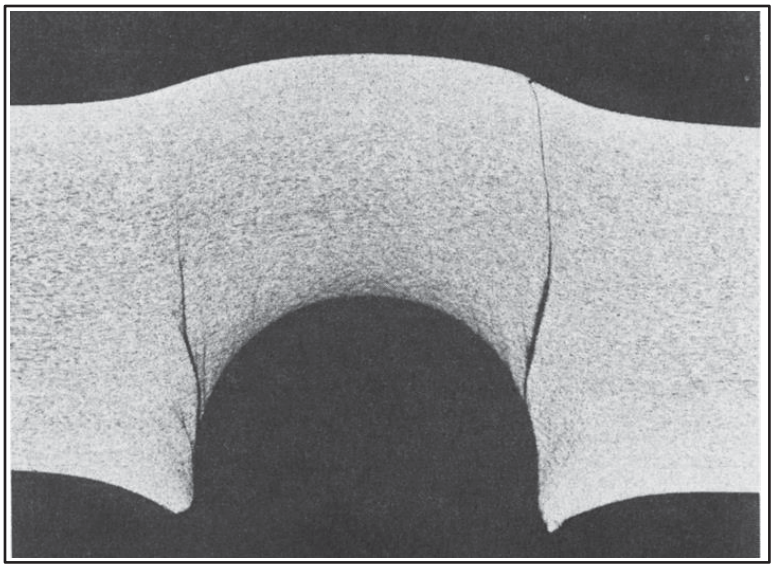

Figure 4.15 Incipient plugging failure
Taken from Backman & Goldsmith (1978, p. 6)

Detailing the above mentioned, the process of a projectile impacting a target plate can be divided into two phases ((Hagg & Sankey, 1974), (Woodward & Cimpoeru, 117–131)):

1. Projectile indentation into the casing, local compression around the impact perimeter with possibly shear along the perimeter (Figure 4.16)
2. Either dishing (thin plates) or plugging (in the case of thick plates)

During the first phase, penetration can occur for a wedge-shaped projectile, which dislocates the target material around its nose, shears the remaining material and enlarges the hole created (ductile hole enlargement mechanism, Figure 4.17). Although possible, this failure scenario reveals a less than optimal casing design. This failure mode should not be considered for developing a casing design method for containment, due to its relatively reduced energy absorption capability.

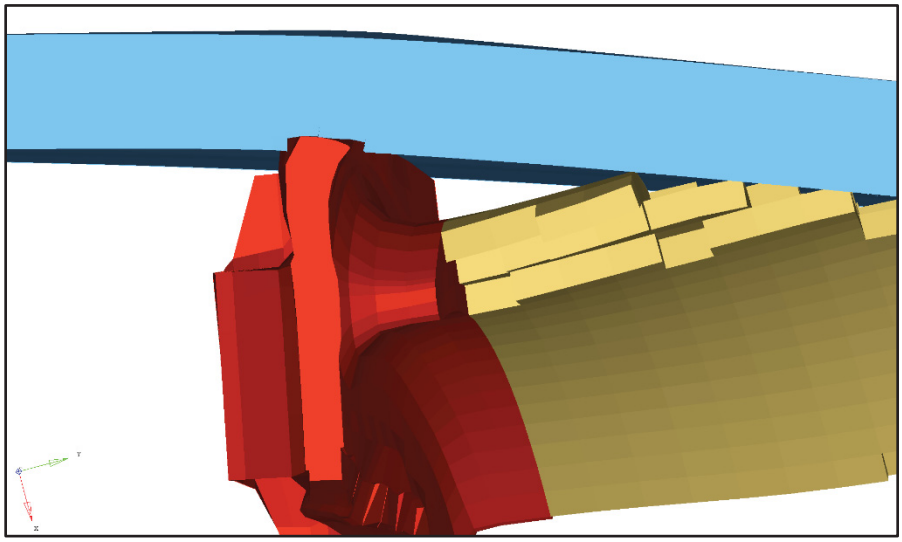

Figure 4.16 FEA minor fragment indentation and shearing of the casing

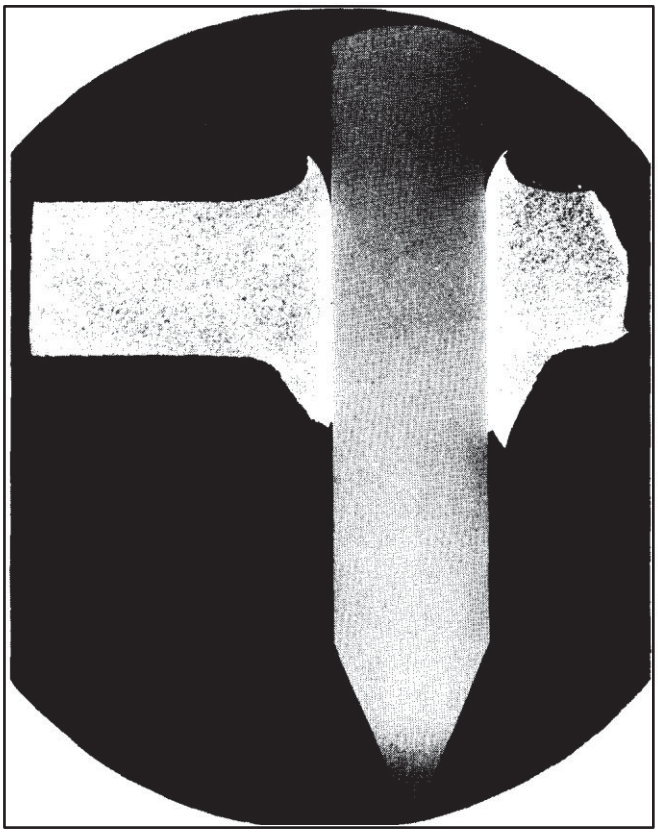

Figure 4.17 Ductile hole formation failure
Taken from Woodward (1978, p. 351)

As mentioned previously, dishing is the most efficient energy absorption method (Corran, Shadbolt, & Ruiz, Impact loading of plates—an experimental investigation, 1983), and the dynamic containment energy increases with increasing thickness, until reaching the ballistic thickness, after which starts decreasing with the development of thermo-plastic instability leading to a shear-based failure (Zaid & Travis, 1974).

A comparison of strain energies corresponding to the three types of loading affecting the impact area (membrane stretching, bending and shear), function of plate thickness is shown in Figure 4.18. The intersection of the membrane stretching curve with the shear curve represents the threshold for plugging failure mode.

Simplified relations are used for the definition of each failure mode. The membrane stretching strain energy ($W_{stretching}$) is expressed in function of the volume of material in the impact area, and the tensile flow stress:

$$W_{stretching} = b \cdot w \cdot t \cdot \varepsilon \cdot \sigma_0 \tag{4.1}$$

where b is the circumferential length of the impact area, estimated at "x" times the platform height h (Figure 4.19), and "x" is discussed in the next pages, based on the FEA results. w is the platform axial length (Figure 4.20), t is the casing or containment ring thickness, ε is the tensile strain and σ_0 is the stress flow simplified to the average of yield and ultimate engineering stresses at lowest strain rate (Børvik & al., 2003).

The bending strain energy ($W_{bending}$) is evaluated as:

$$W_{bending} = M_p \cdot \theta_{bend} \text{ (Szuladzinski, 2009)} \tag{4.2}$$

considering the plastic bending moment equivalent with the one of a beam of length b and height t, $M_p = \sigma_y \cdot \frac{b \cdot t^2}{4}$ (Megson, 2019).

The rotation around the hinge point θ_{bend} can be considered $\theta_{bend} \sim {}^{\delta_{bend}}/_{l}$, where δ_{bend} is the deflection (assumed half thickness) and *l* is the half-width of the beam (b/2 in this case). It is to be noted that the beam length is not constant with the thickness increase, and this term (bending strain energy) needs further development to show a variation as depicted in Figure 4.7. However, this simplified formulation will be used for the purpose of graphical display of the bending mode.

For the shear energy of the impacted section was used the relation:

$$W_{shear} = K \cdot P \cdot \tau_D \cdot t^2 \text{ (Hagg \& Sankey, 1974)} \tag{4.3}$$

K being an experimental constant with a value in the range of 0.3 to 0.5 (considered for this graphic 0.5), P the perimeter of the sheared area (in this case $P = 2 * (w + h)$), and τ_D the dynamic shear strength of the material, as determined during the shear tests.

The plugging threshold is found at the intersection of the stretching curve with the one for shear:

$$\mathrm{b} \cdot w \cdot \mathrm{t} \cdot \varepsilon \cdot \frac{\sigma_y + \sigma_u}{2} = K \cdot 2 \cdot (w + h) \cdot \tau_D \cdot t^2; \tag{4.4}$$

Solving for thickness satisfying this equation yields the trivial solution, and:

$$\mathrm{t} = \frac{\mathrm{b} \cdot w \cdot \varepsilon \cdot \frac{\sigma_y + \sigma_u}{2}}{K \cdot P \cdot \tau_D}; \tag{4.5}$$

The threshold value (t_{th}) is therefore the solution of equation (4.5).

The equations (4.1) to (4.5) are considered for this graphical purpose in their raw form, but further details need to be added. The impact occurs at a velocity where strain rates are not negligible, thus the need for a correction factor accounting for this in both types of failure mode. Also, some additional adjustments need to be made on the impact area geometry.

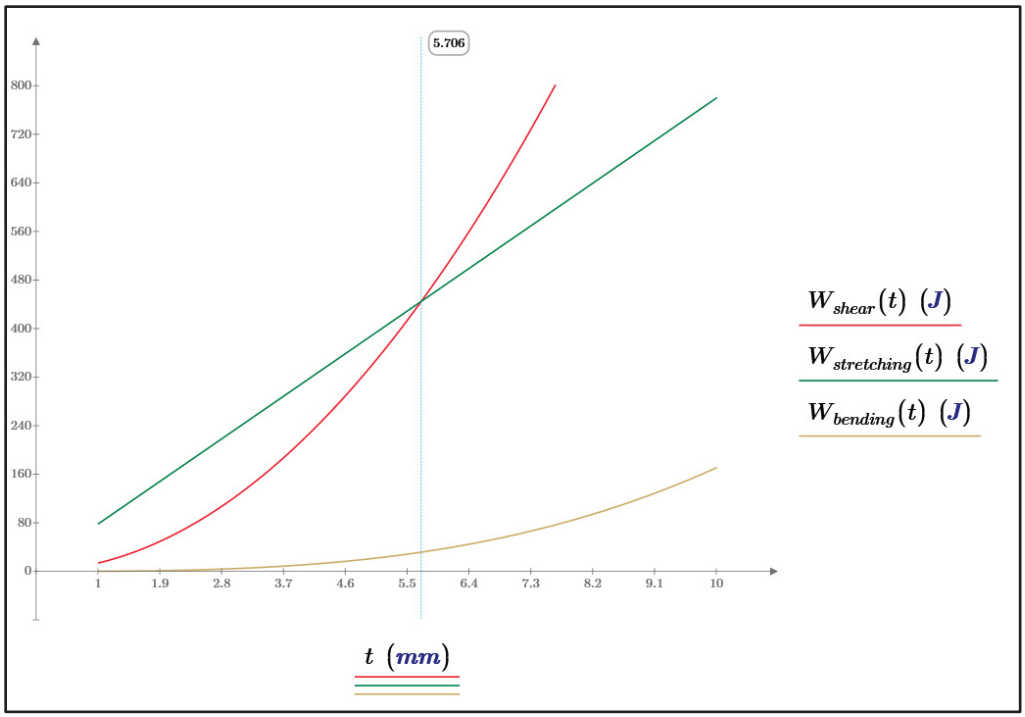

Figure 4.18 Failure modes variation function of thickness

From the above chart (Figure 4.18), it can be observed that for thicknesses smaller than the tensile-shear threshold, the bending strain energy can be neglected due to its magnitude. It is obvious that for a thin case, there is not much strength opposing the fragment advancement in a bending mode, however for a thicker case, the bending contribution becomes non-negligible. Also, the shear strain energy shows a fast increase due to the squared thickness contribution.

The individual curves were developed for a generic fragment as shown in Figure 4.19. As the fragment impacts with the edge of the platform, the height is considered 3.828 mm, the length of the platform w being 34.468 mm (as shown in Figure 4.20).

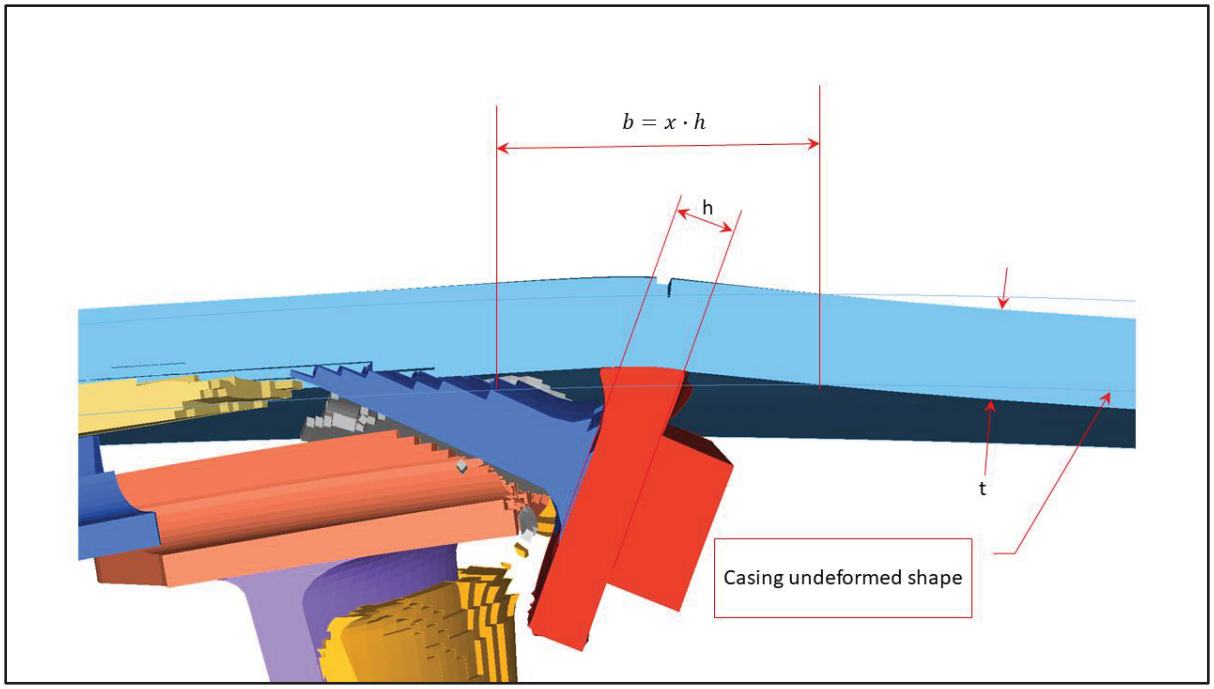

Figure 4.19 Fragment geometrical parameters considered

From all the FEA results, and for an impact of the platform, b is approximated to "x" times the height of the fragment (6 to 8, to be further detailed), as being the length of the plasticized impact area on the outer face of the casing.

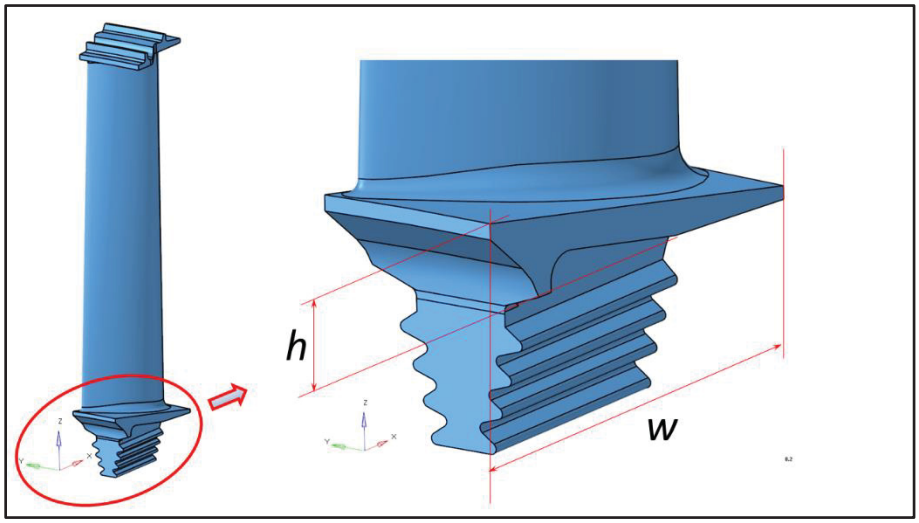

Figure 4.20 Blade root contributing to the impact

For the impact of the shroud, b is the circumferential length of the shroud

Therefore, the dimensions of the fragment (Figure 4.19, Figure 4.20) provide indications about the plugging threshold casing thickness, from which the casing necessary containment thickness calculation should be performed using the appropriate equation (shear or tensile).

4.3 Design equation variables

The rotor fragment impact phenomenon is dependent on multiple factors which can be grouped into three main categories: geometrical parameters, material properties and energetic exchange.

The fragment geometry and the casing thickness influence the failure mode of the casing. Both membrane stretching and plugging plastic energies are dependent on the casing thickness, on the area and on the perimeter of impact.

The mechanical properties of the materials are affected by the impact strain rate, which is dependent on the shaft rotational velocity.

From kinematic perspective, the energy exchange ratio between the blades and the casing is dependent of the blade type (shrouded or unshrouded) and the shape of the blade (LPT stage 1 or 2, or 3, respectively more sturdy or slenderer).

In summary, the equation variables are the area A and perimeter of the impact P, the mass of the fragment m, the rotational velocity ω, the radius of gyration R, the flow stress σ_0, the dynamic shear factor τ_D, and a coefficient of energetic exchange, $K_{exchange}$.

4.4 Design analytical methods for blade containment

Engine manufacturers developed semi-empirical equations for sizing the containment structures. All equations are based on the proportionality of the fragment kinetic energy (KE) with a plastic deformation energy PE (shown in Table 4.1 and further detailed below).

$$PE \sim KE; \tag{4.6}$$

$$PE = KE \cdot K; \tag{4.7}$$

Where K is an empirical coefficient developed by the different engine manufacturers based on testing.

The plastic strain energy formulation for the impact affected volume is:

$$PE = \int_V \sigma \cdot \varepsilon \cdot dV; \tag{4.8}$$

All the following presented methods include different variants of this formulation.

Table 4.1 details some of the particularities of analytical methods employed by some of the OEMS's. Some methods are more empirical than others, most of them are based on shear-based failure mode, the commonality being their usage simplicity (not requiring an important computational effort).

United Technologies addresses separately the containment of fan blades versus compressor and turbine blades, the fan containment being based on the shear failure mechanism, and the compressor and turbine containment being hoop-based. As the UTC's fan blade containment method (shear-based) is very similar to Snecma's formulation, and as the objective of this work is focused on turbine (or compressor) blade fragments, only the equation corresponding to compressor and turbine blade fragments (Heermann, Eriksson, & McClure, 1977) is presented in Table 4.1, as Method 1.

Table 4.1 Existing design analytical methods summary

	Plastic deformation energy PE	Comments
Method 1	$d \cdot b_x \cdot \frac{C \cdot \pi \cdot D}{n} \cdot t \cdot MF \cdot K_1$	Good • Hoop behaviour considered for the ring • Complex (considered speed, different geometrical factors d, C) • Multiple blades fragment definition Suggested improvements • Adding the shear threshold, as the method is not applicable for shear dominant situations
Method 2	$B \cdot U \cdot \varepsilon \cdot t^2$	Good • Simplicity Suggested improvements • A better impacted volume approximation, as currently is in function of the blade height • Adding the membrane stretching threshold • Account for dynamic effect
Method 3	$\frac{1}{\sin(\alpha)} \cdot P \cdot Uds \cdot t^2$	Good • Consideration of the perimeter of the impact area • Dynamic effect included in the shear strength • Multiple-blades fragment can be considered Suggested improvements • Adding the membrane stretching threshold, as the current method might not be accurate for thin casings
Method 4	$\frac{t^2}{K_2}$	Good • Very simple Suggested improvements • More analytical parameters, as the current model is purely empirical

Method 1 is expressed as:

$$CF = \frac{\sum CV \cdot MF}{KE_{TAN}}; \tag{4.9}$$

In this equation, the proportionality coefficient named Containment Factor (CF) is determined as the ratio between the sum of casings hoop potential energies (considering several containment layers) and the tangential kinetic energy of the fragment (KE_{TAN}). The Hoop Potential Energy is expressed function of the product of the Containment Volume (CV), and the static Material Factor (MF, to be detailed in the following pages of this section).

This relation is valid for a single blade released, or for a bigger fragment (intermediate), including disc serrations. For the latter, the circumferential length is increased accordingly corresponding to the circumferential length of the released fragment.

One of the assumptions of this method is that the rotational velocity of the fragment around its axis is considered small comparatively with the tangential KE, and it is included in one of the empirical factors. The thickness (t) can be determined from expressing the volume of the estimated impact area (CV):

$$CV = \sum_{i=1}^{m} (d \cdot b_x \cdot \frac{C \cdot \pi \cdot D \cdot t}{n})_i \tag{4.10}$$

In this equation, d is an empirical dynamic factor related to the axial length of the case, and b_x is the axial projection of the blade tip. c is a non-dimensional factor addressing the effective circumferential length of the case, D_n is the nominal diameter of the casing and n is the number of blades in that stage (Figure 4.21). This formulation is generalized for "m" continuous rings assembled in the containment system and considers even an intermediate fragment formulation; for a single blade release, C=1.

As this method is based on the hoop stress, its applicability is restrained to only those situations where the thickness of the case is smaller than the shear-tensile threshold. The different empirical factors in the UTC method include the circumferential (and axial) enlarged impact area, and a dynamic factor (accounting for the impact velocity, and the resulting strain rate).

Another analytical method for determining the thickness of a containment casing is presented in (McCarthy, Definition of engine debris and some proposals for reducing potential damage to aircraft structure, 1976), by McCarthy, from Rolls-Royce perspective (Figure 4.22), Method 2 in Table 4.1.

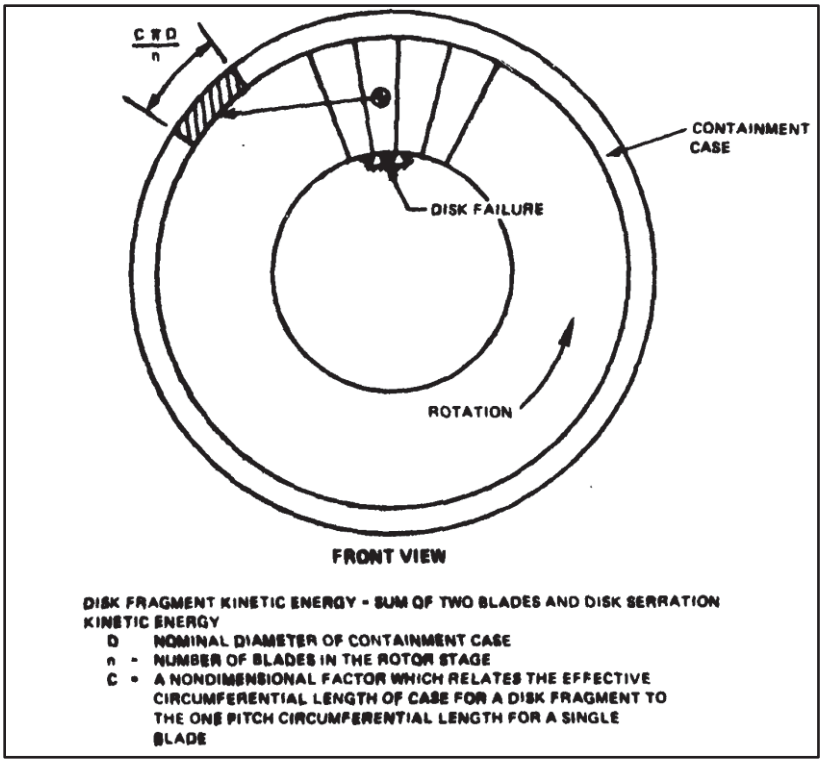

Figure 4.21 Circumferential length considered
Taken from (Heermann, Eriksson, & McClure (1977, p. 11)

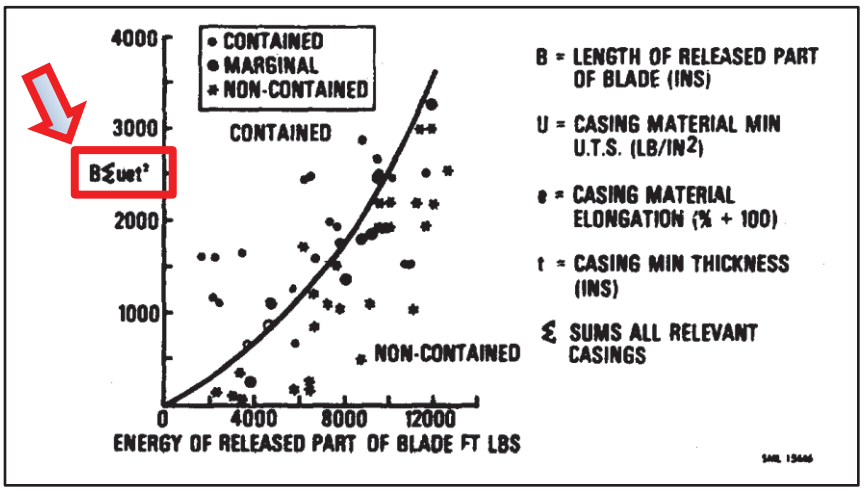

Figure 4.22 Blade Containment criterion
Taken from McCarthy (1976, p. 7-4)

As seen in the graph, the plastic deformation energy is expressed as:

$$PE = B_h \cdot \sum_{i=1}^{m} (U \cdot \varepsilon \cdot t^2)_i \tag{4.11}$$

for multiple containment rings (a total of m layers).

In (4.11), B_h is the blade height, U is the minimum tensile strength (UTS), ε is the elongation and t is the thickness of the respective containment ring. The empirical coefficient is the ratio between the two energies, the threshold between the containment and non-containment (equivalent of the UTC's CF). For this method, its deficiency in addressing a fragment larger than a blade is recognized in the referenced article. Also, this method considers that the impacted area is function of only the blade length and the casing thickness (thickness to the power of 2), and although it seems to be a shear-based method, the mechanical properties are tensile. There is no mention if this method can be applied to fan blades.

Described in the Table 4.1 as Method 3, Snecma proposes for the necessary containment thickness (t), a formulation similar to the UTC fan blade containment:

$$t = \sin(\alpha) \cdot \sqrt{\frac{KE}{P \cdot Uds}}; \text{ thus, if expressing the plastic deformation energy} \tag{4.12}$$

$$PE = \frac{1}{\sin(\alpha)^2} \cdot P \cdot Uds \cdot t^2 \tag{4.13}$$

Where, α is the blade impact angle, P is the perimeter of the shear plug and Uds is the dynamic shear strength. In (Lane, 1989) it is not mentioned if this is valid only for the fan blade containment, or it can be applied to compressor / turbine fragments. Regardless, the formulation is valid for a shear-based failure mode of the casing.

General Electric Corp. uses an empirical relation for determining the minimum containment thickness (Lane, 1989), Method 4 in Table 4.1:

$$t = K_2 \cdot \sqrt{KE}; \text{ with the plastic deformation energy being} \tag{4.14}$$

$$PE = \frac{t^2}{K_2} \tag{4.15}$$

K_2 being an empirically determined constant.

Although the usage of the design method needs to be straightforward, an overly simple method adds unnecessary conservatism. Consideration of important features of gas turbine casings is missing from all these methods: influence of flanges, rails, doglegs and any hoop carrying structure affecting the local stiffness of the casing.

Also, the absence of a threshold delimiting the failure mode reduces the accuracy of the design method, as the shear-based design methods are not optimized for energy absorption - the maximum energy absorption is by membrane stretching (Corran, Shadbolt, & Ruiz, Impact loading of plates—an experimental investigation, 1983).

Another important difference between these methods is the definition of the affected volume of the casing. Considering this criterion, Method 1 (UTC) provides the most detailed definition of the impacted volume, followed by Method 3 (Snecma) which allows flexibility in the determination of the impact area perimeter. Method 2 (Rolls-Royce) considers the blade length, multiplied by the squared thickness, and as observed in the previous chapter (FEA results), the airfoil does not contribute much to the casing damage. Method 4 (GE) does not provide any indications about the impacted area volume.

To evaluate the coefficient of proportionality (K, as mentioned in (4.9)) between the fragment translational KE and the casing plastic deformation energy, the containment thicknesses can be estimated using the four mentioned methods detailed in Table 4.2.

For Method 1, the Containment Factor (Heermann, Eriksson, & McClure, 1977) is renamed to K_1, and includes adjustments for the effective axial length, as well a dynamic factor. The static Material Factor is the plastic strain energy and A is the impact area $A = b_x \cdot \frac{\pi \cdot D}{n}$; where b_x is the axial length of the fragment, therefore *w* in Figure 4.20 ($w_{JT3D} = 35.086\ mm$, and $w_{JT8D} = 45.300\ mm$). The diameters considered are $D_{JT3D} = 895.020\ mm, D_{JT8D} = 715.950\ mm$, and the number of blades were estimated based on the available geometries as $n_{JT3D} = 122$, $n_{JT8D} = 88$. For this calculation, the Material Factor is approximated as the product between the material strain (ε) and the simplest formulation for the average flow stress $\varepsilon \cdot \sigma_0$, where σ_0 is the average between the yield and ultimate engineering stresses (Børvik & al., 2003).

In the case of Method 2, $B_{JT3D} = 130.531\ mm, B_{JT8D} = 112.2\ mm$, *U* is the ultimate tensile stress used in the analyses for the casing in A-286 (*U* = 1011.46 MPa), and e is the failure strain (ε = 0.25).

Method 3 considers the impact perimeter $P = 2 \cdot (h + w)$, the dynamic shear stress Uds (determined during the shear test simulations as 549.779 MPa), and the angle of impact with the casing α = 90°.

For all methods calculations were used the kinetic energies corresponding to the contained cases ($KE_{JT3D} = 29916\ lbf \cdot in = 3380.054\ J$, $KE_{JT8D} = 36275\ lbf \cdot in = 4098.525\ J$.

Table 4.2 Containment thickness estimation based on the existing containment methods

		JT3D	JT8D	JT3D	JT8D
	Containment equation	Proposed K		Containment thickness [mm]	
Method 1	$t = \frac{K_1 \cdot KE}{A \cdot MF}$	0.24	0.40	4.79	4.76
Method 2	$t = K_2 \cdot \sqrt{\frac{KE}{B \cdot U \cdot e}}$	0.47	0.40	4.76	4.81
Method 3	$t = \sin(\alpha) \cdot K_3 \cdot \sqrt{\frac{KE}{Uds \cdot P}}$	0.57	0.56	4.77	4.79
Method 4	$t = K_4 \cdot \sqrt{KE}$	0.00009	0.00008	5.232	5.122

To reach the containment thicknesses of 0.187 in (4.750mm) for both engines, the coefficients of proportionality were approximated for all methods. It is observed that for the hoop-based method (Method 1), the coefficient of proportionality is between 24 and 40% of the KE of the fragment. For Method 2, the coefficient is between 40 and 47%, and for Method 3 is about 56%. As one method is hoop-based, the second one seems to be shear-based but considering tensile material properties, the third one being effectively shear-based and the fourth method being empirical, the proportionality coefficients are accordingly different.

Each of the presented methods is based on different assumptions and each present possibilities for refinement and improvement. The objective of this research is to establish an improved analytical sizing method, which considers all aspects relevant to rotor fragment containment. This method needs to include the tensile membrane contribution, as it is the most efficient mode of energy absorption, but also consider shear when this failure mode is dominant.

4.5 Definition of the new analytical method for preliminary design for fragment containment

A design analytical equation for blade containment can be proposed in the form of equation (4.7):

$$KE_{blade} \cdot K_{exchange} = PE_{casing} \tag{4.16}$$

$K_{exchange}$ being a coefficient considering the energy exchanged between the blade fragment and the casing, determined by analysis and experiment (in this research determined as 6%, as seen in the previous chapter, and as detailed in the following discussions chapter).

Two different scenarios need to be considered in the determination of the exchange coefficient, cases that affect differently the energy balance: shrouded versus shroudless blades fragment.

As the blade shrouds of a shrouded rotor are in contact, the rotor develops a circumferential stiffness at its tip (not possible for a shroudless rotor). Therefore, when the released platform is caught between the casing and the following blade, a shrouded bladed rotor hammers the fragment into the casing, due to the stiffness of the remaining blades, still attached to the disc, and in contact with each other. A shroudless blades rotor interacts differently with the fragment enforced into the casing, at individual blade level, hence encountering a much smaller resistance from the following blades (still attached to the disc). Although part of the intended research objectives of this current work, due to time limitations, this was not addressed and makes the object of future studies as mentioned in the recommendations chapter.

As seen previously, the casing damage is caused by the compact feature of the fragment (such as platform fixing). Accordingly, the impact area (which delimits the volume of material contributing to the membrane stretching and plastic bending), as well as its perimeter (for the shear case), are proportional with the fragment footprint at the end of the impact phase. Even if the impact initiates with a corner of the platform, the released fragment rolls over the casing, driven by the following blades, in the search for its stable equilibrium. For estimating the impact area, Method 1 assumes it as being the circumferential length corresponding to one blade pitch, multiplied by an axial distance. Regarding this axial distance, different manufacturers are estimating it function of the blade chord, which in the case of a shrouded blade, might not be that relevant. Also, this axial dimension (chord length) is usually increased by a certain percentage, specific to each OEM. As this research revealed that the damage to the casing is caused by the bulky feature of the blade fragment (the blade platform and shank towards the firtree), the approach proposed by this research is to consider the geometry of that feature (as shown in Figure 4.20) instead of the airfoil dimensions.

Experimental data and FEA results revealed a close to circular shape of the impact area. As minimizing the impact area is a conservative approach, this research proposes to estimate the impact area as the area of a circle defined by the minimum of the two dimensions (circumferential length C, or the axial length of the platform w).

The circumferential length C is $C_{JT3D} = \pi \cdot {}^{D_{JT3D}}/_{n_{JT3D}}$, respectively $C_{JT8D} = \pi \cdot {}^{D_{JT8D}}/_{n_{JT8D}}$, n being the number of blades, w the axial lengths of the blade platforms.

$$A = \pi \cdot \frac{\min(C, w)^2}{4} \cdot \alpha \tag{4.17}$$

Also observed during FEA, this area needs to be further reduced, accounting for the platform overhang upstream and downstream (which might deform). From FEA it was determined a proportionality coefficient α of 95%.

The shear perimeter P is proportional with the fragment footprint:

$$P = 2 \cdot (h + w) \cdot \beta, \text{ geometry shown in Figure 4.20,} \tag{4.18}$$

As for the area, a correction needs to be applied to the perimeter, as the blade does not impact the casing with its entire footprint; the coefficient b was determined from FEA as being 50%.

Continuing the development of the design analytical equation, the plastic strain energy can then be expressed function of the two failure modes:

- Tensile

$$PE_{tensile} = A \cdot \varepsilon \cdot \gamma \cdot \sigma_0 \cdot \delta \cdot \mathrm{t} \tag{4.19}$$

- Shear (plugging)

$$PE_{shear} = K \cdot P \cdot \tau_D \cdot \theta \cdot t^2 \tag{4.20}$$

Where t is the casing thickness, and the correction coefficients applied to each member of the equations, are further detailed.

For the tensile mode of failure, as the impact occurs at a strain rate different than the quasistatic, a coefficient γ accounts for this factor (in this case, 59.2% of the 0.25 elongation at break). Similarly, as the stress flow was expressed using its simplest formulation (average between the yield and ultimate engineering stresses at quasistatic), the factor δ accounts for the flow stress at the impact strain rate (600 s^-1), in this case $\delta = 0.849$.

The shear failure mode considers the dynamic shear strength, corrected with a factor θ of 0.9, corresponding to the ratio of shear stress at the strain rate over the shear stress at quasistatic.

The threshold thickness determining the transition from the tensile to shear failure mode is therefore based on the fragment geometry, and can be expressed as:

$$t_{th} = \frac{A \cdot \varepsilon \cdot \gamma \cdot \sigma_0 \cdot \delta}{K \cdot P \cdot \tau_D \cdot \theta} \tag{4.21}$$

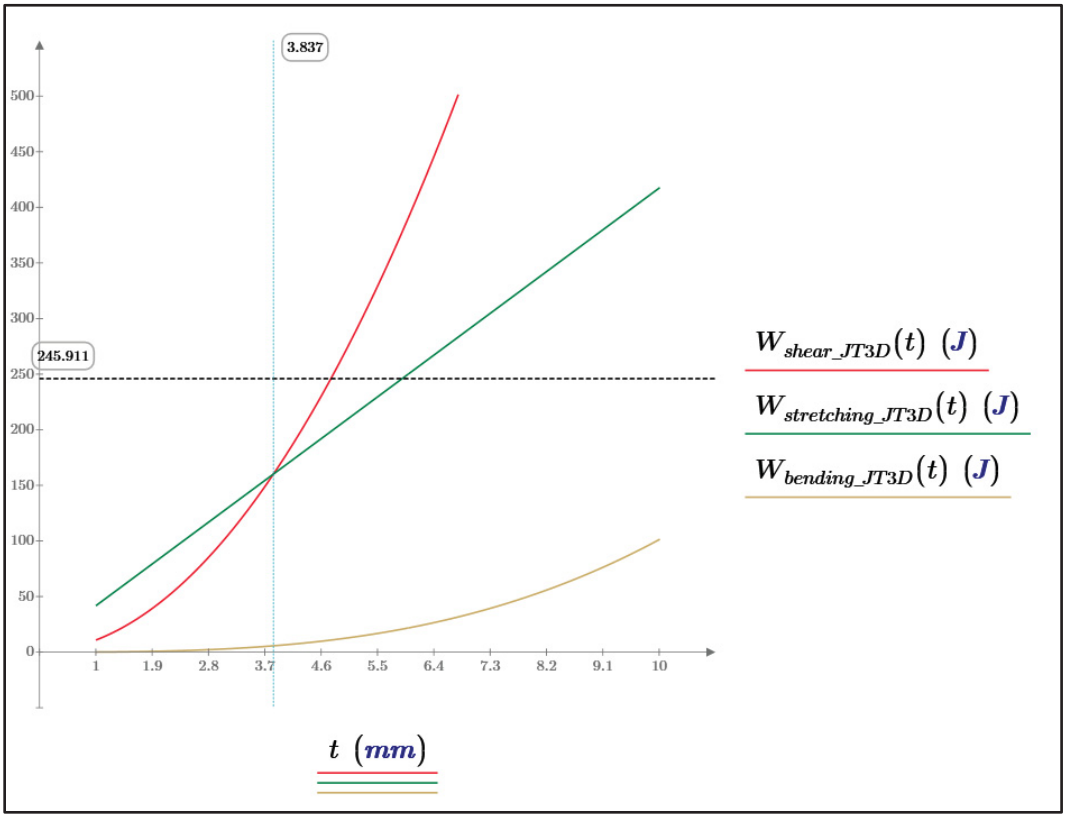

Figure 4.23 Threshold thickness for the JT3D blade fragment

For JT3D fragment, the threshold thickness was determined as being 3.837 mm, and for the JT8D blade fragment, $t_{th} = 3.868$ mm. Expressing the energies for this thickness, JT3D blade fragment can develop an energy of 160.139 J, and JT8D fragment 198.528 J. Comparing with the 6% of the initial kinetic energy ($KE_{fract\ JT3D} = 245.911\,J, KE_{fract\ JT8D} = 202.803\,J$, both engine fragments are situated in the shear failure mode, as can be observed in Figure 4.23 (only JT3D curves shown). It is observed why past the threshold value, the shear method becomes the optimal method.

Hence, for both fragments, the optimum design failure mode becomes shear. The casing thickness can therefore be determined equating the shear formulation with the kinetic energy fraction:

$$t = \sqrt{\frac{KE_{fract}}{K \cdot P \cdot \tau_D \cdot \theta}} \tag{4.22}$$

If the threshold energy is bigger than the KE fraction, then the optimum design mode is tensile, and the required thickness can be formulated as:

$$t = \frac{KE_{fract}}{A \cdot \varepsilon \cdot \gamma \cdot \sigma_0 \cdot \delta} \tag{4.23}$$

Consequently, the plastic strain energy selection function of the failure mode threshold (PE_{th}) and the fraction of the fragment kinetic energy, can be formulated as:

$$PE_{casing} = \begin{cases} PE_{tensile} & PE_{th} > KE_{fract} \\ PE_{shear} & PE_{th} < KE_{fract} \end{cases} \tag{4.24}$$

Therefore, the containment thickness can be expressed function of one of the two modes of failure:

$$t_{cont} = \begin{cases} \frac{KE_{final}}{A \cdot \varepsilon \cdot \gamma \cdot \sigma_0 \cdot \delta} \\ \sqrt{\frac{KE_{final}}{K \cdot P \cdot \tau_D \cdot \theta}} \end{cases} \text{for} \begin{matrix} PE_{th} > KE_{final} \\ PE_{th} < KE_{final} \end{matrix} \tag{4.25}$$

Using the above relations, for $K_{exch} = 0.06, \alpha = 0.95, \beta = 0.5, \gamma = 0.592, \delta = 0.849 \; and \; \theta = 0.9$, the thicknesses are $t_{shear\ JT3D} = 4.755\ mm, t_{tens\ JT3D} = 5.892\ mm, t_{shear\ JT8D} = 3.909\ mm, t_{tens\ JT8D} = 3.951$ mm (details in APPENDIX IV, Figure-A IV-1).

As determined that the shear mode is to be considered, based on the geometries considered, and on the exchanged energy of maximum 6% of the total translational kinetic energy of the blade fragment, the thicknesses necessary for containing the blade fragments for JT3D is 4.755 mm, and for JT8D is 3.909 mm, both validated with the test and FEA.

Resuming the previously discussed, the analytical method for determining the containment thickness for gas turbines casings, during preliminary design, can be formulated as follows:

1. Determine the blade platform dimensions affecting the containment area *h* and *w* (as per Figure 4.20); select the number of the blades (both determined during the advanced design phase of the project)
2. Assume the nominal diameter of the casing D; determine the circumferential length of the impact area
3. Calculate the impact area and perimeter using (4.17) and (4.18)
4. Obtain the casing material characteristics ($\sigma_{0.2}$, UTS, ε, τ_d) at quasistatic, and at the highest strain rate; determine coefficients α, β, γ, δ, θ and σ_0
5. Resolve equation 4.21 for determining the shear threshold (t_{th})
6. From (4.16) establish the plastic energy function of the fragment kinetic energy KE_{fract} and expressing the fragment translational kinetic energy as $KE_{blade} = \frac{I \cdot \omega^2}{2}$

7. Using the determined t_{th} calculate PE_{casing} using either equations (4.22) or (4.23), and compare it with KE_{fract}
8. Calculate the minimum thickness for containment (t_{cont}) by solving the equation (4.25)

4.6 Summary

This chapter is dedicated to assembling a novel analytical method for designing gas turbine casings from rotor blade fragment containment perspective. The timeline of the containment process was presented, and its distinct phases were detailed based on information from the public domain, as well as from finite element analyses performed during this research. As observed during the FEA, the main damage to the casing is caused by the bulky section of the fragment, regardless of if the contact is direct or indirect with the casing. A particular case of a single blade fragment was selected (the shrouded blade), as it is more damaging to the casing than the unshrouded blade fragment, due to the circumferential stiffness of the shrouded blades rotor. Also, the geometric characteristics of the fragment influencing the casing containment capability were identified.

An in-depth review of the possible failure mode associated with the containment problem was also provided in this chapter. The ballistic perspective provided details regarding the parameters to be considered in the containment calculations, and out of the multiple modes, it was evidenced that mainly the shear and tensile (membrane stretching) are the most important failure modes to be considered. Although the bending mode becomes important, its effect up to the threshold point is relatively small, hence for the design method it can be neglected. A threshold marking the transition from tensile to shear was determined function of the fragment geometry.

Subsequently, a few existing similar analytical methods were presented, with advantages as well as opportunities for improvement. It was shown that most of these analytical methods are considering only one mode of failure, which in some cases might not be the optimum. Also, the parameters considered in these equations need some further corrections for improved accuracy.

In the last section of this chapter is proposed a novel approach, better suited to the single blade fragment containment. This improved approach is based on function of the threshold of the failure modes. Additional corrections to the parameters of the equations are proposed, accounting for the percentage of energy exchanged by the blade fragment with the casing only, correcting the impact area geometry, and adjusting the material mechanical properties function of the strain rate. An analytical procedure is proposed to address the gas turbine casings design during the early phases of the project, to address the containment of a single blade fragment released from a turbine rotor as consequence of a rotor failure.

This new, proposed method incorporates details about the possible failure modes of the casing, establishes the threshold between the failure modes and proposes newer alternatives for the preliminary design methods, alternatives including factors not previously accounted for.

CONCLUSION

The objective of this current research is the development of a new analytical method to be used for designing the gas turbine casings to resist impact from rotor fragments, during early phases of design when the detailed geometry is not yet determined. The development of this method is based on finite element analyses correlated with test data. As mentioned previously, this method incorporates details about the possible failure modes of the casing, establishes the threshold between the failure modes and proposes newer alternatives for the preliminary design methods, alternatives including factors not previously accounted for.

As multiple aspects were investigated during the method development, the relevant conclusions are presented accordingly in each designated section of this chapter.

Gas turbine fragment containment

As presented extensively in several chapters of this work, the fragment containment constitutes a primary area of interest for gas turbine manufacturers, especially in the aerospace sector. However, currently there are not many studies detailing the blade rotor fragment impact event identifying the distinct phases of this process. This research revealed the timeline of this impact event, the commonalities and differences between different stages, modules, and fragment type.

A first observation is concerning the first impact, regardless of the type of blade (shrouded, or shroudless): the first impact, when all the translational kinetic energy of the fragment is available, is not that detrimental to the casing but to the blade fragment itself. Only a small amount of that translational kinetic energy is transferred to the casing, causing a small, localized deformation. Subsequently, an important amount of energy is exchanged with the following blades through two interfaces (load paths): one contact between the shroud of the following blade (still attached to the disc) and the airfoil of the released fragment, and the second interface between the airfoil of the following blade and the platform of the released fragment.

The released blade is still in contact with the casing and therefore exchanging energy, however this exchange does not create localized damage on the casing, but on the released blade fragment and to the following blades. This second phase of the impact phenomenon ends when the blade fragment impacts with its root (or platform) and is pushed into the casing by the following blades. A difference is observed between the shrouded and shroudless blades: as all blade shrouds are in contact, the rotor develops a circumferential rigidity (blades in contact will act unitarily, like a wagon wheel), which is mostly responsible for the casing damage, as it is through the following blade shrouds that the remaining fragment is pushed into the casing. The shroudless blades are suffering a more important damage, as they do not benefit of a circumferential stiffness. Hence, the energetic exchange is different during the second impact, and this aspect is relevant for determining the energy exchange coefficient.

Understanding the overall fragment containment phenomenon is paramount for determining the governing equations (from kinematic and dynamic considerations), but not enough, as some aspects need further understanding, particularly the understanding of the failure mode, which is provided by the ballistic perspective.

Fragment containment ballistic considerations

Considering the ballistic aspects, this research revealed the types of failures to which is possibly subjected the casing when impacted by a rotor fragment. The different modes of failure were identified, and the transition between them was noted. As seen previously, the failure mode of the plate is in function of the plate thickness, and that the bending + tensile modes are the most efficient for energy absorption, until a critical thickness, from which the shear mode becomes predominant. This shear mode is triggered by a specific resistance of material, thick enough to oppose locally to the advancement of the projectile. At the shear perimeter, adiabatic shear bands (ASB) are formed, allowing the advancement of the projectile with dislocating the material along the impact perimeter.

The bending mode is not that significant up to the thickness threshold, and increases rapidly after higher values of thicknesses, however the shear mode will still be predominant, hence in this research the bending mode was ignored.

Further development was brought to the definition of the analytical equations for the fragment containment method, as the parameters to be used were identified, as well the method to identify the failure mode threshold. As the rotor fragment impact occurs at sub-ordnance range of velocities, this thickness threshold is function only of the fragment geometry.

The current methods used by the different gas turbine manufacturers employ different variations of these determined equations. It was seen that most of these existing equations are based on the shear mode of failure, which is not the optimum method from energy absorption. However, from a structural integrity perspective, even if for containment reasons the recommended thickness determination is based on the membrane stretching mode, the same casing needs to withstand other operation conditions requiring a thickness beyond the shear threshold. Hence, large engines manufacturers possibly focused on this failure mode based on their acquired knowledge, compared with smaller engines manufacturers who are usually designing casings with smaller thicknesses, more optimized for the membrane stretching failure mode.

Another improvement proposed by this research focuses on the impact area and perimeter, which brings more accuracy to the method. Some works considered a rather rectangular shape of the impact area, and others did not provided details with regards to it. In addition to detailing the impact area geometry (area and perimeter), correction factors are proposed to the material properties to account for the strain rate generated during the impact.

These correction factors were revealed by finite element analyses, correlated with test results. By providing the reasoning behind the analytical formulation, this research opens the path for further consideration in new studies for engine manufacturers and academia, as it will be mentioned in the next section.

Method validation with FEA and tests

As mentioned, the correction coefficients, including the energy exchange coefficient were revealed with the help of finite element analysis, which in turn was validated with testing. Two series of tests were selected for this research, tests performed on casings for aerospace engines deemed representative for large gas turbines (Salvino, DeLucia, & Russo, 1988). Each series of tests demonstrated the containment capability of casings of different thicknesses, and fragments released at different velocities. For both engines (JT3D and JT8D), the containment thickness was 0.187" (4.750 mm). An observation needs to be made about the 0.187" contained thickness, as the report mentioned however for JT3D the thickness of 0.250" in the conclusion and summary, however in the table showing the test results, the thickness of 0.187" shows containment. This study considered this thickness, as it looked to determine the exact containment threshold.

Another observation is about the kinetic energies reported in the test documents, as they were assumed correct, however no indication was provided on how those energies were determined. To obtain these energies, manipulations of densities needed to be operated, hence the recommendations detailed in the next section. However, regardless of the initial KE, the exchange coefficient (blade to casing) revealed consistently for all the analyses performed, as being lower than 10% (achieving containment).

As it was seen in the chapter III (FEA results), the material definition was provided by using the state-of-art Johnson-Cook model. This material included the stress and strain definition, as well as strain rate and temperature variation, and a complex damage failure surface, developed by performing simulations covering as much of the stress triaxiality – Lode parameter domain. The Split-Hopkinson bar testing as well as all specimen testing was replicated via simulations using the newly defined material, with satisfactory results providing confidence in the material model setup.

In addition to the state-of-art material definition, the FE model setup followed the guidelines suggested by the LS-Dyna Aerospace Working Group, which collected recommendations and best practices from representatives of the aerospace industry, under the initiative of FAA.

With employing these previously mentioned methods, the containment tests were successfully simulated. Additionally, the results of these analyses revealed the parameters needed in the analytical equation.

During this research work were performed about 700 various transient analyses, both explicit and implicit, for different configurations and components, and different mesh sizes. Even after all these analyses, some FEA aspects would still require development. All data used in this research were obtained from the public domain, and some aspects showing differences (for example the A-286 stress-strain curves at quasi-static), however assumptions were made and stated for further addressing in subsequent studies, as mentioned in the next section. These future considerations will only increase the accuracy of this proposed method, not modify its content.

In conclusion, this research proposes a novel approach for the development of an analytical method to be used in the early stages of design of gas turbine casing. This method determines the casing minimum thickness to withstand the impact from a blade fragment released after a failure event and was determined with test simulations using best practices and state-of-art methods recommended in the aerospace industry.

RECOMMENDATIONS

Based on the multiple perspectives employed in this work, it is not exaggerated to state that each of the main aspects developed (ballistic, fragment containment and FEA test validation) can constitute a research subject on its own. Despite the impressive number of simulations, future research could further improve this research, by focusing on different aspects. Providing a common ground to the representatives from the aerospace industry or regulatory forums, might generate a concerted effort to the refinement of this proposed analytical method.

Fragment containment suggested future research activities

First recommendation is to get this proposed method tested for different scenarios, the wider the domain, the better understanding of its applicability. A confirmation or suggestion for improvements from small engine manufacturers (and APU manufacturers) can reveal how this method fares with higher rotational velocities, and with thinner casing walls. Industrial applications perspective will shed light on more massive components, where the blades failures and energy exchanges are different.

This methodology is proposed for the single blade fragment containment, although with some additions it can be applied to intermediate fragment containment. The basic phenomenon is common, the same type of failure modes will need to be considered, probably moving the threshold to the right of the domain, as the fragment dimensions increase compared to the casing thickness. For the intermediate fragment, the membrane stretching might become the predominant failure mode.

Due to the unexpectedly high effort for characterizing the Johnson-Cook material model, the unshrouded blade fragment containment was removed from the scope of this research. Also removed were the studies for conical casings containment, the influence of hoop-carrying features as reinforcing ribs, flanges, dog legs, or non-carrying structures effect on the fragment containment, such as seal segments, honeycomb, and other non-structural components. All these aspects should make the objects of further research.

As mentioned, the containment tests referred some KE values for the fragment, but no explanations were provided about how that KE was obtained. The validation of this analytical method with another set of tests would provide more confidence in the method results, thus strongly recommended. A video sequence of an actual test would also provide additional confirmation about the impact timeline.

Ballistic recommended future developments

Further research into the bending failure mode, and on the projectile indentation into the casing would add accuracy to the proposed analytical method. Also, research into the adiabatic shear bands (ASB) formation modelled with FEA can validate the failure mode of the casing.

FEA and validation with testing recommended future studies

Both blade fragment geometries were developed from public domain CAD data, therefore the accuracy of the FE models is debatable. As the focus of this research was on the casing failure, using this less accurate geometries was deemed acceptable. In addition to the blade geometry, future research should focus on the blade failure as well, for a more accurate determination of the energy exchanged between the blades.

The A-286 material testing data is relatively scarce. There were some assumptions made in this research that would benefit from further validation with testing.

APPENDIX I

SPLIT HOPKINSON BAR TEST SIMULATIONS

This section details the FE models and analyses results for the simulations of the individual tests reported in (Nicholas, 1980). These simulations validated the material curves input in the containment FEA, including the material failure criteria.

Two FE models were created based on the test specimen (Figure-A I-1) used in the Split Hopkinson Bar (SHB) series of tests, one with a coarser mesh (0.425 mm element size), and another one with a more refined mesh (0.118 mm element size). The coarse mesh model is used for faster iterations and comparisons with other tests simulations with similar mesh size. The refined model contains 56,280 fully integrated (element form TYPE 2) solid hexahedral elements and 60,420 nodes, as shown in Figure-A I-2. In the gauge section (0.350" length), the elements have an aspect ratio close to 1 and a length of 0.12 mm.

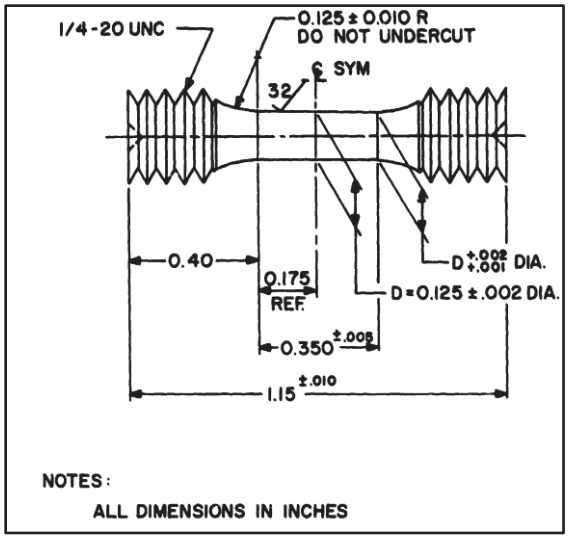

Figure-A I-1 SHB tests specimen
Taken from Nicholas (1980, p. 18)

The top and bottom nodes are contained in two different sets; bottom set of nodes blocked in all directions (translations and rotations), and the top set of nodes blocked all rotations, and translations in x and y directions, allowing the nodes to move only in z direction, with a velocity specific to the test simulated (for a strain rate of 4.4E^-4 /s, the velocity is input as a curve with the constant value of 0.0038 mm/s, from 0 to 50000 seconds).

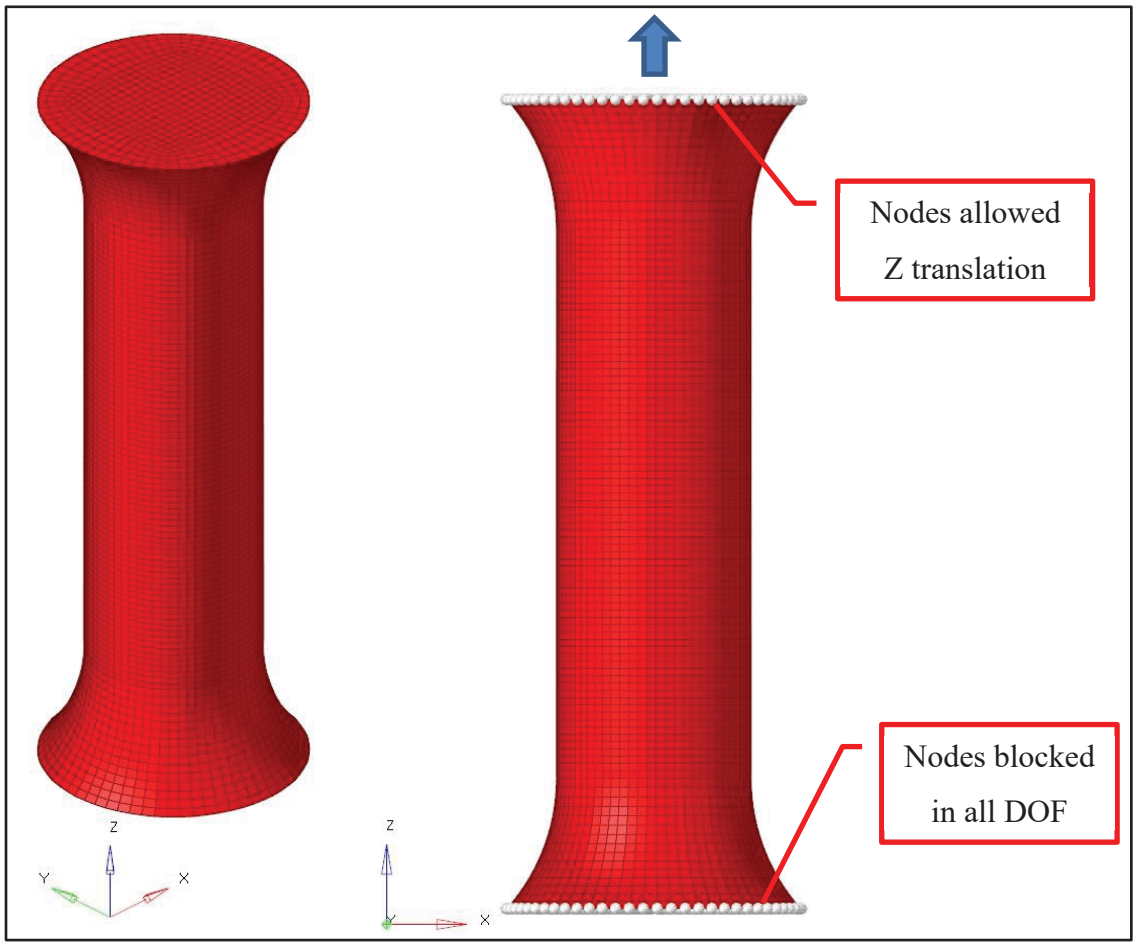

Figure-A I-2 SHP tests specimen FEM (refined mesh shown)

The material properties are considered as shown in Figure-A I-3, center column, referenced in (Kattus, Preston, & Lessley, 1958). The referenced YTS and UTS are slightly adjusted (as shown in Figure-A I-3) to create a smooth transition to the SHB test curve, in the early plastic region (Figure-A I-4).

	[ksi]	[Mpa]
E=	28600	197190.1
YTS =	96.4	682.655
UTS =	146.7	1021.461
$\varepsilon_{failure\ [\%]}$ =	0.25	0.25
$\varepsilon_{uniform}$ =	24.49	24.48
$n_{R\text{-}O}$ =	11.450	11.929

Increased by 18 MPa

Increased by 10 MPa

Figure-A I-3 Material properties considered for the quasi-static stress - strain curve

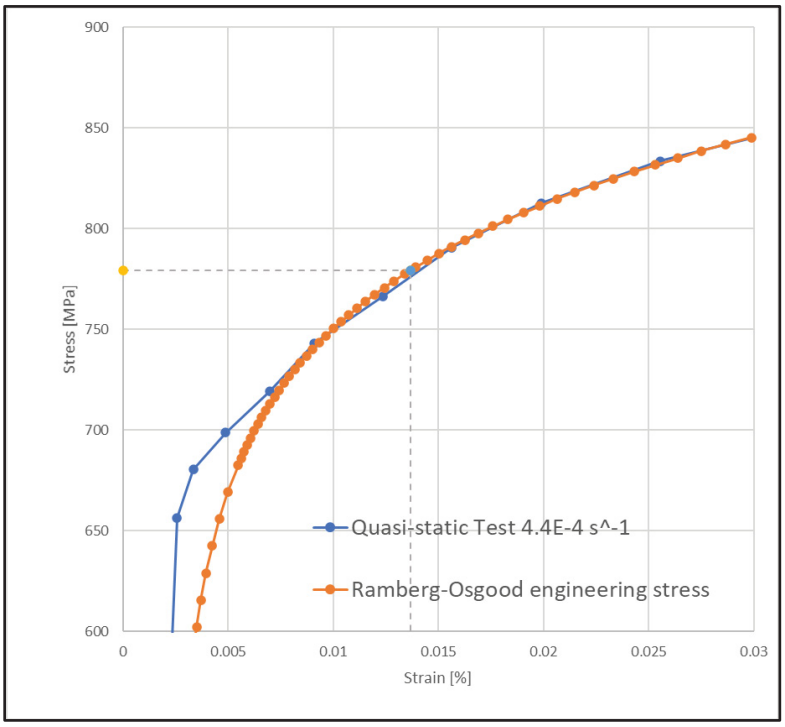

Figure-A I-4 Engineering stress curves

Past the estimated tangency point (or intersection), the engineering stress – strain curve continues with the plastic segment of the quasi-static test curve (considered to be the lowest strain rate data in (Nicholas, 1980), corresponding to the 4.4E-4 s^{-1}). The true stress – true strain curve is generated based on this combined curve, and the necking point is determined at the intersection with its own derivative (tangent modulus), as shown in Figure-A I-5.

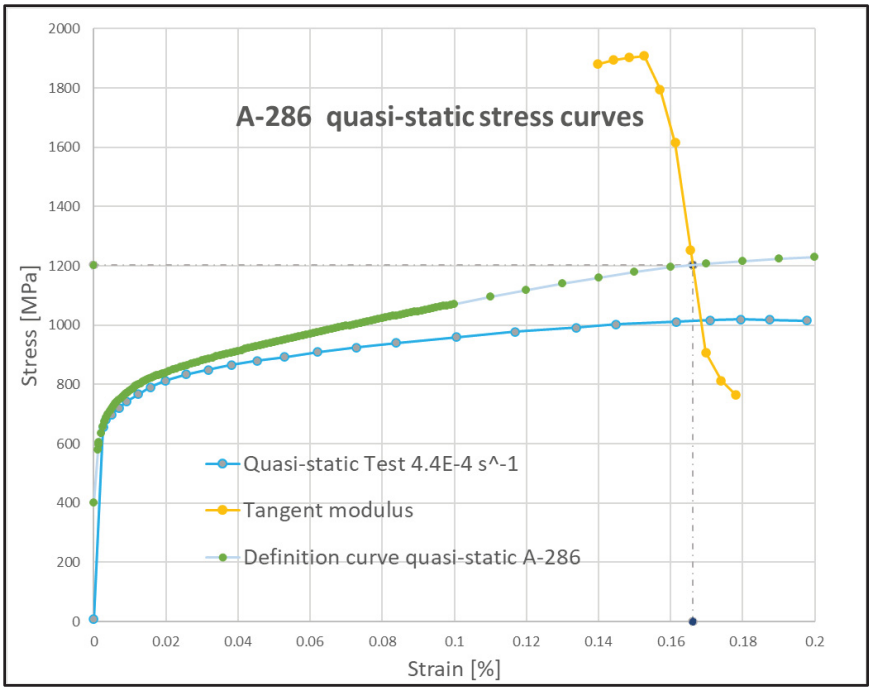

Figure-A I-5 Quasi-static stress and true stress curves

Past the necking point, a series of curves are extrapolated for different hardening coefficients (Figure-A I-6, left image). Iterative analyses are confirming that the curve extrapolated with the index n=0.04 matches the test curve (right image in Figure-A I-6).

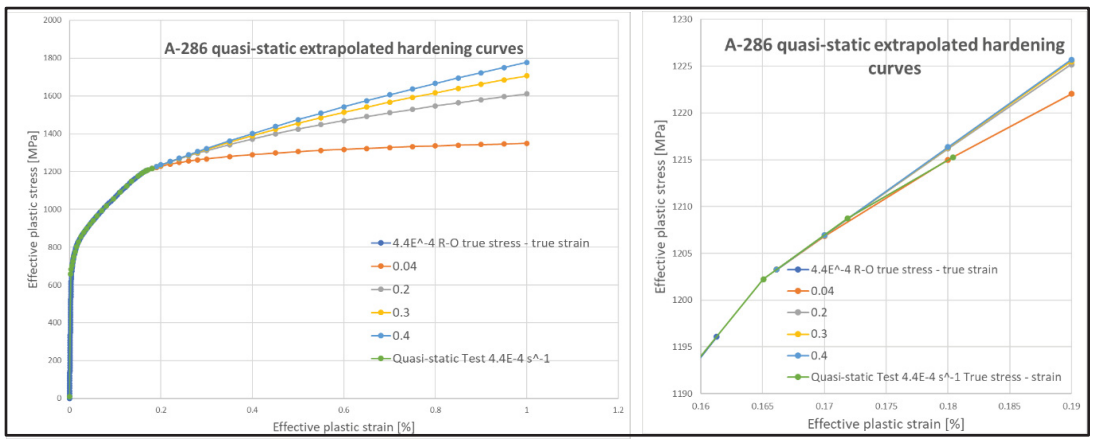

Figure-A I-6 Extrapolated extensions of the quasi-static curve

The elastic portion of the curve is removed from the extended true stress – true strain curve, and the resulting effective plastic stress – effective plastic strain quasi-static curve is loaded in the material card (*MAT_024) of the Split Hopkinson Bar (SHB) test simulation, under the defined curve with id 1111 (complete material card shown in Figure-A I-7).

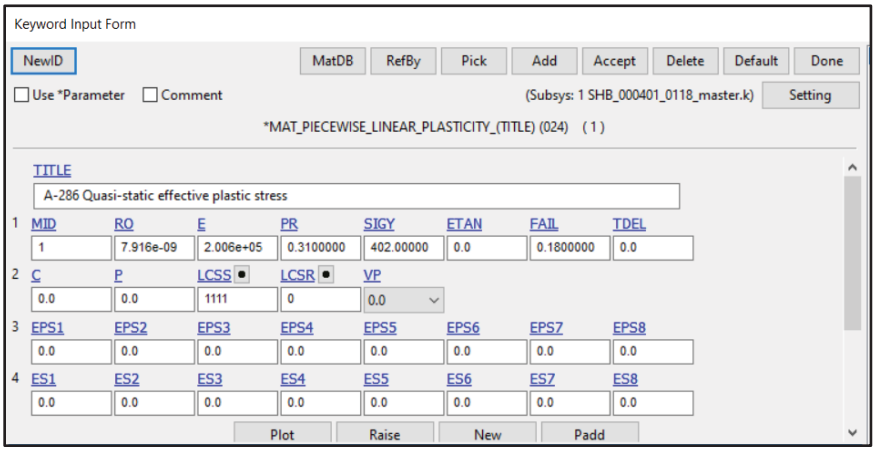

Figure-A I-7 *MAT_024 quasi-static material card

Apart from the 1200°F test simulation, all analyses are coupled (thermo-mechanical), 293K being selected as initial temperature. An isotropic thermal material is defined corresponding to the thermal properties for A-286: the specific heat of 0.42 $^{J}/_{g \cdot {}^{\circ}C}$ = 1.434E+6 $^{mm^2}/_{s^2 \cdot K}$ and a thermal conductivity of 15.1 $^{W}/_{m \cdot K}$ = 15.1 $^{tonne \cdot mm}/_{s^3 \cdot K}$.

At least one cross section is defined in all the specimen models (Figure-A I-8, left), allowing the reading of the resultant force during loading. In addition to the cross sections, several sets of nodes (Figure-A I-8, right) are also tracked during the simulation, their displacements serving to determine different parameters such as the gauge and a virtual extensometer (two nodes spaced vertically at 4.0 mm distance) elongation, the diameter (including the necking) ultimately leading to the determination of the true stress – true strain curve of the specimen.

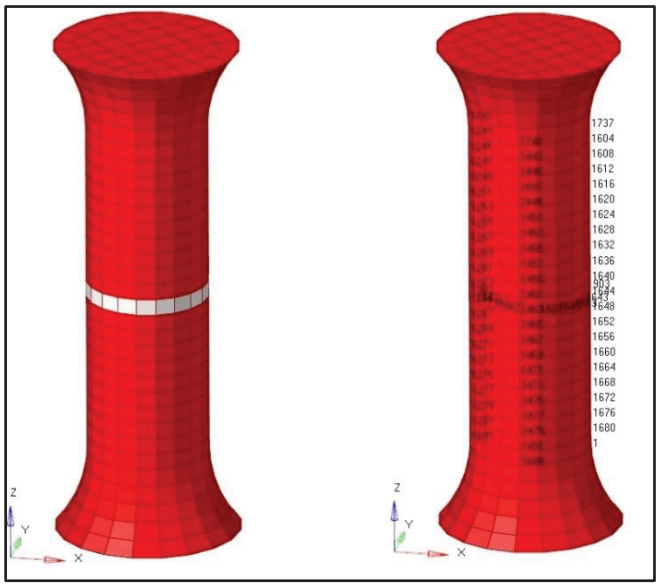

Figure-A I-8 Coarse meshed model - cross section (left)
and set of nodes tracked (right)

After iterative runs (varying the hardening coefficient, loading velocity and the elemental failure strain), the specimen failure (Figure-A I-9) is reached at the desired strain rate (the elemental failure modified to 0.1778); the results of the simulation are shown in Figure-A I-10 and Figure-A I-11.

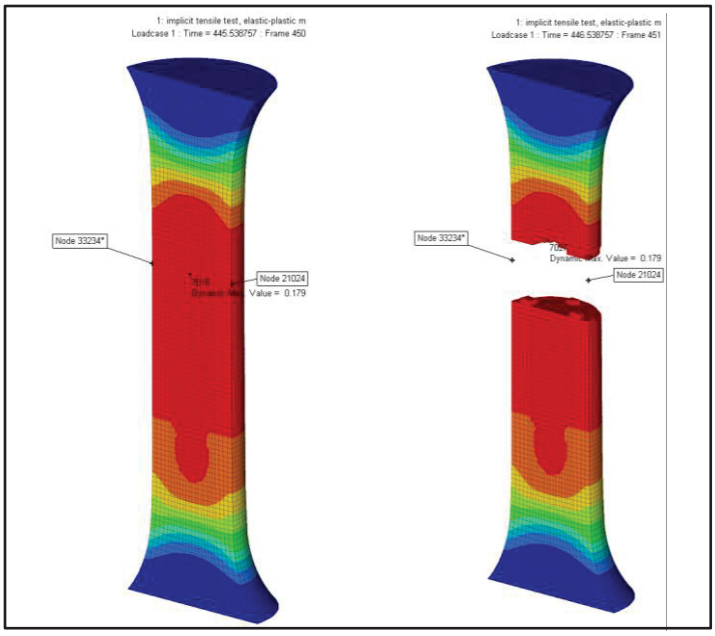

Figure-A I-9 Fine mesh specimen before fracture (left) and
after fracture (right) at a strain rate of 4.4E-4s^-1

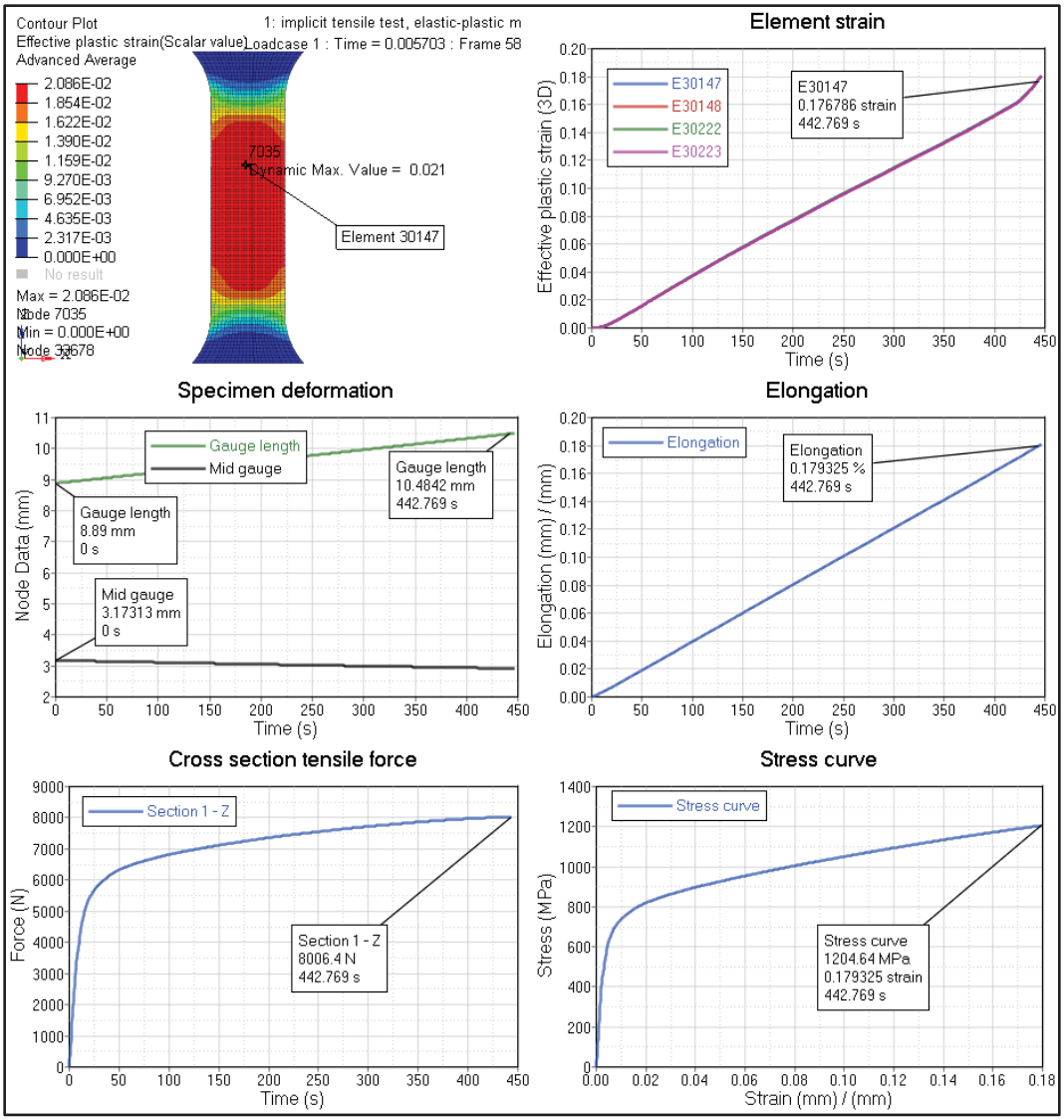

Figure-A I-10 Simulation results specimen testing at 4.4E-4 s^-1 strain rate, refined mesh

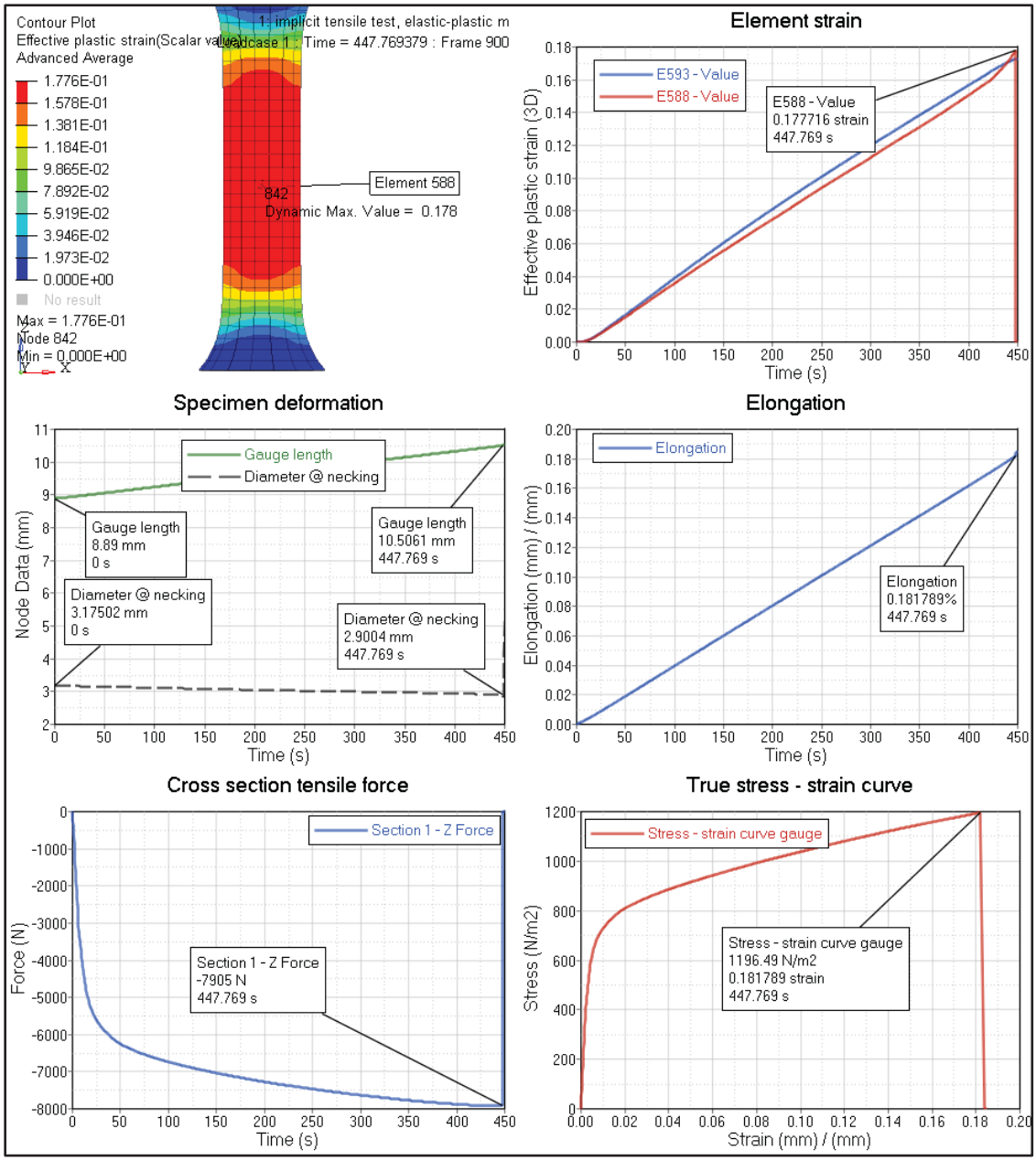

Figure-A I-11 Simulation results specimen testing at 4.4E-4 s^-1 strain rate, coarse mesh

Small differences are observed between the two sets of results (coarse vs refined mesh). These are due to the different elemental response to the loading based on the element size. For *MAT_024, the adjustment is done at the elemental failure strain (EFAIL param).

The stress – strain curves extracted from the results are in good agreement with the true stress – true strain curve processed from the SHB test at 4.4E-4 s^-1 from (Nicholas, 1980) (Figure-A I-12).

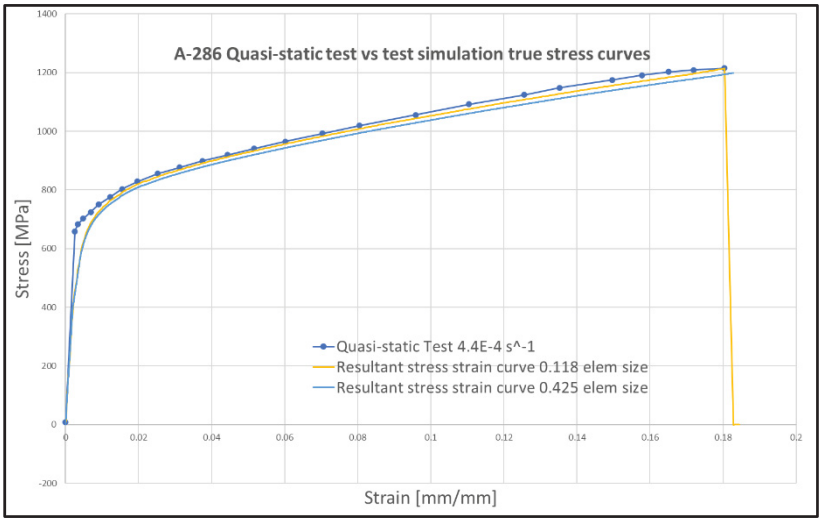

Figure-A I-12 Comparison of test stress curve with the resulting stress curve

The same approach is applied to the 4.4 s^-1 sample as for the 4.4E-4 s^-1 sample simulation. The YTS and UTS stress values from (Kattus, Preston, & Lessley, 1958) are modified such way (Figure-A I-13) to create a smooth transition to the test curve, at the beginning of the plastic domain (Figure-A I-14).

	[Mpa]
E=	197190.1
YTS =	686.655
UTS =	1269.461
$\varepsilon_{failure\ [\%]}$ =	0.168
$\varepsilon_{uniform}$ =	16.16
n_{R-O} =	7.147

Increased with 22 MPa

Increased with 258 MPa

Figure-A I-13 Material properties used to generate the Ramberg engineering stress curve simulating the 4.4 s^-1 strain rate curve

From the intersection point of the test reported curve with the R-O curve generated with the modified values of YTS and UTS, only the test curve segment is considered, the remaining portion of the generated R-O curve is discarded (Figure-A I-14).

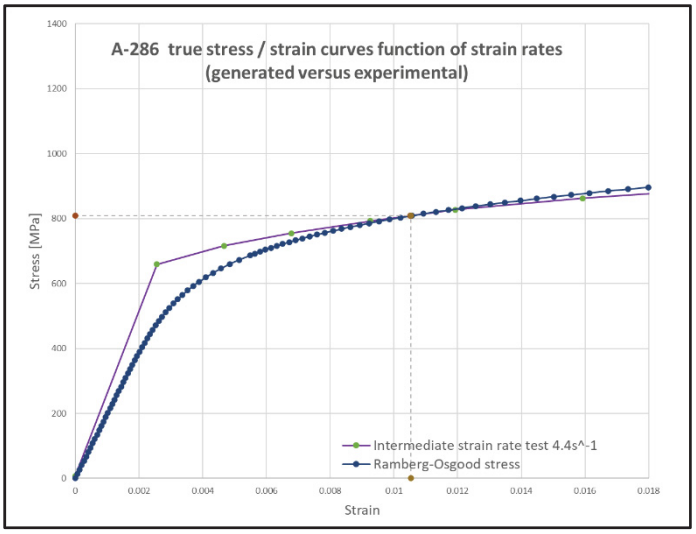

Figure-A I-14 Engineering stress curves corresponding to the SHB test at 4.4s^-1 strain rate

The engineering stress curve obtained by combining the two segments is used to determine the true stress curve corresponding to the strain rate of 4.4s^-1 (Figure-A I-15). As the SHB test curve does not show a necking behaviour, the last two points of the true stress curve are considered for determining the slope of the extension. The extrapolated curves hence continue tangent; iterations (varying the hardening coefficient) are performed for minimizing the eventual deviations from the definition curve.

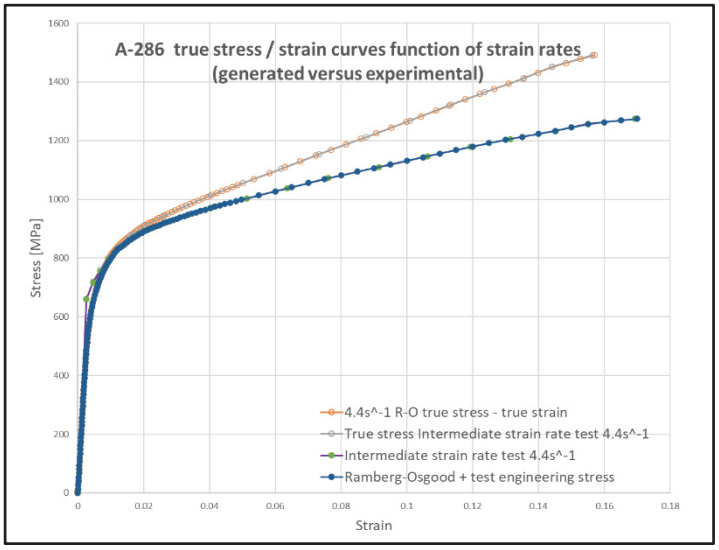

Figure-A I-15 Stress curves corresponding to the SHB test at 4.4s^-1 strain rate

The same two FE models used to assess the 4.4E-4s^-1 strain rate (first one having a coarse mesh to obtain a quick response, and another one with refined mesh to better capture the overall elemental response to the loading) were used to assess the 4.4s^-1 strain rate. The loading is done similarly as for the previous strain rate, by moving the upper set of nodes (Figure-A I-2), however the scale used is different, corresponding to a z translational velocity of 44.7 mm/s (1.490·30.00 mm/s, as shown in Figure-A I-16); the value of 1.49 is obtained iteratively.

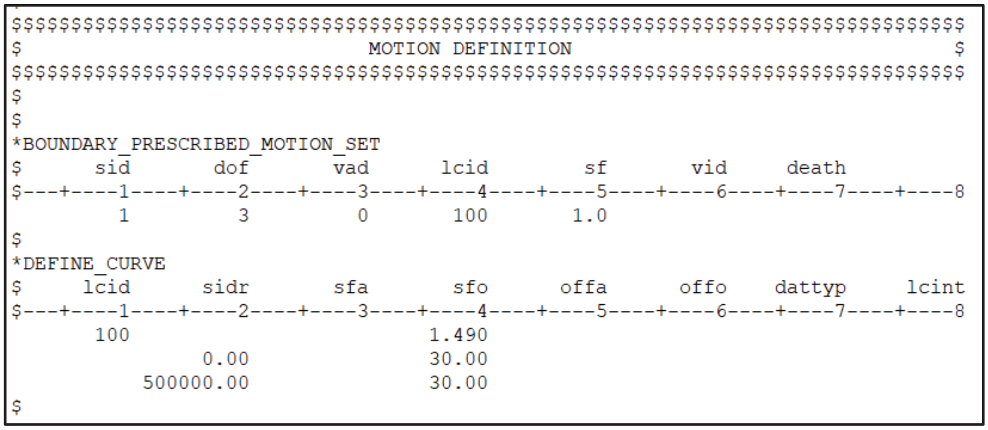

```
$$$$$$$$$$$$$$$$$$$$$$$$$$$$$$$$$$$$$$$$$$$$$$$$$$$$$$$$$$$$$$$$$$$$$$$$$$$$$$$$
$                             MOTION DEFINITION                                $
$$$$$$$$$$$$$$$$$$$$$$$$$$$$$$$$$$$$$$$$$$$$$$$$$$$$$$$$$$$$$$$$$$$$$$$$$$$$$$$$
$
$
*BOUNDARY_PRESCRIBED_MOTION_SET
$      sid       dof       vad      lcid        sf       vid     death
$---+----1----+----2----+----3----+----4----+----5----+----6----+----7----+----8
         1         3         0       100       1.0
$
*DEFINE_CURVE
$     lcid      sidr       sfa       sfo      offa      offo    dattyp     lcint
$---+----1----+----2----+----3----+----4----+----5----+----6----+----7----+----8
       100                         1.490
                0.00               30.00
           500000.00               30.00
$
```

Figure-A I-16 Motion definition corresponding to a strain rate of 4.4s^-1

As the last observed true strain value at the 4.4s^-1 strain rate is 0.1564, the elemental failure strains were modified iteratively, until reaching a specimen strain close to this value, for the two meshed FEM's (EFAIL set to 15.0% for the coarse mesh model, and 14.9% for the refined one).

The results from the two analyses are shown in Figure-A I-17 for the coarse mesh model, and in Figure-A I-18 from the analysis of the refined mesh model (Figure-A I-19). Also, the stresses obtained from the analyses are compared with the stress curve resulting from test and shown in Figure-A I-20. Small deviations are observed (4.38% for the coarse mesh, and 2.87% in the case of the refined mesh) but deemed acceptable. Further corrections are applied to the complete material definition (*MAT_224).

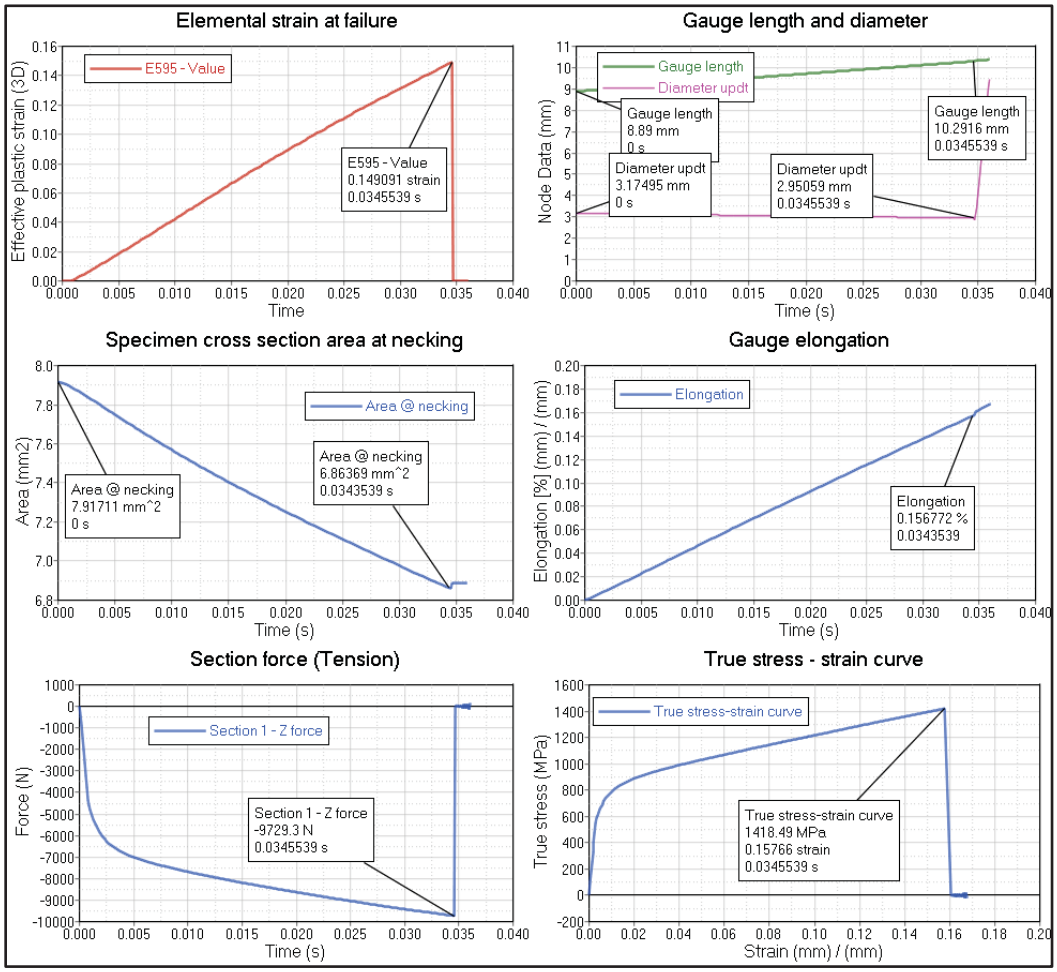

Figure-A I-17 Simulation results specimen testing at 4.4s^-1 strain rate, coarse mesh

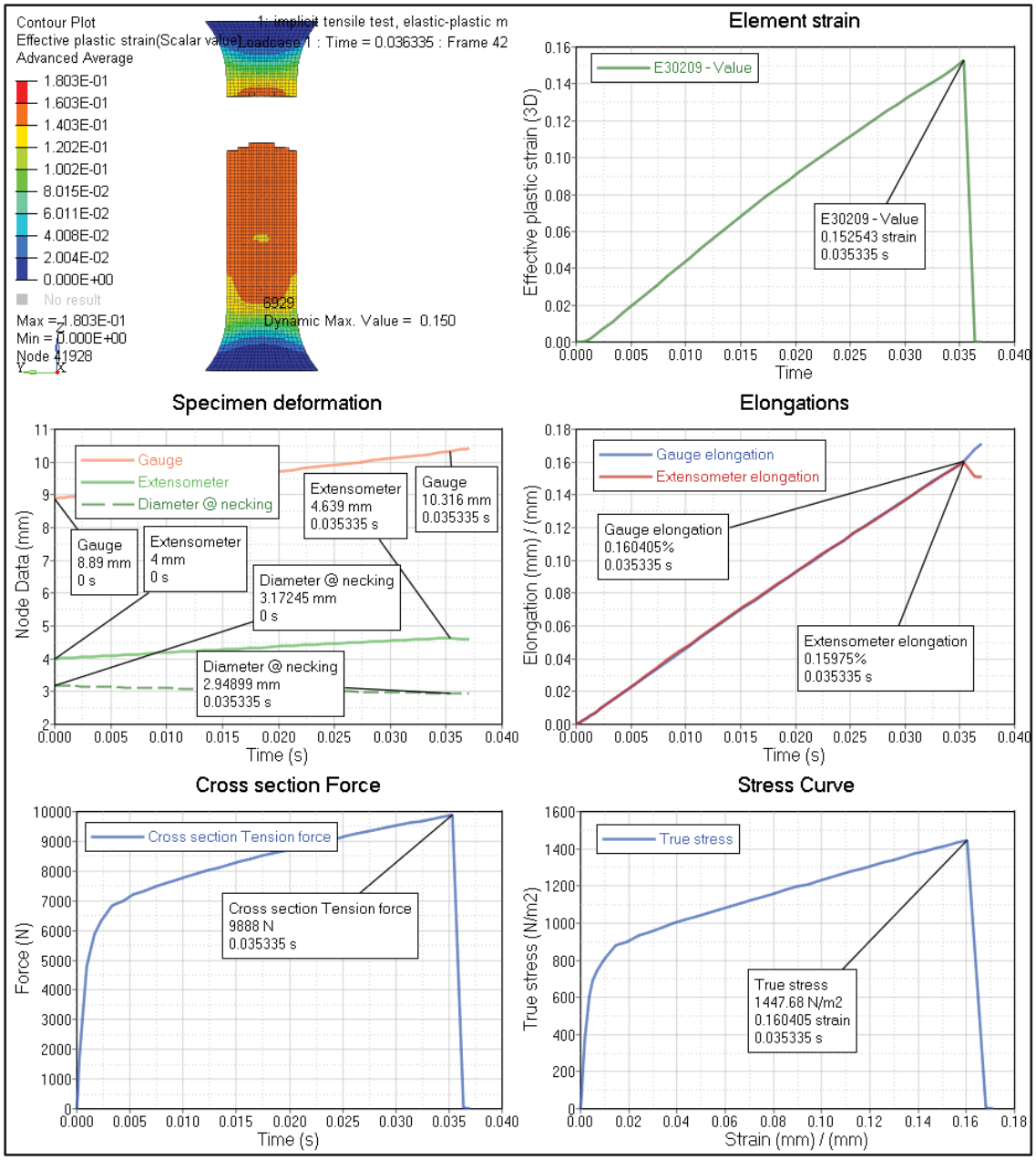

Figure-A I-18 Simulation results specimen testing at 4.4s^-1 strain rate, refined mesh

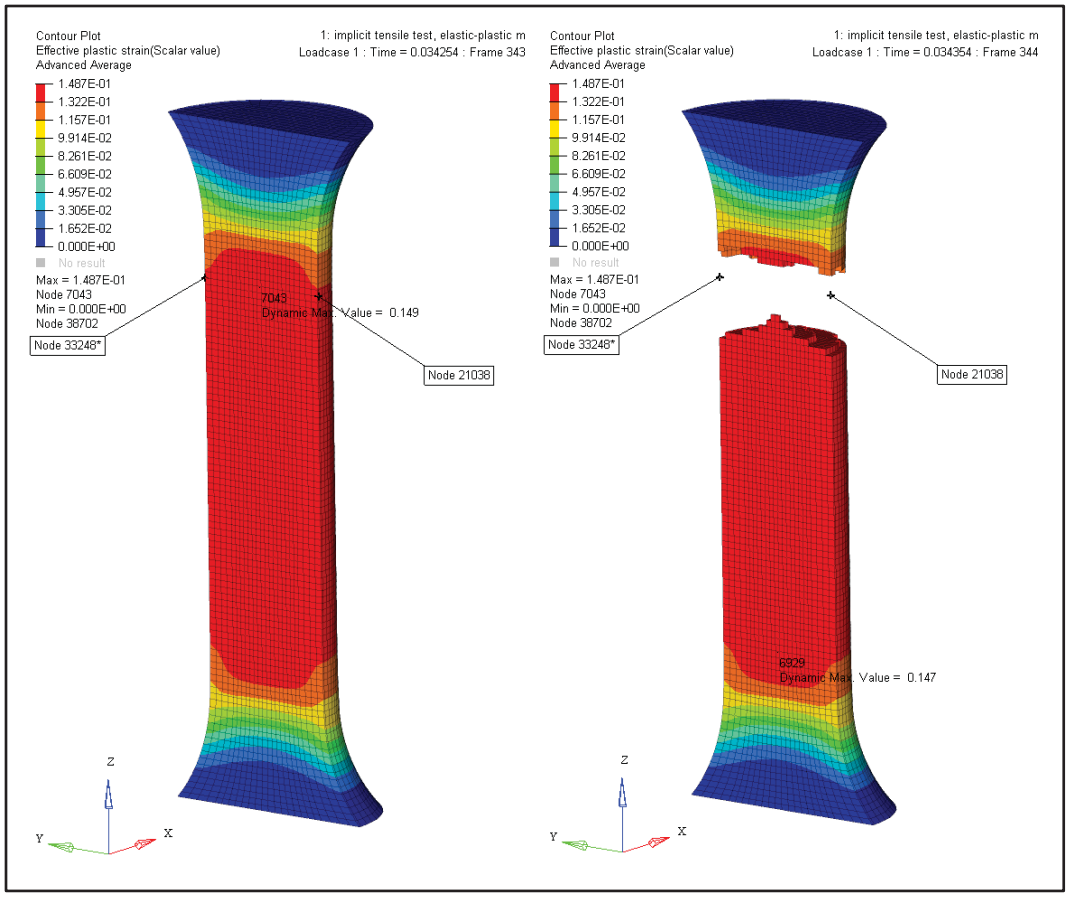

Figure-A I-19 Fine mesh specimen before fracture (left) and after fracture (right) at a strain rate of 4.4s^-1

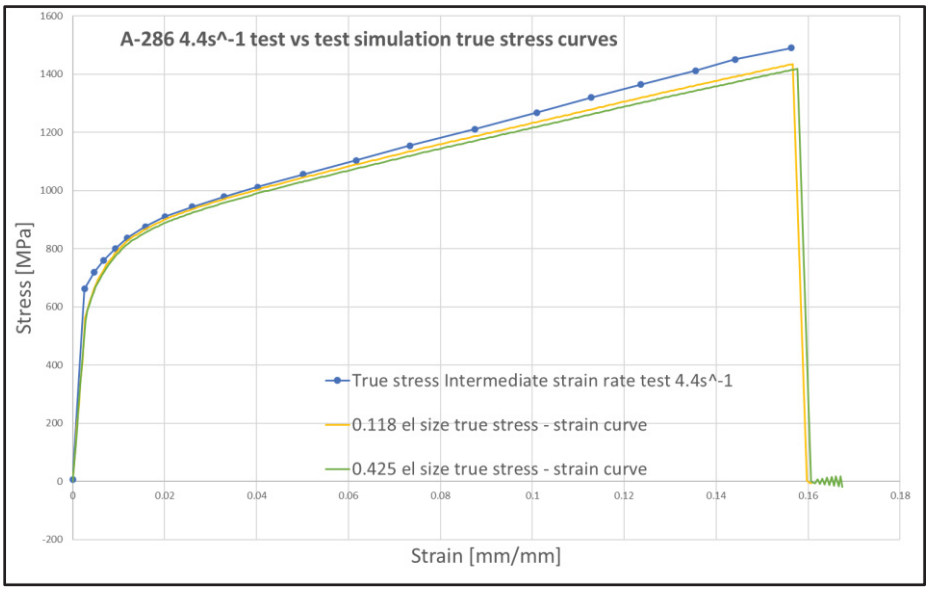

Figure-A I-20 SHB test at 4.4s^-1 true stress curve vs resulting stress curves

Similarly as for the previous strain rates (4.4E-4s^-1 and 4.4s^-1), for the strain rate of 600s^-1, an engineering stress – strain curve is generated using the Ramberg-Osgood method for the elasto-plastic domain, then this curve is continued in the plastic domain with the stress – strain curve from the SHB test. To generate a smooth transition to the test curve corresponding to the 600 s^-1 strain rate, the mechanical properties from (Kattus, Preston, & Lessley, 1958) are modified as shown in Figure-A I-21.

	reported in [80] [ksi]	modified [Mpa]
E=	28600	197190.1
YTS =	96.4	764.6546
UTS =	146.7	1361.461
$\varepsilon_{failure\ [\%]}$ =	0.25	0.148
$\varepsilon_{uniform}$ =	24.49	14.11
$n_{R\text{-}O}$ =	11.450	7.378

Increased with 100 MPa

Increased with 350 MPa

As reported in [79]

Figure-A I-21 Mechanical properties used for generating the R-O curve at 600 s^-1

The engineering stress curve at the strain rate of 600s^-1 is composed on the R-O curve up to the intersection point with the test stress curve, then the remaining segment from the test stress curve (Figure-A I-22).

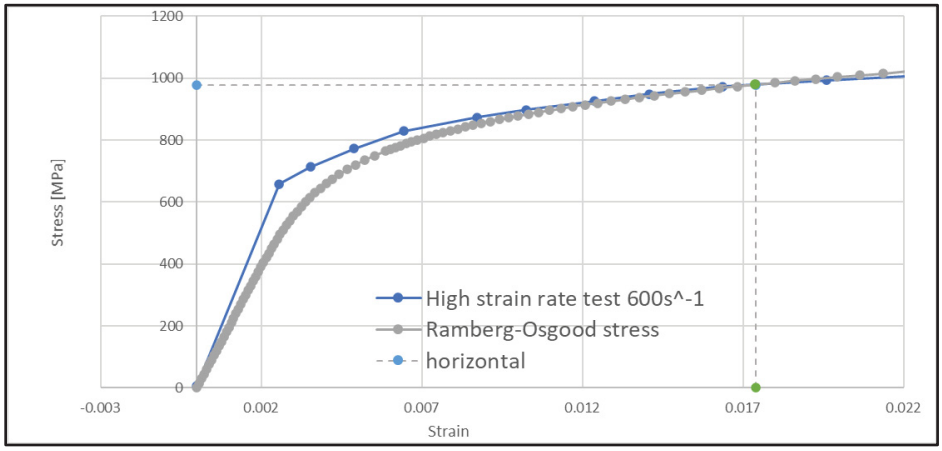

Figure-A I-22 Engineering stress curves corresponding to the SHB test at 600s^-1 strain rate

A true stress – true strain curve is generated from this previously determined engineering stress curve, and in absence of a necking point the last two known points are used to extrapolate the stress curve (curve shown in Figure-A I-23).

The extrapolation curve (Figure-A I-24) is selected based on the slope at the last point, corresponding to a hardening coefficient n=0.1.

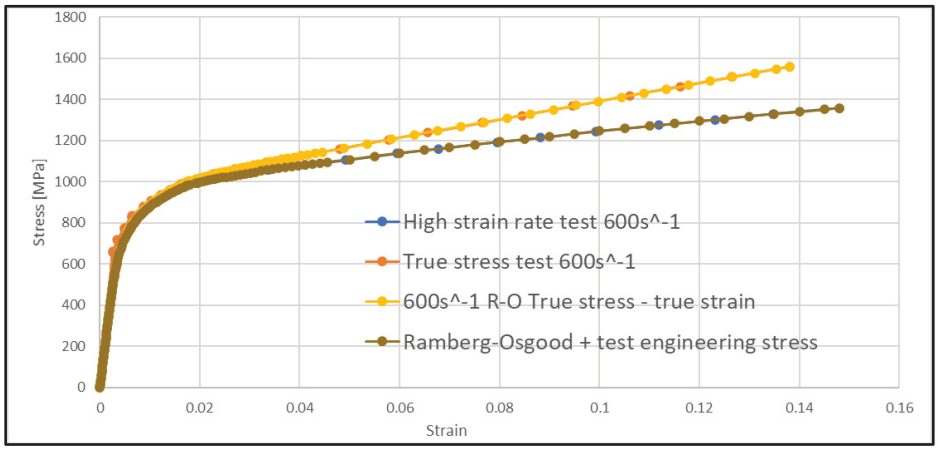

Figure-A I-23 Stress curves corresponding to the SHB test at 600s^-1

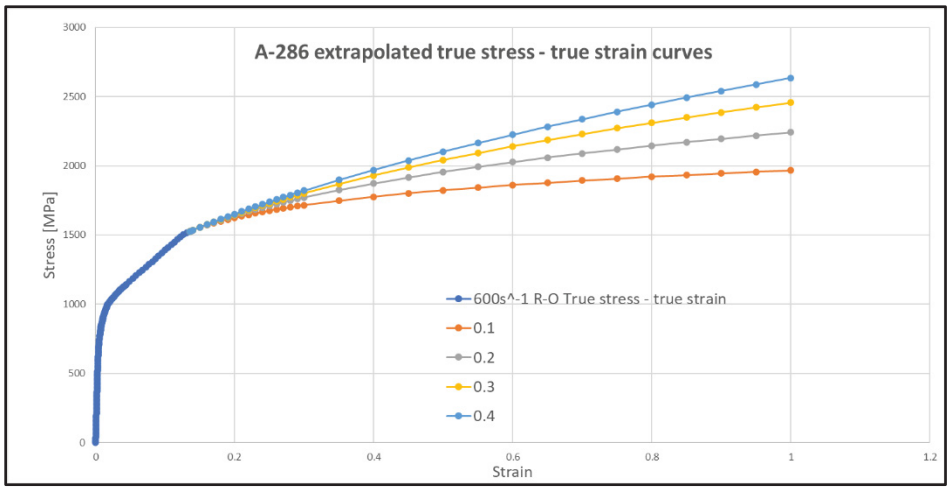

Figure-A I-24 Extrapolated true stress curves corresponding to a strain rate of 600s^-1

The motion is imposed with a curve defined as shown in Figure-A I-25 (scaling factor determined iteratively, until reaching the desired strain rate).

```
$
*DEFINE_CURVE
$     lcid      sidr       sfa       sfo      offa      offo    dattyp     lcint
$---+----1----+----2----+----3----+----4----+----5----+----6----+----7----+----8
       100                            1.17
                 0.00                5200.0
            500000.00                5200.0
$
```

Figure-A I-25 - Prescribed motion definition curve

The 600s^-1 strain rate simulation results are presented in Figure-A I-26 for the coarse mesh and in Figure-A I-27 for the refined mesh.

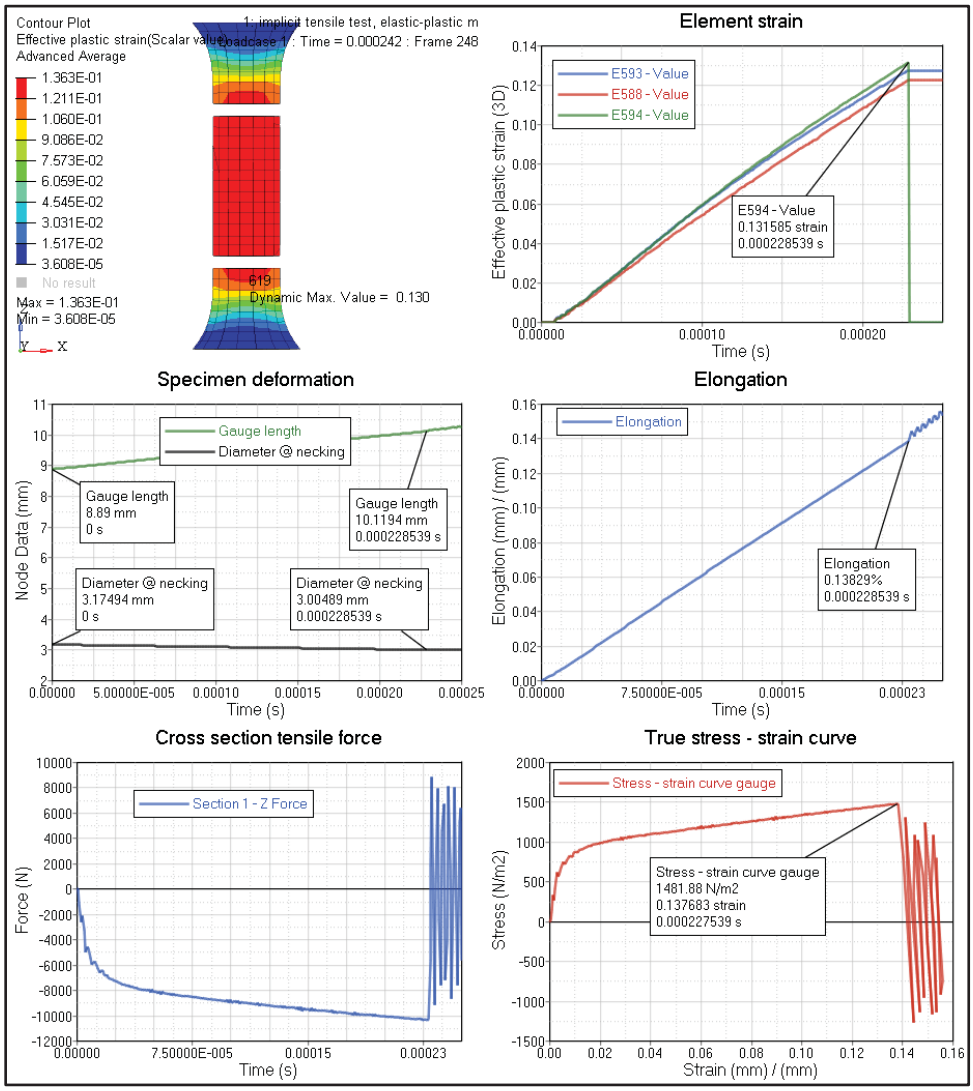

Figure-A I-26 Simulation results specimen testing at 600s^-1 strain rate, coarse mesh

The comparison of the true stress – true strain curves (determined from the simulations versus the test curve at 600s^-1) is shown in Figure-A I-28. A good agreement (3.6% difference) is observed between the curves (test compared with the simulations).

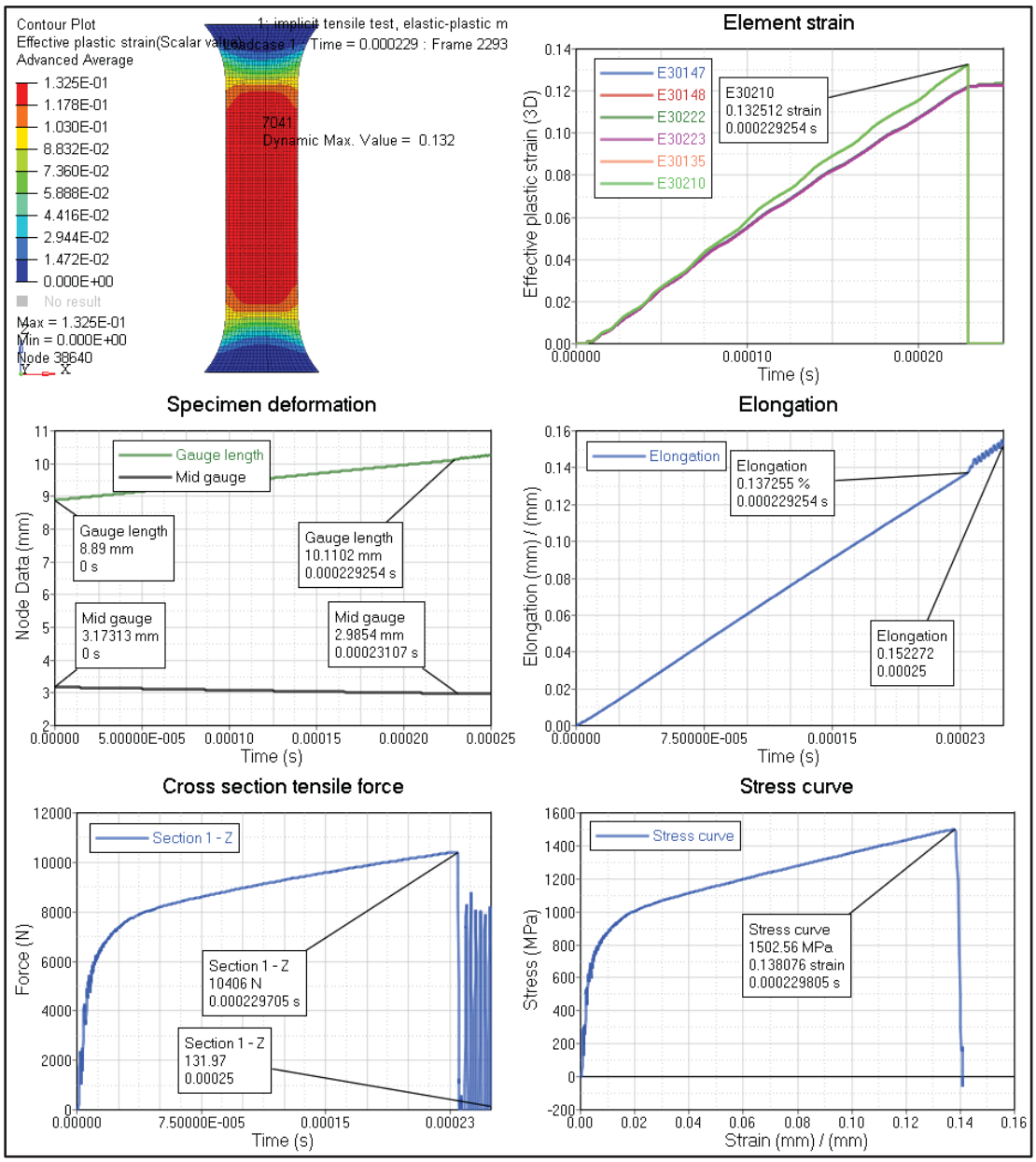

Figure-A I-27 Simulation results specimen testing at 600s^-1 strain rate, refined mesh

The specimen fracture is shown in Figure-A I-29 (coarse mesh shown).

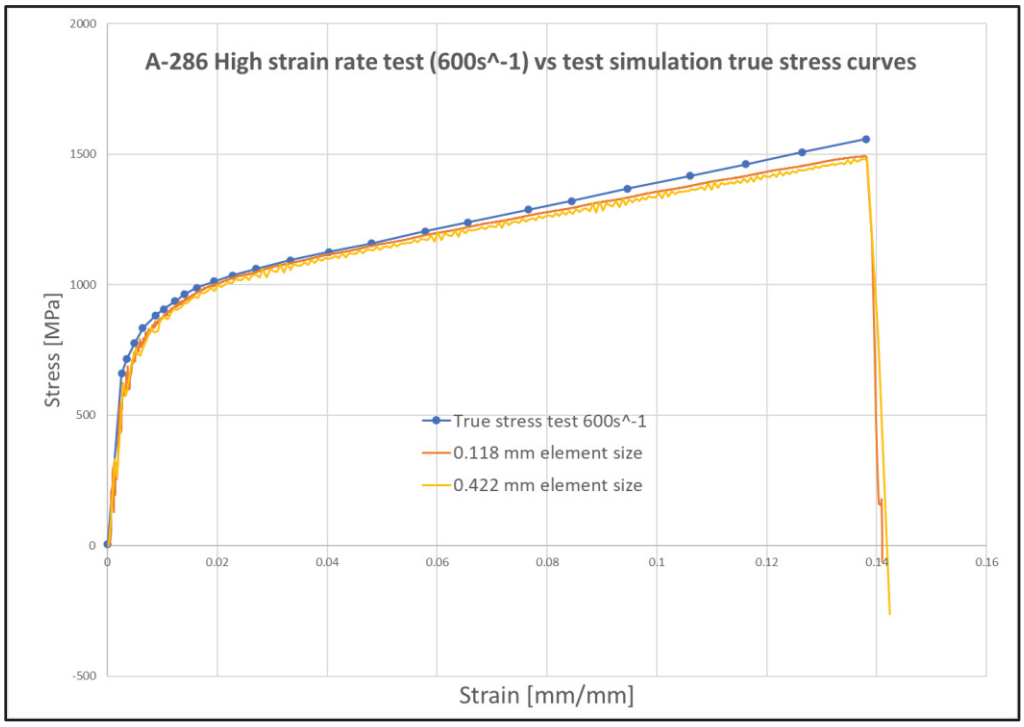

Figure-A I-28 SHB test at 600s^-1 true stress curve vs resulting stress curves

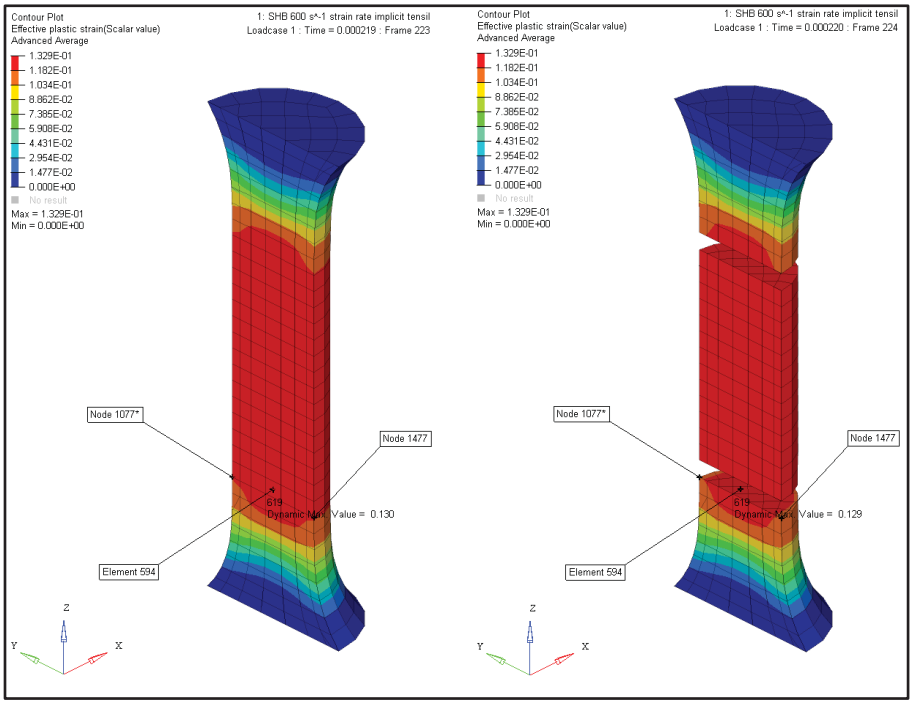

Figure-A I-29 Coarse mesh specimen before fracture (left) and after fracture (right) at a strain rate of 600s^-1

The effective plastic stress function of the effective plastic strain curves is shown in Figure-A I-30, and the full listing of the curves in Table-A I-1.

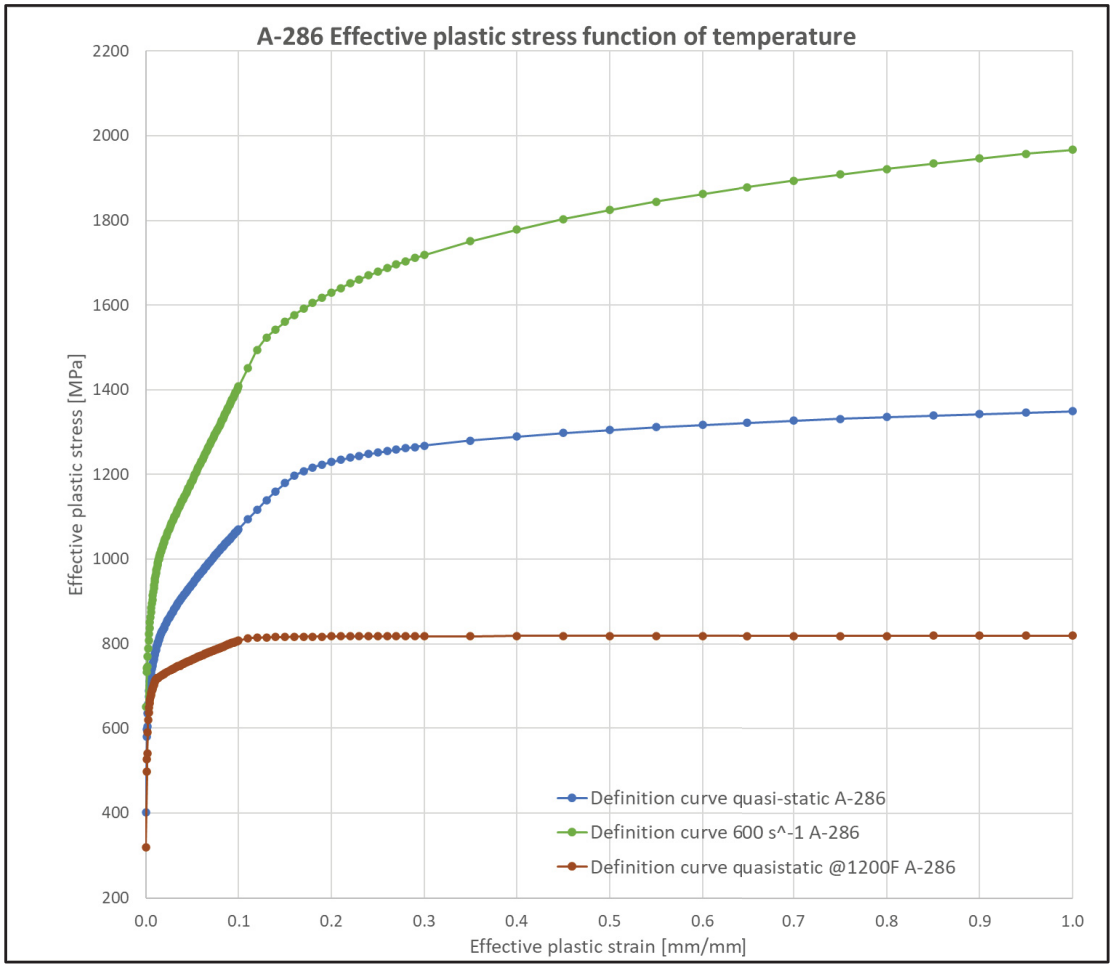

Figure-A I-30 Effective plastic stress function of the effective plastic strain curves for A-286

Table-A I-1 LCK1 Table definition

Definition curve quasi-static A-286			Definition curve 4 s^-1 A-286			Definition curve 600 s^-1 A-286		
0.0000	402.000		0.0000	580.000		0.0000	650	
0.0012	579.650		0.0012	655.171		0.0012	731.887	
0.0014	596.794		0.0014	665.012		0.0014	742.247	
0.0015	604.596		0.0015	669.586		0.0015	747.127	
0.0020	634.610		0.0020	691.002		0.0020	769.863	
0.0025	656.578		0.0025	709.556		0.0025	789.621	
0.0030	673.706		0.0030	726.051		0.0030	807.226	
0.0035	687.726		0.0035	740.855		0.0035	823.087	

Table–A I LCK1 Table definition (continued)

Definition curve quasi-static A-286			Definition curve 4 s^-1 A-286			Definition curve 600 s^-1 A-286		
0.0040	699.521		0.0040	754.348		0.0040	837.546	
0.0045	709.744		0.0045	766.737		0.0045	850.815	
0.0050	718.791		0.0050	778.193		0.0050	863.111	
0.0055	726.897		0.0055	788.868		0.0055	874.581	
0.0060	734.264		0.0060	798.885		0.0060	885.297	
0.0065	741.021		0.0065	808.265		0.0065	895.393	
0.0070	747.278		0.0070	817.060		0.0070	904.955	
0.0075	753.081		0.0075	825.044		0.0075	914.002	
0.0080	758.529		0.0080	832.143		0.0080	922.622	
0.0085	763.641		0.0085	838.529		0.0085	930.870	
0.0090	768.490		0.0090	843.603		0.0090	938.739	
0.0095	773.084		0.0095	848.507		0.0095	946.286	
0.0100	777.446		0.0100	853.418		0.0100	953.549	
0.0105	781.615		0.0105	858.336		0.0105	960.547	
0.0110	785.128		0.0110	863.261		0.0110	967.302	
0.0115	792.875		0.0115	868.192		0.0115	973.830	
0.0120	796.565		0.0120	873.104		0.0120	980.151	
0.0125	800.122		0.0125	877.684		0.0125	986.278	
0.0130	803.560		0.0130	881.671		0.0130	992.229	
0.0135	806.890		0.0135	885.631		0.0135	998.016	
0.0140	810.095		0.0140	889.596		0.0140	1000.895	
0.0145	813.208		0.0145	893.566		0.0145	1004.718	
0.0150	816.239		0.0150	897.541		0.0150	1008.540	
0.0155	819.197		0.0155	901.523		0.0155	1012.256	
0.0160	822.063		0.0160	905.510		0.0160	1015.849	
0.0165	824.852		0.0165	909.317		0.0165	1019.311	
0.0170	827.588		0.0170	912.477		0.0170	1022.779	
0.0175	830.254		0.0175	915.357		0.0175	1026.250	
0.0180	831.609		0.0180	918.148		0.0180	1029.726	
0.0185	832.711		0.0185	920.943		0.0185	1033.208	
0.0190	835.051		0.0190	923.743		0.0190	1036.414	
0.0195	837.393		0.0195	926.544		0.0195	1039.379	
0.0200	839.738		0.0200	929.352		0.0200	1042.234	
0.0210	844.437		0.0210	934.976		0.0210	1047.945	
0.0220	849.149		0.0220	940.615		0.0220	1053.672	
0.0230	853.874		0.0230	945.970		0.0230	1059.390	
0.0240	857.701		0.0240	951.021		0.0240	1064.777	
0.0250	861.319		0.0250	956.067		0.0250	1070.089	
0.0260	864.936		0.0260	961.127		0.0260	1075.415	
0.0270	868.562		0.0270	966.201		0.0270	1080.755	
0.0280	872.197		0.0280	971.288		0.0280	1086.109	
0.0290	875.812		0.0290	976.364		0.0290	1091.476	
0.0300	879.375		0.0300	981.196		0.0300	1096.321	
0.0310	882.873		0.0310	985.830		0.0310	1100.924	
0.0320	886.380		0.0320	990.475		0.0320	1105.497	
0.0330	889.894		0.0330	995.134		0.0330	1110.081	
0.0340	893.417		0.0340	999.806		0.0340	1114.676	
0.0350	896.922		0.0350	1004.488		0.0350	1119.282	
0.0360	900.252		0.0360	1009.158		0.0360	1123.889	
0.0370	903.267		0.0370	1013.667		0.0370	1128.272	
0.0380	906.291		0.0380	1017.998		0.0380	1132.505	
0.0390	909.319		0.0390	1022.256		0.0390	1136.750	
0.0400	912.358		0.0400	1026.526		0.0400	1141.007	

Table–A I LCK1 Table definition (continued)

Definition curve quasi-static A-286			Definition curve 4 s^-1 A-286			Definition curve 600 s^-1 A-286		
0.0410	915.402		0.0410	1030.809		0.0410	1145.297	
0.0420	918.454		0.0420	1035.099		0.0420	1149.646	
0.0430	921.381		0.0430	1039.403		0.0430	1153.994	
0.0440	924.241		0.0440	1043.717		0.0440	1158.343	
0.0450	927.108		0.0450	1048.039		0.0450	1162.720	
0.0460	929.976		0.0460	1052.255		0.0460	1167.393	
0.0470	932.857		0.0470	1056.458		0.0470	1172.067	
0.0480	935.739		0.0480	1060.660		0.0480	1176.740	
0.0490	938.621		0.0490	1064.862		0.0490	1181.413	
0.0500	941.504		0.0500	1069.065		0.0500	1186.090	
0.0510	944.373		0.0510	1073.247		0.0510	1190.775	
0.0520	947.238		0.0520	1077.428		0.0520	1195.460	
0.0530	950.112		0.0530	1081.609		0.0530	1200.145	
0.0540	952.992		0.0540	1085.790		0.0540	1204.830	
0.0550	955.877		0.0550	1089.983		0.0550	1209.323	
0.0560	958.773		0.0560	1094.220		0.0560	1213.693	
0.0570	961.666		0.0570	1098.456		0.0570	1218.063	
0.0580	964.427		0.0580	1102.692		0.0580	1222.433	
0.0590	967.188		0.0590	1106.929		0.0590	1226.803	
0.0600	969.775		0.0600	1111.199		0.0600	1231.201	
0.0610	972.514		0.0610	1115.501		0.0610	1235.601	
0.0620	975.170		0.0620	1119.802		0.0620	1240.002	
0.0630	977.826		0.0630	1124.104		0.0630	1244.402	
0.0640	980.482		0.0640	1128.406		0.0640	1248.808	
0.0650	983.138		0.0650	1132.749		0.0650	1253.233	
0.0660	985.802		0.0660	1137.101		0.0660	1257.658	
0.0670	988.481		0.0670	1141.453		0.0670	1262.083	
0.0680	991.160		0.0680	1145.805		0.0680	1266.508	
0.0690	993.840		0.0690	1150.115		0.0690	1270.943	
0.0700	996.519		0.0700	1154.203		0.0700	1275.387	
0.0710	999.213		0.0710	1158.291		0.0710	1279.831	
0.0720	1001.914		0.0720	1162.378		0.0720	1284.275	
0.0730	1004.614		0.0730	1166.466		0.0730	1288.719	
0.0740	1007.315		0.0740	1170.531		0.0740	1292.888	
0.0750	1010.013		0.0750	1174.575		0.0750	1297.033	
0.0760	1012.640		0.0760	1178.618		0.0760	1301.178	
0.0770	1015.268		0.0770	1182.662		0.0770	1305.323	
0.0780	1017.895		0.0780	1186.706		0.0780	1309.527	
0.0790	1020.522		0.0790	1190.790		0.0790	1313.873	
0.0800	1023.029		0.0800	1194.879		0.0800	1318.218	
0.0810	1025.369		0.0810	1198.968		0.0810	1322.564	
0.0820	1027.710		0.0820	1203.057		0.0820	1326.909	
0.0830	1030.050		0.0830	1207.161		0.0830	1331.471	
0.0840	1032.390		0.0840	1211.301		0.0840	1336.124	
0.0850	1034.750		0.0850	1215.441		0.0850	1340.778	
0.0860	1037.113		0.0860	1219.581		0.0860	1345.432	
0.0870	1039.476		0.0870	1223.721		0.0870	1350.084	
0.0880	1041.840		0.0880	1227.896		0.0880	1354.724	
0.0890	1044.209		0.0890	1232.084		0.0890	1359.365	
0.0900	1046.595		0.0900	1236.272		0.0900	1364.005	
0.0910	1048.981		0.0910	1240.460		0.0910	1368.645	
0.0920	1051.367		0.0920	1244.655		0.0920	1373.078	
0.0930	1053.754		0.0930	1248.890		0.0930	1377.352	

Table–A I LCK1 Table definition (continued)

Definition curve quasi-static A-286			Definition curve 4 s^-1 A-286			Definition curve 600 s^-1 A-286		
0.0940	1056.184		0.0940	1253.124		0.0940	1381.626	
0.0950	1058.633		0.0950	1257.358		0.0950	1385.900	
0.0960	1061.083		0.0960	1261.592		0.0960	1390.176	
0.0970	1063.533		0.0970	1265.869		0.0970	1394.496	
0.0980	1065.987		0.0980	1270.170		0.0980	1398.816	
0.0990	1068.465		0.0990	1274.471		0.0990	1403.136	
0.1000	1070.943		0.1000	1278.773		0.1000	1407.456	
0.1100	1095.127		0.1100	1322.296		0.1100	1451.442	
0.1200	1116.631		0.1200	1363.882		0.1200	1494.253	
0.1300	1139.778		0.1300	1403.813		0.1300	1523.291	
0.1400	1160.364		0.1400	1446.534		0.1400	1542.775	
0.1500	1179.360		0.1500	1470.023		0.1500	1560.528	
0.1600	1197.207		0.1600	1488.820		0.1600	1576.626	
0.1700	1208.447		0.1700	1505.827		0.1700	1591.366	
0.1800	1216.399		0.1800	1521.259		0.1800	1604.969	
0.1900	1223.267		0.1900	1535.397		0.1900	1617.606	
0.2000	1229.264		0.2000	1548.451		0.2000	1629.411	
0.2100	1234.512		0.2100	1560.582		0.2100	1640.493	
0.2200	1239.583		0.2200	1571.919		0.2200	1650.939	
0.2300	1243.942		0.2300	1582.563		0.2300	1660.821	
0.2400	1248.176		0.2400	1592.600		0.2400	1670.201	
0.2500	1251.908		0.2500	1602.097		0.2500	1679.128	
0.2600	1255.546		0.2600	1611.113		0.2600	1687.648	
0.2700	1258.811		0.2700	1619.695		0.2700	1695.797	
0.2800	1262.004		0.2800	1627.887		0.2800	1703.609	
0.2900	1264.908		0.2900	1635.724		0.2900	1711.110	
0.3000	1267.720		0.3000	1643.055		0.3000	1718.145	
0.3500	1279.851		0.3500	1676.653		0.3500	1750.694	
0.4000	1289.724		0.4000	1705.097		0.4000	1778.560	
0.4500	1298.061		0.4500	1729.816		0.4500	1802.972	
0.5000	1305.281		0.5000	1751.712		0.5000	1824.727	
0.5500	1311.654		0.5500	1771.389		0.5500	1844.369	
0.6000	1317.360		0.6000	1789.276		0.6000	1862.292	
0.6500	1322.528		0.6500	1805.684		0.6500	1878.784	
0.7000	1327.253		0.7000	1820.850		0.7000	1894.067	
0.7500	1331.606		0.7500	1834.958		0.7500	1908.314	
0.8000	1335.641		0.8000	1848.152		0.8000	1921.664	
0.8500	1339.404		0.8500	1860.550		0.8500	1934.228	
0.9000	1342.929		0.9000	1872.245		0.9000	1946.097	
0.9500	1346.245		0.9500	1883.317		0.9500	1957.289	
1.0000	1349.376		1.0000	1893.133		1.0000	1967.253	

APPENDIX II

BLADE MATERIAL DEFINITION

For the blades materials (IN713C and Stellite 31), information on public domain is relatively scarce, the definition of the engineering stress function of engineering strain was realized using a Ramberg-Osgood-based formulation:

$$\varepsilon_{eng} = \frac{\sigma_{eng}}{E} + 0.002 \cdot (\frac{\sigma_{eng}}{\sigma_{yield}})^n \text{ (Hill, 1944);} \quad \text{(A II.1)}$$

where ε_{eng} is the engineering strain, σ_{eng} is the engineering stress, E is the Young modulus and σ_{yield} is the 0.2% yield stress. The exponent n is expressed as:

$$n = \frac{\ln (\frac{\varepsilon_{fail} - \frac{\sigma_{ult}}{E}}{0.002})}{\ln (\frac{\sigma_{ult}}{\sigma_{yield}})}; \quad \text{(A II.2)}$$

where ε_{fail} is the elongation at tensile fracture and σ_{ult} is the tensile strength (ultimate stress) of the material.

Subsequently, as per the guidelines in (LS-DYNA Aerospace Working Group, 2011), (Vasko, Tom; LS-DYNA® Aerospace Working Group, 2019), the determined engineering stress-strain curve is converted into the true stress – true strain curve, using:

$$\sigma_{true} = \sigma_{eng} \cdot (1 + \varepsilon_{eng}); \quad \text{(A II.3)}$$

respectively:

$$\varepsilon_{true} = ln(\varepsilon_{eng} + 1); \quad \text{(A II.4)}$$

The effective stress – strain curve input into the MAT_024 in LS-DYNA requires only the plastic portion to be included in the material card. Hence, the effective plastic strain is shifted to the end of the linear domain (proportional limit, as shown in Figure-A II-1):

$$\varepsilon_{pl} = \varepsilon_{true} - \frac{\sigma_{yield}}{E}; \qquad \text{(A II.5)}$$

Therefore, the starting point of the curve defining the effective stress versus effective plastic strain starts with the value 0 for the effective plastic strain, and the proportional limit of that material (at proportional limit the true stress coincides with the engineering stress). The succession of steps mentioned in relations (3.1) to (3.5) is shown in Figure-A II-2.

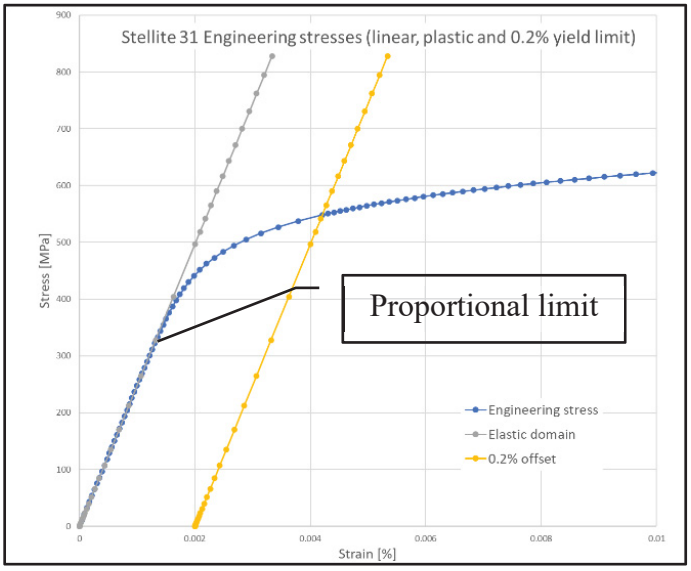

Figure-A II-1 Proportional limit is used as start point in the material card curve definition

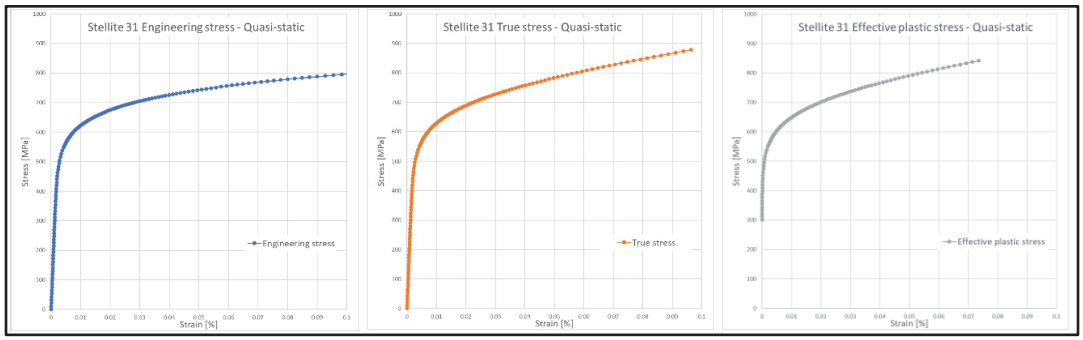

Figure-A II-2 Engineering (left), true (middle) and effective (right) plastic stress curves

Advancing in the plastic domain, the generated effective plastic stress curve needs further processing. Past necking, the equivalent stress is affected by the transversal stress (stress no longer uniaxial), and the stress-strain curve developed as mentioned previously is no longer accurate. Hence, the generated effective plastic stress curve is retained only until the necking point, the second part being discarded and replaced with a corrected portion, extrapolated until 100% plastic strain, to avoid numerical instabilities in LS-DYNA.

The necking point can be found at the intersection of the true stress – true strain curve with its own derivative, as shown below (Buyuk, 2014), (Haight & al., 2016), (Vasko, Tom; LS-DYNA® Aerospace Working Group, 2019):

$$\begin{cases} \sigma_{true} = \sigma_{true}(\varepsilon_{true}) \\ \sigma_{true} = \frac{d\sigma_{true}}{d\varepsilon_{true}} \end{cases}; \tag{A II.6}$$

A method based on Swift's strain hardening equation (Swift, 1952) was developed (LS-DYNA Aerospace Working Group, 2011), (Buyuk, 2014), (Haight & al., 2016), for the extrapolation of the stress-strain curve for LS-DYNA past the necking point.

A series of curves are extrapolated using the following exponential equation (Swift, 1952), (Buyuk, 2014), (Haight & al., 2016), (Vasko, Tom; LS-DYNA® Aerospace Working Group, 2019):

$$\sigma_{true} = k \cdot (\varepsilon_e + \varepsilon_{true})^n; \tag{A II.7}$$

where k, ε_e and n are fitting parameters determined from the boundary condition at necking (continuity and monotonical tangency). The hardening exponent is selected freely from a range between 0 and 1.

Furthermore, k and ε_e are expressed as:

$$k = A \cdot \left(\frac{A \cdot n}{C}\right)^{-n} \tag{A II.8}$$

and

$$\varepsilon_e = \frac{A \cdot n}{C} - B$$

Where A is the true stress at necking (σ_{true}), B is the true plastic strain at necking (ε_{true}), and C is the slope at necking (hardening modulus).

After generating the series of curves (shown in Figure-A II-3) corresponding to each selected exponential coefficient n, the curves are compared with the experimental true stress true strain curve and the hardening exponent is selected for the curve matching the experimental one. As no information was available for the blade materials (Stellite 31 and IN713C), the arbitrary value of n=0.1 was selected for both blade materials. This value simulates the hardening for each material, material curves (effective plastic stress versus effective plastic strain) for both materials are shown in Figure-A II-4. Each material curve is assigned an identification number and is referenced to in the MAT_024 material card, as shown in red circles in Figure-A II-5, respectively Figure-A II-6.

As the blades geometries were approximated, the density of each blade material was adjusted such as to obtain the release kinetic energies for the velocities recorded in the test report.

To the airfoils of both engines' blades were assigned each a separate MAT_024 card, similar as for the shrouds and platforms, excepting having activated a failure criterion under the FAIL field on the first card (red circle in Figure-A II-7).

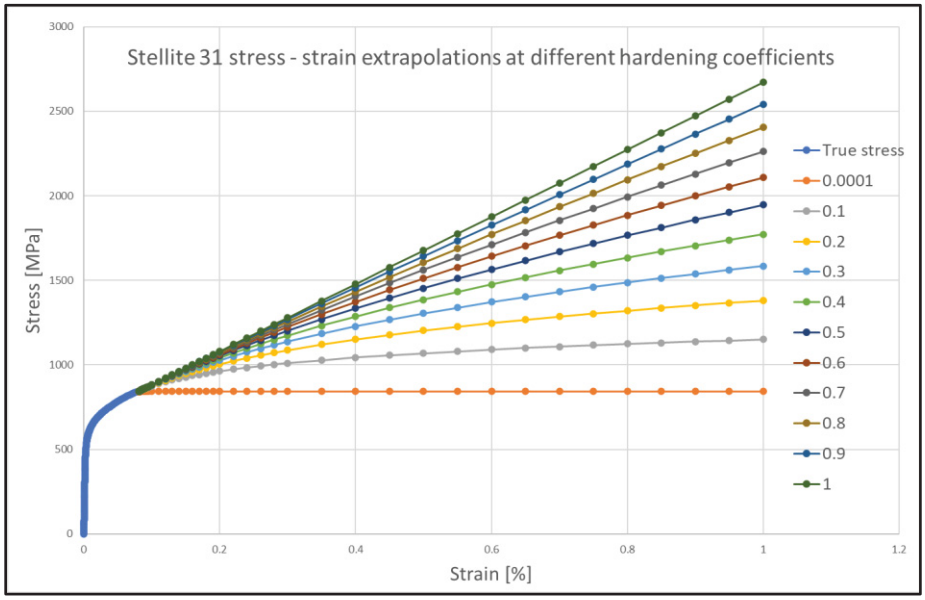

Figure-A II-3 Extrapolated hardening curves for Stellite 31

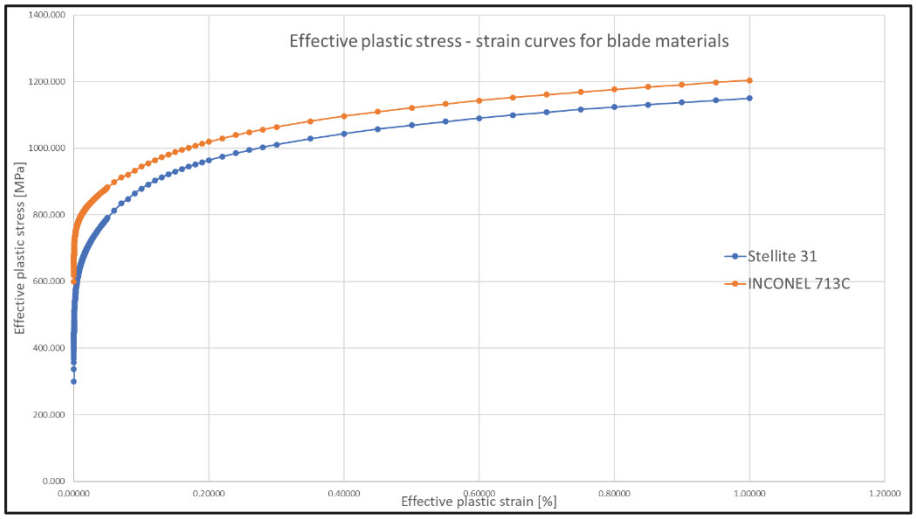

Figure-A II-4 Effective plastic stress vs effective plastic strain curves for blade materials

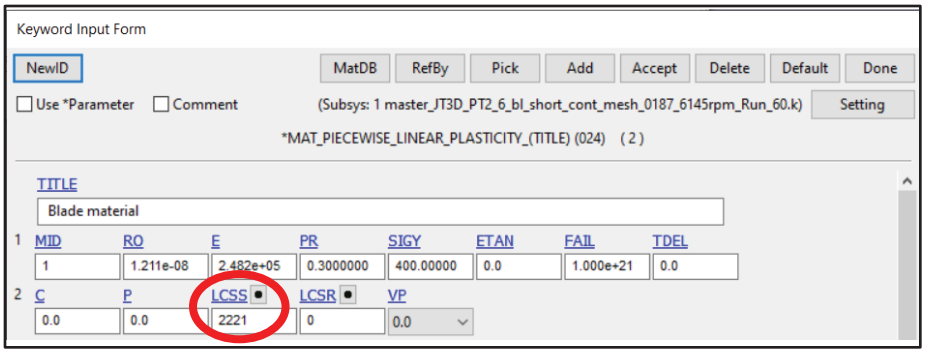

Figure-A II-5 MAT_024 material card for blades in Stellite 31

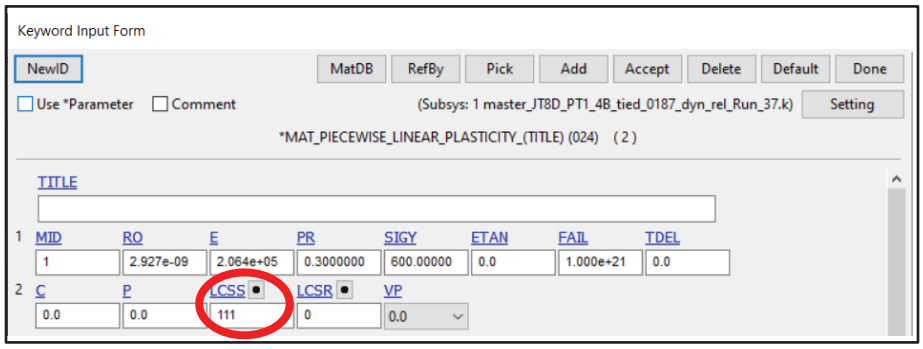

Figure-A II-6 MAT_024 material card for the blades in INCONEL 713C

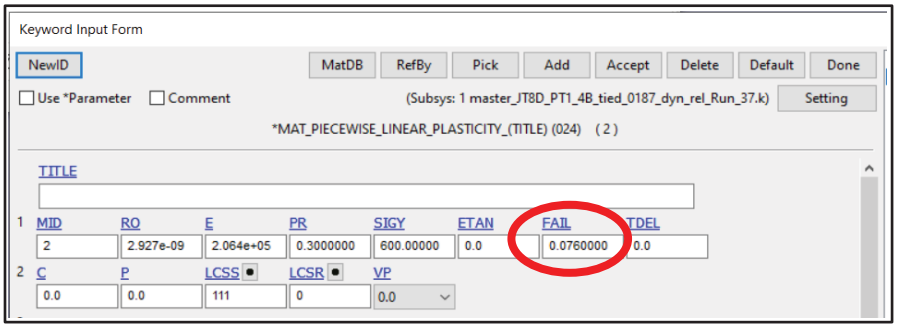

Figure-A II-7 Failure criteria applied on the airfoil (INCONEL 713C shown)

The failure criteria considered for each of the two airfoil materials is the effective plastic strain corresponding to the tensile elongation.

A diagram of the procedure for generating the *MAT_024 card for LS-DYNA is shown in Figure-A II-8. The quasistatic curve obtained as mentioned previously is added to the MAT_024 card for each respective material (Figure-A II-5 and Figure-A II-6). The other parameters mentioned in the material cards are density, Young's modulus, Poisson's ratio and the effective plastic strain stress (coincides with the starting of the defined curve).

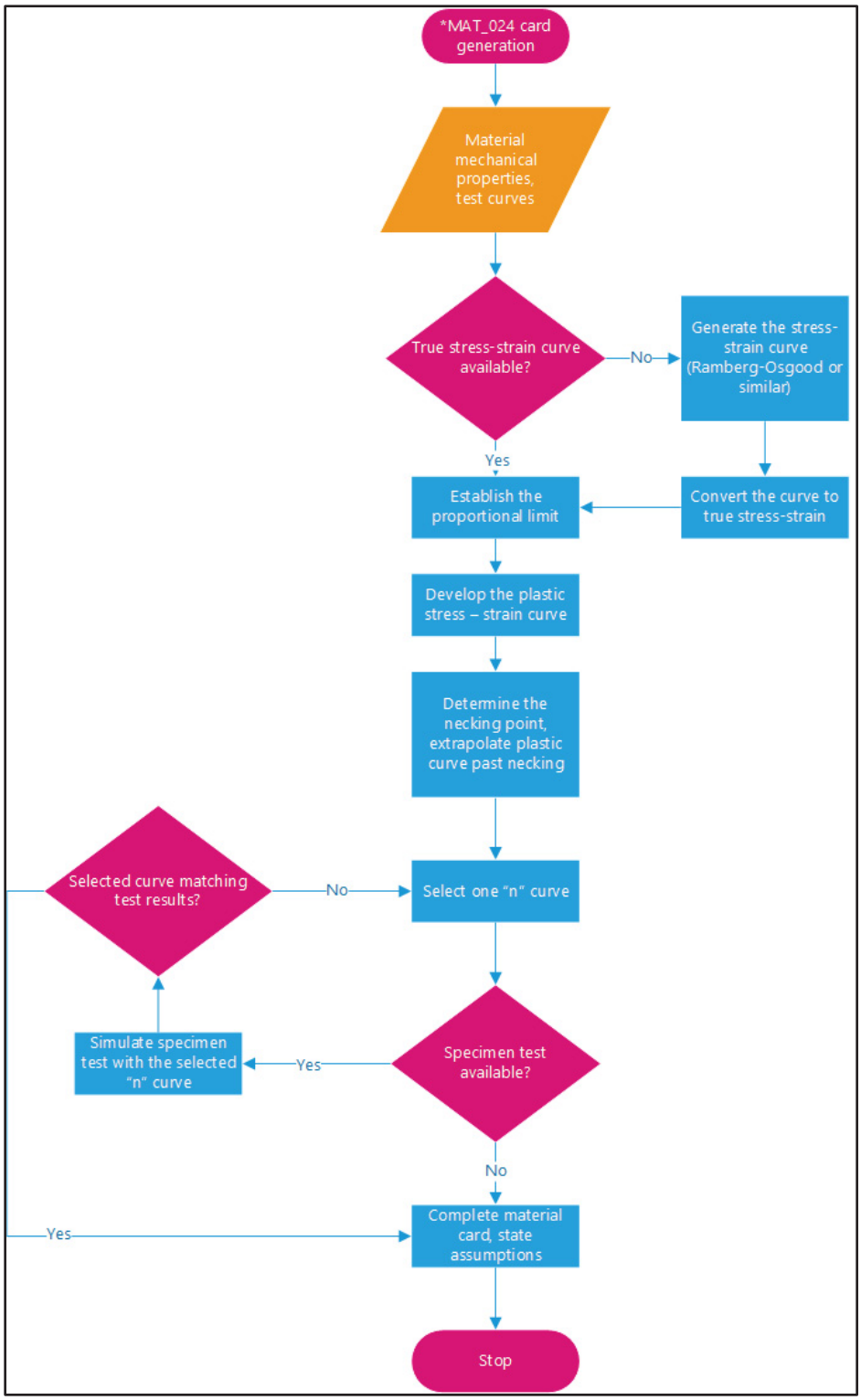

Figure-A II-8 Simplified procedure for generating the *MAT_024 card for LS-DYNA

APPENDIX III

CASING MATERIAL DEVELOPMENT

A series of tests are used to generate all these curves: the strain rates for A-286 are detailed in the experimental work reported in (Nicholas, 1980), the thermal curves are presented in (Kattus, Preston, & Lessley, 1958). For the failure surface generation, the tests presented in (Bao, 2003), (Buyuk, 2014), (Hammer, 2014), (Haight & al., 2016) were replicated with using their original materials, then repeated for A-286, as detailed below. The procedure employed to generate the material card is shown in Figure-A III-1.

Strain rate curves (TABK1)

The different strain rate stress – strain curves for A-286 (Figure-A III-2) were generated with a tensile version of a split Hopkinson bar, for low, intermediate, and high strain rates (Nicholas, 1980). As mentioned in the test report (Nicholas, 1980), the elastic region depicted on the curves does not represent the experimentally obtained data but was rather drawn for completeness of graphical representation. To determine the linear elastic and early plastic portion of the curve to be used in the FE simulations, the Young modulus, yield and ultimate stresses, and the elongation were obtained from Metallic Materials Properties Development and Standardization (MMPDS) (Rice & al., 2003). The curve thus obtained is compared with the quasistatic (considered to be 4E-4 s^-1) and the elasto-plastic curve at room temperature from (Kattus, Preston, & Lessley, 1958) (Figure-A III-3). It is observed a good agreement between the early plastic portion of the curve generated with Ramberg-Osgood method, and the room temperature test curve from (Kattus, Preston, & Lessley, 1958) (Figure-A III-4), hence this curve is retained and merged with the plastic portion of the quasi-static curve from (Nicholas, 1980).

Furthermore, the merged stress – strain curve is intersected with the tangent modulus to determine the necking point (Figure-A III-5), and the portion of the curve post necking is removed and replaced with the extrapolated hardening curve using an exponent of 0.1 (Figure-A III-6).

Similarly as for the material curves used in the blades (*MAT_024), the effective plastic strain – effective plastic stress curve begins at the proportional limit; an example for the quasi-static proportional limit determination is show in Figure-A III-7.

This same approach is used for generating the remaining test curves (at the intermediate strain rate of $4.4 \cdot s^{-1}$, and for the high strain rate at $600 \cdot s^{-1}$, as reported in (Nicholas, 1980). As observed in Figure-A III-2, and in the test report (Nicholas, 1980), the high strain rate curve does not show a necking behaviour, therefore the necking point was assumed to be at the reported failure strain.

The true stress – true strain curves (experimental versus generated with Ramberg-Osgood) are shown in Figure-A III-8, and the effective plastic stress curves (LCK1) are shown in Figure-A III-9.

After having generated the material curves, a set of analyses is performed using each of the determined curves in a *MAT_024 card, to validate the choice of the strain hardening coefficient. The specimen used in the testing is meshed and loaded as during testing, and iterative analyses are performed (Figure-A III-10) until reaching a satisfactory agreement with the test curve.

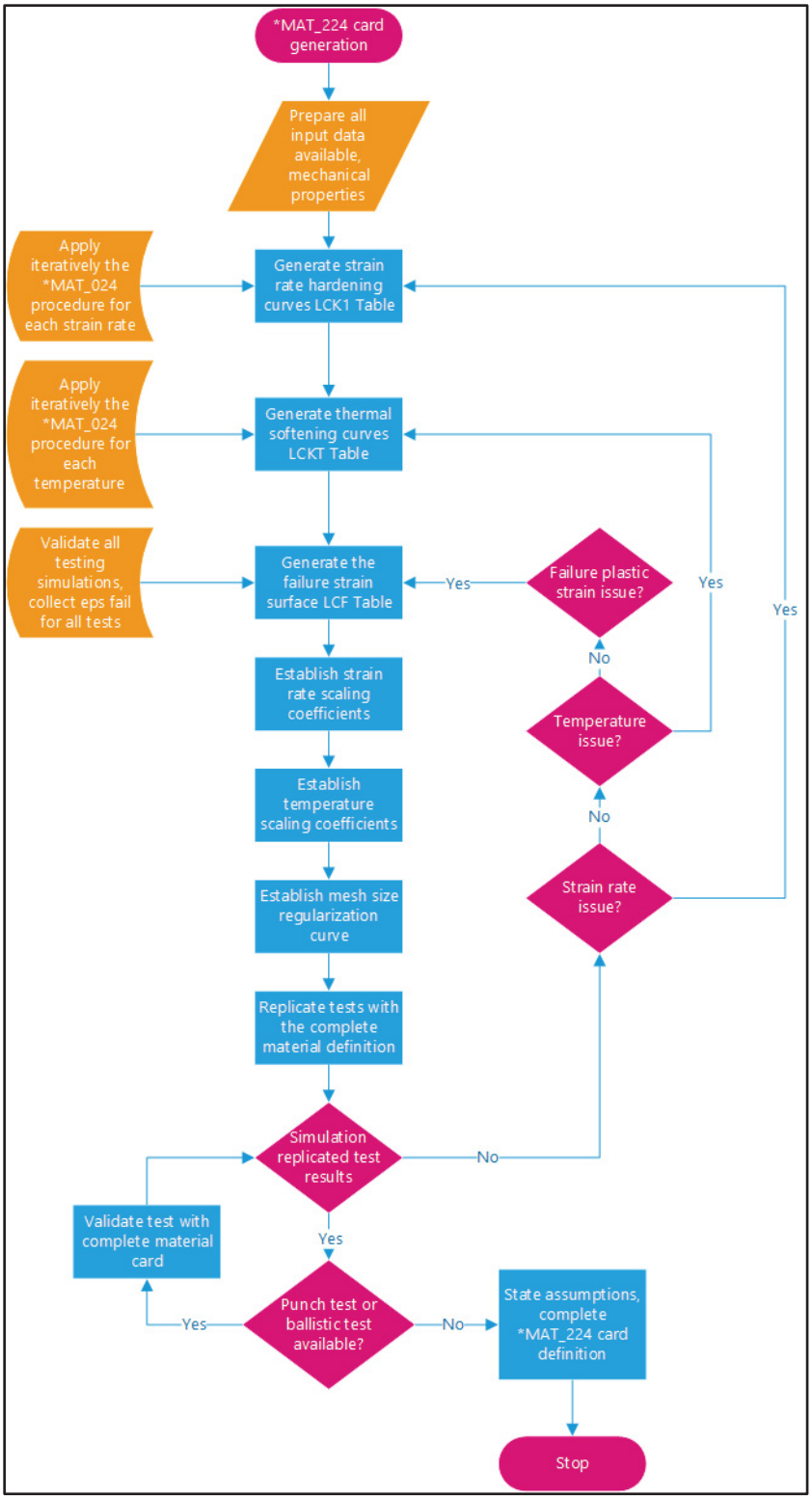

Figure-A III-1 Process flowchart for generating the *MAT_224 card for LS-DYNA

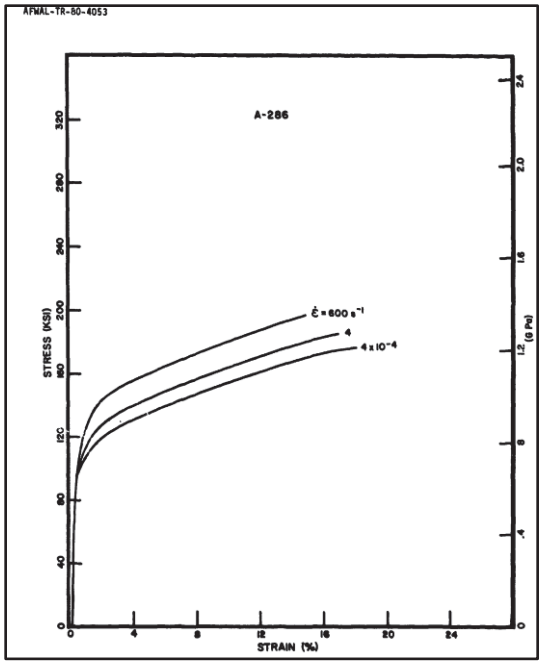

Figure-A III-2 A-286 tensile stress - strain curves
Taken from Nicholas (1980, p. 32)" (Nicholas, 1980)

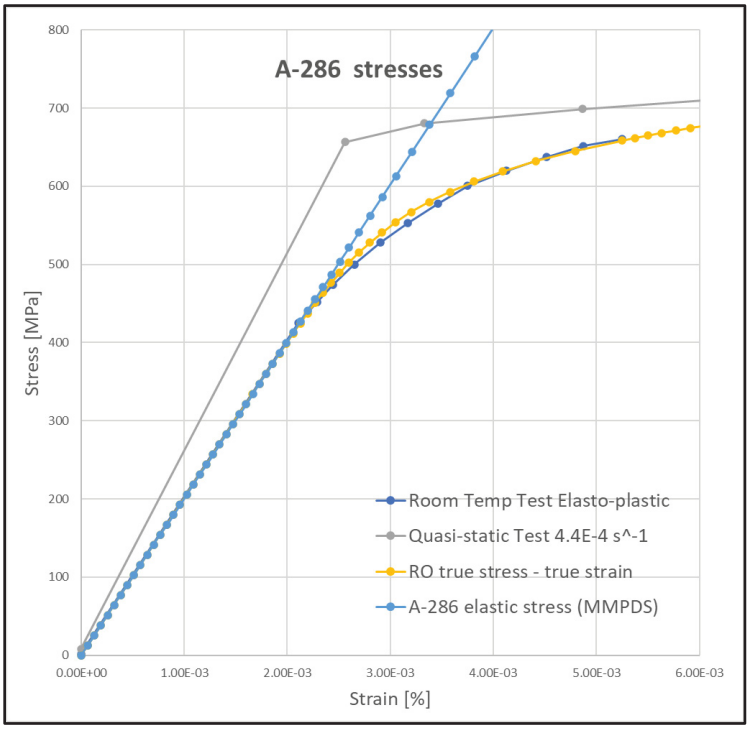

Figure-A III-3 A-286 Young's modulus comparison

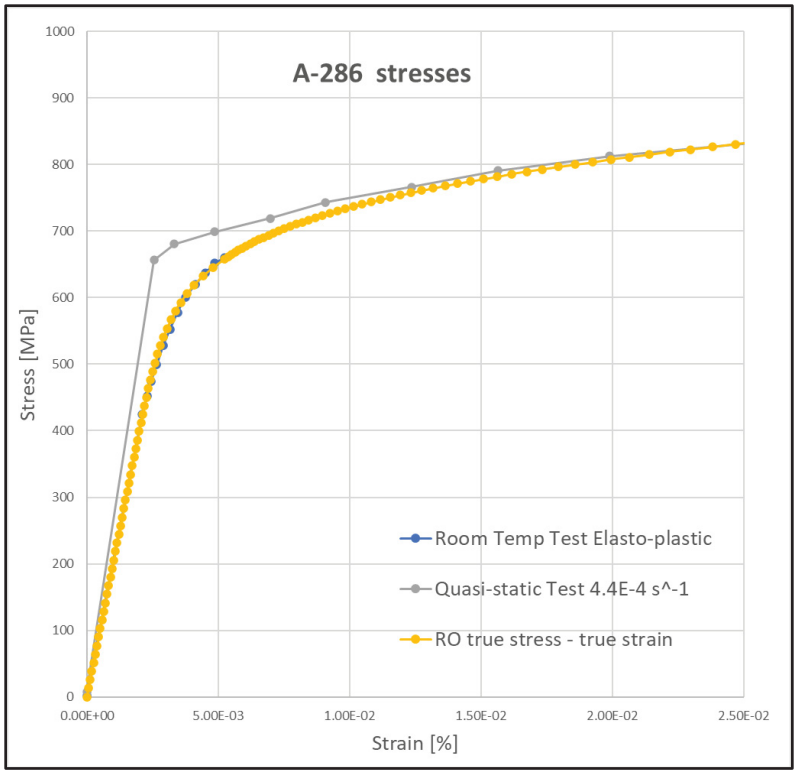

Figure-A III-4 Elastic and early plastic segment of stress-strain quasi-static curves for A-286

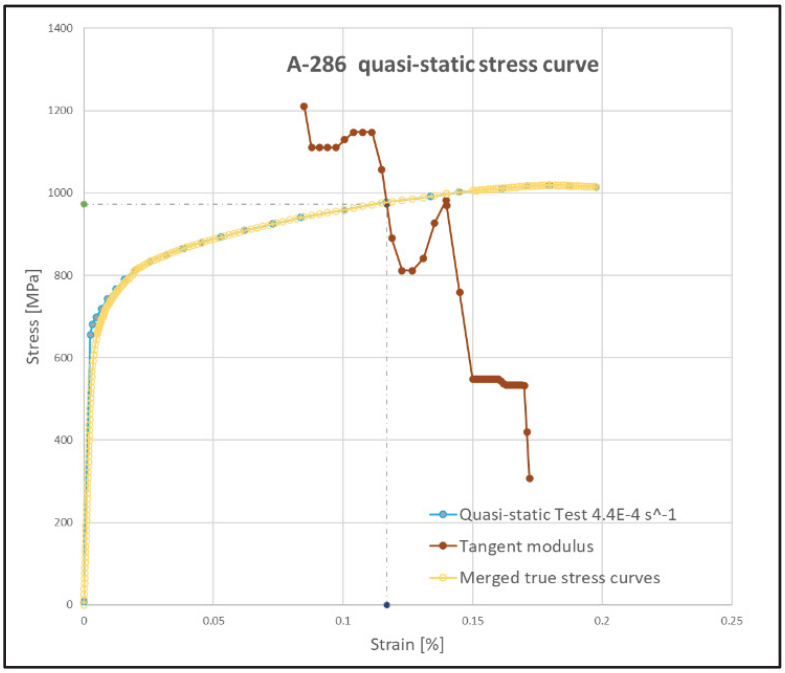

Figure-A III-5 A-286 necking point on the quasi-static true stress - true strain curve

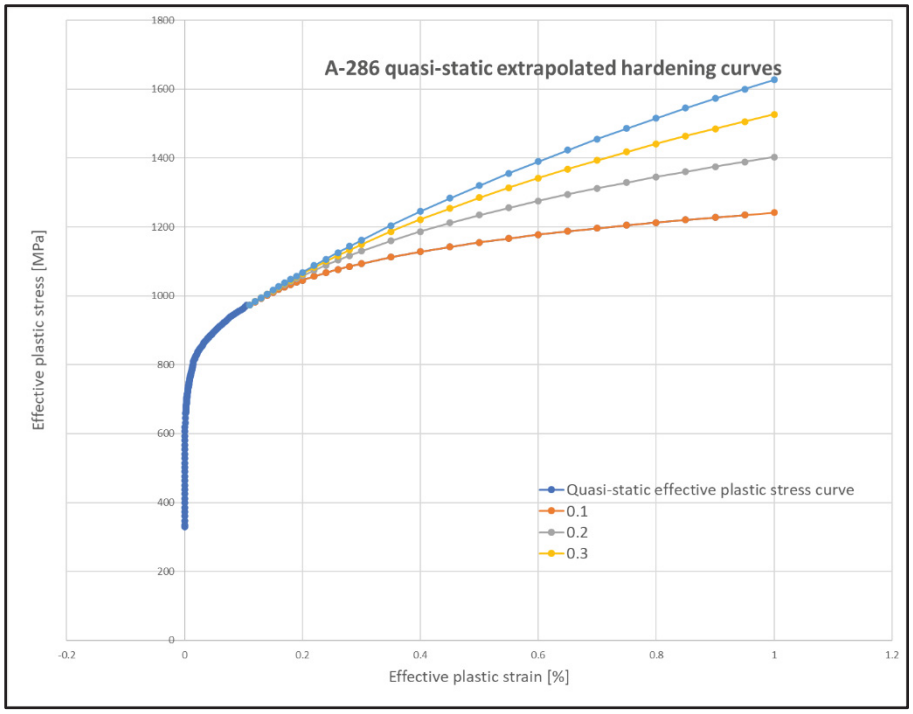

Figure-A III-6 Extrapolated effective plastic stress – strain hardening curves

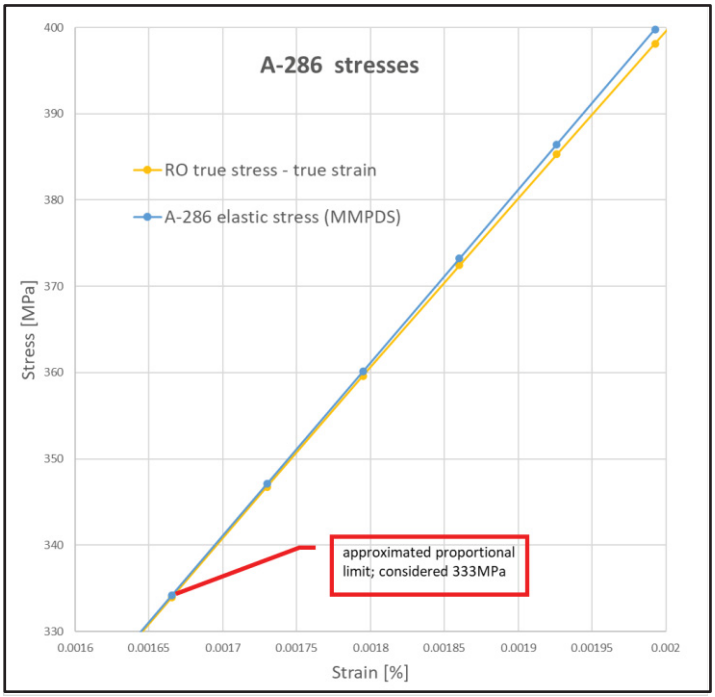

Figure-A III-7 Proportional limit for the A-286 quasi-static true stress - true strain curve

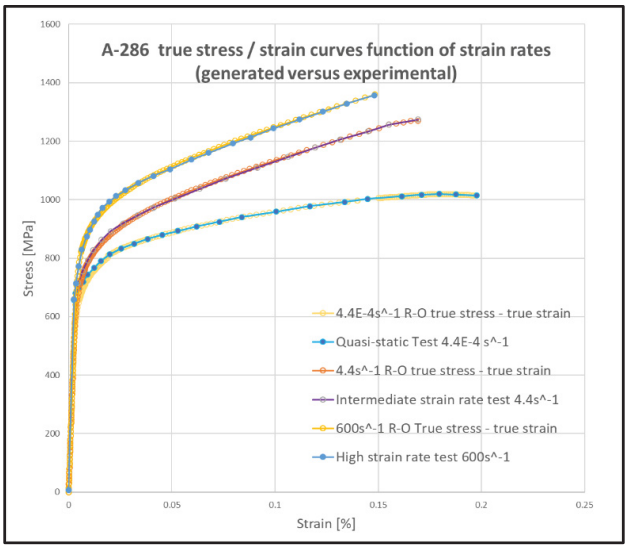

Figure-A III-8 A-286 strain rate true stress - strain curves

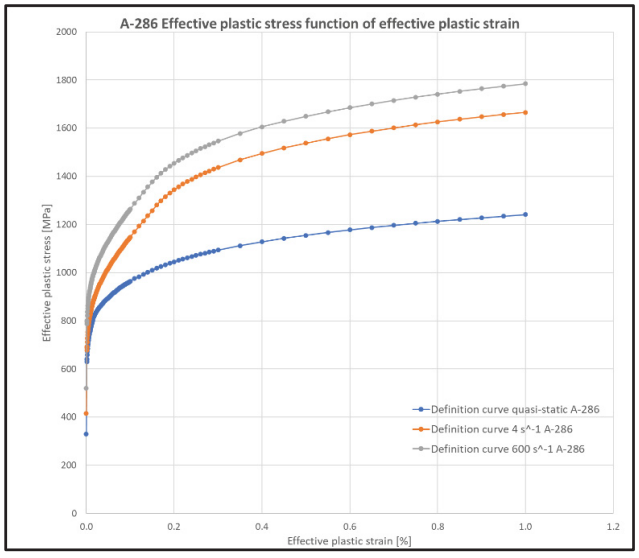

Figure-A III-9 A-286 Effective plastic stress curves at different strain rates (LCK1 curves)

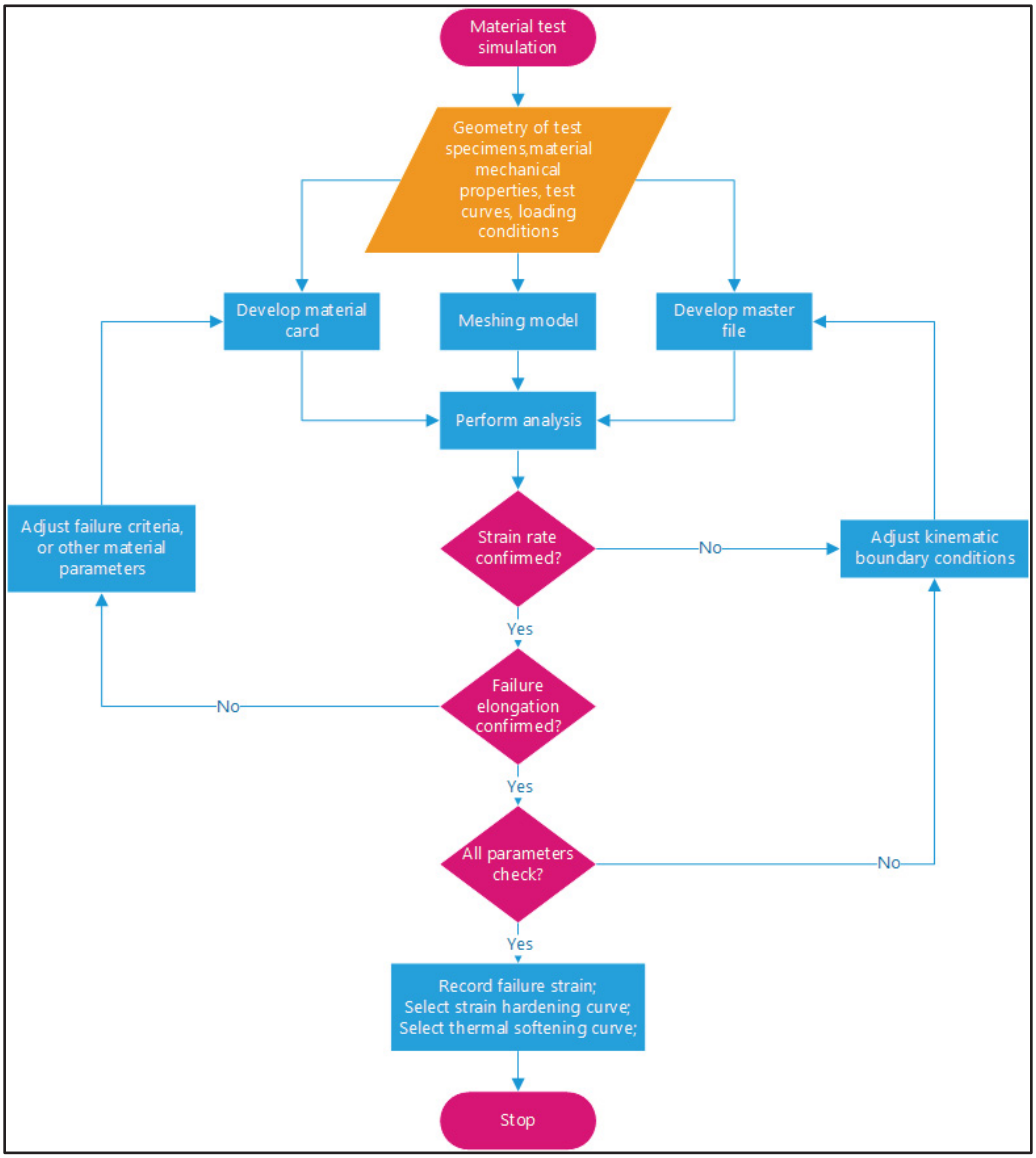

Figure-A III-10 Material test simulation flowchart

A recommended practice (LS-DYNA Aerospace Working Group, 2019) is to generate synthetic curves based on compressive tests (at high strain rates these compression tests show less variation in maintaining a relatively constant strain rate than the tensile) to extend the range of strain rates. In the absence of such compressive test data, it was decided to not pursue this approach, but the reader needs to be advised that such recommendation exists for increasing the accuracy of the method.

Temperature stress – strain curves (TABKT)

As the containment tests were performed at room temperature, the definition of the thermal behaviour is not necessary. However, for the material definition completeness, two curves were defined, showing the behaviour of A-286 at two different temperatures (room temperature and 922K).

For simulating the thermal effect on the effective plastic stress, it was used the set of tests reported in (Kattus, Preston, & Lessley, 1958), however with a few additional assumptions. As it was observed a discrepancy between the plastic domain of the stress curve at room temperature (0.062" sheet metal, 1 hr in argon at 1800F, oil quenched, aged at 1325F 16 hrs) and the previously used quasi-static curve from (Nicholas, 1980) (0.25" bar forging, solution treated 2 hrs at 1650F, oil quenched, aged at 1325F 16 hrs), the room temperature stress curve was considered as per (Nicholas, 1980).

The second definition curve was developed in a similar mode as described in the previous section, starting from the maximum temperature determined in (Kattus, Preston, & Lessley, 1958), at 1200F and 0.5hrs exposure time.

For obtaining this curve it was used the elasto-plastic curve from Fig 25 in (Kattus, Preston, & Lessley, 1958), and the late plastic domain (shown in Figure-A III-11 lower right), which were merged by a generated Ramberg-Osgood portion in the early plastic segment (Figure-A III-12).

The first four extrapolated curves, corresponding to the hardening coefficients 0.001, 0.1, 0.2 and 0.3 are shown in Figure-A III-13. As the test curve was slowly increasing post necking, then decreased, it was considered the smallest hardening exponent generating a line from the necking stress.

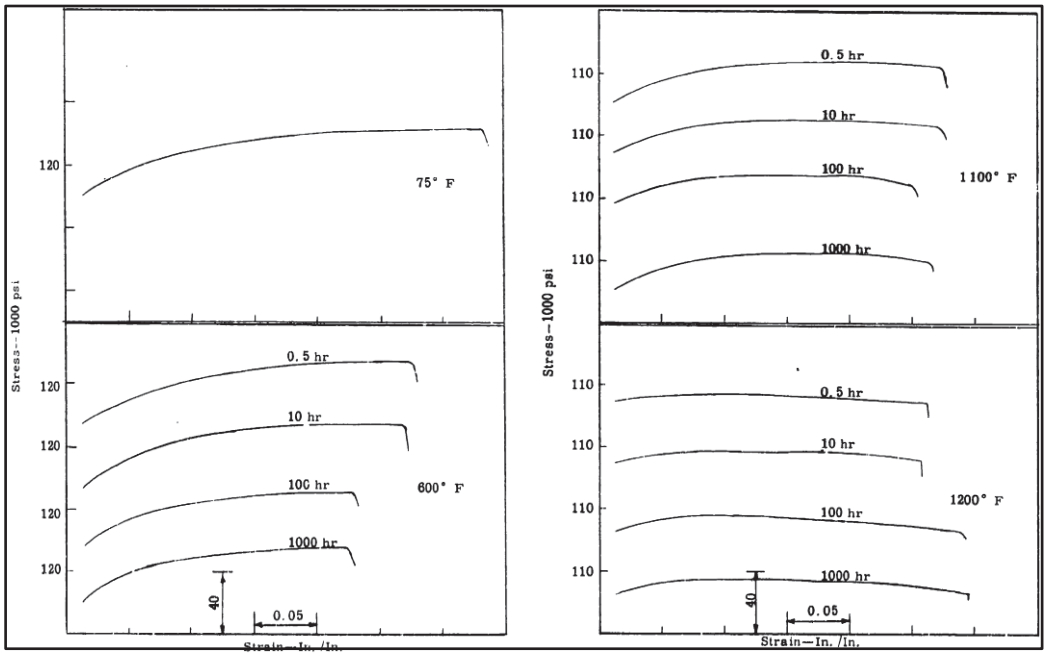

Figure-A III-11 Temperature stress - strain curves for A-286
Taken from Kattus, Preston, & Lessley (1958, p. 59)

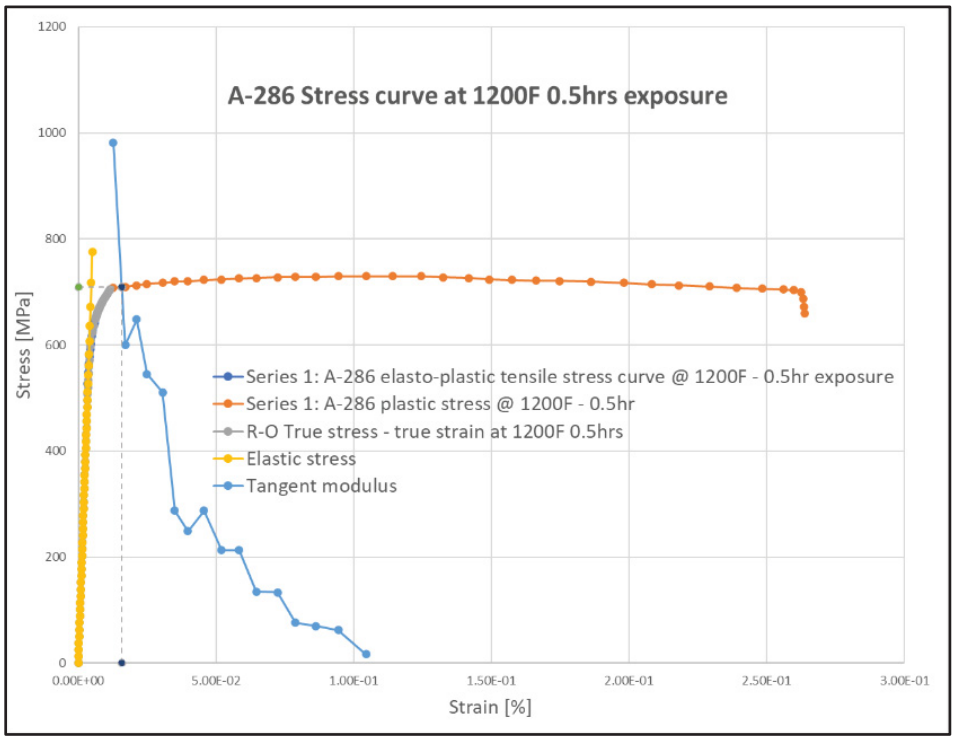

Figure-A III-12 A-286 stress curve at 1200F and 0.5hrs exposure

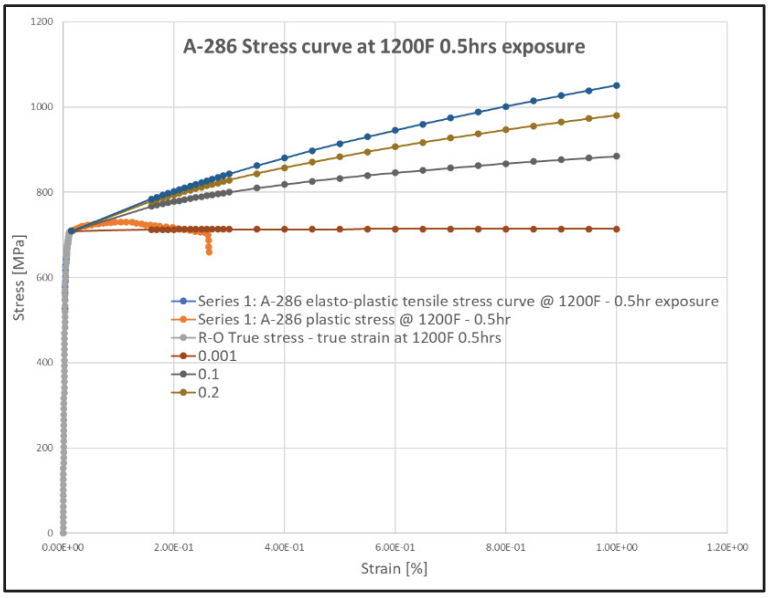

Figure-A III-13 Extrapolated hardening curves for A-286 at 1200F 0.5hrs exposure

For simulating the thermal behaviour of the casings in A-286, two curves are input as defining the LCKT table for the *MAT_224 card, as shown in Figure-A III-14. With these curves, the stress – strain relation input generation is complete, and the next step is the definition of the failure surface.

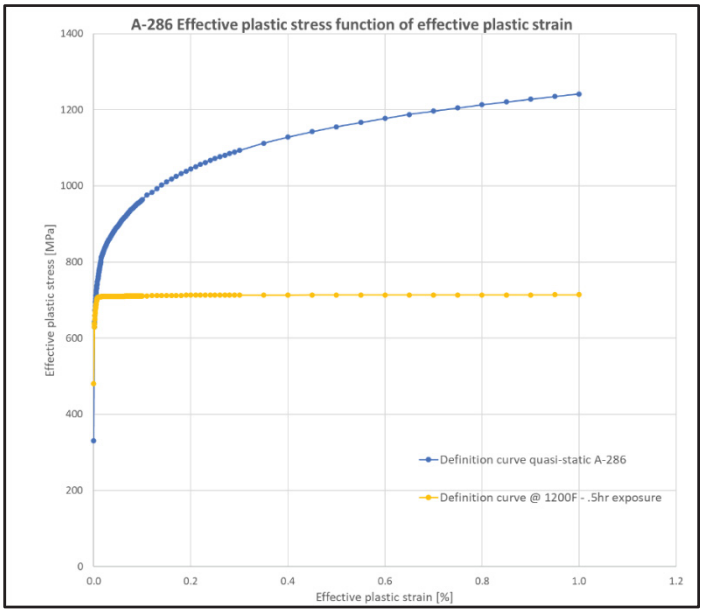

Figure-A III-14 A-286 Effective plastic stress curves at different temperatures (LCKT curves)

Failure surface generation (LCF)

As mentioned in (3.3), when the damage parameter D associated with the J-C material model reaches unity, the element is deleted. Expressed similarly as the stress flow (Buyuk, 2014), the effective plastic failure strain is:

$$\varepsilon_{pf} = \left[D_1 + D_2 \cdot e^{(D_3 \cdot \sigma^*)}\right] \cdot [1 + D_4 \cdot \ln \dot{\varepsilon^*}] \cdot [1 + D_5 \cdot T^*]; \quad \text{(A III.1)}$$

where D_1, D_2, D_3, D_4, D_5 are failure material specific constants, σ^* is the stress triaxiality

$$\sigma^* = \frac{p}{\sigma_{VM}}; \text{ (Buyuk, 2014)} \quad \text{(A III.2)}$$

p being the pressure and σ_{VM} being the von Mises stress ($\sigma_{VM} = \sqrt{\frac{3}{2} \cdot S_{ij} \cdot S_{ij}}$, S_{ij} being the deviatoric stress tensor).

As mentioned previously (for the stress flow expression), $\dot{\varepsilon^*}$ is the normalized effective plastic strain rate, and T^* is the normalized temperature.

The failure surface definition is based on four parameters (or functions) (3.10), the first one expressing the plastic failure strain function of the triaxiality (an example for Al2024-T351 is shown in Figure-A III-15) and the state of stress (Lode parameter) - $f(\sigma^*, \theta_L)$. The Lode parameter is defined as:

$$\theta_L = \frac{27 \cdot J_3}{2 \cdot {\sigma_{VM}}^3} \text{ (Buyuk, 2014)} \quad \text{(A III.3)}$$

J_3 being the third deviatoric stress invariant, $J_3 = \frac{1}{3} \cdot S_{ij} \cdot S_{jk} \cdot S_{ki}$.

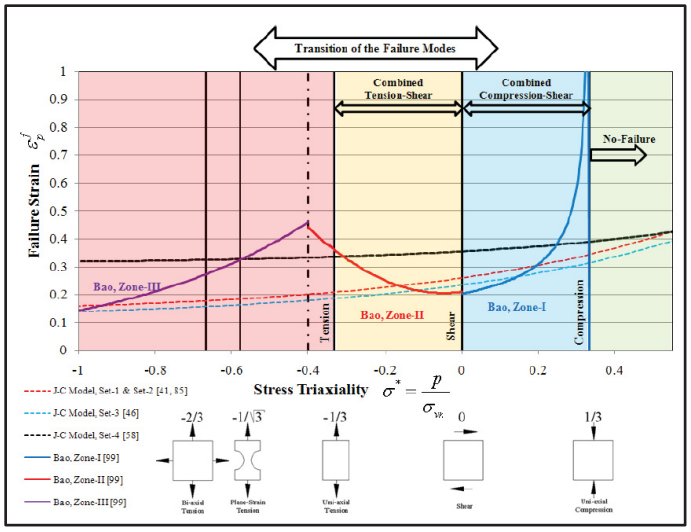

Figure-A III-15 Transition of the failure modes for Al2024-T351
Taken from Buyuk (2014, p. 9)

A depiction of the 3D failure locus function of the stress triaxiality and Lode angle is shown in Figure-A III-16.

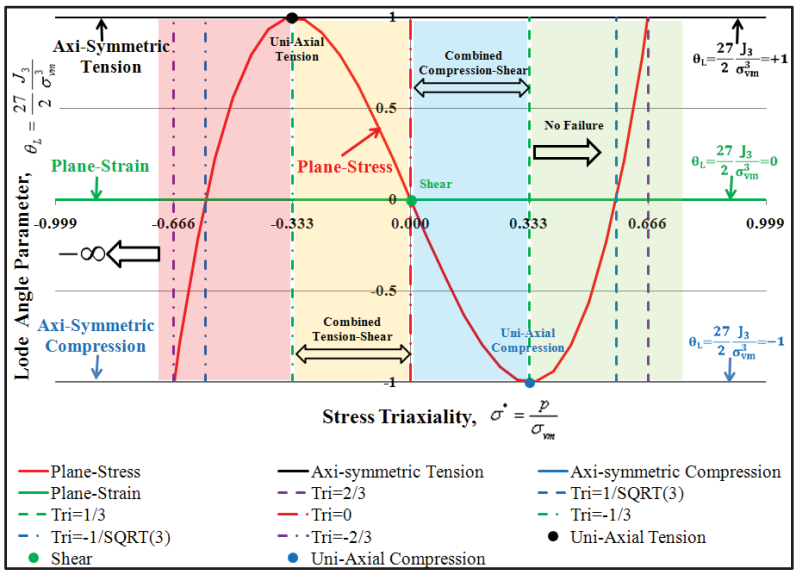

Figure-A III-16 Projection of the 3D failure locus on the stress space defined by triaxiality and Lode parameter
Taken from Buyuk (2014, p. 60)

The second function $g(\dot{\varepsilon}_p)$ expresses the plastic failure strain function of the strain rate, the third one defines the plastic failure strain dependency on the temperature $h(T)$ and the last one - $i(l_e)$ - establishing the dependency of the failure strain of the element size.

To express the first function, a series of tests on different specimen geometries are simulated. These specimen geometries are defined such as to develop a specific stress triaxiality at different Lode parameters under that particular type of loading. Although the intention is to cover the full range of triaxialities and Lode angles as shown in the stress domain in Figure-A III-16, the test selection was rather limited in the public data, and for the uncovered areas of the stress domain, some assumptions were made. It is to be re-stated that the present work does not focus on perfecting the material definition using the Johnson-Cook model, but rather allowing an as accurate as possible response from the impacted casing, and it is based on publicly available information.

All analyses performed under this sub-section replicated tests performed for other materials. In a first phase, an initial analysis of the simulated test considered the material as referenced in the test report, and replicated the results observed during the test. In the second phase, the material was replaced with A-286 and the simulation was repeated. With the exception of a particular occurrence (stress triaxiality -0.333 and Lode theta parameter 1.00), for which the analysis was calibrated with existing testing (Nicholas, 1980), (Kattus, Preston, & Lessley, 1958), all the other failure plastic strains were assumed similar proportions as in the referenced documents (Bao & Wierzbicki, 2004), (Buyuk, 2014), (Hammer, 2014), (Haight & al., 2016).

The series of simulations performed to determine the failure strain surface consists in 28 specimen tests (listed in Table-A III-1) with geometries generating different states of stresses under loading (Figure-A III-17).

The A-286 simulations were performed as well in two phases, the first phase during which the material card is defined as *MAT_024 (therefore a single stress-strain definition curve), and after determining the complete material card, the second phase confirming the complete material definition (*MAT_224).

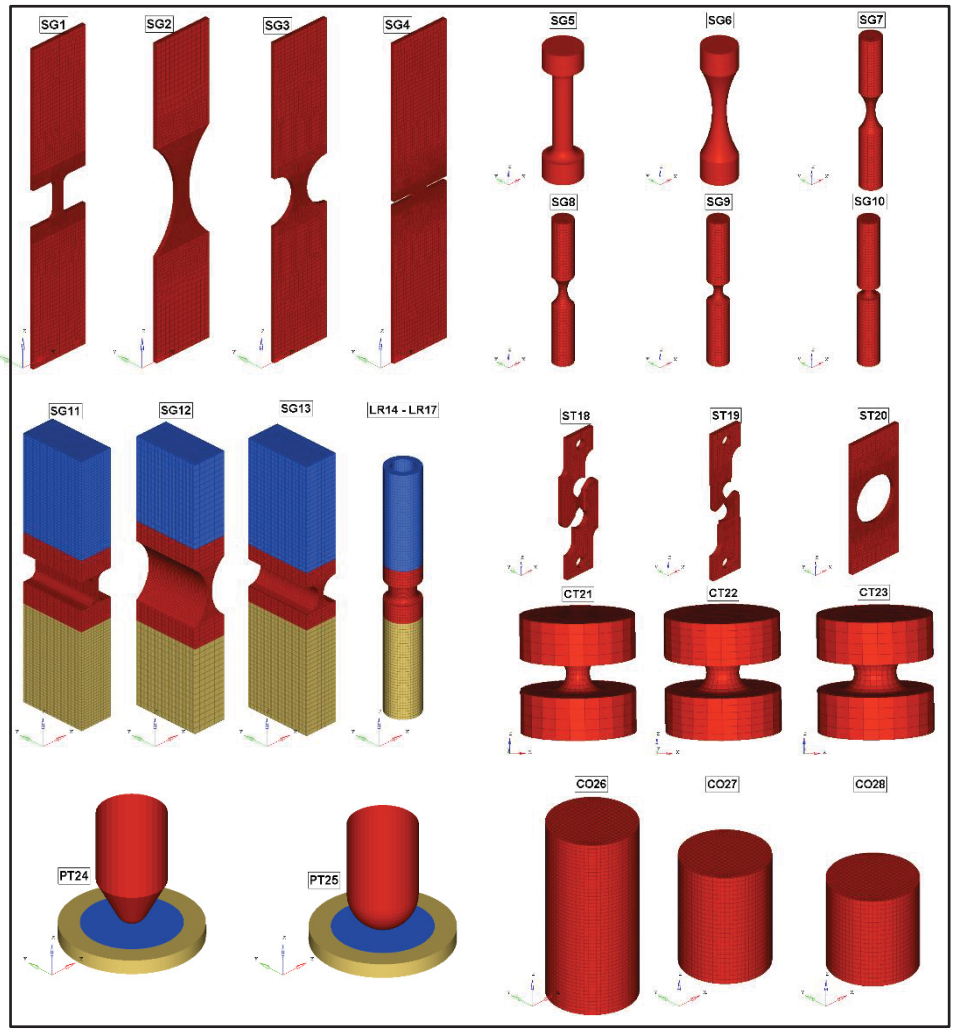

Figure-A III-17 Specimen test simulations used in the generation of the failure plastic strain surface

The failure strains resulting from the second set of analyses are listed in Table-A III-1. The same table also lists the triaxialities and Lode angle parameter as determined from the analyses.

Table-A III-1 A-286 tests simulated for the failure plastic strain surface determination

Name	Description	Triaxiality	Lode param	Failure strain
SG1	Plane stress specimen	-0.348	0.974	0.393
SG2	Plane stress specimen	-0.390	0.847	0.393
SG3	Plane stress specimen	-0.436	0.688	0.355
SG4	Plane stress specimen	-0.344	-0.059	0.265
SG5	Axisymmetric specimen	-0.368	1.000	0.388
SG6	Axisymmetric specimen	-0.445	1.000	0.356
SG7	Axisymmetric specimen	-0.487	0.999	0.330
SG8	Axisymmetric specimen	-0.534	0.996	0.309
SG9	Axisymmetric specimen	-0.708	0.998	0.257
SG10	Axisymmetric specimen	-0.813	0.998	0.266
SG11	Plane strain specimen	-0.546	0.168	0.282
SG12	Plane strain specimen	-0.603	0.155	0.286
SG13	Plane strain specimen	-0.700	0.092	0.302
LR14	Tension & torsion specimen	-0.371	0.880	0.129
LR15	Tension & torsion specimen	-0.156	0.454	0.108
LR16	Torsion specimen	0.000	0.001	0.096
LR17	Compression & torsion specimen	0.160	-0.452	0.123
SH18	Shear specimen	0.026	-0.109	0.273
ST19	Shear & tension specimen	-0.163	0.380	0.336
ST20	Shear & tension specimen	-0.344	0.976	0.341
CT21	Compression specimen	0.421	-0.927	0.651
CT22	Compression specimen	0.457	-0.864	0.572
CT23	Compression specimen	0.501	-0.793	0.517
PT24	Punch specimen	-0.658	0.994	0.091
PT25	Punch specimen	-0.640	-0.994	0.090
CO26	Uniaxial cylindrical compression	0.297	-0.875	0.427
CO27	Uniaxial cylindrical compression	0.182	-0.503	0.340
CO28	Uniaxial cylindrical compression	0.049	-0.439	0.276

As seen in Figure-A III-18, despite the large number of simulated tests, there are still areas in the triaxiality – Lode angle plane uncovered by experiments. For these areas, for the effective plastic failure strain values is assumed a weighted average of the values in the closest known points.

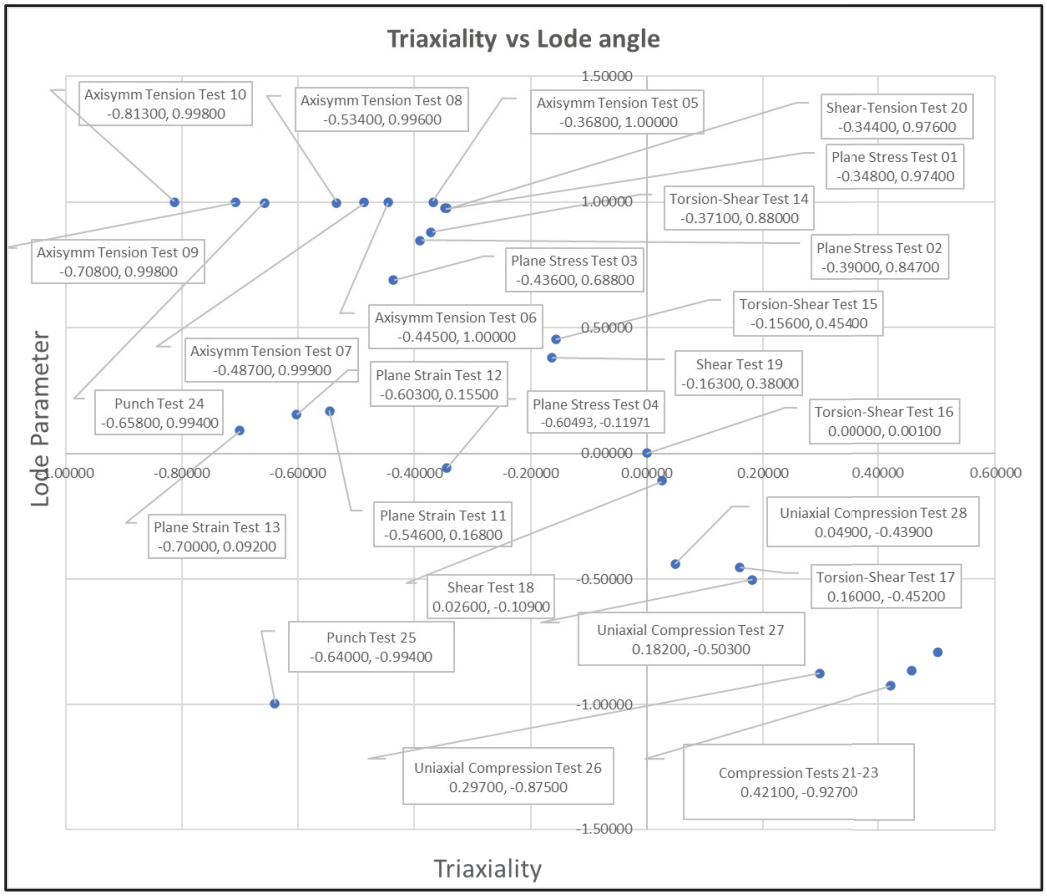

Figure-A III-18 Failure surface plan based on triaxiality and Lode angle

In the triaxiality – effective plastic failure strain plane, the different Lode angle curves were assumed variations as shown in Figure-A III-19. It is a simplified variation, based on assumed effective plastic failure strains, however the curves shapes are similar to the works reported in (Bao, 2003), (Buyuk, 2014), (Hammer, 2014), (Haight & al., 2016) and (Haight S. H., 2016). In addition to this, the full definition of the material card (*MAT_224) used in the simulation of tensile tests (SHB, thermal and containment) is in agreement with the experimental results, hence deemed acceptable for the purpose of this work.

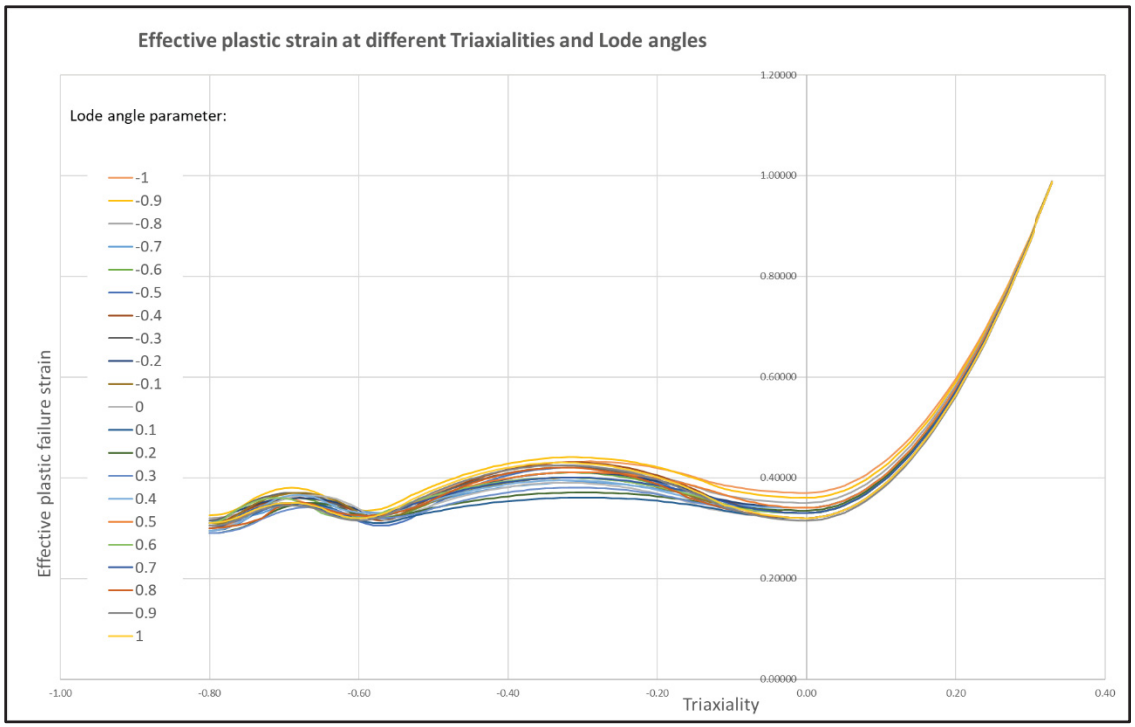

Figure-A III-19 Effective plastic failure strain function of triaxiality at different Lode angles

A 3D representation of the failure surface is shown in Figure-A III-20.

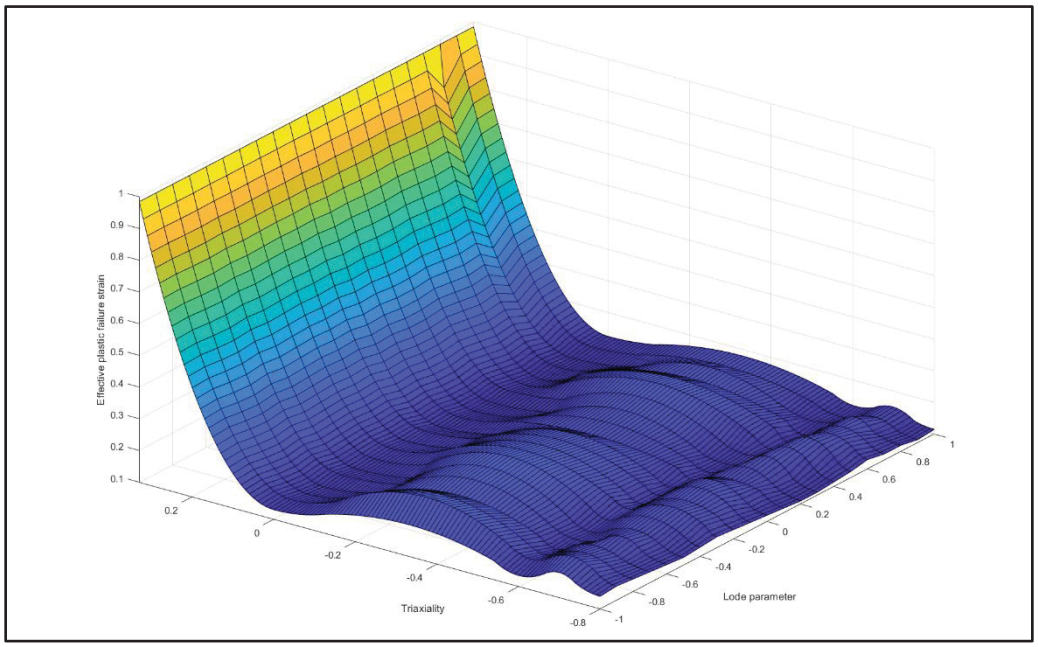

Figure-A III-20 Effective plastic failure strain surface

Past the triaxiality of 0.501, due to the absence of tests, the surface was extended assuming the last know value for the effective plastic strain until the triaxiality of 4.0, then ramped up artificially to 100% to the triaxiality of 5.0, similar as in (Haight & al., 2016). Also, the extension to the other end of the domain (-5.0) is done using the last known value at the corresponding Lode angle parameter (Figure-A III-21).

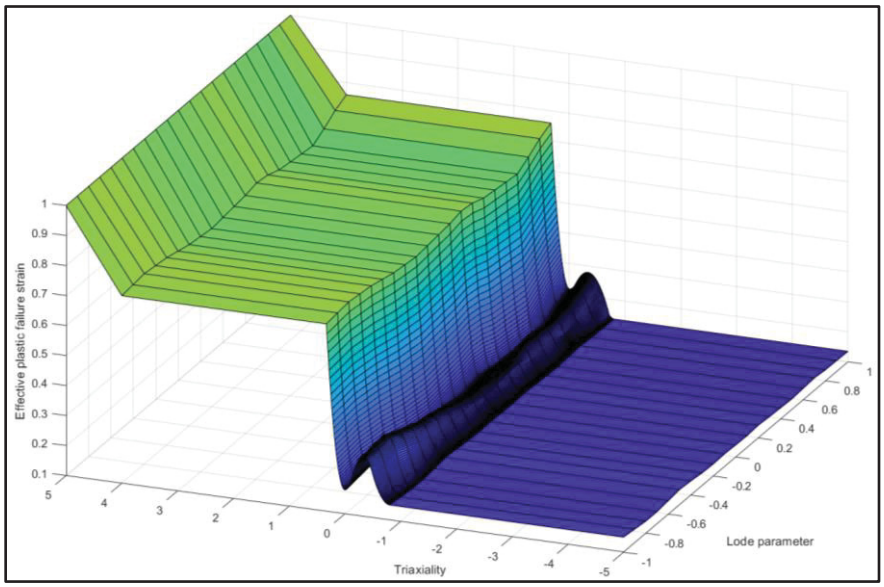

Figure-A III-21 Effective plastic failure surface extended

The failure surface is defined as a table (*DEFINE_TABLE) entry in the *MAT_224 card in LS_DYNA.

Scaling functions generation (LCG, LCH and LCI)

Three functions complete the implementation of the failure surface in the material card: the ***temperature scaling factor***, the ***strain rate scaling factor*** and the ***mesh size regularization*** (defines the plastic failure strain function of the element size). These three functions are defined in the material card as curves or tables of curves.

To determine the temperature scaling factors, the test series reported in (Kattus, Preston, & Lessley, 1958) are used. As the containment tests were performed at the room temperature, the temperature scaling function is based only on 2 points – room temperature, and 1200F.

The temperature scaling factor is defined as:

$$SF_{Temp} = \frac{\varepsilon_{pf}}{\varepsilon_{pf_{RT}}} \text{ (LS-DYNA Aerospace Working Group, 2019)} \quad \text{(A III.4)}$$

Due to the tests taking place at room temperature, the thermal softening effect is not considered, thus the two coefficients of the temperature scaling function are considered equal to 1.0 (Figure-A III-22).

Temperature		Scaling coefficient
K	F	
293.15	68	1.00
922.04	1200	1.00

Figure-A III-22 Temperature scaling curve

As the temperature scaling function is determined for the quasi-static specimen test, this scaling function establishes the elemental failure at different strain rates. For the strain rate function, the SHB simulations used for the generation of LCK1 are re-submitted iteratively, with the full material definition (*MAT_224), until determining the scaling factors corresponding to each strain rate (Figure-A III-23).

Strain rate	Failure strain	Scaling coefficient
0.000422	0.180	1.000
4.340	0.155	0.330
616.000	0.138	0.320

Figure-A III-23 Strain rate scaling curve

The mesh size regularization curve is created to account for the failure strain function of the element size.

The guidelines in (LS-DYNA Aerospace Working Group, 2019) define the element size as the ratio between the element volume and its maximum side area. Similarly (as for the case of LCG - temperature dependency of the failure strain), the quasi-static room temperature analysis is used (and the associated specimen test results), on the same SHB model, but with several different mesh sizes (Figure-A III-24). For elements smaller than 0.118 mm, it is assumed a scaling factor of 1.0. As the tests used as reference represented specimens with a unique triaxiality, this regularization function is represented by a single curve. For future works, if more details are required, tests should be performed supplementing the available data; case in which this regularization function can be defined with a table including curves at multiple triaxialities.

Element size	Failure strain	Scaling Factor
0.0000	0.180	1.000
0.1180	0.17976	0.940
0.3280	0.18053	0.930
0.4250	0.17930	0.920
0.7521	0.17953	0.770
1.5519	0.18163	0.540
2.0000	0.180	0.500

Figure-A III-24 Element size regularization curve

APPENDIX IV

MISCELANEOUS CALCULATIONS

$t := 1 \cdot mm, 1.01 \cdot mm .. 20 \cdot mm$ $m := 3. \cdot 2 = 6$

$h_{JT3D} := 6.305\ mm$ $h_{JT8D} := 2.6\ mm$

$b_{JT3D} := m \cdot h_{JT3D} = 37.83\ mm$ $b_{JT8D} := m \cdot h_{JT8D} = 15.6\ mm$

$w_{JT3D} := 35.086\ mm$ $w_{JT8D} := 45.3\ mm$

$\theta_{JT3D}(t) := \frac{\frac{t}{2}}{\frac{b_{JT3D}}{2}}$ $\theta_{JT8D}(t) := \frac{\frac{t}{2}}{\frac{b_{JT8D}}{2}}$

$h_{JT3D} := 6.305 \cdot mm$ $h_{JT8D} := 5.2\ mm$

$w_{JT3D} := 35.086 \cdot mm$ $w_{JT8D} := 45.3\ mm$

$R_{JT3D} := 447.51 \cdot mm$ $R_{JT8D} := 357.975 \cdot mm$

$D_{JT3D} := 2 \cdot R_{JT3D} = 895.02\ mm$ $D_{JT8D} := 2 \cdot R_{JT8D} = 715.95\ mm$

$n_{JT3D} := 122$ $n_{JT8D} := 88$

$C_{JT3D} := \pi \cdot \frac{D_{JT3D}}{n_{JT3D}} = 23.047\ mm$ $C_{JT8D} := \pi \cdot \frac{D_{JT8D}}{n_{JT8D}} = 25.559\ mm$

$A_{JT3D} := \pi \cdot \frac{min\left(w_{JT3D}, C_{JT3D}\right)^2}{4} = 417.191\ mm^2$

$A_{JT8D} := \pi \cdot \frac{min\left(w_{JT8D}, C_{JT8D}\right)^2}{4} = 513.085\ mm^2$

$P_{JT3D} := 2 \cdot \left(w_{JT3D} + h_{JT3D}\right) = 82.782\ mm$ $P_{JT8D} := 2 \cdot \left(w_{JT8D} + h_{JT8D}\right) = 101\ mm$

$\sigma_{YTS} := 96.4 \cdot ksi = 664.655\ MPa$ $\sigma_{UTS} := 146.7 \cdot ksi = 1011.461\ MPa$ $\varepsilon := 25\%$

$\tau_D := \frac{\sigma_{UTS}}{\sqrt{3}} = 583.967\ MPa$

Figure-A IV-1 Thickness calculations

$K := .5$ $\alpha := .95$ $\beta := .5$ $\gamma := .592$ $\delta := .849$ $\theta := .9$

$$M_{JT3D}(t) := \frac{C_{JT3D} \cdot t^2}{4} \cdot \sigma_{YTS} \qquad M_{JT8D}(t) := \frac{C_{JT8D} \cdot t^2}{4} \cdot \sigma_{YTS}$$

$$W_{bending\_JT3D}(t) := M_{JT3D}(t) \cdot \theta_{JT3D}(t) \qquad W_{bending\_JT8D}(t) := M_{JT8D}(t) \cdot \theta_{JT8D}(t)$$

$$W_{stretching\_JT3D}(t) := \alpha \cdot A_{JT3D} \cdot t \cdot \varepsilon \cdot \gamma \cdot \frac{\sigma_{UTS} + \sigma_{YTS}}{2} \cdot \delta$$

$$W_{stretching\_JT8D}(t) := \alpha \cdot A_{JT8D} \cdot t \cdot \varepsilon \cdot \gamma \cdot \frac{\sigma_{UTS} + \sigma_{YTS}}{2} \cdot \delta$$

$$W_{shear\_JT3D}(t) := K \cdot \tau_D \cdot \theta \cdot P_{JT3D} \cdot \beta \cdot t^2 \qquad W_{shear\_JT8D}(t) := K \cdot \tau_D \cdot \theta \cdot P_{JT8D} \cdot \beta \cdot t^2$$

$$W_{stretch\_and\_bending\_JT3D}(t) := W_{stretching\_JT3D}(t) + W_{bending\_JT3D}(t)$$

$$W_{shear\_and\_bending\_JT3D}(t) := W_{shear\_JT3D}(t) + W_{bending\_JT3D}(t)$$

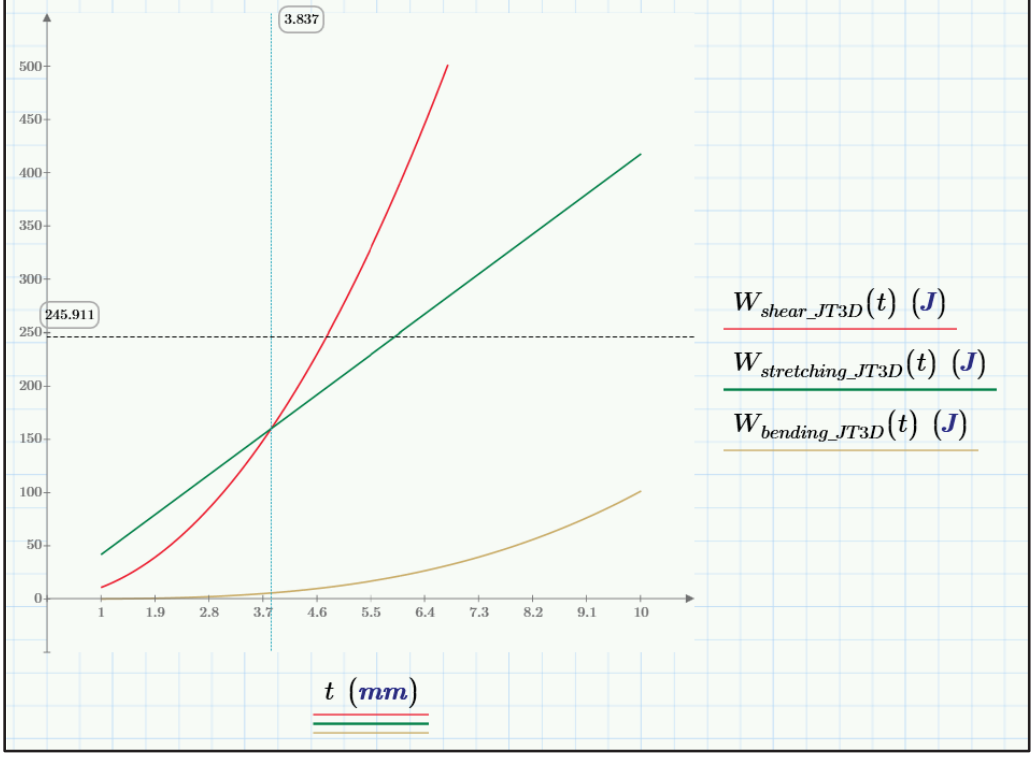

Figure-A IV-2 Thickness calculations (continued)

$$t_{threshold\_JT3D} := \frac{\alpha \cdot A_{JT3D} \cdot \varepsilon \cdot \gamma \cdot \frac{\sigma_{UTS} + \sigma_{YTS}}{2} \cdot \delta}{K \cdot \tau_D \cdot \beta \cdot P_{JT3D} \cdot \theta} = 3.837\ mm$$

$$t_{threshold\_JT8D} := \frac{\alpha \cdot A_{JT8D} \cdot \varepsilon \cdot \gamma \cdot \frac{\sigma_{UTS} + \sigma_{YTS}}{2} \cdot \delta}{K \cdot \tau_D \cdot \beta \cdot P_{JT8D} \cdot \theta} = 3.868\ mm$$

$$W_{stretching\_JT3D}\left(t_{threshold\_JT3D}\right) = 160.139\ J$$

$$W_{shear\_JT3D}\left(t_{threshold\_JT3D}\right) = 160.139\ J$$

$$W_{stretching\_JT8D}\left(t_{threshold\_JT8D}\right) = 198.528\ J$$

$$W_{shear\_JT8D}\left(t_{threshold\_JT8D}\right) = 198.528\ J$$

$$KE_{JT3D} := 36275\ lbf \cdot in = 4098.525\ J \qquad K_{exch} := 6\%$$

$$KE_{JT8D} := 29916\ lbf \cdot in = 3380.054\ J$$

$$KE_{finalJT3D} := K_{exch} \cdot KE_{JT3D} = 245.911\ J$$

$$KE_{finalJT8D} := K_{exch} \cdot KE_{JT8D} = 202.803\ J$$

JT3D Calculation

$$t_{tens\_JT3D} := \frac{KE_{finalJT3D}}{\alpha \cdot A_{JT3D} \cdot \varepsilon \cdot \gamma \cdot \frac{\sigma_{UTS} + \sigma_{YTS}}{2} \cdot \delta} = 5.892\ mm$$

$$t_{shear\_JT3D} := \sqrt{\frac{KE_{finalJT3D}}{K \cdot \tau_D \cdot \beta \cdot P_{JT3D} \cdot \theta}} = 4.755\ mm$$

Figure-A IV-3 Thickness calculations (continued)

JT8D Calculation

$$t_{tens\_JT8D} := \frac{KE_{finalJT8D}}{\alpha \cdot A_{JT8D} \cdot \varepsilon \cdot \gamma \cdot \frac{\sigma_{UTS} + \sigma_{YTS}}{2} \cdot \delta} = 3.951 \ mm$$

$$t_{shear\_JT8D} := \sqrt{\frac{KE_{finalJT8D}}{K \cdot \tau_D \cdot \beta \cdot P_{JT8D} \cdot \theta}} = 3.909 \ mm$$

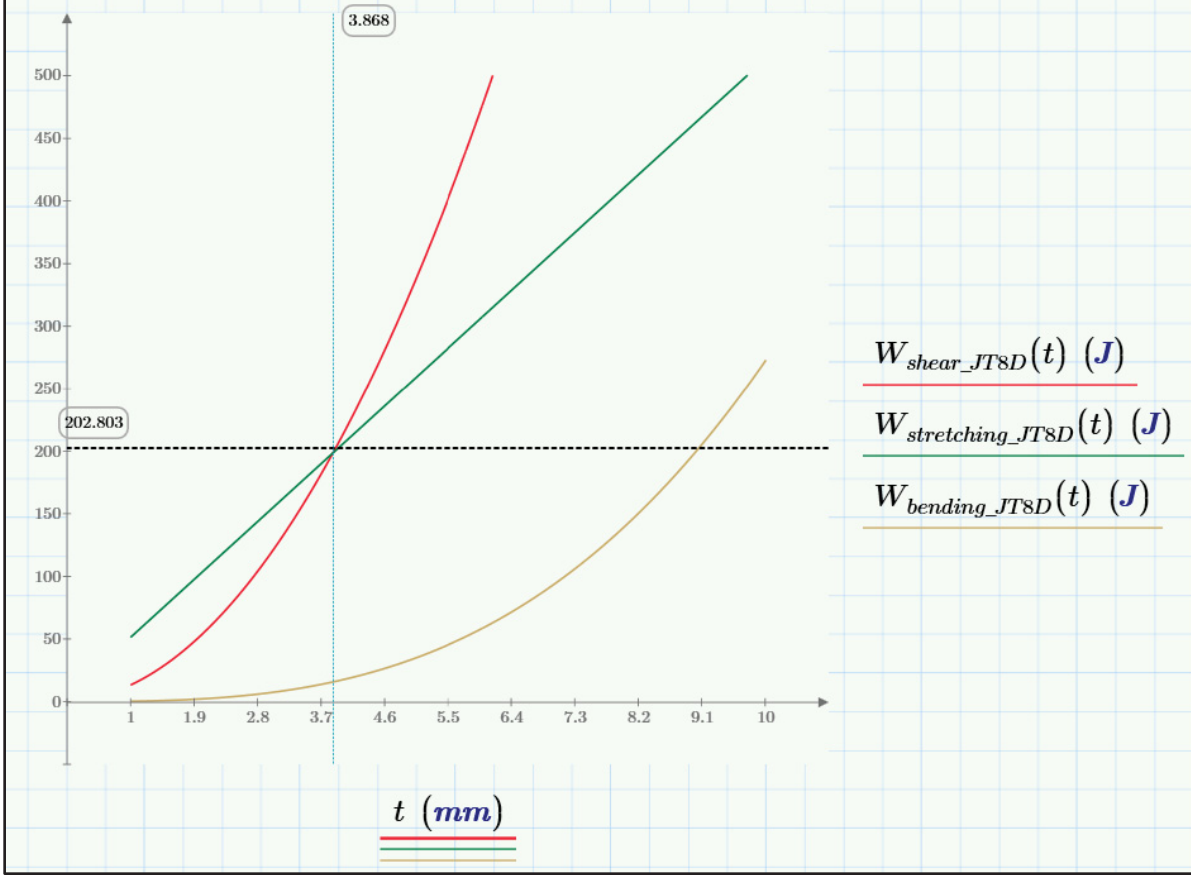

Figure-A IV-4 Thickness calculations (continued)

LIST OF BIBLIOGRAPHICAL REFERENCES

Australian Transport Safety Bureau. (2010). *In-flight uncontained engine failure overhead Batam Island, Indonesia 4 November 2010 VH-OQA Airbus A380–842.* Canberra, Australia: Australian Transport Safety Bureau ATSB Transport Safety Report AO-2010-089.

Australian Transport Safety Report. (2008). *Engine Failure - Jabiru, NT - 11 February 2008 VH-VAZ Beech Aircraft Corporation 1900, Aviation Occurrence Investigation - AO-2008-008.* ATSB Transport Safety Bureau.

Backman, M. E. (1976). *Terminal ballistics.* China Lake, CA: Naval Weapons Center.

Backman, M. E., & Goldsmith, W. (1978). The mechanics of penetration of projectiles into targets. *International Journal of Engineering Science, 16*(1-A), 1-99.

Bao, Y. (2003). *Prediction of ductile crack formation in uncracked bodies.* Massachusetts Institute of Technology.

Bao, Y., & Wierzbicki, T. (2004). On fracture locus in the equivalent strain and stress triaxiality space. *International Journal of Mechanical Sciences, 46(1)*, 81-98.

Børvik, T., & al., e. (2003). Effect of target thickness in blunt projectile penetration of Weldox 460 E steel plates. *International journal of impact engineering, 28*(4), 413-464.

Bretschneider, S., & al., e. (2008). Compressor casing preliminary design based on features. *Turbo Expo: Power for Land, Sea, and Air. Vol. 43154.* Berlin, Germany.

Buyuk, M. (2014). *Development of a new metal material model in LS-DYNA Part 2: Development of a tabulated thermo-viscoplastic material model with regularized failure for dynamic ductile failure prediction of structures under impact loading.* Atlantic City International Airport: US Department of Transportation, Federal Aviation Administration.

Chang, K.-H., Yu, X., & Choi, K. K. (1996). Design sensitivity analysis and optimization (DSO)—Structural reliability analysis. *The First World Congress of Structural and Multidisciplinary Optimization.* Ed. by Olhoff and Rozvany.

Collins, T. P., & Witmer, E. A. (1973). *Application of the Collision-Imparted Velocity Method for Analyzing the Responses of Containment and Deflector Structures to Engine Rotor Fragment Impact.* Cambridge, Massachusetts: Aeroelastic and Structures Research Laboratory, Department of Aeronautics and Astronautics, MIT.

Corbett, G. G., & Reid, S. R. (1993). Quasi-static and dynamic local loading of monolithic simply-supported steel plate. *International journal of impact engineering, 13*(3), 423-441.

Corbett, G. G., Reid, S. R., & Johnson, W. (1996). Impact loading of plates and shells by free-flying projectiles: a review. *International Journal of Impact Engineering, 18*(2), 141-230.

Corran, R. S., Ruiz, C., & Shadbolt, P. J. (1983). On the design of containment shields. *Computers & Structures, 16*(1-4), 563-572.

Corran, R. S., Shadbolt, P. J., & Ruiz, C. (1983). Impact loading of plates—an experimental investigation. *International Journal of Impact Engineering, 1*(1), 3-22.

Crouch, I. G., & Baxter, B. J. (1990). Empirical tests of a model for thin plate perforation. *International journal of impact engineering, 9*(1), 19-33.

Di Sciuva, M., Frola, C., & Salvano, S. (2003). Low and high velocity impact on Inconel 718 casting plates: ballistic limit and numerical correlation. *International journal of impact engineering, 28*(8), 849-876.

Dikshit, S. N., Kutumbarao, V. V., & Sundararajan, G. (1995). The influence of plate hardness on the ballistic penetration of thick steel plates. *International journal of impact engineering, 16*(2), 293-320.

Eryilmaz, I., Guenchi, B., & Pachidis, V. (2019). Multi-blade shedding in turbines with different casing and blade tip architectures. *Aerospace Science and Technology, 87*, 300-310.

Federal Aviation Administration, U.S. Department Of Transportation. (1984). 14 CFR 33.94 - Blade containment and rotor unbalance tests.

Federal Aviation Administration, U.S. Department of Transportation. (1990). *Turbine Engine Rotor Blade Containment/Durability, Advisory Circular AC 33-5.* Federal Aviation Administration, U.S. Deprtment of Transportation.

Federal Aviation Administration, U.S. Department Of Transportation. (1997, March 25). Design Considerations For Minimizing Hazards Caused By Uncontained Turbine Engine and Auxiliary Power Unit Rotor Failure, Advisory Circular 20-128A. *Advisory Circular AC-20-128A*. Washington, D.C., U.S.A.: U.S. Department of Transportation.

Goatham, J. I., & Stewart, R. M. (1976). Missile firing tests at stationary targets in support of blade containment design. *Journal of Engineering for Power*, 159-164.

Gunderson, C. O. (1977). *Study to improve airframe turbine engine rotor blade containment.* LONG BEACH CA: DOUGLAS AIRCRAFT CO.

Hagg, A. C., & Sankey, G. O. (1974, April). The containment of disk burst fragments by cylindrical shells. *Journal of Engineering for Power*, 114-123. Retrieved from http://gasturbinespower.asmedigitalcollection.asme.org

Haight, S. H. (2016). An anisotropic and asymmetric Material Model for Simulation of Metals under Dynamic Loading. Fairfax, Va: Diss. George Mason University.

Haight, S., & al., e. (2016). *Development of a titanium alloy Ti-6Al-4V material model used in LS-DYNA.* Washington, DC: George Mason University, The George Washington University, NASA Glenn Research Center.

Hammer, J. T. (2014). *Plastic deformation and ductile fracture of Ti-6Al-4V under various loading conditions.* Columbus, OH: The Ohio State University.

Haynes Stellite Company. (1960, November). HAYNES STELLITE ALLOY No. 31: High Heat Resistant Alloy. *Alloy Digest*. Upper Montclair, New Jersey: Engineering Alloys Digest, Inc. doi:doi: https://doi.org/10.31399/asm.ad.co0008

He, Q., & al., e. (2012). Simulation methodology development for rotating blade containment analysis. *Journal of Zhejiang University SCIENCE A, 13*(4), 239-259.

He, Q., & al., e. (2013). Perforation of aero-engine fan casing by a single rotating blade. *Aerospace Science and Technology, 25*(1), 234-241.

He, Q., & al., e. (2016). Multi-blade effects on aero-engine blade containment. *Aerospace Science and Technology, 49*, 101-111.

Heermann, K. F., Eriksson, R. H., & McClure, K. R. (1977). *Study to Improve Turbine Engine Rotor Blade Containment.* East Hartford, CT: PRATT AND WHITNEY AIRCRAFT GROUP EAST HARTFORD CT COMMERCIAL PRODUCTS DIV.

Hill, H. N. (1944). Determination of stress-strain relations from" offset" yield strength values. Pittsburgh, Pa: Aluminum Co Of America .

Hunter, I., & al. (1999). Analysis Of Hot Section Failures On Gas Turbines In Process Plant Service. *Proceedings of the 28th Turbomachinery Symposium.* Texas A&M University. Turbomachinery Laboratories.

Japan Transport Safety Board. (2011). *Nippon Cargo Airlines Co. Ltd JA01KZ, Aircraft Serious Incident Investigation Report AI2011-5.* Japan Transport Safety Board.

Johnson, G. R. (1983). A constitutive model and data for materials subjected to large strains, high strain rates, and high temperatures. *Proc. 7th Inf. Sympo. Ballistics*, (pp. 541-547).

Johnson, G. R., & Cook, W. H. (1985). Fracture characteristics of three metals subjected to various strains, strain rates, temperatures and pressures. *Engineering fracture mechanics, 21*(1), 31-48.

Kattus, J. R., Preston, J. B., & Lessley, H. L. (1958). *Determination of Tensile, Compressive, Bearing and Shear Properties of Sheet Steels at Elevated Temperatures.* BIRMINGHAM, AL: SOUTHERN RESEARCH INST.

Kazempour-Liasi, H., Shafiei, A., & Lalegani, Z. (2019). Failure Analysis of First and Second Stage Gas Turbine Blades. *Journal of Failure Analysis and Prevention, 19*(6), 1673-1682.

Lane, A. D. (1989). *Development of an advanced fan blade containment system.* PHOENIX AZ: ADVANCED STRUCTURES TECHNOLOGY INC.

Leech, J. W., Witmer, E. A., & Yeghiayan, R. P. (1971). *Dimensional analysis considerations in the engine rotor fragment containment/deflection problem.* Cambridge, Massachusetts: Aeroelastic and Structures Research Laboratory, Department of Aeronautics and Astronautics, MIT.

Liu, D., & Stronge, W. J. (2000). Ballistic limit of metal plates struck by blunt deformable missiles: experiments. *International journal of solids and structures, 37*(10), 1403-1423.

Livermore Software Technology. (2020, September 9). *LS-DYNA R12 Keyword Manual Vol II.* Retrieved 08 10, 2021, from http://ftp.lstc.com/anonymous/outgoing/marleigh/manual/LS-DYNA_Manual_Volume_II_R12_Ver2.pdf

LS-DYNA Aerospace Working Group. (2011). *Modeling Guidelines Document V19-1.* Livermore: Solihull: LS-DYNA Aerospace Working Group.

LS-DYNA Aerospace Working Group. (2019, September 29). *https://awg.lstc.com/tiki-index.php.* Retrieved May 16, 2021, from https://awg.lstc.com/tiki-index.php?page=Material+Model+User+Guides+New

Mangano, G. J. (1972). *Rotor Burst Protection Program. Phases VI & VII-Exploratory Experimentation to Provide Data for the Design of Rotor Burst Fragment Containment Rings.* NAPTC-AED-1968, US Navy.

Martino, A. A., & Mangano, G. J. (1969). *Rotor Burst Protection Program Initial Test Results.* NAVAL AIR PROPULSION TEST CENTER PHILADELPHIA PA AERONAUTICAL ENGINE DEPT.

Mathis, J. A. (1997). *Design Procedures and Analysis of Turbine Rotor Fragment Hazard Containment.* Wichita State Univ KS Dept of Mechanical Engineering.

McCallum, R. B., Leech, J. W., & Witmer, E. A. (1969). *Progress in the Analysis of Jet Engine Burst-Rotor Containment Devices.* Cambridge: MIT Aeroelastic and Structures Research Laboratory.

McCarthy, D. (1976). Definition of engine debris and some proposals for reducing potential damage to aircraft structure. *AGARD Specialists Meeting on Impact Damage Tolerance of Struc*, (pp. 10 p(SEE N 76-19471 10-39)).

McCarthy, D. (1976). Definition of engine debris and some proposals for reducing potential damage to aircraft structure. *AGARD Specialists Meeting on Impact Damage Tolerance of Struc. 10 p(SEE N 76-19471 10-39).*

McCarthy, D. (1977). *Types of rotor failure and characteristics of fragments.* Derby, United Kingdom: MIT - An Assessment of Technol. for Turbojet Engine Rotor Failures.

McCarthy, D. (1977). *Types of rotor failure and characteristics of fragments.* Derby: Rolls-Royce Limited.

Megson, T. H. (2019). *Structural and stress analysis.* Butterworth-Heinemann.

Nicholas, T. (1980). *Dynamic tensile testing of structural materials using a split Hopkinson bar apparatus.* WRIGHT-PATTERSON AFB OH: AIR FORCE WRIGHT AERONAUTICAL LABS.

O'Dowd, D. O. (2010). *Aero-thermal performance of transonic high-pressure turbine blade tips.* Oxford: Oxford University.

Pereira, J. M., & Lerch, B. A. (2001). Effects of heat treatment on the ballistic impact properties of Inconel 718 for jet engine fan containment applications. *International Journal of Impact Engineering, 25*(8), 715-733.

Radin, J. a. (1988). Normal projectile penetration and perforation of layered targets. *International Journal of Impact Engineering, 7*(2), 229-259.

Regulation, Federal Aviation. (1992). *part 33, Airworthiness Standards: Aircraft Engines.* Federal Aviation Administration.

Rice, R. C., & al., e. (2003). *Metallic materials properties development and standardization (MMPDS) Handbook.* NTIS Virginia Scientific Report.

Ridley, B. (2018). *Impact Studies of Containment Ring during Blade Shed in Turbofan Engines.* Toronto: Department of Mechanical and Industrial Engineering, University of Toronto.

Rolls-Royce. (2022, April 29). *https://www.rolls-royce.com/products-and-services/civil-aerospace/airlines/trent-1000.aspx#section-related-stories*. (Rolls-Royce plc 2021) Retrieved April 27, 2021, from https://www.rolls-royce.com/products-and-services/civil-aerospace/airlines/trent-1000.aspx#section-related-stories: https://www.rolls-royce.com/products-and-services/civil-aerospace/airlines/trent-1000.aspx#section-related-stories

Rossman, Axel; Institute of Thermal Turbomachinery and Machine Dynamics; Graz University of Technology. (2021, May 4). *Aeroengine Safety.* Retrieved May 4, 2021, from Aeroengine Safety: https://aeroenginesafety.tugraz.at/doku.php?id=start

SAE International Engineering Society for Advancing Mobility Land Sea Air and Space. (1996). *Report On Aircraft Engine Containment.* Warrendale, PA: SAE International.

Salvino, J. T., DeLucia, R. A., & Russo, T. (1988). *Experimental Guidelines for the Design of Turbine Rotor Fragment Containment Rings.* TRENTON NJ: NAVAL AIR PROPULSION CENTER.

Saravanamuttoo, H., Rogers, G., Cohen, H., & Straznicky, P. (2009). *Gas Turbine Theory.* Harlow: Pearson Education Limited.

Sarkar, S., & Atluri, S. N. (1995). Finite Element Analysis of Engine Rotor Failure and Containment. In *Contemporary Research in Engineering Science* (pp. 468-490). Berlin: Springer-Verlag.

Sarkar, S., & Atluri, S. N. (1995). Impact Loads and Containment Aspects during a Rotor Failure in Aircraft Jet Engines. In *Computational Mechanics' 95* (pp. 2165-2170). Berlin, Heidelberg: Springer.

Sarkar, S., & Atluri, S. N. (1996). Failure analysis of aircraft engine containment structures. *FAA-NASA Symposium on the Continued Airworthiness of Aircraft Structures, Proceedings. Vol. 1.* Atlanta, GA.

Shadbolt, P. J., Corran, R. S., & Ruiz, C. (1983). A comparison of plate perforation models in the sub-ordnance impact velocity range. *International Journal of Impact Engineering, 1*(1), 23-49.

Stewart, M. (2018). *Surface Production Operations: Volume IV: Pumps and Compressors.* Gulf Professional Publishing.

Stotler, C. L., & Coppa, A. P. (1979). *Containment of composite fan blades.* Cincinnati: General Electric Company, Aircraft Engine Group.

Swift, H. (1952). Plastic instability under plane stress. *Journal of the Mechanics and Physics of Solids, 1*(1), 1-18.

Szuladzinski, G. (2009). *Formulas for mechanical and structural shock and impact.* CRC Press.

Tansel, D. (2010). *Ballistic penetration of hardened steel plates.* Ankara, Turkey: Middle East Technical University.

Teng, X., & Wierzbicki, T. (2008). Gouging and fracture of engine containment structure under fragment impact. *Journal of Aerospace Engineering, 21*(3), 174-186.

The Nickel Institute. (n.d.). Engineering Properties of ALLOY 713C. *The Nickel Institute*. Retrieved August 10, 2021, from https://nickelinstitute.org/media/2487/alloys-713c_337.pdf

Transportation Safety Board of Canada. (2014). *Uncontained Turbine Rotor Failure BOMBARDIER INC. BD-500-1A10 (C SERIES CS100), C-FBCS.* Gatineau: Transportation Safety Board of Canada.

Vasko, Tom; LS-DYNA® Aerospace Working Group. (2019, September 29). **MAT_224 User Guide.* Retrieved 08 10, 2021, from https://awg.lstc.com/tiki-download_file.php?fileId=1648

Witmer, E. A., & Spilker, R. L. (1977). *Analysis of simple 2-D and 3-D metal structures subjected to fragment impact.* Cambridge: Aeroelastic and Structures Research Laboratory, Department of Aeronautics and Astronautics, Massachusetts Institute of Technology.

Woodward, R. L. (1978). The penetration of metal targets by conical projectiles. *International Journal of Mechanical Sciences, 20*(6), 349-359.

Woodward, R., & Cimpoeru, S. (117–131). A study of the perforation of aluminium laminate targets. *International Journal of Impact Engineering, 21*(3), 1998.

Xuan, H., Hu, Y., Wu, Y., & He, Z. (2018). Containment ability of Kevlar 49 composite case under spinning impact. *Journal of Aerospace Engineering, 31*(2), 04017096.

Zaid, A. I., & Travis, F. W. (1974). An examination of the effect of target thickness in the perforation of mild steel plate by a flat-ended projectile. *International Journal of Mechanical Sciences 16.6*, 373-383.

Zukas, J. (1980). *Impact Dynamics: Theory and Experiment.* Aberdeen Proving Ground, Maryland: U.S. Army Armament Research and Development Command, Ballistic Research Laboratory.